



HAL
open science

Optimisation de fabrication de cellules solaires tandem perovskite/CIGS

Vincent Dufoulon

► **To cite this version:**

Vincent Dufoulon. Optimisation de fabrication de cellules solaires tandem perovskite/CIGS. Science des matériaux [cond-mat.mtrl-sci]. Institut Polytechnique de Paris, 2023. Français. NNT : 2023IP-PAX060 . tel-04496224

HAL Id: tel-04496224

<https://theses.hal.science/tel-04496224v1>

Submitted on 8 Mar 2024

HAL is a multi-disciplinary open access archive for the deposit and dissemination of scientific research documents, whether they are published or not. The documents may come from teaching and research institutions in France or abroad, or from public or private research centers.

L'archive ouverte pluridisciplinaire **HAL**, est destinée au dépôt et à la diffusion de documents scientifiques de niveau recherche, publiés ou non, émanant des établissements d'enseignement et de recherche français ou étrangers, des laboratoires publics ou privés.



Optimisation de fabrication de cellules solaires tandem perovskite/CIGS

Thèse de doctorat de l'Institut Polytechnique de Paris
préparée à l'École polytechnique

École doctorale n°626 École doctorale de l'Institut Polytechnique de Paris
(ED IP Paris)

Spécialité de doctorat: Physique de la matière condensée

Thèse présentée et soutenue à Palaiseau, le 07 Juillet 2023, par

Vincent Dufoulon

Composition du Jury :

Jessica de Wild (Professeure, Hasselt University)	Rapporteur Présidente du jury
Polina Volovitch (Maître de Conférences, Chimie ParisTech)	Rapporteur
Jérémy Barbé (Maître de Conférences, CNRS)	Examineur
Robert Hoye (Professeure, Oxford University)	Examineur
Daniel Lincot (Directeur de recherche émérite, CNRS)	Invité
Philip Schulz (Directeur de Recherche, CNRS, IPVF)	Directeur de thèse
Jean-Paul Kleider (Directeur de recherche, CNRS, GEEPS, U-PSaclay)	Co-encadrant de thèse
Muriel Bouttemy (Ingénieure de recherche, CNRS, UVSQ)	Co-encadrante de thèse
Nathanaëlle Schneider (Chargée de recherche, CNRS, IPVF)	Co-encadrante de thèse

Acknowledgments

The PhD candidate is grateful for funding from the European Union's Horizon 2020 research and innovation program under grant agreement no. 850937 (PERCISTAND).

Acronyms

2PACz	2-(9 <i>H</i> -Carbazol-9-yl)ethyl)-phosphonic acid
ACN	Acetonitrile
ALD	Atomic Layer Deposition
AZO	Aluminium Zinc Oxide
CIGS	Copper Indium Gallium Selenium
CBM	Conduction Band Minimum
CPD	Contact Potential Difference
CIGS	Cu(In _{1-x} Ga _x)Se ₂
CTL	Charge Transport Layer
CV	Cyclic Voltammetry
DMF	Dimethylformamide
DMSO	Dimethyl Sulfoxide
EQE	External Quantum Efficiency
ETL	Electron Transport Layer
FA	Formamidinium
FAI	Formamidinium Iodide
Fc	Ferrocene
FWHM	Full Width at Half Maximum
HOMO	Highest Occupied Molecular Level
HTL	Hole Transport Layer
ITO	Indium Tin Oxide
IZO	Indium Zinc Oxide
KP	Kelvin Probe
LUMO	Lowest Unoccupied Molecular Level
MA	Methylammonium
MAI	Methylammonium Iodide
Me-nickelocene	bis(methylcyclopentadienyl)nickel(II)
MeO-2PACz	2-(3,6-Dimethoxy-9 <i>H</i> -carbazol-9-yl)ethyl)-phosphonic acid
MHP	Metal Halide Perovskite
MPPT	Maximum power point tracking
Ni(amd)₂	Bis(N,N'-di- <i>t</i> -butylacetamidinato)nickel(II)
NiO %	Relative proportion of stoichiometric NiO compared to all NiO _x H _y subspecies
NiO_x	Nickel Oxide

Np-AZO	Aluminium zinc oxide nanoparticles
Np-ZnO	Zinc oxide nanoparticles
NS	Number of Sweeps
PES	Photoemission Spectroscopy
PL	Photoluminescence
PSC	Perovskite solar cell
PV	Photovoltaic
SEM	Scanning Electron Microscope
SnO₂	Tin Oxide
TCO	Transparent Conductive Oxide
TF	Transmission Function
TiO₂	Titanium Dioxide
UPS	Ultraviolet Photoelectron Spectroscopy
UV	Ultraviolet
UV-Vis	Ultraviolet - Visible
UV-O₃	Ultraviolet Ozone
VBM	Valence Band Maximum
WF	Work Function
XPS	X-ray Photoelectron Spectroscopy
XRD	X-ray Diffraction

Table of Contents

Acknowledgments /

Acronyms //

Table of Contents /V

List of Figures VII

List of Tables XIV

General Introduction	1
1. Chapter 1	4
Background and Objectives	
1.1. Introduction.....	6
1.2. General principle of solar cells	6
1.2.1. General principle of a semiconductor.....	6
1.2.2. General structure of a solar cell.....	8
1.2.3. Characteristics of a solar cell	9
1.2.3.1. Open-circuit voltage.....	9
1.2.3.2. Short-circuit current.....	10
1.2.3.3. Fill factor	10
1.2.3.4. Power conversion efficiency	11
1.2.4. Detailed balance model for a single junction solar cell	11
1.3. Two-terminal tandem solar cells	12
1.3.1. Principle of tandem solar cells	12
1.3.2. Monolithic integration	13
1.3.2.1. Tunnel-recombination junction	14
1.4. CIGS alloys	15
1.4.1. CIGS structure and composition	15
1.4.2. Architecture of solar cell derived from CIGS alloys	16
1.4.2.1. Substrate and back contact anode	16
1.4.2.2. Buffer layer	16
1.4.2.3. Transparent conductive cathode.....	17
1.4.3. Specificities of low-bandgap Cl(G)S solar bottom cells for monolithic tandem integration ...	17
1.5. Hybrid lead-halide perovskite solar cell	18
1.5.1. Hybrid lead-halide perovskite structure and composition.....	18
1.5.2. Mixed halide perovskite top cell design for monolithic tandem integration.....	19
1.6. State-of-the-art of monolithic integration of mixed halide perovskite/CIGS tandem solar cells	20
1.7. Overview	
2. Chapter 2	22
Methods	
2.1. Fabrication methods.....	23
2.1.1. Atomic Layer Deposition (ALD)	24
2.1.2. Spin coating.....	25
2.1.3. Preparation of Cl(G)S absorber layers	27
2.1.3.1. Co-evaporation	27
2.1.3.2. Sequential deposition	27
2.1.4. Chemical bath deposition (CBD)	28
2.1.5. Sputter deposition	28

2.1.6.	Thermal evaporation	28
2.1.7.	Bromine wet etching of Cl(G)S absorber layers.....	29
2.1.7.1.	Setup to smoothen small-scale Cl(G)S samples (size between 1*1 cm ² and 2*2 cm ²)	29
2.1.8.	KCN treatment	30
2.1.9.	HCl treatment	30
2.2.	Characterization techniques	30
2.2.1.	X-ray diffraction (XRD)	30
2.2.2.	Atomic Force Microscopy (AFM).....	31
2.2.2.1.	Kelvin probe force microscopy (KPFM).....	31
2.2.3.	Scanning Electron Microscopy (SEM)	32
2.2.4.	Photoemission spectroscopy	32
2.2.4.1.	X-Ray photoemission spectroscopy (XPS).....	34
2.2.4.2.	Ultraviolet photoemission spectroscopy (UPS)	34
2.2.5.	Inductively coupled plasma optical emission spectroscopy (ICP-OES).....	34
2.2.6.	Glow discharge optical emission spectroscopy (GD-OES)	35
2.2.7.	X-ray fluorescence (XRF)	35
2.2.8.	Cyclic voltammetry (CV).....	36
2.2.9.	Current density-voltage (J-V) measurement.....	37
2.2.10.	External Quantum efficiency (EQE).....	38
2.3.	Overview	
3.	Chapter 3	39
	Low temperature HTL development	
3.1.	Introduction.....	41
3.1.1.	NiO _x as HTL for perovskite solar cells	41
3.1.2.	Small carbazole-based molecules as HTL for perovskite solar cells	42
3.2.	Low temperature ALD-NiO _x layers for HTL application in perovskite solar cell	44
3.2.1.	Evaluation of the electron-blocking properties of NiO _x films prepared by ALD.....	45
3.2.1.1.	Calibration of a Ag/AgNO ₃ reference electrode	46
3.2.1.2.	Evaluation of the MV/MV ⁺ and MV ⁺ /MV ²⁺ redox potentials.....	47
3.2.1.3.	Evaluation of the electron blocking properties of ALD-NiO _x films for different thickness and deposition temperature	48
3.2.1.4.	Effect of post-annealing on the electron blocking properties of ALD-NiO _x films	50
3.2.2.	Chemical composition and electronic properties of NiO _x films prepared by ALD and sputtering.....	51
3.2.2.1.	Chemical composition and electronic properties of ALD-NiO _x films using Me-nickelocene as nickel precursor and O ₂ plasma as oxidizer.....	52
3.2.2.2.	Chemical composition and electronic properties of NiO _x films prepared by plasma sputtering deposition	58
3.2.2.3.	Chemical composition and electronic properties of sputtered NiO _x films after post-annealing.....	62
3.2.3.	Applications of low-temperature ALD-NiO _x in perovskite solar cells	68
3.2.4.	Enhancement of PV parameters of p-i-n perovskite solar cells by tuning the surface chemistry of NiO _x	70
3.2.4.1.	Effect of UV-Ozone post-treatment on the surface chemistry of sol-gel NiO _x films	72
3.2.4.2.	Effect of UV-Ozone post-treatment and surface recovery of the surface chemistry of combustion NiO _x films	73
3.2.4.3.	Surface-tuned NiO _x layers as HTL for perovskite solar cells: Effect of surface recovery after UV-Ozone and FAI quenching.....	75

3.2.4.4. Surface-tuned NiO _x layers as HTL for perovskite solar cells: Effect of surface recovery after UV-Ozone, FAI quenching and FAI excess	80
3.3. Self-assembled monolayer of small organic molecules as HTL in PSCs.....	85
3.3.1. SAMs HTL in devices	85
3.3.2. Morphological and structural properties of perovskite layers	89
3.4 Interim summary	
4. Chapter 4	94
Semi-transparent perovskite solar cell for monolithic tandem integration	
4.1. Introduction.....	95
4.1.1. Bathocuproine (BCP).....	95
4.1.2. ZnO.....	96
4.1.3. SnO ₂	96
4.2. Development of a metal oxide based ETL for semi-transparent p-i-n PSCs	97
4.2.1. ETL adaptation to plasma sputtering condition	97
4.2.1. J-V characterization of opaque PSCs using an organic or hybrid bilayer as ETL.....	98
4.2.1.2. J-V characterization of opaque PSCs using PCBM/np-ZnO or PCBM/np-AZO as ETL	102
4.2.1.3. Morphology of the PCBM/np-metal oxide bilayer prepared by spin-coating	107
4.2.1.4. J-V characterization of semi-transparent PSCs using AZO or ITO as front TCO.....	109
4.3. Optimization of ETL and TCO for semi-transparent PSCs.....	112
4.4. Interim summary	
5. Chapter 5	121
CI(G)S morphological adaptation to monolithic integration	
5.1. Introduction.....	123
5.2. Proof of concept: Planarization of co-evaporated CI(G)S samples	123
5.2.1. Influence of velocity and treatment time parameters of a Br-etching wet process over the thickness and roughness of CI(G)S layers.....	124
5.2.1.1. Co-evaporated CI(G)S morphology after Br-etching (80 rpm)	124
5.2.1.2. Co-evaporated CI(G)S morphology after Br-etching (40 rpm & 30 rpm)	128
5.2.2. Reliability and homogeneity	130
5.2.2.1. Reliability of the Br-etching process (40 rpm)	131
5.2.2.2. Reproducibility of the Br-etching process (30 rpm, 4 min)	133
5.2.2.3. Thickness homogeneity of co-evaporated CI(G)S layers prior to Br-etching	135
5.2.2.4. Thickness homogeneity of co-evaporated CI(G)S layers after Br-etching.....	137
5.2.3. Influence of Br-etching and KCN treatment over the surface chemistry of CI(G)S	140
5.2.3.1. Qualitative assessment over the surface chemistry of CI(G)S by XPS analysis	140
5.2.3.2. Evolution Na and Cd content at the CI(G)S surface after Br-etching and KCN treatment .	143
5.2.3.3. Elemental composition of CI(G)S absorber layers by GD-OES.....	144
5.2.3.4. Elemental composition of CI(G)S absorber layers by XPS analysis.....	146
5.2.4. J-V and EQE characterization of devices based on as-prepared and smoothed CI(G)S	147
5.3. Interim summary	
Conclusion and Suggestions	152
References	157
Annexe	166
Résumé en Français	168

List of Figures

FIGURE 1 SCHEMATIC OF THE TARGET ARCHITECTURES IN THIS THESIS FOR **(A)** A SINGLE JUNCTION CI(G)S SOLAR CELL COMPLETED FROM A PLANARIZED ABSORBER LAYER **(B)** A SINGLE JUNCTION SEMI-TRANSPARENT SOLAR CELL **(C)** A MONOLITHIC PEROVSKITE/CI(G)S TANDEM SOLAR CELL. 2

FIGURE 2 BAND STRUCTURES FOR **(A)** AN IDEAL BLACK BODY, CHARACTERIZED BY AN ALMOST CONTINUOUS SUCCESSION OF AVAILABLE ELECTRONIC STATES AND **(B)** A SEMICONDUCTOR WHOSE ELECTRONIC STATES ARE CHARACTERIZED BY A VALENCE BAND AND A CONDUCTION BAND SEPARATED BY AN ENERGY BAND GAP BETWEEN THE VALENCE BAND MAXIMUM (*VBM*) AND CONDUCTION BAND MINIMUM (*CBM*). **(C)** SCHEMATIC REPRESENTATION OF THE EXCITATION OF AN ELECTRON FROM THE VALENCE BAND TO THE CONDUCTION BAND THROUGH THE ABSORPTION OF A PHOTON, FOLLOWED BY THERMAL RELAXATION TO THE *CBM*. 7

FIGURE 3 **(A)** SCHEMATIC REPRESENTATION OF A COMPLETE SOLAR CELL **(B)** SEPARATION AND CHARGE COLLECTION OF CHARGE CARRIERS DURING SOLAR CELL OPERATION 8

FIGURE 4 ILLUSTRATION OF THE MAJOR RECOMBINATION PROCESSES THAT CAN OCCUR IN A SOLAR CELL. 9

FIGURE 5 SCHEMATIC FOR A TANDEM SOLAR CELL CONSTITUTED OF TWO ABSORBER LAYERS IN **(A)** FOUR-TERMINAL AND **(B)** TWO-TERMINAL CONFIGURATION. 13

FIGURE 6 **(A)** BAND DIAGRAM FOR A MONOLITHIC TANDEM CELL. RECOMBINATION AT THE INTERFACE BETWEEN TWO SUBCELLS IN A 2T TANDEM SOLAR CELL THROUGH **(B)** AN IDEAL ESAKI TUNNEL JUNCTION AND **(C)** A RECOMBINATION JUNCTION, MORE COMMON IN PEROVSKITE TANDEMS. E_{F1} , E_{F2} , E_{F3} AND E_{F4} REPRESENT THE QUASI-FERMI LEVELS OF THE ABSORBER LAYERS WHEN THE CELL IS UNDER ILLUMINATION. 14

FIGURE 7 UNIT CELL FOR A $\text{Cu}(\text{In,Ga})\text{Se}_2$ CHALCOPYRITE, WITH A AND C AS THE LATTICE CONSTANTS. 15

FIGURE 8 EXAMPLES OF ARCHITECTURES FOR CIGS SOLAR CELLS USING CdS AND I-ZNO (LEFT) OR Zn(O,S) AND ZnMGO (RIGHT) AS BUFFER LAYERS, AND A Ni/Al/Ni METAL GRID. 17

FIGURE 9 UNIT CELL FOR A ABX_3 PEROVSKITE CUBIC STRUCTURE, WITH THE BX_6 OCTAHEDRA HIGHLIGHTED IN PURPLE (LEFT) AND TYPICAL ARCHITECTURE FOR A SEMI-TRANSPARENT PEROVSKITE SOLAR CELL (RIGHT). 19

FIGURE 10 SCHEMATIC REPRESENTATION OF AN ALD CYCLE FOR THE SYNTHESIS FOR A BINARY AB COMPOUND (FROM [HTTPS://WWW.ATOMICLIMITS.COM/](https://www.atomiclimits.com/)) 24

FIGURE 11 SCHEMATIC OF THE SETUP EMPLOYED FOR BROMINE WET ETCHING OF CI(G)S ABSORBER LAYERS FOR SAMPLE SIZE OF THE ORDER OF $1 \times 1 \text{ cm}^2$ TO $2 \times 2 \text{ cm}^2$. THE SAMPLE IS ATTACHED FACE DOWN TO A ROTATING-DISK ELECTRODE AND DIPPED IN THE ETCHING SOLUTION WHILE ROTATING..... 29

FIGURE 12 LEWIS REPRESENTATION OF **(A)** 2PACz AND **(B)** MeO-2PACz 43

FIGURE 13 VOLTAMMOGRAM RECORDED WITH AN ITO SAMPLE AS WORKING ELECTRODE, IN ACN MEDIA USING 10 mM FERROCENE AS THE REDOX SPECIE AND 0.1 M LiClO ₄ AS SUPPORTING ELECTRODE RECORDED FOR (A) 10 CYCLES AND (B) 50 CYCLES AT A SCAN RATE OF 800 mV/s. IN BOTH FIGURES DATA POINTS ARE REPRESENTED USING A GRADIENT OF COLOR FROM YELLOW (1 ST CYCLE) TO DARK RED (LAST CYCLE). VOLTAGE IS REPORTED AGAINST A Ag/AgNO ₃ 0.01 M REFERENCE ELECTRODE.	46
FIGURE 14 VOLTAMMOGRAM RECORDED WITH AN ITO SAMPLE AS WORKING ELECTRODE, IN ACN MEDIA USING 0.1 mM MV AS THE REDOX SPECIE AND 0.1 M LiClO ₄ AS SUPPORTING ELECTRODE RECORDED FOR 6 CYCLES AT SCAN RATE OF 200 mV/s. VOLTAGE IS REPORTED AGAINST A Ag/AgNO ₃ 0.01 M REFERENCE ELECTRODE.	47
FIGURE 15 VOLTAMMOGRAMS RECORDED USING NiO _x /ITO SAMPLES OF VARYING THICKNESS AS WORKING ELECTRODE, IN ACN MEDIA CONTAINING 0.1 mM MV AS REDOX SPECIE AND 0.1 M LiClO ₄ AS SUPPORTING ELECTRODE FOR (A) 100°C PREPARED ALD-NiO _x AND (B) 160°C PREPARED ALD-NiO _x AT SCAN RATE OF 200 mV/s. VOLTAGE IS REPORTED AGAINST A Ag/AgNO ₃ 0.01 M REFERENCE ELECTRODE.....	49
FIGURE 16 VOLTAMMOGRAMS RECORDED WITH DIFFERENT NiO _x /ITO SAMPLES BEFORE AND AFTER 300°C POST-ANNEALING FOR 1 HOUR AS WORKING ELECTRODE, IN ACN MEDIA CONTAINING 0.1 mM MV AS REDOX SPECIE AND 0.1 M LiClO ₄ AS SUPPORTING ELECTRODE FOR (A) 100°C PREPARED ALD-NiO _x AND (B) 160°C PREPARED ALD-NiO _x AT A SCAN RATE OF 200 mV/s. 2 SAMPLES WERE USED FOR POST-ANNEALING DATA FOR HOMOGENEITY PURPOSE. FOR EACH SERIES OF SAMPLE, A REFERENCE ITO SAMPLE WAS MEASURED BEFORE (REF ITO) AND AFTER (REF ITO END) NiO _x FILMS TO ASSESS WHETHER OR NOT A LOSS OF CURRENT OCCURRED DURING THE EXPERIMENT. VOLTAGE IS REPORTED AGAINST A Ag/AgNO ₃ 0.01 M REFERENCE ELECTRODE.....	50
FIGURE 17 WORK FUNCTION (A) AND VBM VALUES (B) EXTRACTED FORM UPS SPECTRA, BY FERMI EDGE DETERMINATION. (C) SUMMARY OF THE WORK FUNCTION AND VALENCE BAND MAXIMUM MEASUREMENTS BY KPFM AND UPS FOR ALL THE SAMPLES. WE CAN OBSERVE SYSTEMATICALLY HIGHER WF MEASURED BY KPFM COMPARED TO THIS MEASURED BY UPS; BOTH HOWEVER SHOWS SIMILAR TRENDS.	53
FIGURE 18 XPS SPECTRA FOR (A) Ni 2P _{3/2} AND (B) O 1s REGIONS, (C) NiO %, AS THE PROPORTION OF STOICHIOMETRIC NiO COMPARED TO OTHER NiO _x H _y SUBSPECIES AT THE SURFACE OF THE SAMPLE CALCULATED FROM THE Ni 2P _{3/2} REGION AND (D) MAXIMUM O 1s BINDING ENERGY SHIFT FOR NiO _x SAMPLES PREPARED BY ALD AT DIFFERENT TEMPERATURES.....	55
FIGURE 19 SUMMARY OF THE WORK FUNCTION AND VALENCE BAND MAXIMUM MEASUREMENTS BY KPFM AND UPS FOR SPUTTERED-NiO _x SAMPLES PREPARED AT KIT.	59
FIGURE 20 XPS SPECTRA FOR (A) Ni 2P _{3/2} AND (B) O 1s REGIONS, (C) NiO%, AS THE PROPORTION OF STOICHIOMETRIC NiO COMPARED TO OTHER NiO _x H _y SUBSPECIES AT THE SURFACE OF THE SAMPLE CALCULATED FROM THE Ni 2P _{3/2} REGION AND (D) MAXIMUM O 1s BINDING ENERGY SHIFT FOR NiO _x SAMPLES PREPARED BY SPUTTERING AT KIT.	61
FIGURE 21 SUMMARY OF THE WORK FUNCTION AND VALENCE BAND MAXIMUM MEASUREMENTS BY KPFM AND UPS FOR SPUTTERED-NiO _x SAMPLES PREPARED AT IMEC.	64
FIGURE 22 XPS SPECTRA FOR (A) Ni 2P _{3/2} AND (B) O 1s REGIONS, (C) NiO%, AS THE PROPORTION OF STOICHIOMETRIC NiO COMPARED TO OTHER NiO _x H _y SUBSPECIES AT THE SURFACE OF THE SAMPLE CALCULATED FROM THE Ni 2P _{3/2} REGION AND (D) MAXIMUM O 1s BINDING ENERGY SHIFT FOR NiO _x SAMPLES PREPARED BY SPUTTERING FOR DIFFERENT POST-ANNEALING TEMPERATURES.....	65

FIGURE 23 (LEFT) ARCHITECTURE OF P-I-N PEROVSKITE SOLAR CELLS PREPARED FOR J-V EXPERIMENT USING NiO _x AS HTL. LAYERS WERE DEPOSITED AT DIFFERENT TEMPERATURE BY ALD FROM ME-NICKELOCENE PRECURSOR AND O ₂ PLASMA AS OXIDIZER (RIGHT) NUMBER OF SOLAR DEVICES PREPARED AND NUMBER OF WORKING SOLAR CELLS (I.E. PCE>1%) PER CONDITION.	68
FIGURE 24 PV PARAMETERS MEASURED FOR PEROVSKITE SOLAR CELLS FABRICATED USING ALD PREPARED NiO _x FROM ME-NICKELOCENE PRECURSOR AND O ₂ PLASMA AS OXIDIZER AT DIFFERENT TEMPERATURE AS HTL. SOLAR CELL STACK WAS GLASS/ITO/NiO _x /PEROVSKITE/PCBM/BCP/AG	69
FIGURE 25 XPS SPECTRA FOR (A) Ni 2P _{3/2} AND (B) O 1S REGIONS, (C) NiO %, AS THE PROPORTION OF STOICHIOMETRIC NiO COMPARED TO OTHER NiO _x H _y SUBSPECIES AT THE SURFACE OF THE SAMPLE CALCULATED FROM THE Ni 2P _{3/2} REGION AND (D) MAXIMUM O 1S BINDING ENERGY SHIFT FOR NiO _x SAMPLES PREPARED BY SOL-GEL BEFORE AND AFTER UV-O ₃ TREATMENT.	72
FIGURE 26 XPS SPECTRA FOR (A) Ni 2P _{3/2} AND (B) O 1S REGIONS, (C) NiO %, AS THE PROPORTION OF STOICHIOMETRIC NiO COMPARED TO OTHER NiO _x H _y SUBSPECIES AT THE SURFACE OF THE SAMPLE CALCULATED FROM THE Ni 2P _{3/2} REGION AND (D) MAXIMUM O 1S BINDING ENERGY SHIFT FOR NiO _x SAMPLES PREPARED BY SOL-GEL BEFORE AND AFTER UV-O ₃ TREATMENT OR UV-O ₃ + A TREATMENT.....	74
FIGURE 27 (LEFT) ARCHITECTURE OF SOLAR CELLS PREPARED FOR J-V EXPERIMENT USING DIFFERENT NiO _x POST-DEPOSITION TREATMENT (RIGHT) NUMBER OF SOLAR DEVICES PREPARED AND NUMBER OF WORKING SOLAR CELLS (I.E. PCE > 1%) PER CONDITION.	76
FIGURE 28 PV PARAMETERS RECORDED AFTER 4 DAYS AFTER FABRICATION FOR PEROVSKITE CHAMPION CELLS USING NiO _x AFTER DIFFERENT POST-DEPOSITION TREATMENT AS HTL.	77
FIGURE 29 PV PARAMETERS RECORDED AFTER 15 DAYS AFTER FABRICATION FOR PEROVSKITE CHAMPION CELLS USING NiO _x AFTER DIFFERENT POST-DEPOSITION TREATMENT AS HTL.	78
FIGURE 30 J-V CURVES RECORDED FOR PEROVSKITE CHAMPION CELLS USING NiO _x AFTER DIFFERENT POST-DEPOSITION TREATMENT AS HTL (A) 4 AND (B) 15 DAYS AFTER FABRICATION. FULL AND DASHED LINES RESPECTIVELY INDICATE FORWARD AND REVERSE CURRENT.....	79
FIGURE 31 (LEFT) ARCHITECTURE OF SOLAR CELLS PREPARED FOR J-V EXPERIMENT USING DIFFERENT NiO _x POST-DEPOSITION TREATMENT AND/OR EXCESS FAI IN PEROVSKITE PRECURSOR SOLUTION (RIGHT) NUMBER OF SOLAR DEVICES PREPARED AND NUMBER OF WORKING SOLAR CELLS (I.E. PCE > 1%) PER CONDITION.	81
FIGURE 32 PV PARAMETERS RECORDED 3 DAYS AFTER FABRICATION FOR PEROVSKITE SOLAR CELLS USING NiO _x AFTER DIFFERENT POST-DEPOSITION TREATMENT AS HTL, OR WITH FAI EXCESS ADDED DIRECTLY IN SOLUTION.	82
FIGURE 33 J-V CURVES RECORDED FOR PEROVSKITE CHAMPION CELLS USING NiO _x AFTER DIFFERENT POST-DEPOSITION TREATMENT AS HTL, OR WITH FAI EXCESS DIRECTLY ADDED IN SOLUTION (A) 3 AND (B) 14 DAYS AFTER FABRICATION. FULL AND DASHED LINES RESPECTIVELY INDICATE FORWARD AND REVERSE.	83
FIGURE 34 PV PARAMETERS RECORDED 14 DAYS AFTER FABRICATION FOR PEROVSKITE SOLAR CELLS USING NiO _x AFTER DIFFERENT POST-DEPOSITION TREATMENT AS HTL, OR WITH FAI EXCESS ADDED DIRECTLY IN SOLUTION.	84
FIGURE 35 (LEFT) ARCHITECTURE OF SOLAR CELLS PREPARED FOR J-V EXPERIMENT USING DIFFERENT TYPES OF SAM MOLECULES AS HTL AND DIFFERENT PbI ₂ SUPPLIER FOR PEROVSKITE PRECURSOR SOLUTION (RIGHT) NUMBER OF SOLAR DEVICES PREPARED AND NUMBER OF WORKING SOLAR CELLS (I.E. PCE > 1%) PER CONDITION.	86
FIGURE 36 PV PARAMETERS RECORDED BEFORE LIGHT SOAKING FOR PEROVSKITE SOLAR CELLS USING 2PACz OR MeO-2PACz AS HTL AND PbI ₂ FROM DIFFERENT SUPPLIERS.....	87

FIGURE 37 PV PARAMETERS RECORDED AFTER LIGHT SOAKING FOR PEROVSKITE SOLAR CELLS USING 2PACz OR MeO-2PACz AS HTL AND PbI ₂ FROM DIFFERENT SUPPLIERS.	88
FIGURE 38 J-V CURVES RECORDED FOR PEROVSKITE CHAMPION CELLS USING 2PACz OR MeO-2PACz AS HTL AND PbI ₂ FROM DIFFERENT SUPPLIERS (A) BEFORE AND (B) AFTER 5 MINUTES LIGHT SOAKING. FULL AND DASHED LINES RESPECTIVELY INDICATE FORWARD AND REVERSE CURRENT.	88
FIGURE 39 SEM IMAGES RECORDED FOR TRIPLE CATION PEROVSKITE LAYERS DEPOSITED ON TOP OF (A) 2PACz OR (B) UV-O ₃ TREATED NiO _x . THE MAGNIFICATION OF THE IMAGE WAS NOT IDENTICAL FOR BOTH IMAGES:	90
FIGURE 40 XRD DIFFRACTOGRAMS FOR TRIPLE CATION PEROVSKITE LAYERS DEPOSITED OVER NiO _x (RED, YELLOW) OR MeO-2PACz (BLUE) HTL. TWO IDENTICAL SAMPLES WERE SYNTHESIZED AND CHARACTERIZED PER CONDITION FOR EXPERIMENTAL REPEATABILITY.....	91
FIGURE 41 LEWIS STRUCTURE FOR BATHOCUPROINE	96
FIGURE 42 (LEFT) ARCHITECTURE OF OPAQUE SOLAR CELLS PREPARED FOR J-V EXPERIMENT USING DIFFERENT TYPES OF ETL (RIGHT) NUMBER OF SOLAR DEVICES PREPARED AND NUMBER OF WORKING SOLAR CELLS (I.E. PCE > 1%) PER CONDITION.	99
FIGURE 43 PV PARAMETERS RECORDED FOR OPAQUE PEROVSKITE SOLAR CELLS USING EITHER PCBM/BCP, NP-ZNO, PCBM/NP-ZNO OR PCBM/NP-AZO AS ETL.	100
FIGURE 44 J-V CURVES RECORDED FOR PEROVSKITE CHAMPION CELLS USING PCBM/BCP, NP-ZNO, PCBM/NP-ZNO AND PCBM/NP-AZO AS ETL. FULL AND DASHED LINES RESPECTIVELY INDICATE FORWARD AND REVERSE CURRENT.	101
FIGURE 45 (LEFT) ARCHITECTURE OF OPAQUE SOLAR CELLS PREPARED FOR J-V EXPERIMENT USING DIFFERENT TYPES OF ETL LAYERS (RIGHT) NUMBER OF SOLAR DEVICES PREPARED AND NUMBER OF WORKING SOLAR CELLS (I.E. PCE > 1%) PER CONDITION.	103
FIGURE 46 PV PARAMETERS RECORDED 3 DAYS AFTER FABRICATION FOR OPAQUE PEROVSKITE SOLAR CELLS USING EITHER PCBM/NP-ZNO OR PBM/NP-AZO AS ETL. METAL OXIDE LAYER WAS SPIN COATED EITHER ONE TIME (AZO 1, ZNO 1) OR TWO TIMES (AZO 2, ZNO 2) ON TOP OF THE PCBM LAYER.	104
FIGURE 47 PV PARAMETERS RECORDED 7 DAYS AFTER FABRICATION FOR OPAQUE PEROVSKITE SOLAR CELLS USING EITHER PCBM/NP-AZO OR PBM/NP-ZNO AS ETL. METAL OXIDE LAYER WAS SPIN COATED EITHER ONE TIME (AZO 1, ZNO 1) OR TWO TIMES (AZO 2, ZNO 2) ON TOP OF THE PCBM LAYER.	105
FIGURE 48 J-V CURVES RECORDED FOR PEROVSKITE CHAMPION CELLS USING PCBM/NP-AZO OR PCBM/NP-ZNO AS ETL, (A) 3 DAYS AND (B) 7 DAYS AFTER FABRICATION. FULL AND DASHED LINES RESPECTIVELY INDICATE FORWARD AND REVERSE CURRENT. METAL OXIDE LAYER WAS SPIN COATED EITHER ONE TIME OR TWO TIMES ON TOP OF THE PCBM LAYER.	106
FIGURE 49 SURFACE SEM IMAGES OF PEROVSKITE P-I-N SOLAR CELLS USING MeO-2PACz AS HTL (A) A PCBM/AZO BILAYER AS ETL AND (B) A PCBM/ZNO BILAYER AS ETL. NP-METAL OXIDE LAYERS WERE DEPOSITED TWICE BY SPIN COATING ON TOP OF PCBM.	108
FIGURE 50 CROSS-SECTION SEM IMAGE FOR A P-I-N PEROVSKITE SOLAR CELL PREPARED USING (A) NiO _x AS ETL AND A PCBM/BCP BILAYER AS ETL OR (B) MeO-2PACz ANCHORED TO ITO AS HTL AND A PCBM/NP-AZO BILAYER AS ETL OR (C) MeO-2PACz ANCHORED TO ITO AS HTL AND A PCBM/NP-ZNO BILAYER AS ETL. NP-METAL OXIDE LAYERS WERE DEPOSITED TWICE BY SPIN COATING ON TOP OF PCBM.....	108

FIGURE 51 (LEFT) ARCHITECTURE OF SEMI-TRANSPARENT SOLAR CELLS PREPARED FOR J-V EXPERIMENT USING PCBM/NP-ZNO AS ETL AND SPUTTERED AZO AS FRONT TCO (RIGHT) NUMBER OF SOLAR DEVICES PREPARED AND NUMBER OF WORKING SOLAR CELLS (I.E. PCE > 1%) PER CONDITION.	110
FIGURE 52 AVERAGE PV PARAMETERS RECORDED 7 DAYS AFTER FABRICATION FOR SEMI-TRANSPARENT PEROVSKITE SOLAR CELLS USING PBM/NP-ZNO AS ETL AND SPUTTERED AZO AS FRONT TCO. PARAMETERS WERE EXTRACTED FOR J-V CURVES UNDER BOTH FRONT AND REAR ILLUMINATION.	111
FIGURE 53 J-V CURVES RECORDED UNDER FRONT (BROWN) AND REAR (ORANGE) ILLUMINATION, FOR PEROVSKITE CHAMPION CELLS USING PCBM/NP-AZO AS ETL AND SPUTTERED AZO AS FRONT TCO. FULL AND DASHED LINES RESPECTIVELY INDICATE FORWARD AND REVERSE CURRENT.	111
FIGURE 54 (LEFT) ARCHITECTURE OF SEMI-TRANSPARENT SOLAR CELLS PREPARED FOR J-V EXPERIMENT USING DIFFERENT TYPES OF ETL AND TCO LAYERS (RIGHT) NUMBER OF SOLAR DEVICES PREPARED AND NUMBER OF WORKING SOLAR CELLS (I.E. PCE > 1%) PER CONDITION.	113
FIGURE 55 PV PARAMETERS RECORDED UNDER REAR ILLUMINATION FOR SEMI-TRANSPARENT PEROVSKITE SOLAR CELLS USING EITHER PCBM/NP-ZNO OR C ₆₀ /ALD-SNO ₂ AS ETL AND EITHER ITO OR AZO AS FRONT TCO. J _{sc} VALUES WERE CORRECTED BY EQE, AND PCE VALUES WERE MODIFIED ACCORDINGLY.	115
FIGURE 56 PV PARAMETERS RECORDED UNDER FRONT ILLUMINATION FOR SEMI-TRANSPARENT PEROVSKITE SOLAR CELLS USING EITHER PCBM/NP-ZNO OR C ₆₀ /ALD-SNO ₂ AS ETL AND EITHER ITO OR AZO AS FRONT TCO. J _{sc} VALUES WERE RECORDED BY EQE, AND PCE VALUES WERE CORRECTED ACCORDINGLY.	116
FIGURE 57 J-V CURVES FOR CHAMION CELLS UNDER (A) REAR AND (C) FRONT ILLUMINATION AND EQE SPECTRA UNDER (B) REAR AND (D) FRONT ILLUMINATION FOR SEMI-TRANSPARENT PEROVSKITE SOLAR CELLS USING EITHER C ₆₀ /BCP OR PCBM/NP-ZNO AS ETL, AND EITHER ITO OR AZO AS FRONT TCO.	118
FIGURE 58 10*10 MM ² AND 50*50 MM ² AFM IMAGES ACQUIRED FOR 1*1 CM ² Cl(G)S SAMPLES ETCHED AT 80 RPM FOR 30 SEC, 1 MIN, 2 MIN, 5 MIN AND 10 MIN COMPARED TO AN AS-PREPARED REFERENCE. PEAK TO VALLEY DISTANCE IS INDICATED BY VERTICAL ARROWS.	126
FIGURE 59 CROSS-SECTION SEM IMAGES ACQUIRED FOR (LEFT) AS-PREPARED, (MIDDLE) 1 MIN ETCHED AND (RIGHT) 10 MIN ETCHED Cl(G)S ABSORBER LAYERS.	127
FIGURE 60 5*5 MM ² AND 10*10 MM ² AFM IMAGES ACQUIRED FOR 1*1 CM ² Cl(G)S SAMPLES ETCHED AT 40 RPM FOR 30 SEC, 1 MIN, 1 MIN 30 SEC AND 2 MIN AND COMPARED TO AN AS-PREPARED REFERENCE (5*5 MM ² AND 50*50 MM ² IMAGES). PEAK TO VALLEY DISTANCE IS INDICATED BY VERTICAL ARROWS.	129
FIGURE 61 ICP DOSAGE FOR CU, IN, GA, SE AND NA FROM BR SOLUTIONS AFTER ETCHING OF Cl(G)S ABSORBER LAYERS AT 40 RPM FOR 2 MIN, 4 MIN AND 6 MIN. VALUES IN MG WERE NORMALIZED WITH VOLUME OF SOLUTION AND SAMPLE AREA. HYPOTHETICAL LINEAR CONCENTRATION RELATIONSHIP BETWEEN CU, IN AND SE CONCENTRATION AS A FUNCTION OF ETCHING TIME WERE REPRESENTED BY DASHED LINES.	131

FIGURE 62 5*5 MM ² AND 30*30 MM ² AFM IMAGES ACQUIRED FOR 2*2 CM ² Cl(G)S SAMPLES ETCHED AT 40 RPM FOR 2 MIN, 4 MIN AND 6 MIN AND COMPARED TO AN AS-PREPARED REFERENCE (5*5 MM ² AND 50*50 MM ² IMAGES). PEAK TO VALLEY DISTANCE IS INDICATED BY VERTICAL ARROWS.	132
FIGURE 63 ICP DOSAGE FOR CU, IN, GA, SE AND NA FROM THREE BR SOLUTIONS USED TO ETCH Cl(G)S ABSORBER LAYERS AT 30 RPM FOR 4 MIN. VALUES IN MG WERE NORMALIZED WITH VOLUME OF SOLUTION AND SAMPLE AREA TO YIELD VALUES IN MG.L ⁻¹ .M ⁻²	134
FIGURE 64 5*5 MM ² AND 30*30 MM ² AFM IMAGES ACQUIRED FOR THREE 2*2 CM ² Cl(G)S SAMPLES ETCHED AT 30 RPM FOR 4 MIN AND ONE AS-PREPARED REFERENCE SAMPLE (5*5 MM ² AND 50*50 MM ² IMAGES). PEAK TO VALLEY DISTANCE IS INDICATED BY VERTICAL ARROWS.....	135
FIGURE 65 SCHEMATIC OF 2 Cl(G)S PARENT SAMPLES OF 5*5 CM ² AREA CUT IN TWO HALF-SAMPLES A AND B OF 2.5*5 CM ² AREA. CUTTING LINES ARE INDICATED BY DOTTED LINES. L-P: LEFT-POSITION. R-P: RIGHT-POSITION. MID: MIDDLE	136
FIGURE 66 THICKNESS OF Cl(G)S AND MO LAYERS ACROSS TWO Cl(G)S SAMPLES GROWN BY CO-EVAPORATION ON TOP ON A MO LAYER, PRIOR TO BR WET ETCHING. TWO SAMPLES, (A) A AND (B) B, WERE MEASURED FOR REPRODUCIBILITY. THICKNESS VALUES WERE MEASURED FROM CROSS-SECTION SEM IMAGES TAKEN AT 7 POSITIONS FOR TWO 2.5*5 CM ² HALF-SAMPLES. THESE HALF-SAMPLES WERE OBTAINED FROM TWO DISTINCT 5*5 CM ² PARENT SAMPLES CUT IN HALF.	137
FIGURE 67 SCHEMATIC OF 2 Cl(G)S PARENT SAMPLES OF 2*2 CM ² AREA CUT IN TWO HALF-SAMPLES C AND D OF 1*2 CM ² AREA. ETCHING PARAMETERS WERE 40 RPM FOR 1 MIN AND 2 MIN, RESPECTIVELY. CUTTING LINES ARE INDICATED BY DOTTED LINES. L-P: LEFT-POSITION. R-P: RIGHT-POSITION. MID: MIDDLE	138
FIGURE 68 THICKNESS OF Cl(G)S AND MO LAYERS ACROSS TWO Cl(G)S SAMPLES GROWN BY CO-EVAPORATION ON TOP ON A MO LAYER, AFTER (A) 1 MIN AND (B) 2 MIN OF BR ETCHING AT 40 RPM. THICKNESS VALUES WERE MEASURED FROM CROSS-SECTION SEM IMAGES TAKEN AT 3 POSITIONS FOR TWO 1*2 CM ² HALF-SAMPLES. THESE HALF-SAMPLES WERE OBTAINED FROM TWO DISTINCT 2*2 CM ² PARENT SAMPLES CUT IN HALF.....	138
FIGURE 69 SUPERIMPOSED XPS SPECTRA FOR Cl(G)S SAMPLES RECORDED IN THE (A) CU 3P, (B) CU 2P _{3/2} , (C) IN 4D AND (D) SE 3D REGIONS. FOR EACH GRAPH, FROM TOP TO BOTTOM: AS-PREPARED Cl(G)S SAMPLE, Cl(G)S SAMPLE AFTER BR-ETCH (4 MIN, 40 RPM), AND Cl(G)S SAMPLES AFTER BR-ETCH (4 MIN, 40 RPM) AND KCN TREATMENT.....	141
FIGURE 70 SUPERIMPOSED XPS SPECTRA FOR Cl(G)S SAMPLES RECORDED IN THE (A) Cd 3D _{5/2} AND (B) NA 1S REGIONS. FOR EACH GRAPH, FROM TOP TO BOTTOM: AS-PREPARED Cl(G)S SAMPLE, EDGE, AND CENTER OF A Cl(G)S SAMPLE AFTER BR-ETCHING (10 MIN, 80 RPM)	143
FIGURE 71 ELEMENTAL PROFILE OF AS-PREPARED Cl(G)S LAYERS PREPARED BY CO-EVAPORATION ESTABLISHED USING GD-OES. Cl(G)S DEPTH WAS MEASURED BY CROSS-SECTION SEM AND ELEMENTAL PROFILES WERE CALIBRATED FROM XRF MEASUREMENTS.	145
FIGURE 72 (LEFT) ARCHITECTURE OF SOLAR CELLS PREPARED FOR J-V EXPERIMENT USING EITHER AS-PREPARED OR SMOOTHED Cl(G)S (RIGHT) NUMBER OF SOLAR DEVICES PREPARED AND NUMBER OF WORKING SOLAR CELLS (I.E. PCE > 1%) PER CONDITION.	147
FIGURE 73 (A) EQE SIGNAL AND (B) J-V CURVE FOR Cl(G)S SOLAR CELLS BASED ON AS-PREPARED (BLACK) AND SMOOTHED (RED) Cl(G)S ABSORBERS LAYERS. J-V CURVE WAS RECORDED USING A 4 PROBES SETUP. FORWARD AND REVERSE CURRENT ON J-V CURVE ARE DEPICTED IN FULL AND DOTTED LINES, RESPECTIVELY.....	148

FIGURE 74 SURFACE SEM IMAGES OF A 3.25*3.25 CM² SEQUENTIAL Cl(G)S SAMPLE BEFORE (LEFT) AND AFTER (RIGHT) ETCHING USING A SETUP ADAPTED FOR SAMPLE SIZES IN THE ORDER OF 5*5 CM²..... 150

List of Tables

TABLE 1 RESULTS OF KPFM MEASUREMENTS ON ALD-NiO _x SAMPLES FOR DIFFERENT DEPOSITION TEMPERATURES. FOR EACH SAMPLE, ON THE TOP LINE WE CAN SEE AFM TOPOGRAPHY, IN THE MIDDLE RMS ROUGHNESS (RT), AND ON THE BOTTOM RESPECTIVE SURFACE POTENTIAL DISTRIBUTION (CPD VALUES). IMAGE SIZE: 10 X 10 MM ²	52
TABLE 2 Ni/C ELEMENTAL RATIO IN ALD-NiO _x SAMPLES AS A FUNCTION OF TEMPERATURE DEPOSITION, FROM THE Ni 2P _{3/2} AND C 1S REGIONS OF THE XPS SPECTRA.....	54
TABLE 3 RESULTS OF KPFM MEASUREMENTS ON SPUTTERED-NiO _x SAMPLES PREPARED FOR DIFFERENT DEPOSITION TEMPERATURE AND OXYGEN FLUX CONDITIONS. FOR EACH SAMPLE, ON THE TOP LINE WE CAN SEE AFM TOPOGRAPHY, IN THE MIDDLE RMS ROUGHNESS (RT), AND ON THE BOTTOM RESPECTIVE SURFACE POTENTIAL DISTRIBUTION (CPD VALUES). IMAGE SIZE: 10 X 10 MM ²	58
TABLE 4 Ni/C ELEMENTAL RATIO IN SPUTTERED-NiO _x SAMPLES FROM KIT AS A FUNCTION OF TEMPERATURE DEPOSITION, FROM THE Ni 2P _{3/2} AND C 1S REGIONS OF THE XPS SPECTRA.	60
TABLE 5 RESULTS OF KPFM MEASUREMENTS ON SPUTTERED-NiO _x SAMPLES PREPARED FOR DIFFERENT POST-ANNEALING TEMPERATURE. FOR EACH SAMPLE, ON THE TOP LINE WE CAN SEE AFM TOPOGRAPHY, IN THE MIDDLE RMS ROUGHNESS (RT) OF SAMPLE, AND ON THE BOTTOM RESPECTIVE SURFACE POTENTIAL DISTRIBUTION (CPD VALUES). IMAGE SIZE: 10 X 10 MM ²	63
TABLE 6 Ni/C ELEMENTAL RATIO IN SPUTTERED-NiO _x SAMPLES FROM IMEC AS A FUNCTION OF TEMPERATURE DEPOSITION, FROM THE Ni 2P _{3/2} AND C 1S REGIONS OF THE XPS SPECTRA.	64
TABLE 7 Ni/C ELEMENTAL RATIO MEASURED BY XPS BASED ON THE Ni 2P _{3/2} AND C 1S REGIONS FOR NiO _x SAMPLES PREPARED BY (A) SOL-GEL PROCESS BEFORE AND AFTER UV-O ₃ AND (B) COMBUSTION PROCESS BEFORE AND AFTER UV-O ₃ OR UV-O ₃ + A TREATMENT.....	73
TABLE 8 FINAL THICKNESS, DISSOLUTION RATE AND ROOT MEAN SQUARE (RMS) ROUGHNESS FOR Cl(G)S ABSORBER LAYERS CHEMICALLY ETCHED AT 80 RPM BETWEEN 30 SEC AND 10 MIN.	124
TABLE 9 FINAL THICKNESS, DISSOLUTION RATE AND RT FOR Cl(G)S ABSORBER LAYERS CHEMICALLY ETCHED AT 40 RPM AND 30 RPM FOR DURATIONS BETWEEN 30 SEC AND 4 MIN. *: RT VALUE OBTAINED FROM A 50*50 MM ² AFM IMAGE.....	128
TABLE 10 FINAL THICKNESS, DISSOLUTION RATE AND RT VALUES FOR Cl(G)S ABSORBER LAYERS CHEMICALLY ETCHED AT 40 RPM FOR DURATIONS BETWEEN 2 MIN AND 6 MIN. ² : RT VALUE OBTAINED FROM A 50*50 MM ² AFM IMAGE.	132
TABLE 11 FINAL THICKNESS, DISSOLUTION RATE AND RT VALUES FOR THREE Cl(G)S ABSORBER LAYERS CHEMICALLY ETCHED AT 30 RPM FOR 4 MIN. *: RT VALUE OBTAINED FROM A 50*50 MM ² AFM IMAGE.	133
TABLE 12 AVERAGE VALUES FOR Cl(G)S ABSORBER LAYER THICKNESS FOR SAMPLE A AND B, CALCULATED FROM THICKNESS MEASUREMENTS FOR 5 SERIES OF 3 CONSECUTIVES SEM IMAGES FOR EACH SAMPLE.....	139
TABLE 13 AVERAGE ATOMIC PERCENTAGE AND STANDARD DEVIATION FOR THE MAIN ELEMENTS OF AN AS-PREPARED Cl(G)S SAMPLE PREPARED BY CO-EVAPORATION FROM XRF MEASUREMENTS AT 36 DIFFERENT POSITIONS.....	145
TABLE 14 ELEMENTAL COMPOSITION OF Cl(G)S SAMPLES BEFORE AND AFTER BR-ETCHING.	146

General Introduction

Electricity production from solar energy has drastically increased during the last decades. In 2021, solar photovoltaic (PV) generation increased worldwide by a record 179 TWh to exceed 1 000 TWh¹. In the USA, costs of utility-scale PV installations have experienced a five-fold decrease during the last decade². Crystalline Si is the current technology dominating the market for this application³.

There is however a growing demand for lightweight, flexible PV modules, and thin-film technologies might be more suited for these applications than crystalline Si^{3,4}. CIGS ($\text{Cu}(\text{In}_{1-x}\text{Ga}_x)\text{Se}_2$) is a well-established technology for flexible PV, and lead halide perovskite solar cells have recently emerged as a high performance thin-film technology. Interestingly, the bandgap of both absorber layers can be tuned by adjusting their chemical composition.

This last feature would be particularly interesting for tandem applications, where two or more solar cells are stacked on top of each other to increase the absorption of solar energy on a wider range of wavelength, and connected either mechanically (4-terminal integration, 4T) or both mechanically and electronically (2-terminal integration, 2T). In particular, monolithic (i.e. 2-terminal) integration reduces the manufacturing costs of the processed tandem cell, at the expense of introducing a current-matching constraint for the two subcells due to their electrical connection in series.

As the efficiency of other tandem combination such as III-V/III-V or even perovskite/silicon reached 30% PCE for two junctions, that of perovskite/CIGS is still lagging behind at 25%, for both 2-terminal and 4-terminal configurations⁵.

The subject of this thesis, within the frame of the Horizon 2020 project PERCISTAND supported by European Union, is to study different possibilities for perovskite/CIGS monolithic tandem integration leading to the fabrication of high efficiency solar cells.

In this work, I solely focus on the p-i-n architecture for both single-junction and tandem devices. When fabricating 2T tandem cells, I deposit the hole transport layer (HTL) from the perovskite top-cell directly on the front transparent conductive oxide (TCO) of the CI(G)S subcell. For single-junction perovskite solar cells, I start by depositing the HTL on a fluorine-doped tin oxide (FTO) or indium-doped tin oxide (ITO) coated glass. The HTL is typically a NiO_x layer or a self-assembly monolayer of small organic molecules. The perovskite layer is then deposited on top of the HTL by spin-coating if not stated otherwise. Either [6,6]-phenyl-C₆₁-butyric acid methyl ester (PCBM) or C₆₀ is then deposited as electron transport layer (ETL), followed by bathocuproine (BCP), ZnO-np, or SnO₂ as a buffer layer for metal evaporation in the case of opaque cells or TCO sputtering for semi-transparent and tandem solar cells.

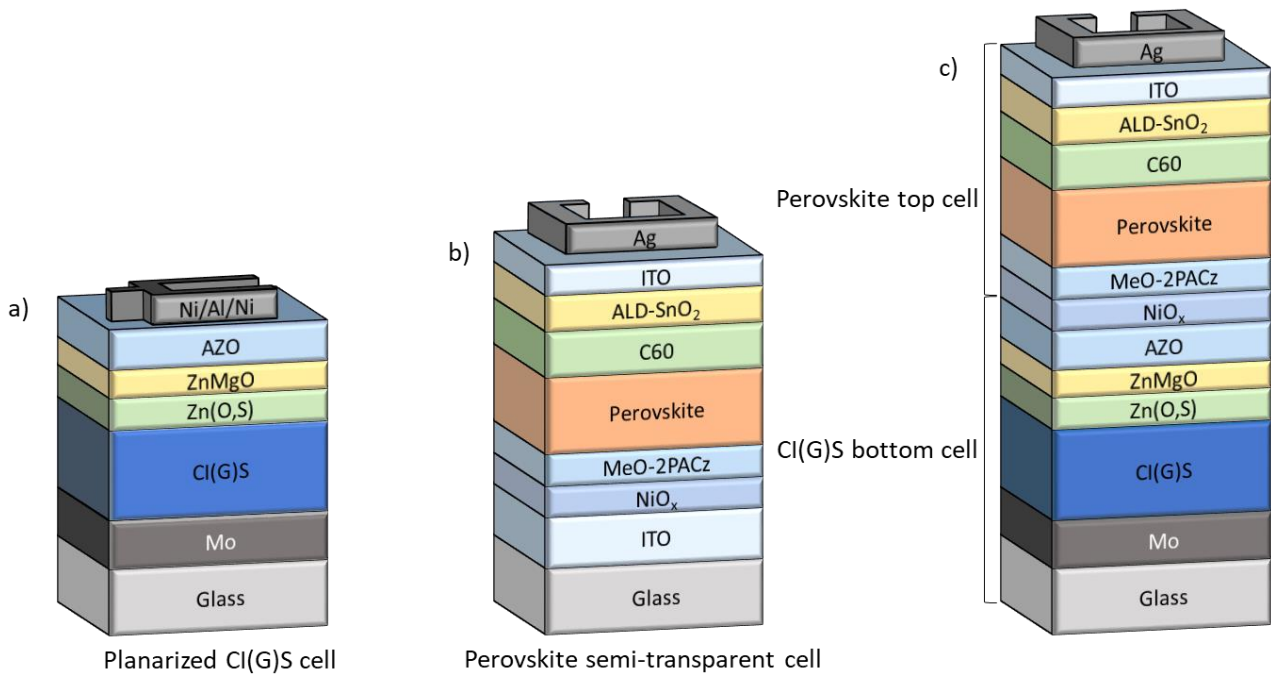


Figure 1 Schematic of the target architectures in this thesis for (a) a single junction CI(G)S solar cell completed from a planarized absorber layer (b) a single junction semi-transparent solar cell (c) a monolithic perovskite/CI(G)S tandem solar cell.

- **Chapter 1** establishes the theory of solar cells, from the basic properties of semiconductors to the principle of monolithic tandem devices. It also introduces the perovskite and CI(G)S technologies, as well as a state-of-the-art regarding their monolithic integration in tandem solar cells.
- **Chapter 2** is dedicated to the different methods that we used to fabricate samples and solar cell devices. The techniques and systems that permitted to characterize thin films and solar cells are also reviewed.
- **Chapter 3** focuses on the different low-temperature deposition processes for perovskite HTL in monolithic tandem applications. We particularly developed on how the low-temperature constraint, induced by the direct deposition of the HTL on top of the CI(G)S subcell, would affect the chemical environment of nickel and oxygen for NiO_x layers prepared by atomic layer deposition (ALD) and sputtering. We also studied how these properties would affect the PV performances of the perovskite top cell. Then, we introduce small organic molecules in self-assembly monolayers (SAM) as HTL for perovskite solar cells.

- **Chapter 4** describes the adaptation of an established p-i-n opaque architecture for perovskite solar cells in semi-transparent configuration, necessary for tandem application to transmit higher wavelength radiations to the CI(G)S subcell. We present and apply different architectures that could be resilient to harsh TCO sputtering conditions. Then, we optimize the cathode side of opaque and semi-transparent devices based on ETL bilayers composed of a fullerene derivative and a metal oxide layer.
- **Chapter 5** was dedicated to the wet chemical etching of CI(G)S absorber layers, to smoothen their surface and reach a mean roughness that would be more practical for subsequent deposition of the perovskite top cell layers. We first show the adaptation of an established process for CIGS etching based on a HBr:Br₂:H₂O solution on CI(G)S layers prepared by co-evaporation. Then, we study the change in surface chemistry associated to this process, including the variation in alkali concentration at the surface. In our last section, we compare the subtle differences in PV parameters for solar cells prepared out of as-prepared and planarized CI(G)S samples.

Finally, in the conclusion we describe the fabrication of prototype monolithic perovskite/CI(G)S tandem solar cells based on different architecture from these three approaches as an outlook on the further development of this technology.

Chapter 1

Background and Objectives

Summary: In this chapter, we review the basic concepts of solar cells, starting from the properties of semiconductors to the working principles of tandem solar cells. We then introduce the perovskite and CIGS technologies, as well as the major challenges to their monolithic integration in two terminal devices. We finally provide a state-of-the-art of the different strategies mentioned in literature to circumvent them.

Contents

1.1. Introduction	6
1.2. General principle of solar cells	6
1.2.1. General principle of a semiconductor	6
1.2.2. General structure of a solar cell	8
1.2.3. Characteristics of a solar cell	9
1.2.3.1. Open-circuit voltage	9
1.2.3.2. Short-circuit current	10
1.2.3.3. Fill factor	10
1.2.3.4. Power conversion efficiency	11
1.2.4. Detailed balance model for a single junction solar cell	11
1.3. Two-terminal tandem solar cells	12
1.3.1. Principle of tandem solar cells	12
1.3.2. Monolithic integration	13
1.3.2.1. Tunnel-recombination junction	14
1.4. CIGS alloys	15
1.4.1. CIGS structure and composition	15
1.4.2. Architecture of solar cell derived from CIGS alloys	16
1.4.2.1. Substrate and back contact anode	16
1.4.2.2. Buffer layer	16
1.4.2.3. Transparent conductive cathode	17
1.4.3. Specificities of low-bandgap Cl(G)S solar bottom cells for monolithic tandem integration ...	17

1.5. Hybrid lead-halide perovskite solar cell	18
1.5.1. Hybrid lead-halide perovskite structure and composition	18
1.5.2. Mixed halide perovskite top cell design for monolithic tandem integration	19
1.6. State-of-the-art of monolithic integration of mixed halide perovskite/CIGS tandem solar cells	20
1.7. Overview	

1.1. Introduction

In this chapter, I review the theoretical framework that will later serve to interpret our results in the following chapters. I first describe the general principle of solar cells, starting from the description of semiconductors to the detailed balance limit for single junction photovoltaic devices. Then, I follow with the depiction of a two-terminal solar cell that could overcome this thermodynamic limitation to the efficiency of solar cells. I then introduce the technologies of CI(G)S and perovskite solar cells, and study the state-of-the-art regarding their integration in two-terminal tandem solar cells. This chapter is completed by a general overview of the thesis.

1.2. General principle of solar cells

I first introduce the general working principles of a solar cell, and the main architecture and characteristics associated to it. We then describe the detailed balance limit, which sets a thermodynamic limit to the power conversion efficiency (PCE) of solar cells, and develop it for a single junction solar cell.

1.2.1. General principle of a semiconductor

The black body model defines a theoretical material that fully absorbs radiation of all photons of incident angle or energy $h\nu$, where h is Planck's constant and ν the photon's frequency. Its absorptance would be $a(h\nu) = 1$

From an electronic perspective, this characteristic is possible if a continuous and uninterrupted range of excitation energies are available for the electrons. Additionally, relaxation of energy through radiative emission and thermal relaxation in this model would be well represented by a quasi-continuum of electronic states in its band structure as described in **Figure 2a**.

This is not the case for semiconductors, as shown on **Figure 2b**. Semiconductors are materials for which occupied electronic states are separated by a band gap, which is devoid of available states. The band gap separates the valence band and the conduction band, which individually could be approximated as continuum of available electronic states. In quantitative terms it is equal to the difference between the conduction band minimum (*CBM*) and the valence band maximum (*VBM*). Most of the electronic states would be occupied in the valence band, and unoccupied in the conduction band. We can consider unoccupied states in the valence band as "holes", and treat them as charge carriers since electrons filling them will leave unoccupied states themselves.

The thermodynamic work required to add one electron to a body is called the Fermi level (E_F). As it is a thermodynamic quantity, it does not necessarily have to correspond to an actual available electronic state. In fact, for semiconductors the Fermi level can lie within the bandgap. For an intrinsic

semiconductor, that is a material where the concentration of electrons in the conduction band is equal to that of holes in the valence band, the Fermi level is nearly equidistant from the CBM and the VBM. For n-type and p-type semiconductors, the Fermi level lies respectively closer and further to the CBM than to the VBM, which respectively corresponds to a superior and inferior concentration of electrons in the conduction band compared to that of holes in the valence band. A semiconductor is considered degenerate if its E_F lies within either band.

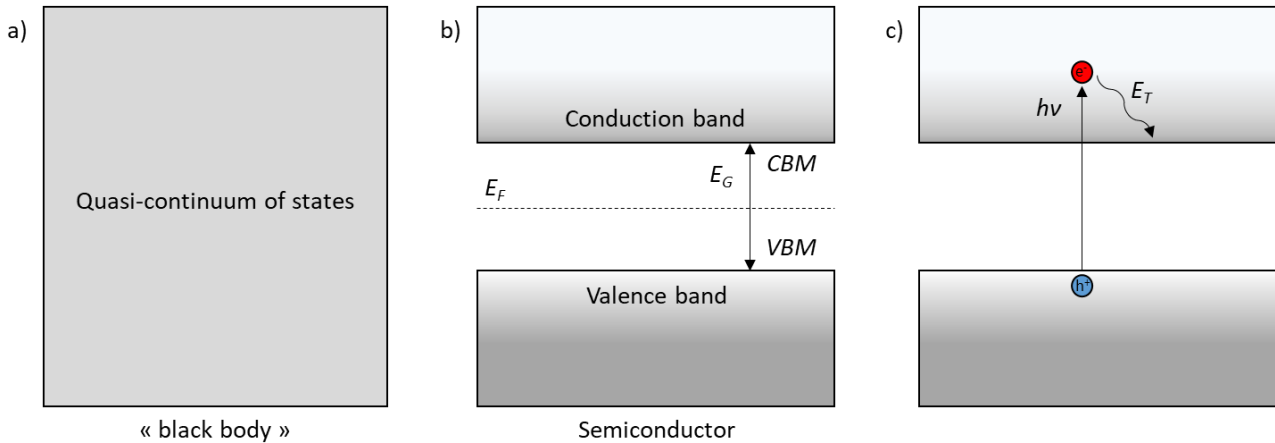


Figure 2 Band structures for (a) an ideal black body, characterized by an almost continuous succession of available electronic states and (b) a semiconductor whose electronic states are characterized by a valence band and a conduction band separated by an energy band gap between the valence band maximum (VBM) and conduction band minimum (CBM). (c) Schematic representation of the excitation of an electron from the valence band to the conduction band through the absorption of a photon, followed by thermal relaxation to the CBM.

Reciprocally, the workfunction (WF) defines the energy needed to remove an electron from a solid to vacuum. It should therefore correspond to the difference between the vacuum level and E_F . In practice however, most WF measurements are recorded as a difference between the surface potential and E_F .

Excitation of electrons through the absorption of a photon has thus to follow the condition $h\nu > E_G$, where E_G corresponds to the energy band-gap. This excitation promotes an electron e^- from the valence band to the conduction band, and leaves a hole h^+ in the valence band. A schematic of the process is given in **Figure 2c**. Other photons are either reflected, or transmitted through the material. Electrons excited in a semiconductor by the absorption of a photon of energy $E_T = h\nu$ generally experience thermal relaxation (i.e. emit a phonon) to reach the CBM, as most states lying in the conduction band are unoccupied. Generated holes will also rapidly reach the VBM by thermal relaxation of electrons of higher energy within the valence band. We can assume that these processes

are much faster than carrier diffusion and collection. After excitation, electrons in the CBM can relax to the valence band through different mechanisms, such as the emission of a photon of energy E_G . Likewise, this process generally occurs at a slower pace than thermal relaxation to the CBM. Thus, virtually all electrons and holes lie at their respective CBM and VBM.

1.2.2. General structure of a solar cell

The general principle of a solar cell is to use a semiconductor material as an “absorber” layer to promote electrons through the collection of photons, and to collect the charge carriers (i.e. electrons and holes) at distinct positions before they recombine. The whole process from carrier generation to collection can be divided in three steps:

- Promotion of an electron from the valence band to the conduction band
- Separation of the photo-generated charge carriers within the junction
- Collection of the separated carriers at the terminals of the junction

Separation and transport of photo-generated charge carriers are stimulated by establishing a potential gradient within the absorber layer under illumination^{6,7}. In practice, it can be achieved by intercalating an absorber layer between a n-type semiconductor and a p-type semiconductor as shown on **Figure 3a**. A heterojunction can also be formed directly between a n-type and a p-type absorber layers.

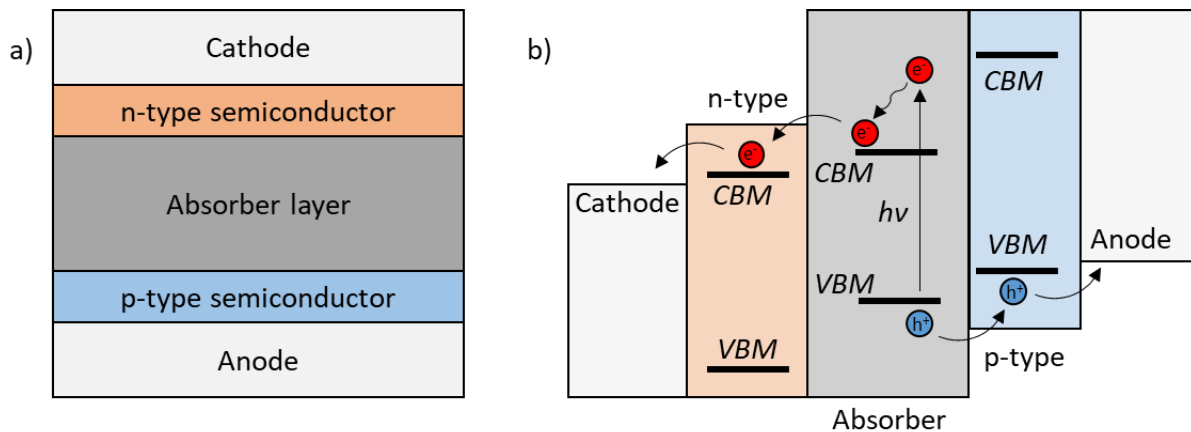


Figure 3 (a) Schematic representation of a complete solar cell **(b)** Separation and charge collection of charge carriers during solar cell operation

For maximal collection, the CBM and VBM for the n-type and p-type layers should be respectively positioned at a slightly lower and higher level compared to that of the absorber layer.

Reciprocally, charge transport layer (CTL) should present effective blocking properties regarding non-desired carriers, i.e. holes for the n-type layer and electrons for the p-type layer to prevent recombination at the interface of the absorber and either CTL. The VBM and CBM for the n-type and p-type layer should therefore be respectively positioned at a significantly lower and higher level compared to that of the absorber layer.

1.2.3. Characteristics of a solar cell

A solar cell converts the thermal radiation of the sun (P_{sun}) into electrical power (P) which is the product of electrical current (I) and voltage (V).

$$(1.1) \quad P = I \cdot U$$

The function of a solar cell thus consists in the generation of a photocurrent and a photovoltage⁸. Generation of a photovoltage arises from the promotion of an electron from the valence band to the conduction band of an absorber layer, and photocurrent is simply defined by the number of charge carriers that reach both cell terminals.

1.2.3.1. Open-circuit voltage

The open-circuit voltage (V_{oc}) is the maximum voltage that a solar cell can deliver. If intraband relaxation processes occur significantly faster than charge separation and collection at selective contacts, V_{oc} is ultimately limited by the bandgap of the absorber layer. Further limitations arise from radiative and non-radiative recombination processes.

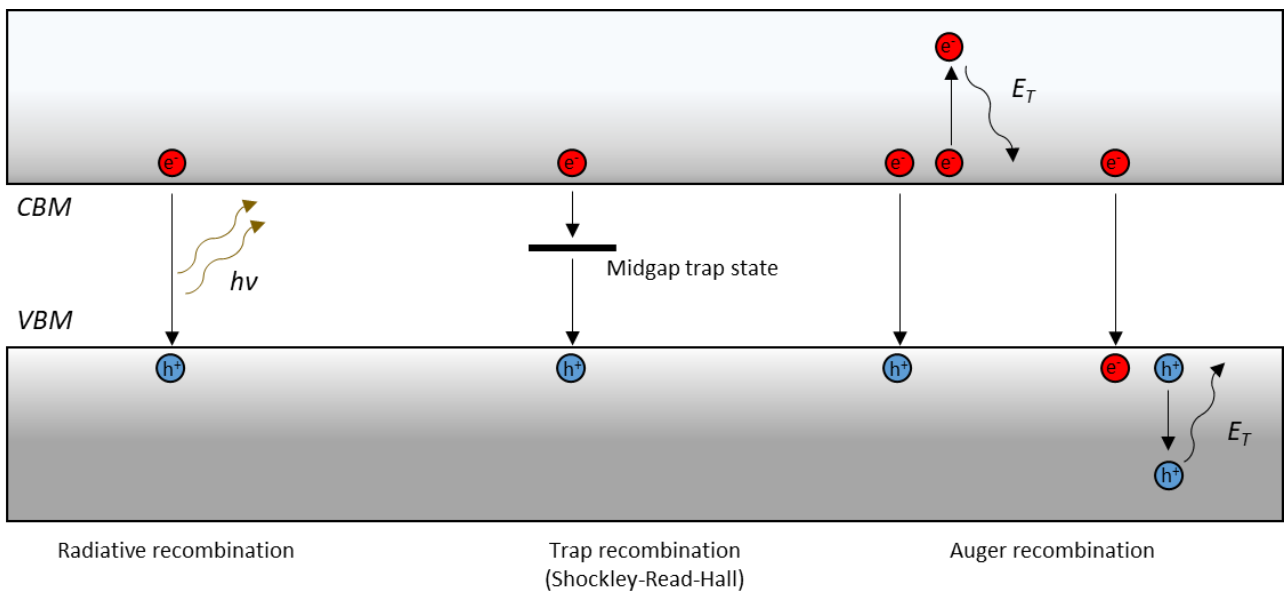


Figure 4 Illustration of the major recombination processes that can occur in a solar cell.

Radiative recombination is the reciprocal process to photon absorption, i.e. the emission of a photon by the recombination of an electron from the conduction band and a hole from the valence band. Non-radiative recombination consists of two main processes: Shockley-Read-Hall (SRH) trap-assisted recombination and Auger recombination.

Defects in the crystal lattice of the absorber material or interfaces in the whole device are likely to present available energetic states located within the bandgap, i.e. midgap trap states. SRH recombination is the thermal relaxation of electrons to the valence band using these traps as intermediate states.

Auger recombination is the direct relaxation of a conduction band electron to the valence band through the excitation of a secondary charge carrier. This carrier is first excited to one of its intraband state, and the extra energy is then released through thermal relaxation.

1.2.3.2. Short-circuit current

The short-circuit current (I_{sc}) is the photocurrent of the solar cell in short-circuit condition, that is when the voltage across the cell is zero. I_{sc} depends on multiple factors, such as the area of the solar cell, the optical properties of the layers in the device and the solar spectrum. In general, current can be expressed in current density (J_{sc}) to use a quantity to remove its dependency to the solar cell area.

J_{sc} is principally limited by the bandgap of the absorber material, which sets an energy threshold for the absorption of photons. Photons of energy $h\nu < E_G$ thus cannot contribute to J_{sc} .

1.2.3.3. Fill factor

J_{sc} and V_{oc} are the maximum respective current and voltage from a solar cell. At both these operating points, the solar cell power is however zero. As voltage bias applied to an operating solar cell is increased from 0 to V_{oc} , current density will decrease from J_{sc} to 0. Therefore, from equation (1.2), maximum power generation is a compromise between maximizing current and voltage during solar cell operation. The fill factor (FF) is defined as the ratio of the maximum power from the solar cell (P_{MP}) and the product of V_{oc} and J_{sc} .

$$(1.2) \quad FF = \frac{P_{MP}}{V_{oc}J_{sc}} = \frac{V_{MP}J_{MP}}{V_{oc}J_{sc}}$$

In an ideal solar cell, the FF is already < 1 . Series resistance (R_s) and shunt resistance (R_{sh}) are the principal factors that further decrease the FF .

R_s represents the bulk resistance of the components of the solar cell, and the resistance at their interfaces. A higher R_s results in a lower current density during operation, mainly in the region of potential where applied voltage $> V_{MP}$.

R_{sh} represents the resistance of alternative current pathways that would reduce the current flowing through the cell and its V_{oc} . A higher R_{sh} is beneficial for the solar cell, since it means a lesser tendency for charge carriers to follow these alternative pathways.

1.2.3.4. Power conversion efficiency

Power conversion efficiency (PCE) is defined as the ratio between the power output of the solar cell and P_{sun} . It is thus closely related to V_{oc} , J_{sc} and FF , but also depends on the spectrum and intensity of the incident sunlight.

$$(1.3) \quad PCE = \frac{P_{MP}}{P_{sun}} = \frac{V_{oc} \cdot J_{sc} \cdot FF}{P_{sun}}$$

Illumination under AM 1.5G conditions of light spectrum and intensity and a temperature of 25°C are the standard for V_{oc} , J_{sc} , FF and PCE measurements.

1.2.4. Detailed balance model for a single junction solar cell

Based on thermodynamic considerations, it is possible to establish a theoretical limit over the PCE of a solar cell as a function of the bandgap of the absorber layer. First, maximum J_{sc} and V_{oc} are both related to E_G . Increasing the bandgap of an absorber material would increase the upper limit of V_{oc} but decrease that of the J_{sc} . Therefore, the ideal value of E_G consists in a compromise between these two parameters to maximize the power of the solar cell. Depending on the specifications of each model, different optimal values of E_G can be derived.

The original detailed balance limit was derived by only considering the radiative aspect of recombination processes, which counterbalance absorption of photons according to the principle of detailed balance⁹. For a single junction solar cell at 25°C, and assuming a solar spectrum equivalent to AM 1.5G, this model predicts that a maximum PCE of 33.16 % could be reached with an absorber layer bandgap of 1.34 eV¹⁰.

However, the detailed balance limit does not take into account several factors such as non-radiative recombination processes which further decrease the performance of the cell. Currently, the record PCE for a single junction solar cell is 29.1 % and has been reached using a GaAs absorber material¹¹.

1.3. Two-terminal tandem solar cells

The main purpose of the tandem architecture is to overcome the limitation in PCE for a single junction solar cell, by combining different absorber layers in a single solar stack. In general, each absorber material is dedicated to a particular region of the solar spectrum and has a different value of E_G . The detailed balance limit has been established for a tandem cell constituted of two absorber layers of bandgap E_{G1} and E_{G2} ¹². In four-terminal configuration, calculations based on the AM 1.5G solar spectrum predict that a maximum PCE of 46.0 % can be reached with $E_{G1} = 1.73$ eV and $E_{G2} = 0.94$ eV¹³. For two-terminal devices, close limit of PCE at 45.7% can be reached with $E_{G1} = 1.60$ eV and $E_{G2} = 0.94$ eV.

1.3.1. Principle of tandem solar cells

A tandem solar cell constituted of two absorber layers can be assembled in four-terminal (4T) and two-terminal (2T) configurations. Designs implying three terminals have also been proposed to overcome the limitation of either architecture. In 4T configuration, the tandem cell is constituted of two solar cells contacted independently, and in general superimposed on top of each other. They are mechanically and optically connected but electrically independent, leading to the additivity of their photocurrents. This configuration leaves a certain flexibility in cell design. Additionally, the PCE of a 4T device is less sensitive to variations in the illumination spectrum than that of a 2T device.

Indeed, in a 2T tandem cell both subcells are optically and electrically connected in series, which leads to the additivity of their respective photovoltage. In this configuration, deposition process of the top cell should be compatible with the bottom cell in terms of temperature, surface roughness and chemical compatibility.

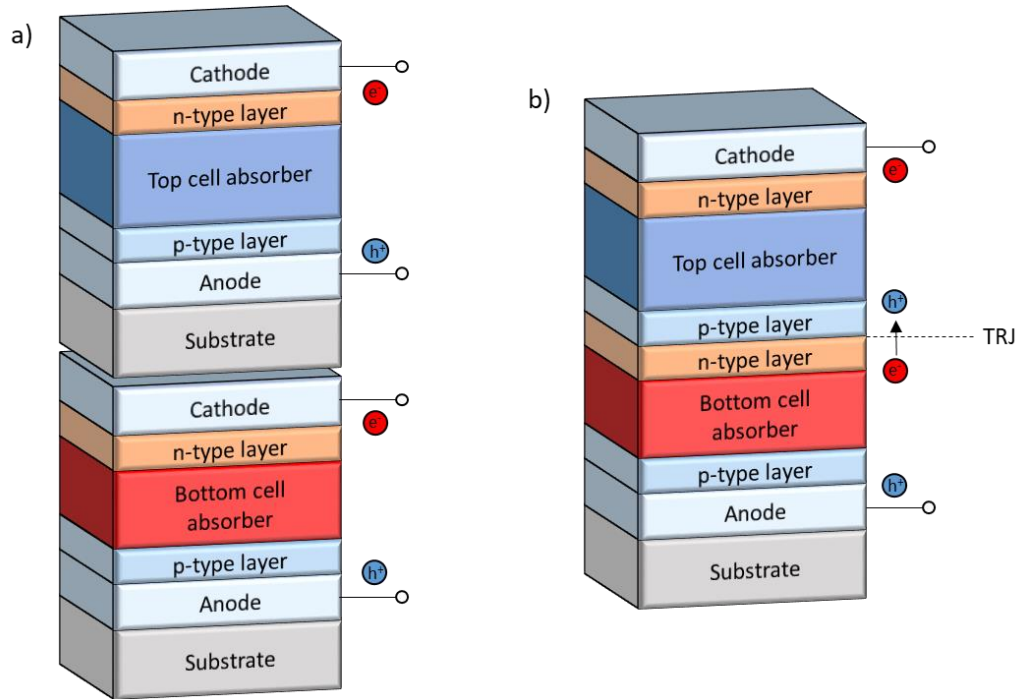


Figure 5 Schematic for a tandem solar cell constituted of two absorber layers in **(a)** four-terminal and **(b)** two-terminal configuration.

Additionally, this design introduces a tunnel-recombination junction (TRJ) sandwiched between both subcells. In this region, carriers that are not collected at the anode or the cathode recombine as shown on **Figure 5**. Overall, electrical connection results in a current matching condition between both subcells. One beneficial consequence of this configuration is to remove the lateral sheet resistance contribution from two former anode and cathode to the FF of the entire stack. But the current delivered by the tandem cell is now limited by the cell with the smallest current. In practice, current matching can be optimized to maximize J_{sc} for a particular solar spectrum. But compared to 4T devices, 2T tandem cells during operation will present higher deviation of PCE from ideal as illumination intensity and wavelength vary in the course of a day.

1.3.2. Monolithic integration

Nonetheless, the constraints induced by electrical connection are counterbalanced by simplified manufacturing processes and connectivity at the module level, as well as lower costs related to substrate fabrication. These advantages could render monolithic integration more suited to industrial applications compared to four-terminal integration.

1.3.2.1. Tunnel-recombination junction

The TRJ is a key element of a 2T tandem cell that can strongly affect J_{sc} , FF and V_{oc} ¹⁴. **Figure 6a** shows the formation of a RJ between the conduction band of a n-type and the valence band of a p-type layer. Electrons in a TRJ recombine with holes by interband quantum-tunneling. Ideally, to avoid significant voltage loss during recombination, electrons and holes should lie at similar energy levels. As depicted in **Figure 6b**, this can be achieved in an Esaki diode where degenerately doped n-type and p-type materials are put in contact. In this situation, the Fermi level would lie within their respective conduction and valence band.

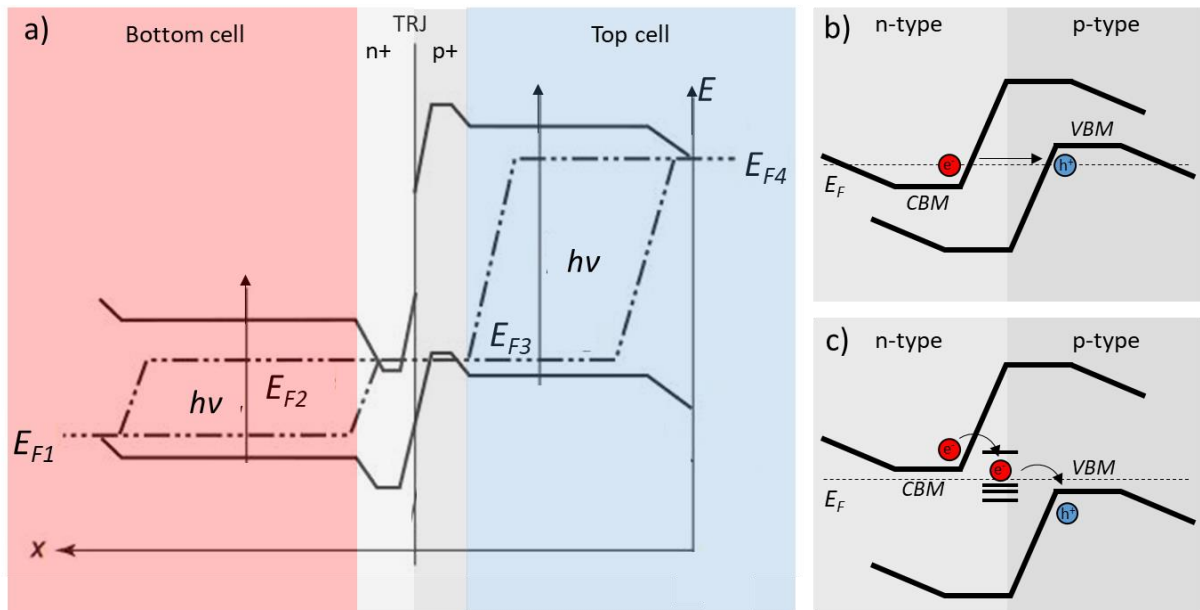


Figure 6 (a) Band diagram for a monolithic tandem cell¹. Recombination at the interface between two subcells in a 2T tandem solar cell through (b) an ideal Esaki tunnel junction and (c) a recombination junction, more common in perovskite tandems. E_{F1} , E_{F2} , E_{F3} and E_{F4} represent the quasi-fermi levels of the absorber layers when the cell is under illumination.

In practice, this ideal goal can be difficult to reach when one of the component of the TRJ is, for example, a perovskite solar cell (PSC) HTL or ETL as these components are rarely degenerately doped layers¹⁴. **Figure 6c** shows the alternative recombination mechanism when the Fermi level of materials constituting the TRJ lie within their bandgap. In this situation, resistive loss could be minimized by promoting trap assisted tunneling, i.e. tunneling of carriers to intermediate midgap

¹ Inspired from [15]

states before recombination. Strategies to enhance this phenomena would involve inserting an interlayer within the TRJ¹⁴.

1.4. CIGS alloys

Since the synthesis of chalcopyrite CuInSe₂ by Han et al. in 1953, CIGS has progressively been implemented in solar cells and PCE > 23 % can now be reached with single junction devices^{16,17}. As a thin film technology, CIGS is relevant for flexible applications. Its bandgap can be readily tuned by modifying its elemental composition, which makes it an ideal candidate for single junction as well as tandem application^{18,19}. Notably, efficiencies > 22 % and > 19 % have been recorded for bandgap absorber layers of 1.14 eV and 1.00 eV^{20,21}. For flexible devices, over 21 % PCE has also been reached on polyimide substrate²². However, while low bandgap CI(G)Se devices can exhibit reasonable PV performances, there has been a growing uncertainty regarding the possibility to achieve similar efficiency with its high bandgap counterpart CGS.

1.4.1. CIGS structure and composition

The term CIGS refers to a quaternary I-III-VI alloy of Cu(In,Ga)Se₂ composition. CIGS crystallizes in the tetragonal chalcopyrite structure depicted in **Figure 7**, with In and Ga occupying the same atomic sites.

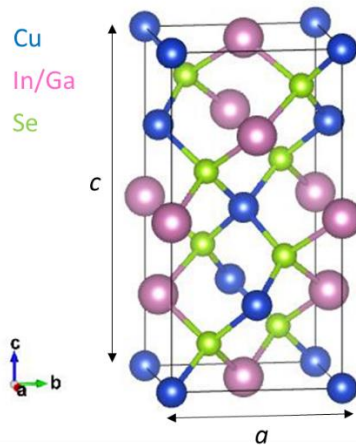


Figure 7 Unit cell for a Cu(In,Ga)Se₂ chalcopyrite, with a and c as the lattice constants.

CIGS is a p-type semiconductor which functionally acts as the main absorber layer in CIGS solar cells. In high efficiency devices, a p-n junction is often formed in contact with a n-type CdS layer. The bandgap of CIGS is typically tuned by modifying the $[Ga] / ([Ga] + [In])$ ratio (GGI). A transition from CuInSe₂ (CIS) to CuGaSe₂ (CGS) would shrink the lattice of the crystal, decreasing the constants a and c from 5.780 Å to 5.607 Å and from 11.604 Å to 10.990 Å²³. As a result, the bandgap would vary from 1.04 eV for CIS to 1.68 eV for pure CGS²⁴. Intermediate bandgap values can be

reached by tuning the GGI between 0 to 1. For high bandgap applications, Se can be also substituted by sulfur²⁵.

In addition to optimizing the absorption of light to a certain range of wavelength, it is often beneficial to tune the GGI across an absorber layer to form a graded bandgap CIGS layer. GGI would be preferably lower at the bulk and higher at the anode and cathode sides²⁵. Increasing the GGI at the anode side would result in a grading of the conduction band, creating a quasi-electric field that would drive excited electrons away from the anode. As a result, J_{sc} increases by an enhanced carrier collection. V_{oc} is also higher due to the lower back contact recombination²⁶. Higher GGI at the front cathode side would increase the J_{sc} by improving the absorption of photons via lower band gaps²⁶.

Intrinsic p-type doping of CIGS can be achieved by tuning the $[Cu] / ([Ga] + [In])$ ratio (CGI). Cu deficiency induces the formation of V_{Cu} states, which can act as acceptor states and have a low formation energy. They can form neutral pairs with $(In^{2+}_{Cu}, Ga^{2+}_{Cu})$, and in general CIGS has a certain defect tolerance as off stoichiometry compounds can be formed²⁷.

CIGS absorber layers can also be doped by alkali incorporation²⁸. Na generally diffuses from the soda-lime glass (SLG) substrate to the CIGS layer, and other species such as K and Rb can be implemented through post-deposition treatments (PdT). These species passivate the CIGS absorber surface as well as its grain boundaries, and increase the p-type carrier concentration in the layer. This phenomenon results in a lower E_F , and ultimately in an increase in V_{oc} and FF for completed cells.

1.4.2. Architecture of solar cell derived from CIGS alloys

1.4.2.1. Substrate and back contact anode

Thus, SLG is often used as substrate for CIGS solar cell fabrication as a Na reservoir. A typical architecture would then rely on Mo as back contact anode for (i) ohmic contact with CIGS (ii) adhesion of CIGS on top of Mo (iii) formation of a thin $MoSe_2$ interlayer during CIGS deposition and (iv) permeability of the layer to Na migrating from the substrate²⁹.

For monolithic tandem application, the low transmittance of Mo implies that the opto-electrical interface between the two subcells has to be established at the n-type front side of the CIGS solar cell.

1.4.2.2. Buffer layer

As stated before, n-type CdS is often used as a 40-80 nm buffer layer following CIGS deposition on Mo. The role of the buffer layer is to protect CIGS during subsequent sputtering process, and to act as an electron selective layer in the device³⁰. Environmental and health issues are nonetheless related to the use of Cd³¹. Another drawback of using CdS for this role is its bandgap of 2.4 eV, which

competes with CIGS for the absorption of photons in the high energy range³². Alternative buffer layers such as Zn(O,S) exist, but lower overall efficiencies are reached using these materials despite their higher bandgap³¹.

On top of the buffer layer and before TCO deposition, a small resistive layer of around 100 nm is deposited to avoid shunt pathways across the device³³. Intrinsic ZnO (i-ZnO) is preferred for CdS, while ZnMgO is usually adopted with Zn(O,S) buffer layers²⁵. Architectures for typical CIGS cells using CdS and Zn(O,S) are shown on **Figure 8**.

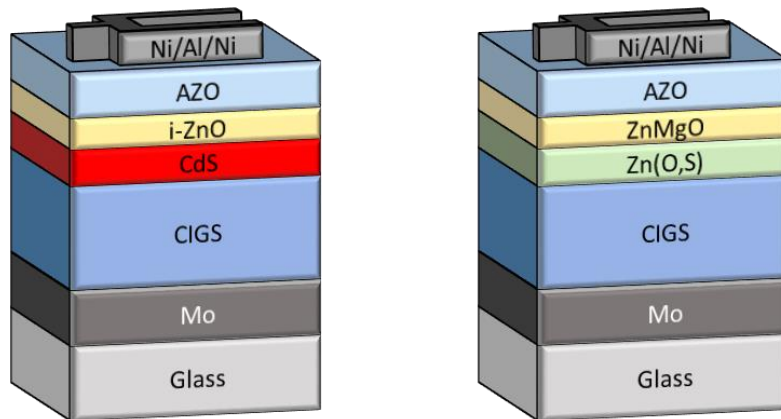


Figure 8 Examples of architectures for CIGS solar cells using CdS and i-ZnO (*left*) or Zn(O,S) and ZnMgO (*right*) as buffer layers, and a Ni/Al/Ni metal grid.

1.4.2.3. Transparent conductive cathode

Finally, a degenerately doped metal oxide layer is generally deposited by sputtering on top of the device and acts as a front transparent conductive layer. In this regard, the choice of material and layer thickness in the architecture consists in a compromise between transparency and lateral conductivity. Aluminum-doped zinc oxide (AZO) is used for this purpose in most architectures. Its thickness is generally 300 nm. Lateral conductivity of the device can also be improved by depositing a metal grid consisting in a succession of Ni/Al/Ni layers on top of the TCO²⁵.

1.4.3. Specificities of low-bandgap CI(G)S solar bottom cells for monolithic tandem integration

For low-bandgap devices, PCE can be improved by modifying the composition of CIGS and the architecture of the cell. The bandgap of the absorber material can be minimized using a CIS composition, however pure CIS solar cells are particularly subjected to back contact recombination. A single grading is often implemented by adding Ga at the Mo interface to limit back surface recombination²⁰. Such compositions are denoted here as CI(G)S.

As high energy photons are mainly exploited by the top cell in tandem configuration, the 2.4 eV bandgap of CdS would no longer be an issue regarding parasitic absorption and this material is often used as buffer layer in tandem devices^{5,20,21}.

Finally, replacing AZO by indium zinc oxide (IZO) as window layer would improve the performance of low bandgap CI(G)S solar cells, by limiting parasitic absorption in the near-infrared (NIR) region²⁰. The optimal window layer thickness for the bottom cell would remain only a matter of optical optimization, as lateral conductivity of the unwired TCO would be of little importance in a monolithic tandem design.

1.5. Hybrid lead-halide perovskite solar cell

Hybrid metal-halide perovskite (MHP) has been first employed in photovoltaic devices in 2009 as sensitizers in dye-sensitized solar cells³⁴. Since then, they were mainly employed as absorber layers in solar cells of increasing efficiencies over the last decade, with a current record $> 25\%$ ¹⁷. Due to their high absorptivity, high efficiency MHP absorbers can be deposited in thin films of thickness between 500 nm and 1 μm and are thus compatible with flexible architectures. Likewise to CIGS, MHP have a tunable bandgap depending on their composition ranging from < 1.5 eV for pure FAPbI₃ to > 2.3 eV for CsPbBr₃^{35,36}. This range of values makes MHP suited for both single junction applications and as absorber layer for a specific wavelength range in tandem architectures.

1.5.1. Hybrid lead-halide perovskite structure and composition

The term “perovskite” was first coined by Gustav Rose in 1839 after the mineralogist Count Lev Alekseyevich von Perovski. Back then it was employed to define the newly discovered mineral calcium titanate (CaTiO₃), but now can design any compound adopting a ABX₃ crystal structure. In its ideal cubic form depicted in **Figure 9**, the ABX₃ perovskite phase consists in a central B-site cation 6-fold coordinated to X-site anions in an octahedral fashion. Interstitial gaps at the corners are filled with monovalent A-site cations. Depending on their composition, perovskite compounds can also adopt orthorhombic, tetragonal and occasionally rhombohedral phases³⁵. The term perovskite can also describe a layered compound where ABX₃ layers are separated by thin sheets of an intrusive compound.

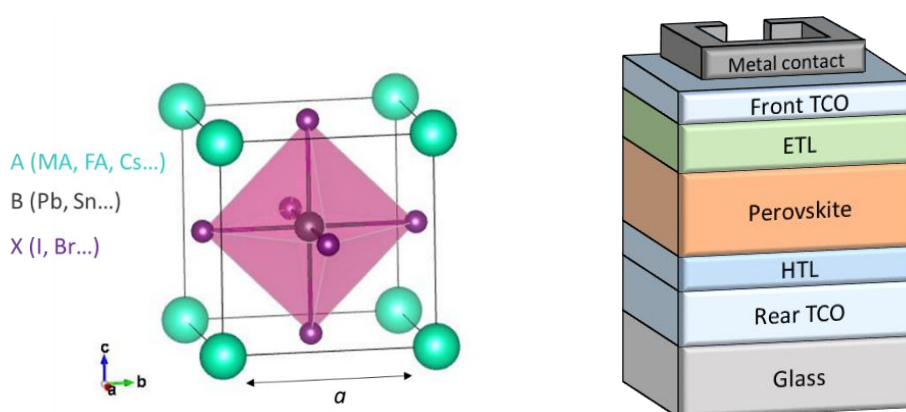


Figure 9 Unit cell for a ABX_3 perovskite cubic structure, with the BX_6 octahedra highlighted in purple (*left*) and typical architecture for a semi-transparent perovskite solar cell (*right*).

Several combinations of cation-anions pairing exist for the A, B and X ions. For most perovskite compounds, A and B are metal cations where A as a larger radius than B and X positions are filled with oxygen atoms. In the case of MHP, Pb^{2+} occupies the B position while X is a monovalent halide anion, generally I^- or Br^- . A^+ sites are filled with monovalent organic or metal compounds, usually methylammonium (MA^+), formamidinium (FA^+), Cs^+ or Rb^+ cations³⁷. MHP fully adopting this structure can be designed as 3D, while layered compounds where MHP slabs are separated by sheets of organic species are usually referred to as 2D perovskites.

Although most fabrication processes aim to synthesize the cubic black phase perovskite for photovoltaic applications, for many structural phase transition also occur to orthorhombic or tetragonal phases at certain conditions of temperature and pressure³⁵. Moreover, exposure to moisture, high temperature, radiations and oxidative environments are known to trigger degradation processes for MHP compounds and derived solar cells. They have been extensively described in literature over the years along with various approach to circumvent them and extend the operative lifetime of MHP based photovoltaic devices³⁸.

One of these approaches has been to employ 2D perovskite compounds, either as absorber layers of their own or as thin layers at the interface of a 3D perovskite phase and an adjacent material in a device. These layered structures are composed of MHP structures separated by monolayers of organic spacers of bigger size than typical A^+ cations³⁹.

1.5.2. Mixed halide perovskite top cell design for monolithic tandem integration

To reach a bandgap between 1.6 eV and 1.7 eV, composition of the perovskite layer can be tuned by varying the MA, FA and Cs content for the A cation and the I/Br ratio for the X halide anion.

Indium zinc oxide (IZO) can be used as a window layer to maximize transmittance in the near-infrared (NIR) region for the bottom cell⁵. Likewise, in p-i-n configuration a high transmittance HTL such as NiO_x or organic molecules as a self-assembly monolayer (SAM) can be implemented to increase the current generated by the bottom cell^{5,40,41}.

1.6. State-of-the-art of monolithic integration of mixed halide perovskite/CIGS tandem solar cells

High efficiency CI(G)S solar cells presently rely on a p-i-n architecture with the cathode on the transparent side. To fabricate a monolithic perovskite/CI(G)S tandem solar cell, it is thus necessary to keep the p-i-n architecture for perovskite top-cell deposition to ensure that electrons and holes from both subcells recombine at their interface.

Drastic improvement has been reported in recent years regarding monolithic perovskite/CI(G)S solar cells. Among the various factors that can influence performances, particular attention has been given to the adaptation of the CI(G)S bottom cell morphology and the development of a tunneling/recombination junction (TRJ) connecting the two subcells. Interface engineering encompassing these two factors have been proposed by Han et al., who achieved a record efficiency of 22.4 %. The CIGS bottom cell had the classical structure ending with the ZnO. It was then covered with an ITO layer which served as the back contact of an inverted p-i-n perovskite top cell, with PTAA as a hole transport layer. Recombination process would likely occur between the ITO layer and PTAA. However, a detailed analysis of the transfer mechanism, which encompasses rectification in each sub-cell and would thus be instrumental for current matching, has not been presented. A key point was the planarization of the CIGS bottom cell via mechanical polishing of the ITO layer to avoid shunts with the perovskite junction.

Due to the thermal sensitivity of CI(G)S solar cells using CdS as a buffer layer, low temperature processes should also be favored during top cell deposition. This is especially the case for devices using NiO_x as HTL for the perovskite subcell, as this material is often annealed between 250 °C and 300°C in high efficiency devices⁴⁰. NiO_x could be grown by atomic layer deposition (ALD) without post-annealing treatment, which could however impair the efficiency of the solar cell⁴². This approach was followed in the work of Jost et al. with a 21.6 % tandem cell developed on a rough CIGS surface without any planarization step⁴⁰. In order to prevent shunt pathways, a thin nickel oxide layer was conformably deposited on the rough CI(G)S surface by ALD, and then PTAA was deposited as HTL. In that case, the recombination junction was likely between ZnO (n+) and NiO (p+). The mechanism

of charge transfer was also not investigated in detail. Without using PTAA, stable devices at 18 % PCE were obtained.

Another option employed by Al-Ashouri et al. has been to use a SAM layer constituted of organic molecules as HTL, which can be deposited by dip-coating at room temperature to ensure a conformal coverage regardless of the roughness of the substrate^{5,41}. PCE of 23.6% was reached by depositing small molecules named “2PACz” (2-(9*H*-Carbazol-9-yl)ethyl)-phosphonic acid) directly on top of the front TCO of a CI(G)S bottom cell, before perovskite layer deposition. They claimed that the small organic molecules to be arranged as a monolayer. By processing highly efficient perovskite standalone cells using 2PACz between ITO and the perovskite layer, the authors showed that the small organic molecules played the role of a HTL. The mechanism of charge transfer in this unusual architecture was not clarified, although charge carriers are likely to recombine between the front TCO layer of CIGS and 2PACz.

From this last approach, Marco et al. principally optimized the cell architecture for current matching⁵. They adapted the bandgap of the CIGS bottom cell absorber layer to a lower value, applied antireflective coating of their devices and used IZO as a window layer for both subcells to increase the amount of transmitted near-infrared light received by the CIGS subcell. The bandgap of the perovskite subcell could also be tuned by varying the stoichiometry of Br in the precursor solution. The authors also inserted a thin NiO_x layer between the IZO and “MeO-2PACz” (2-(3,6-Dimethoxy-9*H*-carbazol-9-yl)ethyl)-phosphonic acid) layer, and reached values of PCE of 24.9 %.

1.7. Overview

In this chapter, starting from the fundamentals properties of semi-conductors we derived the principal physical quantities that will be used for characterization of samples during the course of this thesis. We also reviewed the different solar cell technologies that are the subject of this study, that is p-i-n perovskite and CI(G)S solar cells, designed for single junction or tandem configuration. We also introduced the current state-of-the-art for the monolithic integration of perovskite/CI(G)S tandem cells with the principal achievements and challenges in this domain. Ideally, the perovskite topcell should be fully processable at low temperature and conformably deposited on rough substrates. The deposition of the HTL layer on top of the degenerately doped n-type window layer of the CIGS subcell should form a proper TRJ were electrons and holes recombine without resistive loss.

Chapter 2

Methods

Summary: Introducing the techniques and methods employed to prepare and study the samples.

Contents

2.1. Fabrication methods	23
2.1.1. Atomic Layer Deposition (ALD).....	24
2.1.2. Spin coating.....	25
2.1.3. Preparation of Cl(G)S absorber layers	27
2.1.3.1. Co-evaporation	27
2.1.3.2. Sequential deposition	27
2.1.4. Chemical bath deposition (CBD).....	28
2.1.5. Sputter deposition	28
2.1.6. Thermal evaporation	28
2.1.7. Bromine wet etching of Cl(G)S absorber layers.....	29
2.1.7.1. Setup to smoothen small-scale Cl(G)S samples (size between 1*1 cm ² and 2*2 cm ²)	29
2.1.8. KCN treatment	30
2.1.9. HCl treatment	30
2.2. Characterization techniques	30
2.2.1. X-ray diffraction (XRD)	30
2.2.2. Atomic Force Microscopy (AFM).....	31
2.2.2.1. Kelvin probe force microscopy (KPFM).....	31
2.2.3. Scanning Electron Microscopy (SEM)	32
2.2.4. Photoemission spectroscopy	32
2.2.4.1. X-Ray photoemission spectroscopy (XPS).....	33
2.2.4.2. Ultraviolet photoemission spectroscopy (UPS)	34
2.2.5. Inductively coupled plasma optical emission spectroscopy (ICP-OES).....	34
2.2.6. Glow discharge optical emission spectroscopy (GD-OES)	35
2.2.7. X-ray fluorescence (XRF)	35
2.2.8. Cyclic voltammetry (CV).....	36
2.2.9. Current density-voltage (J-V) measurement.....	37
2.2.10. External Quantum efficiency (EQE).....	38
2.3. Overview	

2.1. Fabrication methods

Summary - Perovskite solar cell		
Functionality	Material	Deposition method(s)
HTL	2PACz, MeO-2PACz	Spin coating (p.25)
	NiO _x	ALD (p.24) Spin coating (p.25) Sputter deposition (p.28)
Absorber layer	Perovskite	Spin coating (p.25)
ETL	PCBM	Spin coating (p.25)
	Np-ZnO	Spin coating (p.25)
	C ₆₀	Thermal evaporation (p.28)
	SnO ₂	ALD (p.24)
Interlayer	BCP	Spin coating (p.25)
	Np-AZO	Spin coating (p.25)
Electrode	ITO, FTO, IZO	Sputter deposition (p.28)
	Ag	Thermal evaporation (p.28)

Summary - CIGS solar cell		
Functionality	Material	Deposition method(s)
Absorber layer	CIGS, CI(G)S	Co-evaporation (p.27) Sequential deposition (p.27)
Buffer layer	Zn(O,S)	CBD (p.28)
	ZnMgO	Sputter deposition (p.28)
Electrode	Mo	Sputter deposition (p.28)
	AZO	Sputter deposition (p.28)

2.1.1. Atomic Layer Deposition (ALD)

ALD is a gas phase deposition method based on surface reactions to grow thin films⁴³. The substrate is alternatively exposed to vapor phase reactants, which are pumped or purged away between each surface reaction step. Reactions in ALD are self-limiting, in the sense that only a finite amount of reactive species reacts with a finite number of available surface sites during each step of the process.

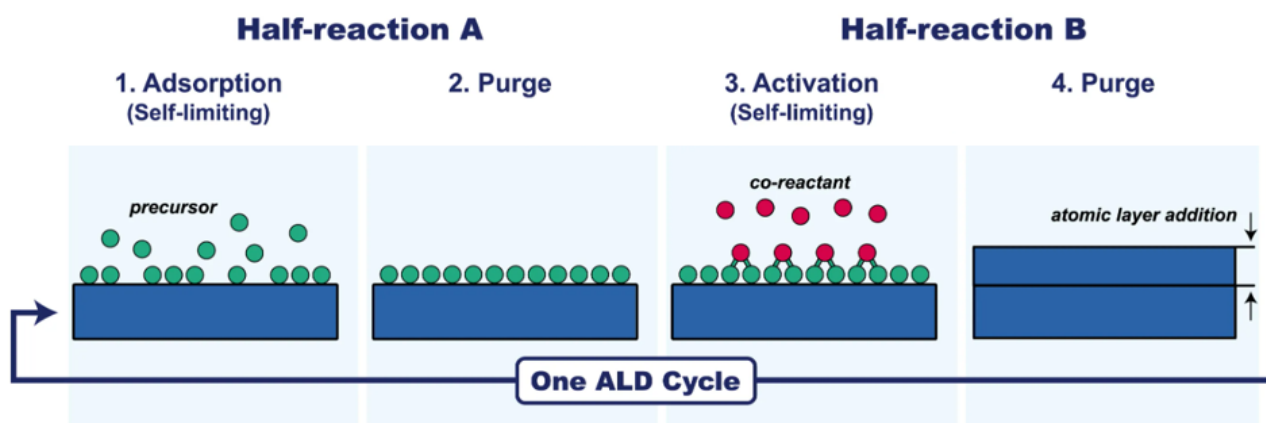


Figure 10 Schematic representation of an ALD cycle for the synthesis for a binary AB compound

(From <https://www.atomiclimits.com/>)

For each step, these surface sites should also be completely saturated to ensure conformal and uniform deposition of the target material independently of the substrate morphology⁴³. This condition can be met by optimizing the deposition temperature and the time parameters for each step, i.e. for reactant exposure and purging durations. For a given ALD system, growth per cycle (GPC) can be plotted against each time parameter while keeping the others relatively large. These plots are referred to as saturation curves, as GPC reaches a plateau for high duration values. Ideally, these values should be minimized for practical reasons while maintaining a high GPC to ensure saturation. A complete ALD cycle is depicted on **Figure 10**. In theory, ALD allows for an atomic layer control over the film thickness. Control of the layer thickness is however limited by the nucleation phase, during which the growth rate of the deposited material is dependent on the substrate.

ALD can be carried out under soft conditions. Indeed, deposition pressure can vary between 100 mTorr for plasma ALD and atmospheric pressure (~ 760 Torr) in viscous flow reactors⁴³. For each ALD system, the process is characterized by the “ALD window”, i.e. the range of temperature for which GPC is constant. In this region, reactants have enough energy to react and would neither condense, decompose or desorb from the substrate. This temperature is typically between RT and 400°C.

ALD has been a technique of interest in the development of perovskite solar cells, in particular in the pursue of minimizing shunt pathways in device by the deposition of homogeneous and conformal charge transport layers⁴⁴.

During the course of this thesis, ALD was used to grow either NiO_x films on ITO/FTO substrates or SnO₂ on top of C₆₀ for perovskite solar cells in p-i-n configuration.

NiO_x films from IPVF were prepared in a BENEQ TFS-200 apparatus, using bis(N,N'-di-*t*-butylacetamidinato)nickel(II) (Ni(amd)₂) as Ni precursor and H₂O as oxidizer at a deposition temperature of 160°C or 100°C while T_{source} was maintained at 80°C. Time parameters were 0.6/0.03/0.3/1.6/5 s (Ni(amd)₂) || 0.8/5 s (H₂O). Before deposition, ITO and FTO substrates were cleaned in ultrasonic bath in 2% soap in water solution for 40 min, followed by deionized water for 10 min, acetone for 15 min and IPA for 15 min. N₂ flow was used to dry the substrates. They were then submitted to UV-Ozone treatment for 15 min before introduction in the ALD chamber.

NiO_x films received from ZSW for characterization were prepared using bis(methylcyclopentadienyl)nickel(II) (Me-nickelocene) as Ni precursor and either oxygen-plasma or O₃ as oxidizer at a deposition temperature of 75°C, 100°C, 150°C, 200°C or 250°C. Before deposition, ITO substrates were cleaned according to a specific procedure not detailed here.

2.1.2. Spin coating

Spin-coating is a straightforward, simple wet process to deposit thin films. In short, material precursors are mixed in a solution which is then dropped on a spinning substrate, either before (static mode) or while spinning (dynamic mode). For perovskite deposition, dropping an anti-solvent during the final phase of the spinning process induces rapid and dense nucleation that leads to an uniform and pinhole free film⁴⁵. Morphological properties of the deposited layer depend on the wettability of the precursor solution solvent over the substrate, substrate morphology, spinning speed and spinning time.

Chlorobenzene and ethyl acetate were alternatively used as anti-solvent for perovskite deposition, without distinctive differences in layer morphology, structure or completed cell PV parameters. Except for NiO_x deposition, all materials were deposited in a nitrogen filled Jacomex glove-box.

Triple-cation perovskite precursor solution was prepared in a nitrogen filled Jacomex glove-box by dissolving 507 mg of PbI₂, 73 mg of PbBr₂, 172 mg of formamidinium iodide (FAI) and 22 mg of methylammonium bromide (MABr) in 1 mL of a 4:1 volumic ratio of N,N-Dimethylformamide (DMF):Dimethylsulfoxide (DMSO) solvent. Complete dissolution of the precursors was ensured by

either 2 hours stirring at ambient temperature or 70°C heating for one hour. Afterwards, 40 μL of a 386 mg/mL solution of CsI in DMSO was added for a final solution stoichiometry of $\text{Cs}_{0.05}\text{FA}_{0.85}\text{MA}_{0.10}\text{Pb}_{1.04}(\text{I}_{0.84}\text{Br}_{0.16})_3$.

Likewise, double-cation perovskite precursor solution was prepared by dissolving 564 mg of PbI_2 , 79 mg of PbBr_2 , 173 mg of formamidinium iodide (FAI) and 112.24 mg of CsI in 1 mL of a 4:1 volumic ratio of DMF:DMSO solvent for a final solution stoichiometry of $\text{Cs}_{0.25}\text{FA}_{0.75}\text{Pb}_{1.00}(\text{I}_{0.91}\text{Br}_{0.09})_3$.

Complete dissolution of either type of precursor solution was ensured by 2 hours stirring at ambient temperature or 70°C heating for one hour. 40 μL of precursor solution was then spin coated in static mode with a two-step method: 1000 rpm for 10 seconds followed by 6000 rpm for 30 seconds. 12 seconds before the end of the second step, 150 μL of chlorobenzene (CB) was dropped on the spinning substrate. Perovskite films were then annealed at 100°C for 30 min.

2PACz and MeO-2PACz were deposited by spin-coating 40 μL of a 0.01 M solution in EtOH at 2500 rpm for 35 seconds in static mode. We waited 5 seconds between dropping the solution and starting the spin-coating program.

NiO_x layers prepared by sol-gel and combustion process were deposited by spin-coating.

For solution-processed NiO_x we dissolved 290.79 mg of $\text{Ni}(\text{NO}_3)_2$ (1 mmol) in 940 μL of ethylene glycol and added 60 μL of ethylene diamine (0.9 mmol) in a nitrogen filled Jacomex glove-box. The solution was left to stir overnight. In ambient atmosphere, 40 μL of solution was spin-coated at 3000 rpm for 30 seconds in static mode. Films were then annealed at 300°C for one hour in air.

For combustion NiO_x we dissolved 290.79 mg of $\text{Ni}(\text{NO}_3)_2$ in 10 mL 2-methoxyethanol in a nitrogen filled Jacomex glove-box. After dissolution, 10 μL of acetylacetonate were added. The solution was then left to stir overnight. In ambient atmosphere, 40 μL of solution was spin-coated at 3000 rpm for 30 seconds in static mode. Deposited films were annealed at 250 °C for 45 min in air.

PCBM layers were deposited by spin-coating 40 μL of a 20 mg/mL solution in CB at 2000 rpm for 40 seconds in dynamic mode.

BCP layers were deposited by spin-coating 40 μL of a 0.5 mg/mL solution in isopropanol (IPA) at 2000 rpm for 40 seconds in dynamic mode.

Np-ZnO and np-AZO layers were deposited by spin-coating 40 μL of a commercial solution from Sigma Aldrich in isopropanol at 4000 rpm for 30 seconds in dynamic mode.

2.1.3. Preparation of CI(G)S absorber layers

2.1.3.1. Co-evaporation

Thermal co-evaporation is a common practice for deposition of CIGS and have led to higher records efficiencies in solar cells^{46,47}. Cu, In, Ga and Se are simultaneously evaporated in a high vacuum chamber. Source temperatures are maintained high enough to melt the components and facilitate evaporation. Deposition conditions typically imply an excess concentration of Se in the chamber, because of his small sticking coefficient⁴⁸. The fluxes of Cu, In and Ga are tuned during the process to yield the desired composition.

A three-step process can be adopted for CIGS deposition. This method would intrinsically yield a higher GGI at the cathode and anode sides of the absorber layer as compared to the bulk, which would be beneficial for the cell. The Se concentration is constant during the whole process to sustain an excess concentration in the chamber. At the first stage of the process, In and Ga are evaporated at a substrate temperature of 350 °C - 400 °C to from an (In,Ga)₂Se₃ precursor. Then, temperature is increased to 425 °C - 500 °C and Cu flux is turned on while In and Ga fluxes are turned on to convert the precursor to Cu(In,Ga)Se₂. At the end of the second stage, CIGS formation is complete and Cu_xSe binary phases start to form. This change in chemistry can be determined by “end-point detection”, as substrate temperature drop due to the higher emissivity of Cu_xSe as compared to CIGS⁴⁸. During the third phase of the process, temperature of the second phase is maintained. In and Ga fluxes are turned on again while turning off the Cu source. During this last stage, Cu_xSe phases are converted to CIGS and CGI can be tuned to yield a Cu poor absorber layer^{49,50}.

This process can be readily adapted to CI(G)S, by considerably limiting the amount of Ga evaporated during the first phase and turning the source off for the third stage²¹. This adapted process would result in a single Ga grading in the absorber layer.

2.1.3.2. Sequential deposition

Although high PCE records for CIGS solar cells were reached using co-evaporated chalcopyrite absorber layers, sequential deposition is considered as more adequate for industrial mass production due to the good uniformity, low cost, and high deposition rate of the technique. Sequential deposition consists in a two-step process. A layer composed of metallic precursors (Cu, In, Ga) is first deposited by sputtering, and then converted to CIGS by thermal evaporation of Se. During the thermal evaporation step, the substrate is typically kept at high temperature such as 500°C.

The Ga/(Ga + In) ratio can be controlled by varying the composition of the metallic precursor layer, and small band gap layers can be obtained by limiting the amount of deposited Ga. Layers synthesized by this method typically exhibit a higher surface roughness compared to that of co-evaporated CI(G)S⁵¹.

CI(G)S samples prepared by co-evaporation and sequential deposition were provided by the Nederlandse Organisatie voor Toegepast Natuurwetenschappelijk Onderzoek (TNO).

2.1.4. Chemical bath deposition (CBD)

CBD is a way to conformably deposit metal oxide films by immersing a substrate in a liquid solution of precursors. For a given substrate, solution temperature, pH as well as concentration and precursor species are the main factors that influence the film chemistry and thickness⁵². CBD is commonly used for the deposition of a CdS or Zn(O,S) buffer layer on top of rough CIGS substrates.

Zn(O,S) layers were prepared by CBD using ZnSO₄ as zinc donor. Species concentrations were 0.65 M for SC(NH₂)₂, 0.15 M for ZnSO₄ and 2 M for NH₃ while the temperature of the bath was maintained at 80 °C. After Zn(O,S) deposition, the samples were rinsed in NH₃ solution and de-ionized water to avoid Zn(OH)₂ post-precipitation at the surface of the films⁴⁹.

2.1.5. Sputter deposition

Sputter deposition is a physical vapor deposition process, to deposit thin films. In ultrahigh vacuum, ion bombardment of a source material or target composed of the thin film elements provoke their vaporization. The vapor phase will then deposit on the substrate to form the wanted material⁵³.

Mo, Zn_{0.75}Mg_{0.25}O, AZO, IZO and ITO layers were deposited by sputtering using a Plassys MP 500 S and/or a Plassys 600 S.

2.1.6. Thermal evaporation

Metal contacts as well as C₆₀ were deposited by thermal evaporation. Thickness of the metal layers were 80 nm, and that of C₆₀ layer was 15 nm.

2.1.7. Bromine wet etching of CI(G)S absorber layers

In order to decrease the surface roughness of CI(G)S layers prepared by co-evaporation or sequential deposition, we employed a chemical etching protocol based on a 0.2M HBr : H₂O : 0.02M Br₂ solution described in 2012 by Bouttemy et al., inspired by an earlier report using a KBr:H₂O:Br₂ solution from Canava et al.⁵⁴⁻⁵⁶.

Bromine wet process was carried out at Institut Lavoisier de Versailles (ILV).

2.1.7.1. Setup to smoothen small-scale CI(G)S samples of the order of 1*1 cm² to 2*2 cm²

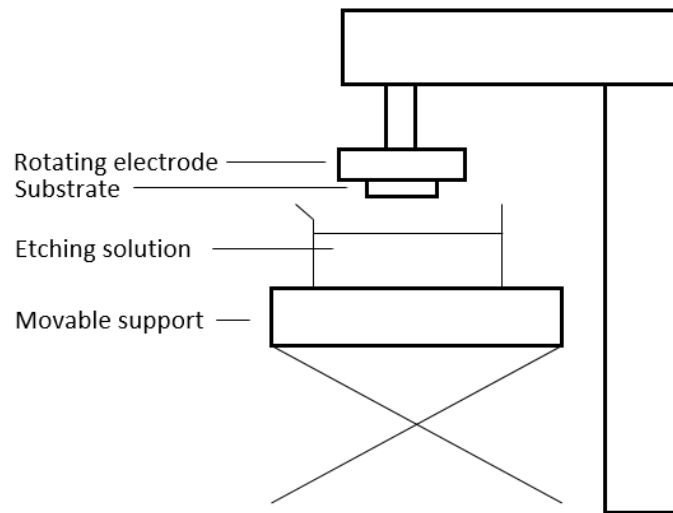


Figure 11 Schematic of the setup employed for bromine wet etching of CI(G)S absorber layers for sample size of the order of 1*1 cm² to 2*2 cm². The sample is attached face down to a rotating-disk electrode and dipped in the etching solution while rotating.

A similar setup suited for small scale substrates as the one employed earlier by ILV team was used for the study (**Figure 11**). As the composition and roughness of TNO's samples was somehow different from the CIGS one on which the dissolution protocol was established, a first step dedicated to the optimization of the dissolution conditions (time – rotation speed) for TNO's samples was realized^{55,56}. Not only the difference in composition (only CIS at the surface, Ga only present at the rear interface) was considered but also the requirement to decrease the roughness from 60 nm to 30 nm while conserving a thickness around 2000 nm, meaning a reduction of only few hundreds of nm. Shortly, a beaker containing the etching solution is situated on a support whose height can be modulated for the introduction and extraction of the sample fixed using carbon tape face down on the rotating electrode. After we start the rotation of the electrode, the height of the support is increased

to dip the spinning sample into the etching solution while avoiding the formation of air bubbles at the solid/liquid interface.

During the course of this study, we limited ourselves in optimizing the spinning speed and dipping time parameters while HBr and Br₂ concentrations were fixed at respectively 0.2 M and 0.02 M. We also systematically used the same beaker for etching solutions to preserve similar hydrodynamic conditions during experiments.

2.1.8. KCN treatment

Se⁰ phases are formed after HBr:Br₂:H₂O wet process of CI(G)S samples, and would be detrimental for solar cell performances. These phases can be removed by KCN treatment (0.1 mol L⁻¹, 5 min) before completion of solar cells⁵⁴.

2.1.9. HCl treatment

For Glass/Mo/CI(G)S/CdS stacks provided by TNO, the CdS capping layer was dissolved by stirring the samples in a 1 M HCl solution for 2 min. They were then washed thoroughly with deionized water and dried with a N₂ gun.

2.2. Characterization techniques

2.2.1. X-ray diffraction (XRD)

X-ray diffraction (XRD) is a commonly used technique to study crystal structures. It is based on the constructive interference of a scattered beam after hitting a periodic material and being collected by a detector. The beam is constituted of collimated monochromatic X-rays emitted from a cathode tube, and the angle θ between the incoming rays and the surface of the material is varied over a certain range of values during measurement to yield a diffractogram (photon counts against 2θ angle). Constructive interference occurs only for situations when the interaction between the incident beam and lattice planes obey Bragg's law:

$$(2.1) \quad n\lambda = 2d\sin(\theta)$$

Where n is an integer, λ the wavelength of the incident photon and d the interplanar spacing of the periodic material. Information that can be extracted from a diffractogram includes crystal structure, orientation and grain size⁵⁷.

We used a Panalytical analyzer for XRD measurements and the Highscore software package to remove background noise and extract peak information from diffractograms.

2.2.2. Atomic Force Microscopy (AFM)

AFM is a precise tool to probe the topography at the surface of a material down to a nanometric scale. The probe consists in a tip mounted on the end-point of a cantilever. At the other edge of the cantilever is mounted a piezoelectric actuator, that maintains the tip at a constant force or constant height above the sample during measurement. At the tip-side, a laser beam hits the cantilever and the reflected light is collected by a position sensitive photodetector which provides cantilever deflection feedback.

The principle of AFM operation is that of feedback mechanisms between the piezoelectric actuator and the photodetector, while scanning the surface of the sample with the tip.

In intermittent or tapping AFM mode, the piezoelectric actuator applies a force on the cantilever to provoke oscillations at or close to its resonance frequency. Amplitudes of oscillation are typically in the range of 20 nm to 100 nm when the tip is not in contact with the sample. Interacting with a bump or a depression over the surface during scanning will respectively trigger a decrease or increase in oscillation amplitude. This variation is recorded by the photodetector, which generates a signal sent to the piezoelectric element. In response, the piezoelectric adjusts the height of the tip to maintain a constant amplitude (or force). This signal is plotted as the height of the sample in the z-direction against the x-y lateral position of the tip over the sample⁵⁸.

2.2.2.1. Kelvin probe force microscopy (KPFM)

KPFM is a non-destructive technique to probe surface topography of samples while providing a spatial distribution of the surface potential, from which WF values can be derived.

It consists in the mounting of a Kelvin probe (KP) over an AFM platform. KP is a technique that measure the contact potential difference (CPD) between the tip of the KP and its surface. By subtracting the CPD to the WF of the tip, one can obtain a value of WF at the surface of the sample. Coupling with AFM then permits to recover a spatial distribution of surface potential⁵⁹.

For AFM measurements at IPVF, we used an Agilent Technologies 5600LS tapping mode system to measure the roughness of the samples, with ACL tips from AppNano. AFM and KPFM measurements were also performed at the Laboratoire de Génie Electrique et Génie Electronique de Paris (GEEPS).

2.2.3. Scanning Electron Microscopy (SEM)

SEM is a characterization technique that can provide information over the topography, morphology and composition of samples through high-resolution magnified images. A low-energy electron beam is emitted from an electron gun, and provides energy to the electron of the sample after getting focused by magnetic field lenses and metals slits through a vacuum column. The interaction between the primary electrons from the column and the sample generates secondary, backscattered and diffracted backscattered electrons. While secondary electrons provide information regarding the morphology of the surface, backscattered electrons are rather sensitive to the differences in atomic number between elements and contrast can provide compositional information. Signal from the electrons are collected by detectors to generate an image. Contrarily to optical systems, SEM is not diffraction limited and can generate images with a very high spatial resolution, down to 1 nm⁶⁰.

The SEM images were acquired from secondary and back-scattered electrons using a Zeiss Merlin VP compact 35 field emission gun (FEG) scanning electron microscope.

2.2.4. Photoemission spectroscopy

Photoemission spectroscopy is a non-destructive technique to study the chemical and electronic properties of surface and near-surface regions of conductive materials. This technique is based on the photoelectric effect, and generally consists in three steps.

First, high-energy photons irradiate the samples and excite electrons from core levels or in the valence band down to several nm below the surface. During this work, we used ultraviolet photoemission spectroscopy (UPS) and X-ray photoemission spectroscopy (XPS). Therefore, sources used for generation of photons were respectively a gas discharge lamp (He^I, He^{II} at 21.2 eV and 40.8 eV) and a monochromatized X-ray anode (Al-K α at 1486.6 eV). After excitation, a hole is created in the level from which the photoelectrons are emitted. Photoelectrons then move upward towards the surface. During this phase these electrons can experience scattering (elastic or inelastic) which may result in a transfer of energy to other electrons in their environment. This process is called secondary electron scattering and these electrons contribute to the background of the captured photoelectron spectra. The deexcitation proceed by filling the previous hole by an electron situated in a higher energy level and the residual energy lead to either emission of fluorescence or of the departure of another electron of valence levels (Auger process). Analyses are realized under UHV conditions (3.10^{-7} mbar) to maximize the electrons collection and preserve the surface state. Finally, electrons which have enough energy to leave the surface of the material into ultrahigh vacuum and emitted in the collection solid

angle of the detector arrive at the entry of the analyser and contribute to the XPS spectrum. From the kinetic energy of detected photoelectrons, we can access to their initial binding energy in the material which provides chemical and electronic information about the surface of the sample.

When the sample and the spectrometer are grounded to the same reference, they are at the same Fermi level. The measured kinetic energy of photoelectrons can thus be calculated:

$$(2.2) E_k = h\nu - E_B - WF_{sp}$$

Where E_k is the measured kinetic energy of the photoelectron, $h\nu$ the photon energy, E_B the initial binding energy of the electron in the material and WF_{sp} is the work function of the spectrometer⁶¹. WF_{sp} being at the Fermi level is set to 0 in this configuration what can be verified using a reference sample, such as the surface of metallic gold. Thus, the binding energy can be derived from the kinetic energy and above known parameters.

The probing depth of photoemission spectroscopy mainly depends on the photon energy used to excite the photoelectrons and the selected photopeaks. It is related to the inelastic mean free path of photo-emitted electrons in the solid, that is the average length that it can pass before transferring energy to electrons around them by inelastic scattering. Inelastic mean free path thus depends on the excitation energy, and thus on the detected kinetic energy of the photoelectron.

2.2.4.1. X-Ray photoemission spectroscopy (XPS)

Compared to UPS, XPS is more commonly used to derive chemical and electronic information about samples, usually solid surfaces. Photons from excitation X-rays beam typically have an energy of 1486.6 eV when using an Al K α radiation source⁶¹⁻⁶³.

An XPS spectrum provides qualitative and quantitative information. Based on their relative and absolute positions, intensity and shapes, photopeaks are attributed to specific orbitals of individual elements of the periodical table (except for H and He with Al-k α source) and their associated chemical environment by the study of the chemical shifts.

Additionally, quantitative data are obtained from peaks area, taking account for the emission probability (sensitivity factor), the escape depth and instrumental factor correction among them the transmission function of the spectrometer^{61,63}.

XPS characterization of samples was performed using a Thermofisher ScientificTM Nexsa spectrometer with a spot size of 400 μ m. Acquisition parameters for survey spectra and high energy

resolution spectral windows are CAE (Constant analyzer Energy) 100 eV, step 1 eV dwell time 100 ms and CAE 20 eV, step size 0.1 eV, dwell time 100 ms respectively.

2.2.4.2. *Ultraviolet photoemission spectroscopy (UPS)*

With excitation energies within the ultraviolet range, UPS is the most surface-sensitive photoemission spectroscopy technique. UPS is mainly used to determine the WF and VBM of irradiated samples⁶¹.

Signal from detected UV-excited photoelectrons can be represented by a photoelectron distribution curve. The acquired data should be calibrated using a clean metal, such as gold. Its Fermi edge serve as reference point for the binding energy scale to find the valence band offset and the WF at the surface of the sample. Different procedure can be employed but usually these values can be determined by linear fitting or semi-logarithmic plot between the edge and the background of the spectra. Those two methods could lead to different WF and VBM values, as the low density of states near the leading edge can lead to errors in VBM determination using linear fitting. Thus, semi-logarithmic plot should result in more precise values but the best procedure appears to use both methods and compare them to each other as well as to the literature⁶⁴.

UPS analysis were carried out using a Thermofisher ScientificTM Escalab 250 Xi setup. The energy scale was calibrated with a sample of sputtered gold assuming that its fermi level edge would lie at 0 eV. The other spectra were therefore shifted accordingly. Semi-logarithmic plot was used to determine the WF and the VBM of the samples.

2.2.5. **Inductively coupled plasma optical emission spectroscopy (ICP-OES)**

ICP-OES is a tool to determine the elemental composition of a sample. The sample should be in a form that can be effectively vaporized and atomized, such as droplets of solution.

The sample to analyze is conducted through a nebulizer into a spray chamber. As an aerosol, it is led into a high temperature (6000 K – 8000 K) Ar plasma generated by radiofrequency. Desolvation, vaporization and atomization processes successively remove the solvent from the aerosol droplets, vaporize the sample molecules into gas phase and break them into atoms. Excitation and ionization then occur by collision with high energy electrons and/or charge transfer from Ar⁺ species. Excited atoms finally return to their ground state, emitting characteristic photons that are collected by an optical detector to determine the elemental composition of the sample.

The advantage of ICP-OES is the high temperature and high electron density ($10^{14} \text{ cm}^{-3} - 10^{16} \text{ cm}^{-3}$) of its plasma, which effectively atomizes, excites and ionizes nearly all elements in a variety of matrices^{65,66}.

ICP-OES measurements were performed at ILV using an Agilent spectrometer.

2.2.6. Glow discharge optical emission spectroscopy (GD-OES)

GD-OES is a destructive technique to derive the elemental profile through the depth of a sample. It repeats sequences of glow discharge at low pressure to sputter the surface of a sample and optical emission spectroscopy observation to identify the sputtered species.

The glow discharge plasma is generally constituted of pure Ar cations that are accelerated towards the sample, which acts as a cathode. This sputtering process ablates the sample, and released atoms are promoted to an excited state by energy transfer from the plasma. They subsequently return to their ground state by emitting light forming a glow, whose wavelength is specific to the atom species. Collection of these photons by an optical detector provides a weighted elemental composition over the ablated section, and the GD-OES sequence can be repeated. A crater is progressively formed in the sample as the instrument records its elemental profile.

One drawback of GD-OES is the difficulty to obtain reliable information about the surface of the sample, as the plasma is not stabilized at the beginning of the measurement. Another limitation is that the method is not suited either to obtain information about interfaces. Indeed, the curvature of the crater implies that information from its center and its edges do not represent the same sample depth, but signals from these regions are recorded simultaneously^{67,68}.

GD-OES analysis was performed on CI(G)S samples using a GD-Profilier 2 from Horiba, and weighted elemental compositions were normalized over the depth of CI(G)S by XRF measurements.

2.2.7. X-ray fluorescence (XRF)

XRF is a non-destructive method to determine the bulk elemental composition of solid materials. It consists in the irradiation of a sample by a primary X-ray source, generally an X-ray tube, followed by the emission of fluorescent X-rays from the samples that are collected by a detector.

When a sample is irradiated by primary X-rays, core electrons that absorb the incident photons can be ejected to outer shells or emitted as photo-electrons. Outer shell electrons relax as a response to fill the vacancies, and transfer the difference of energy between their initial and final state either by Auger effect or fluorescence. Auger effect would result in the transmission of energy to other

electrons in the environment, while fluorescence would result in the emission of this energy as an X-ray photon.

This photon would carry the footprint of the element from which it was emitted, since its energy corresponds to a difference in energy between two specific orbitals. It is therefore possible to identify the elemental species constitutive of a sample with XRF.

Due to matrix effects, quantification is however not straightforward. Indeed, XRF can probe elements deeper below the surface of a sample as compared to XPS. For a CIGS sample, XPS analysis would probe the chemical state of electrons from up to a few nanometers below the surface while XRF signal would be received from electrons up to a few microns deep. This allows to determine the bulk elemental composition of sample, but at the same time introduces a mismatch between peak intensity and concentration due to attenuation and enhancement phenomena in the sample matrix. For precise quantification, it is therefore necessary to calibrate the instrument with samples of similar sample matrix properties and known elemental composition⁶⁹.

XRF spectra were recorded using a Fisherscope X-Ray XDV apparel.

2.2.8. Cyclic voltammetry (CV)

CV is a potential sweep technique that can be employed to study reduction and oxidation processes, generally between soluted ions and the surface of a solid electrode. A setup would be composed of a working electrode, a counter electrode and a reference electrode immersed in an electrolyte solution. Voltage bias can be applied between the working and the counter electrodes, and current would be recorded. A potentiostat is employed to control the applied potential of the working electrode as a function of the potential of the reference electrode⁷⁰.

For each reversible redox reaction occurring in the system, cyclic voltammograms contain information about the oxidation and reduction steps. Nernst equation relates the potential of an electrochemical cell E to the formal potential of a redox process E° and the concentrations of the oxidized and reduced species at equilibrium.

$$(2.3) E = E^\circ + \frac{RT}{F} \ln \frac{[Ox]}{[Red]}$$

R is the gas constant, T is the temperature in K, and F is the Faraday constant. The redox couple half-wave potential (E_p) can be determined graphically, from the oxidation potential (E_{ox}) and the reduction potential (E_{red}).

$$(2.4) E_p = \frac{(E_{ox} + E_{red})}{2}$$

All CV experiments mentioned in Chapter 3 were conducted in acetonitrile (ACN) with a 0.1 M concentration of LiClO₄, which served as supporting electrolyte to circumvent the low conductivity of ACN. Additionally, active area of the working electrode was defined using an elastic piece of tape resilient to the ACN media, which did not leave a consistent surface area between samples. Thus, there might be small discrepancies between the current values shown here and the actual current per centimeter square flowing through the NiO_x or ITO surface. Thickness values for NiO_x layers were obtained by XRR measurements, for which experimental details are not developed in this study. NiO_x thickness is here expressed either in terms of ALD cycles or directly in nm calculated from XRR measurements.

2.2.9. Current density-voltage (J-V) measurement

J-V is a commonly carried out measurement to determine the PV parameters of a solar cell. A solar simulator irradiates the sample with an illumination spectrum that mimics natural sunlight (usually in the form of the AM 1.5G standard), while a voltage is applied in forward and reverse bias. The current output from the terminals of the cell is measured as applied voltage changes. J_{sc} , V_{oc} , FF and PCE of the solar cell can be derived by varying the voltage bias from short-circuit to open circuit.

The drawback of using J-V measurements to determine the PV parameters of a solar cell is that there is a spectral mismatch between the solar simulator and the actual AM 1.5G standard spectra. This mismatch can induce deviations in V_{oc} , FF and particularly J_{sc} values. J_{sc} values can also be determined from EQE measurements, which will likely not exactly represent the J_{sc} during operation either as the cell is illuminated at a small intensity and one wavelength range at a time using this technique.

While perovskite and tandem solar cells were measured by wiring each cell terminal to one probe, CI(G)S solar cells were measured by four-point probe or four probe measurements, by wiring each terminal to two probes. This setup permits to remove the lateral sheet resistance contribution of the contacts from the R_s of the device, and would represent the contribution of a bottom cell in a monolithic tandem device with better accuracy.

Additionally, CI(G)S cells were annealed at 250°C in vacuum for 10 minutes and left under AM 1.5G light soaking for at least two hours IV measurements.

Solar cells were illuminated using an AAA sun simulator of Oriel Sol3A, with an aperture area of 0.09 cm² for opaque perovskite, CI(G)S solar cells tandem solar cells. Aperture area was defined at 0.16 cm² for semi-transparent perovskite solar cells. A voltage bias was forwardly and reversely applied to the devices using a digital source meter (Keithley 2400).

2.2.10. External Quantum efficiency (EQE)

EQE measurement is a technique to measure the ability of a solar cell to convert photons into collected charge carriers depending of the wavelength of the incident radiation. EQE is given as a ratio of the number of collected charge carriers over the number of incident photons, and is plotted against the wavelength of the latter.

The J_{sc} of the solar cell can be then integrated from the EQE signal for any illumination spectra:

$$(2.5) J_{sc} = -q \int_0^{\infty} EQE(\lambda) \phi(\lambda) d\lambda$$

Here q is the elementary charge, $\phi(\lambda)$ the photon flux and $EQE(\lambda)$ the EQE signal.

EQE spectra were acquired using a Oriel IQE200 system coupled with a source meter (Keithley 2400) and a 300W xenon lamp. The range of wavelength was between 300 nm and 850 nm for perovskite solar cells, and between 300 nm and 1400 nm for CI(G)S solar cells.

2.3. Overview

In this chapter, we presented the techniques employed to fabricate and characterize the samples of this study. When not stated otherwise, samples were prepared and characterized at IPVF. In the context of the PERCISTAND collaboration, other samples were provided by partners: In Chapter 3, ALD and sputtered NiO_x samples were fabricated by the Zentrum für Sonnenenergie und Wasserstoff (ZSW), the Karlsruher Institut für Technologie (KIT) and the Interuniversitair Micro-Electronica Centrum (IMEC) and in Chapter 5, all CI(G)S samples employed for smoothing, characterization and solar cell fabrication were provided by TNO.

Chapter 3

Low temperature HTL development

***Summary:** In this chapter, we study different low-temperature routes for HTL deposition in perovskite solar cells. Our candidates of interest are NiO_x and small organic molecules self-assembled as a monolayer HTL. In particular, we evaluate the chemical and physical properties of NiO_x deposited by ALD and sputtering for different thickness, deposition temperature, annealing temperature conditions and oxygen flux during fabrication. Our goal is primarily to determine whether or not low-temperature processes affect the performances of solar cells based on NiO_x layers. Then, we review the properties of solar cells prepared from ALD-NiO_x for different deposition temperatures. We also review the properties of NiO_x layers whose surface chemistry was modified by UV-O₃, subsequent annealing and FAI passivation. Solar cells are fabricated from these layers to identify a link between the surface chemistry of the layers and PV parameters in devices. Finally, the properties of solar cells prepared from 2PACz and MeO-2PACz are reviewed, as well as the structural properties of perovskite layers deposited either on top of NiO_x or SAM HTL.*

Contents

3.1. Introduction	41
3.1.1. NiO _x as HTL for perovskite solar cells	41
3.1.2. Small carbazole-based molecules as HTL for perovskite solar cells	42
3.2. Low temperature ALD-NiO_x layers for HTL application in perovskite solar cell	44
3.2.1. Evaluation of the electron-blocking properties of NiO _x films prepared by ALD	45
3.2.1.1. Calibration of a Ag/AgNO ₃ reference electrode	46
3.2.1.2. Evaluation of the MV/MV ⁺ and MV ⁺ /MV ²⁺ redox potentials.....	47
3.2.1.3. Evaluation of the electron blocking properties of ALD-NiO _x films for different thickness and deposition temperature	48
3.2.1.4. Effect of post-annealing on the electron blocking properties of ALD-NiO _x films	50
3.2.2. Chemical composition and electronic properties of NiO _x films prepared by ALD and sputtering.....	51
3.2.2.1. Chemical composition and electronic properties of ALD-NiO _x films using Me-nickelocene as nickel precursor and O ₂ plasma as oxidizer	52
3.2.2.2. Chemical composition and electronic properties of NiO _x films prepared by plasma sputtering deposition	58
3.2.2.3. Chemical composition and electronic properties of sputtered NiO _x films after post-annealing.....	62

Prospective

3.2.3. Applications of low-temperature ALD-NiO _x in perovskite solar cells	68
3.2.4. Enhancement of PV parameters of p-i-n perovskite solar cells by tuning the surface chemistry of NiO _x	70
3.2.4.1. Effect of UV-Ozone post-treatment on the surface chemistry of sol-gel NiO _x films	72
3.2.4.2. Effect of UV-Ozone post-treatment and surface recovery of the surface chemistry of combustion NiO _x films	73
3.2.4.3. Surface-tuned NiO _x layers as HTL for perovskite solar cells: Effect of surface recovery after UV-Ozone and FAI quenching.....	75
3.2.4.4. Surface-tuned NiO _x layers as HTL for perovskite solar cells: Effect of surface recovery after UV-Ozone, FAI quenching and FAI excess	80
3.3. Self-assembled monolayer of small organic molecules as HTL in PSCs	85
3.3.1. SAMs HTL in devices	85
3.3.2. Morphological and structural properties of perovskite layers	89
3.4 Interim summary	

3.1. Introduction

3.1.1. NiO_x as HTL for perovskite solar cells

Nickel oxide (NiO_x) has been extensively used for various applications, including perovskite solar cells (PSC) in which it acts as a hole transport layer (HTL)^{44,71,72}. Indeed, NiO_x is one of a few p-type metal oxides and its valence band position generally leads to good energy alignment with lead halide perovskite compounds^{71,73,74}. This high band gap semiconductor ($E_g > 3.4$ eV) also combines the properties of a high optical transmittance and high chemical stability^{71,72,75,76}. Additionally, nickel is an abundant metal and NiO_x is a low cost material, in contrast to most organic compounds reported for HTL applications in PSCs^{71,72,76}. It has the drawback of having a relatively low conductivity, which means that high efficiency devices typically use a 10 – 20 nm thick nickel oxide layer to act as an effective electron blocking layer while limiting series resistance during operation^{76–78}. The low conductivity of NiO_x can be mitigated by extrinsic doping strategies to increase the p-type character of the semiconductor, a method that has been extensively explored to improve the performances of PSCs over the last decade using metals such as Cu, Li, Cs or even La^{76,77,79–86}. Additionally, relatively low V_{oc} values have been routinely reported for PSCs using NiO_x as HTL, likely related to the interfacial chemistry between lead halide perovskite compounds and Ni³⁺ sites at the surface of NiO_x samples⁸⁷. Again, several strategies have been proposed to solve this issue and non-certified power conversion efficiency (PCE) values above 22% have been reported using surface modified NiO_x as HTL⁷⁵. Among the other parameters that have been related to the PV parameters of PSCs, defects in the structure of stoichiometric NiO have been previously linked to a better conductivity of the sample⁸⁸. Additionally, Ni vacancies at the NiO_x/perovskite interface in the stoichiometric NiO structure have been described as beneficial for VBM alignment⁸⁹.

Structurally, stoichiometric NiO adopts a rocksalt cubic formation composed of octahedral Ni²⁺ connected to six O²⁻ atoms. However, the surface chemistry of most synthesized NiO_x films usually present several subspecies of NiO_xH_y formula, namely Ni(OH)₂, NiOOH and metallic nickel⁹⁰. Ni(OH)₂ and NiOOH are reported to adopt different phases: β -Ni(OH)₂, α -Ni(OH)₂, β -NiOOH and γ -NiOOH. Each consists in NiO₂ slabs whose tetrahedrally-coordinated hydrogen atoms lie in the interslab space⁹¹. α -Ni(OH)₂ and γ -NiOOH differ from β -Ni(OH)₂ and β -NiOOH, respectively, in that their interslab space also contains polar species such as H₂O, OH⁻, SO₄²⁻, or CO₃²⁻. The presence of Ni₂O₃ in NiO_x samples is also sometimes mentioned but remains uncertain. From computational modeling, oxidation degree of nickel in Ni(OH)₂ and NiOOH subspecies is evaluated between +2 and

+3. As it is not possible to reduce Ni below its +2 oxidation degree in nickel oxide compounds, deficit in oxygen in stoichiometric NiO structures can result in the formation of metallic Ni⁰ phases.

To our knowledge, the link between the structural or chemical composition of NiO_x and the performances of resulting PSCs has not been clearly established in literature. Nonetheless, the influence of superficial Ni³⁺ sites over the V_{oc} of complete devices has been studied through the degradation process triggered by their catalytic activity regarding elements of the perovskite layer⁸⁷. The chemical states of Ni atoms from the surface of the layer can typically be probed by XPS. However, in the case of NiO_x the resulting spectrum has been proven difficult to interpret due to the complexity of its shake-up structure. Many different procedures have been reported in literature to qualitatively and quantitatively study the chemical environment of nickel in NiO_x from these data, but none of them has been fully satisfactory. Often, the most straightforward methods treat the shake-up structure of the Ni 2p region in an approximative way which generate inconsistencies between the quantitative composition in NiO_x subspecies from the Ni 2p and the O 1s spectra. On the other hand, approaches that aim to accurately translate the theoretical framework behind these structures can result in a significant mismatch between the fitting envelope and the XPS signal^{42,87,90,92-96}.

Many methods have been reported to deposit NiO_x layers for perovskite solar cell application such as sputtering, sol-gel processes, nanoparticles synthesis and atomic layer deposition (ALD)⁷¹. Compared to other techniques, ALD does not necessarily result in the highest PCE values⁷⁵. However, it has the particularity to grow conformal, homogenous thin layers even on rough substrate^{44,97,98}. It also allows to finely tune the thickness of the deposited material⁹⁸. Also, low-temperature deposition is possible by ALD even though post-annealing at 300°C of resulting NiO_x layers can dramatically improve the performances of PSCs^{40,42}. This statement might differ depending on the ALD process conditions, i.e Ni precursor, oxidizer and deposition temperature. Conformability on rough surfaces and low-temperature deposition are particularly relevant features in the case of two terminal perovskite/CIGS tandem solar cells fabrication, where the layers constituting the perovskite top cell layers have to be deposited on a CIGS subcell at low temperature^{5,40,41,99}. NiO_x is also a promising HTL for p-i-n perovskite solar cells in 2T tandem application, as tuning its p-type character by intrinsic and extrinsic doping is of interest for TRJ design.

3.1.2. Small carbazole-based molecules as HTL for perovskite solar cells

Employing a thin film of anchoring, small molecules as a hole selective layer on its own in a perovskite solar cell was introduced in 2019 by Magomedov et al.¹⁰⁰. Since then, this method permitted the production of single junction p-i-n devices and perovskite/CIGS monolithic tandem

cells with PCE respectively above 21 % and 23 %⁴¹. The molecules used as HTL in these cases were 2PACz and MeO-2PACz, and could be deposited either by spin-coating or by dip coating. They are constituted of or derived from a carbazole ring attached through an ethyl bridge at its amine end to a phosphonic acid anchoring group, as shown in **Figure 12**.

Structurally, the authors suggested that the small molecules would form a monolayer on top of metal oxide substrates by condensation of their phosphonic acid anchoring group. The exact arrangement of the layer is however still up to debate. While other authors observed a self-limiting behavior for MeO-2PACz growth on top of metal oxide substrates, they also pointed out that the molecules might self-arrange by forming multilayers rather than as a monolayer¹⁰¹.

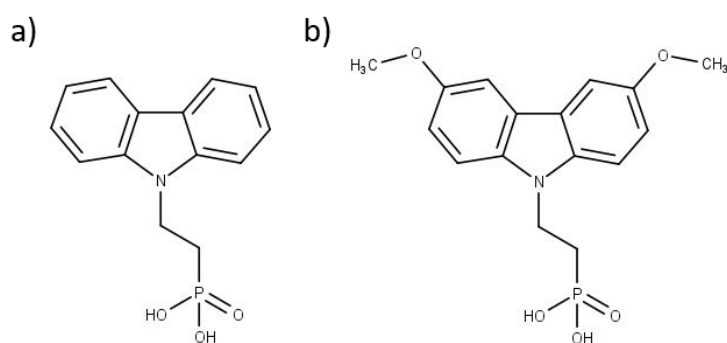


Figure 12 Lewis representation of (a) 2PACz and (b) MeO-2PACz

SAMs HTL differ from their metal oxide or polymer based counterparts in that a thickness of a few nanometers is sufficient so they can act as a charge selective layer, while at least a tenth of nanometers thickness is usually necessary for the latter to fulfill this role^{78,101}. This characteristic is beneficial both in terms of vertical electrical conductivity and optical transmittance.

As mentioned in chapter 1 and 2, degradation process can occur in single junction CI(G)S solar cells when exposed to temperatures < 200°C. This constraint has to be taken into account for monolithic tandem integration to design the perovskite top cell architecture. In literature, most methods described to deposit NiO_x at low temperature for perovskite solar cell application rely on either nanoparticles synthesis or ALD process. It has nonetheless been suggested that PV parameters of solar cells would be enhanced when ALD-NiO_x was annealed at 300°C in air after deposition⁴⁰. This consideration is likely to differ depending on the specificity of the ALD process, such as Ni precursor, oxidizer and temperature process. At the same time, particularly high PV performances have been reported using carbazole-based HTL in literature, which led us to consider the possibility to integrate them in our tandem architecture.

In the first section of this chapter, I study a low temperature route on different ALD process for NiO_x fabrication. I first characterized the optical, chemical and electronic properties of films prepared either at 100°C or 160°C according to a protocol described in **2.1.1**. The effect of post-treatment in air is discussed regarding the electron blocking properties of NiO_x films. I then evaluated the PV performances obtained with single junction perovskite solar cells using this material as HTL, and studied the effects of other post-treatments to tune the surface of NiO_x.

In the following part, I explore the use of small carbazole based molecules as HTL in perovskite solar cell single junction. I also study the growth of a perovskite layer either on top of NiO_x or MeO2PACz, and the possible integration of the small molecules as a HTL bilayer with NiO_x for tandem application.

3.2. Low temperature ALD-NiO_x layers for HTL application in perovskite solar cell

Here I focus on the development and characterization of a suitable NiO_x layer prepared by ALD for TRJ application in a perovskite/CI(G)S monolithic tandem solar cell. ALD allows for the deposition of thin, conformal NiO_x layers at 100°C - 160°C, which is particularly suited for deposition on top of rough CI(G)S subcell⁴⁰. To evaluate if high temperature processing of NiO_x is optimal for solar cell fabrication, I also study the composition and electrochemical properties for a series of ALD-NiO_x samples prepared at ZSW between 75°C and 250°C and the PV performances of derived PSCs. Additionally, this study was repeated for series of NiO_x samples prepared by sputtering and provided by KIT and IMEC, which differed by preparation conditions and post-annealing temperature.

Our first subsection is dedicated to the evaluation of the electron blocking properties of NiO_x layers deposited on ITO by ALD at 100°C and 160°C for different thickness values by cyclic voltammetry. Then, I focus on the characterization of NiO_x samples prepared at different temperatures by ALD and sputtering by analyzing samples using KPFM, X-ray photoemission spectroscopy and ultraviolet photoelectron spectroscopy. These techniques allow to access the composition as well as the chemical and electronic properties of NiO_x. From some of these layers, perovskite single-junction solar cells are fabricated and characterized by J-V and EQE measurements to understand the effect of various parameters on the performance of devices. Finally, I explore the effect of post-treatment processes such as annealing or UV-Ozone treatment on the properties of NiO_x layers and derived perovskite solar cells.

3.2.1. Evaluation of the electron-blocking properties of NiO_x films prepared by ALDⁱⁱ

As mentioned earlier, for HTL application a NiO_x layer should be the thinnest possible to minimize the vertical series resistance of the cell. However, the role of the HTL is also to block electron transfer from the perovskite layer to the electrode by 1) conformal deposition on top of the electrode and 2) limiting electron tunneling through the layer. Electron-blocking properties are enhanced by increasing the thickness of the material and thus the number of ALD cycles during deposition. We therefore aimed to find an optimal thickness for NiO_x films prepared by ALD on ITO substrates. To do so, we evaluated the electron-blocking properties of NiO_x prepared at 100°C and 160°C of varying thickness by the mean of CV measurements.

We first considered the ferrocene/ferrocenium (Fc/Fc⁺) couple in ACN as electrolyte to evaluate the electron blocking properties of NiO_x layers, as this well-defined redox couple is commonly used to calibrate reference electrodes in non-aqueous media¹. Using the same electrolyte for electrode calibration and NiO_x film characterization would additionally reduce the chance of cross-contamination from traces of product left in glassware after cleaning. Additionally, employing a well-defined scan sweep window with Fc/Fc⁺ can result in a single reversible oxidation/reduction step on a voltammogram, which allows for straightforward data interpretation. We used LiClO₄ as supporting electrolyte at a concentration of 0.1 M for every solution in this section. In this report, we refer to the value of 380 mV against SCE for the half-wave potential of the Fc/Fc⁺ couple proposed by Pavlishchuk et al.².

However, based on preliminary experiments using a thick NiO_x layer prepared by ALD (850 cycles) on ITO as a working electrode, we noticed a symmetrical pattern on the reduction and oxidation regions of the voltammogram which indicated that ferrocenium reduction could occur at the surface of a ITO/NiO_x working electrode. This phenomena would occur because the reduction potential of ferrocene/ferrocenium (0.39 V (vs. SCE)) is higher than the flat band potential of NiO_x, (estimated around 0.12 V (vs. SCE) by Chan et al.)¹⁰⁴.

This led us to employ methyl viologen (MV/MV⁺; MV⁺/MV²⁺) instead, which has already been reported in literature to evaluate the electron blocking properties of NiO_x films on ITO or FTO⁷⁸. Indeed, the two reduction steps for this molecule are reported to occur at -0.32 V and between -0.6 and -0.7 V (vs. NHE) resulting in the formation of respectively MV⁺ and MV. These reduction

ⁱⁱ Cyclic voltammetry setup and experimental protocols were realized in collaboration with André Grishin. ALD-NiO_x layers were prepared by Damien Coutancier.

potentials are supposedly far below the flat band potential of our NiO_x samples, but would result in reversible reduction on a bare Pt, ITO or FTO electrode. Methyl viologen is thus a good candidate to evaluate the homogeneity of NiO_x layers deposited over these TCOs^{78,104}.

3.2.1.1. Calibration of a Ag/AgNO₃ reference electrode

We first prepared an in-house Ag/AgNO₃ 0.01 M reference electrode suited for CH₃CN environment. Then, we calibrated it against the potential of the well-defined Fc/Fc⁺ couple¹⁰². To do so, we induced voltage bias using a 10 mM ferrocene solution and two Pt wires as working and counter electrodes. After preliminary experiments using this setup, our Pt counter electrode occasionally turned black. We interpreted this change in color as the deposition of one of the dissolved species during the repeated voltammetry cycles, either solid Li or ferrocene.

After repeated experiments, this problem could be levered by increasing the surface of the counter electrode and adjusting the scan rate. The distance between the working and counter electrodes was also diminished to a few centimeters in order to facilitate charge transfer.

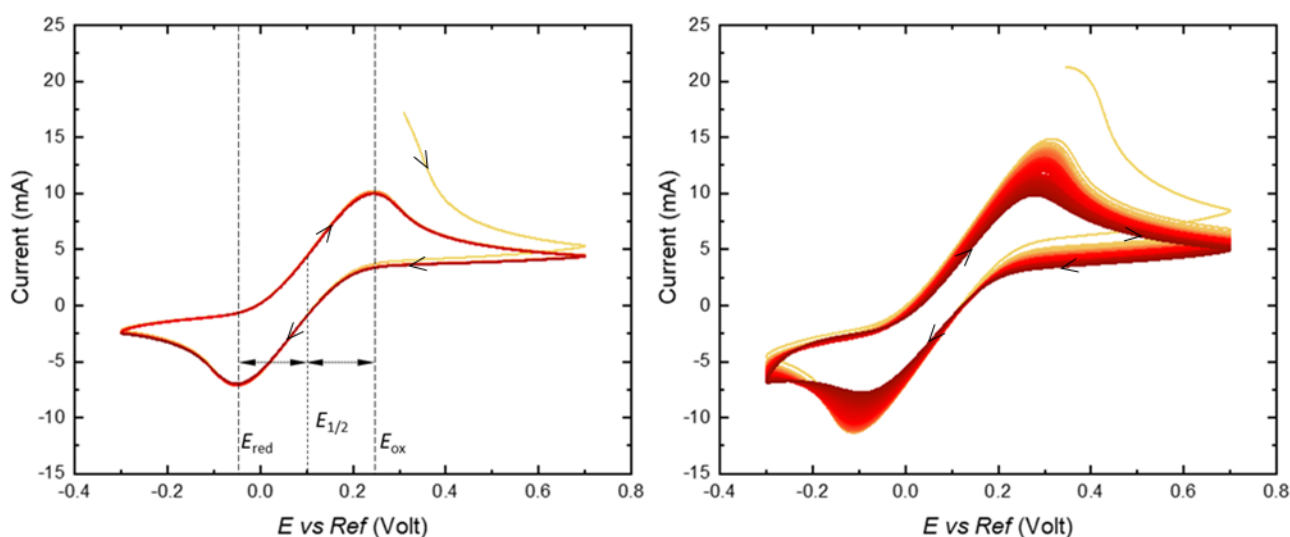


Figure 13 Voltammogram recorded with an ITO sample as working electrode, in ACN media using 10 mM ferrocene as the redox specie and 0.1 M LiClO₄ as supporting electrode recorded for (a) 10 cycles and (b) 50 cycles at a scan rate of 800 mV/s. In both figures data points are represented using a gradient of color from yellow (1st cycle) to dark red (last cycle). Voltage is reported against a Ag/AgNO₃ 0.01 M reference electrode.

Figure 13 presents two different voltammograms recorded to calibrate our reference electrode using 10 mM ferrocene as the redox specie. The stability of our system was assessed after 10 cycles and 50 cycles. Oxidation and reduction peak positions and intensity seemed unchanged after 10 cycles,

indicating that our system was stable. However, by repeating our experiment for 50 cycles we could notice a decrease in current and a shift in reduction and oxidation potentials from cycle to cycle.

The maximum oxidation and reduction currents were respectively detected at 0.318 V (vs Ref) and at -0.111 V (vs Ref). Using Eq. (2.4), we determined the half-wave potential of our Fc/Fc⁺ couple at +0.104 V (vs Ref). Previous measurements of the Fc/Fc⁺ couple against Ag/Ag⁺ reference electrode at similar concentration in ACN yielded values for half-wave potentials between +0.087 V (vs Ref) and +0.089 V (vs Ref)^{102,103}. We therefore observed a reasonable deviation of around +16 mV between our measured value and the literature references. Referring to a conversion constant of -298 mV between a standard Ag/AgNO₃ 0.01 M and the SCE system, we considered a standard potential for our electrode (vs Ref) at -272 mV (vs SCE)¹⁰³.

3.2.1.2. Evaluation of the MV/MV⁺ and MV⁺/MV²⁺ redox potentials

In the next step of our study, we assessed the reduction and oxidation potential of our methyl viologen redox mediator using our calibrated reference electrode. To this end, we used a similar setup as presented in the beginning of this subsection by changing the 10 mM Fc mediator to 0.1 mM MV²⁺ and using an ITO film on glass as working electrode instead of a Pt wire.

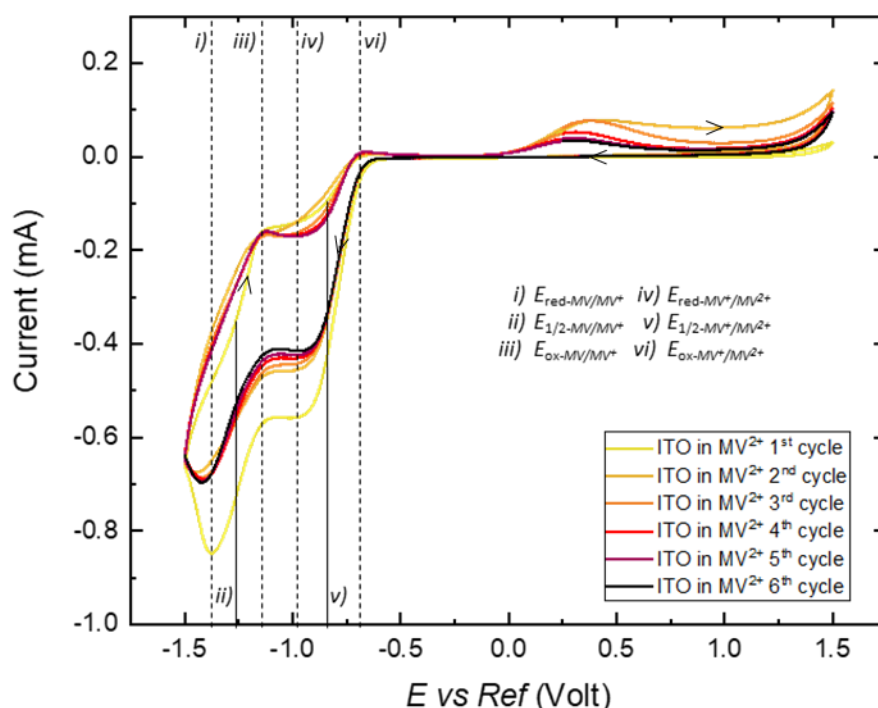


Figure 14 Voltammogram recorded with an ITO sample as working electrode, in ACN media using 0.1 mM MV as the redox specie and 0.1 M LiClO₄ as supporting electrode recorded for 6 cycles at scan rate of 200 mV/s. Voltage is reported against a Ag/AgNO₃ 0.01 M reference electrode.

Voltammetry cycles using such a setup are presented in **Figure 14**. We note that the shape of the voltammogram changes after the first reduction step, with lower intensity reduction and oxidation peaks. After removing the working electrode from the solution, we noticed a transparent compound deposited on its active area that could be easily washed off with acetone. It could correspond to neutral MV deposition, which would adsorb at the surface of ITO after the second reduction step and fail to completely oxidize after the second oxidation step. The accumulation of solid mediator at the surface of ITO would provoke ohmic losses, and explain the less intense oxidation and reduction signals from cycle to cycle. Ohmic losses could also result in a shift of the apparent half-wave potential of the electrolyte. Indeed, from the first C-V cycle we experimentally detected the $E_{1/2}$ of MV^+/MV at -1.114 V (vs Ref), and that of MV^{2+}/MV^+ at -0.840 V (vs Ref). Other authors reported half-wave potentials for MV^+/MV and MV^{2+}/MV^+ in ACN at respectively -1.195 V (vs Ref) and -0.775 V (vs Ref) in our system, for deviations of +81 mV and -65 mV between our values and the literature references¹⁰⁵.

3.2.1.3. Evaluation of the electron blocking properties of ALD-NiO_x films for different thickness and deposition temperatures

I finally performed similar CV measurements using the same setup with either glass/ITO or NiO_x on glass/ITO films as the working electrode. **Figure 15** shows voltammograms using NiO_x layers of different thickness as working electrode, deposited either at 100 or 160°C on ITO. Slightly different maximum current values were measured in positive bias for all NiO_x samples. However, this region of voltage was swept through at the beginning of the experiment and the intensity of the recorded peaks is likely to depend on the state of the system before introduction of the working electrode. It is thus difficult to comment on this region for now. For both 100°C and 160°C deposited NiO_x layers, we observed a general trend of decreasing maximum current in negative voltage bias as the thickness of the film increases.

For 100°C prepared samples, the absolute value of current at -1.75 V (vs Ref) progressively decreased from 1 mA to close to 0 mA as the number of ALD cycles was increased from 125 to 250. Oddly, an absolute value of current of approximately 0.2 mA was measured for a NiO_x film obtained after 62 ALD cycles. We would indeed expect the absolute value of current to decrease with the thickness of the film, and this measurement represents an outlier value.

Different causes might explain this behavior. First, tape was used to define an active area of 1 cm² on the samples. The tape material was chosen for its robustness in ACN, but was also elastic so it was not easy to maintain a constant active area from sample to sample. A higher recorded current I might

thus not correspond to a higher current density J . Likewise, it is also possible that tape was not well applied on the 125 cy NiO_x working electrode, which would expose underneath area and effectively increase the active area. Finally, in our case, the homogeneity of ALD NiO_x layer was strongly dependent upon the absence or presence of solvent traces that could appear during the drying step after cleaning the ITO samples. The presence of solvent traces often prevented the deposition of NiO_x , leaving an exposed area of ITO to the electrolyte. For these reasons, it is possible that the higher absolute value of current measured for the 125 cycles samples compared to the 62 cycles was not related to a higher absolute value of current density through the NiO_x layer.

For 160°C prepared samples, the absolute value of current at -1.75 V (vs Ref) progressively decreased from 1 mA to close to 0 mA as the number of ALD cycles is increased from 85 to 350. We notice that the current values measured for ALD- NiO_x films was sometimes superior to that of ITO, which was not expected due to the higher resistivity of the NiO_x layer. This behavior might be again explained by a difference in active area between samples.

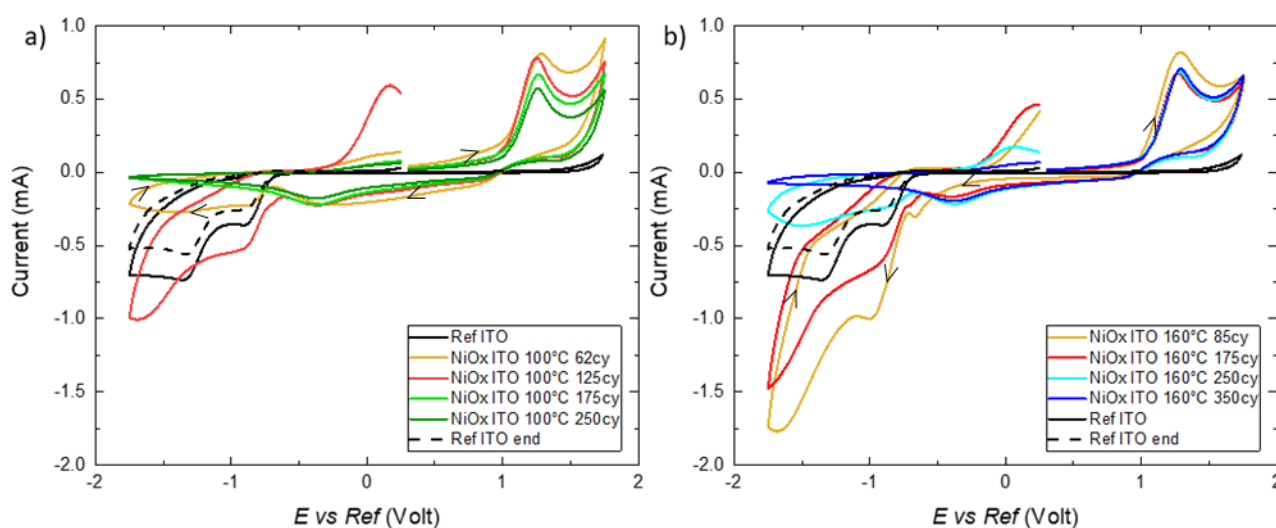


Figure 15 Voltammograms recorded using NiO_x/ITO samples of varying thickness as working electrode, in ACN media containing 0.1 mM MV as redox specie and 0.1 M LiClO_4 as supporting electrode for (a) 100°C prepared ALD- NiO_x and (b) 160°C prepared ALD- NiO_x at scan rate of 200 mV/s . Voltage is reported against a $\text{Ag/AgNO}_3\ 0.01\text{ M}$ reference electrode.

Nonetheless and according to our expectation, current under negative voltage bias was almost completely suppressed for samples prepared after 175 and 350 ALD cycles for 100 and 160°C samples, respectively. For the 160°C series, negative bias current was already strongly attenuated after 250 ALD cycles.

We therefore concluded that for our samples, the ideal thickness for HTL application should be between 125 and 175 cycles for 100°C prepared NiO_x and between 250 and 350 cycles for 160°C prepared NiO_x samples. These cycles would correspond to a thickness approaching 10 nm for the 100°C samples and 15 nm for the 160°C samples. Indeed, NiO_x thickness should be kept as small as possible to minimize series resistance in devices but high enough to effectively block electrons during operation.

3.2.1.4. Effect on post-annealing treatment on the electron blocking properties of ALD-NiO_x films

To understand if post-deposition annealing has an influence over the electron blocking properties of NiO_x, we performed CV measurements on glass/ITO/NiO_x films prepared either at 100°C and 160°C and annealed at 300°C for one hour under ambient atmosphere. We based our study on 15 nm thick NiO_x films. Corresponding CV responses are reported in **Figure 16**. We observed that similar electric response to voltage bias was observed for films before and after post-annealing, regardless of the deposition temperature. This observation solely informed us about the ability for electrons to reach the ITO layer through the HTL, and post-treatment could have an effect on the NiO_x films chemical and physical properties.

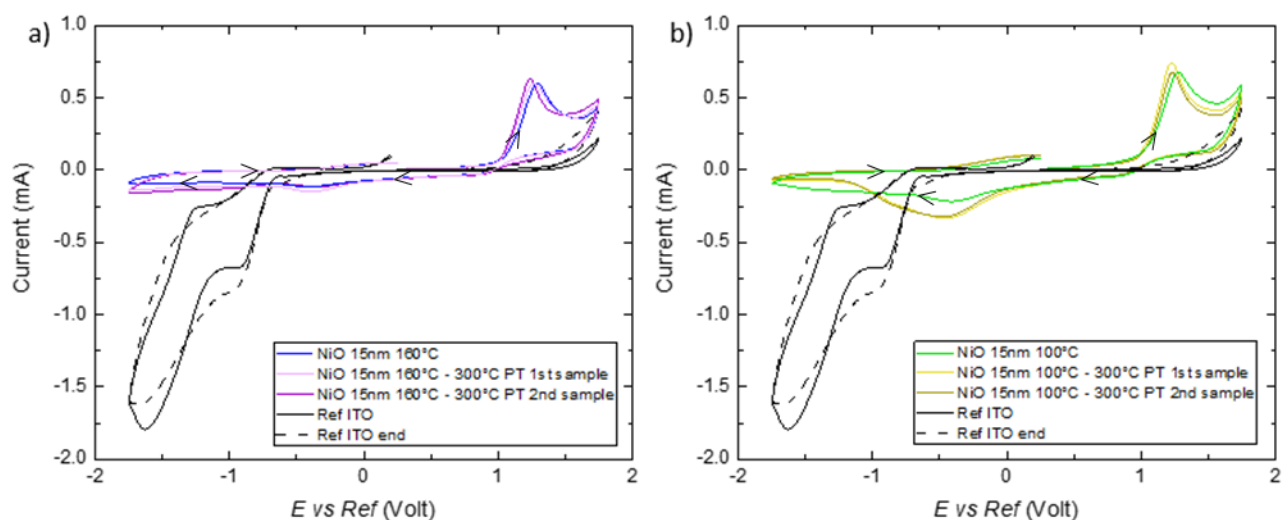


Figure 16 Voltammograms recorded with different NiO_x/ITO samples before and after 300°C post-annealing for 1 hour as working electrode, in ACN media containing 0.1 mM MV as redox specie and 0.1 M LiClO₄ as supporting electrode for (a) 100°C prepared ALD-NiO_x and (b) 160°C prepared ALD-NiO_x at a scan rate of 200 mV/s. 2 samples were used for post-annealing data for homogeneity purpose. For each series of sample, a reference ITO sample was measured before (Ref ITO) and after (Ref ITO end) NiO_x films to assess whether or not a loss of current occurred during the experiment. Voltage is reported against a Ag/AgNO₃ 0.01 M reference electrode.

To conclude, we prepared ALD-NiO_x films of different thickness and temperature deposition. We then measured the electrical response from a CV setup using these samples as working electrodes. A threshold thickness of 10 nm (175 cycles) for 100°C and 15 nm (250 cycles) for 160°C was sufficient to dampen the current under negative voltage bias compared to bare glass/ITO samples. Overall, these results showed the homogeneity of the ALD-NiO_x layer and a conformal deposition over the ITO substrates, nonetheless balanced by an improper coverage when they were not dried properly.

3.2.2. Chemical composition and electronic properties of NiO_x films prepared by ALD and sputteringⁱⁱⁱ

In this section, we studied the influence of deposition process and post-annealing treatment over the physical and chemical surface properties of NiO_x layers prepared by ALD and sputtering. To do so, we first employed UPS surface analysis and Kelvin probe force microscopy (KPFM) to probe the work function and homogeneity of the NiO_x layers. Then, we used XPS to evaluate the chemical composition at the surface of our film from the Ni 2p_{3/2} region. Finally, we investigated how the features in the O 1s region could relate to the chemical composition or electronic properties of the NiO_x samples.

In 3.2.2.1, we used these tools to investigate the influence of the deposition temperature over the surface properties of ALD-NiO_x grown on top of ITO at ZSW using different precursors compared to the IPVF process studied in 3.2.1. In short, Me-nickelocene served as Ni precursor and oxygen plasma was used as oxidizer. A detailed protocol for their preparation is provided in 2.1.1.

A second series of NiO_x samples was prepared by sputtering at KIT to study the combined effect of oxygen flux during deposition and a 01:30 h post-annealing treatment. In total, 4 samples each representing a combination of these features were studied in 3.2.2.2.

Finally, a third series of sputtered-NiO_x samples was prepared by IMEC to study the effect of post-annealing temperature over the surface properties of the layers in 3.2.2.3.

ⁱⁱⁱ XPS and UPS acquisition were conducted at ILV by Muriel Bouttemy and Matthieu Frégnaux. Ni 2p_{3/2} signal decomposition was conducted in collaboration with Solène Béchu and Mirella Al Katrib. Interpretation of the O 1s signal was realized in collaboration with Javid Hajhemati and Nitin Mallik. AFM and KPFM acquisition was conducted at GEEPS by José Alvarez. UPS data fitting and preparation of figures were realized by Aleksandra Bojar.

3.2.2.1. Chemical composition and electronic properties of ALD-NiO_x films using Me-nickelocene as nickel precursor and O₂ plasma as oxidizer

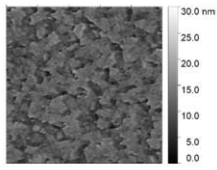
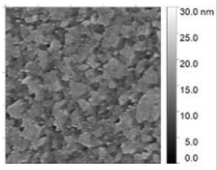
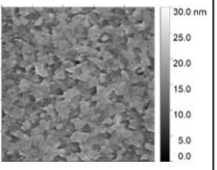
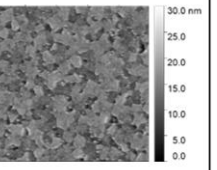
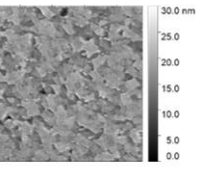
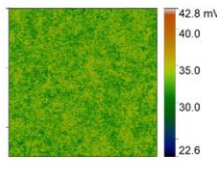
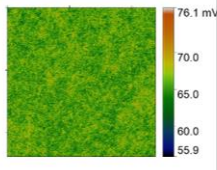
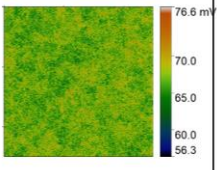
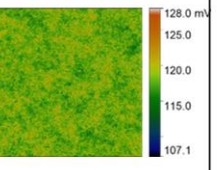
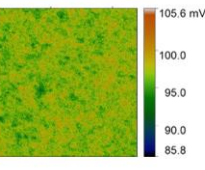
Five ALD-NiO_x samples were prepared at ZSW according to the following deposition temperatures:

- 75 °C
- 100 °C
- 150 °C
- 200 °C
- 250 °C

I) Effect of deposition temperature on the workfunction

AFM and KPFM images acquired for ALD NiO_x samples prepared at these different temperatures are reported in **Table 1**. Similar root mean square roughness values of around 3.0 nm were found for all the samples. Similarly, average contact potential difference (CPD) values between 0.03 V and 0.10 V were measured for all samples, although we noticed a subtle trend of higher CPD values as deposition temperature increased. Corresponding WF values were between 4.82 eV and 4.91 eV, with a subtle trend of lower WF values with increasing temperature. For each sample, we noticed only small deviation of CPD across the image which can indicate a rather homogenous surface.

Table 1 Results of KPFM measurements on ALD-NiO_x samples for different deposition temperatures. For each sample, on the top line we can see AFM topography, in the middle RMS roughness (Rt), and on the bottom respective surface potential distribution (CPD values). Image size: 10 x 10 μm²

75 °C	100 °C	150 °C	200 °C	250 °C
				
Rt = 2.5 nm	Rt = 2.7 nm	Rt = 2.9 nm	Rt = 3.0 nm	Rt = 3.0 nm
				
Average CPD = 0.03 V	Average CPD = 0.07 V	Average CPD = 0.07 V	Average CPD = 0.12 V	Average CPD = 0.10 V

Absolute WF and valence band maximum (VBM) values extracted from UPS spectra are presented on the **Figure 17a**. Once again, very close WF values were found for all samples between 4.00 and 4.20 eV, with a subtle trend of decreasing WF with deposition temperature. The VBM positions were also similar between -0.50 and -0.60 eV for all samples. It should be noted that WF measurements can be sensitive to adsorbed species at the surface of samples when they are exposed to ambient air¹⁰⁶. The summary of the WF measurements is shown on the **Figure 17c**. To evaluate the carbon contamination at the surface of the ALD-NiO_x samples, Ni/C elemental ratio of the different NiO_x samples are reported in **Table 2**. Close values between 0.78 and 0.89 are reported, with an outlier at 0.55 for 150°C deposited NiO_x. The signal in the C 1s region might include diverse contributions from species such as adsorbed CO₂, nickel carbonates, as well as C-C and C-O bonds from various atmospheric contaminants and potential organic residues from ALD. The exact nature of the carbon containing species might differ from sample to sample, and therefore the influence of carbon contamination on the measured WF value might not be consistent within series of samples.

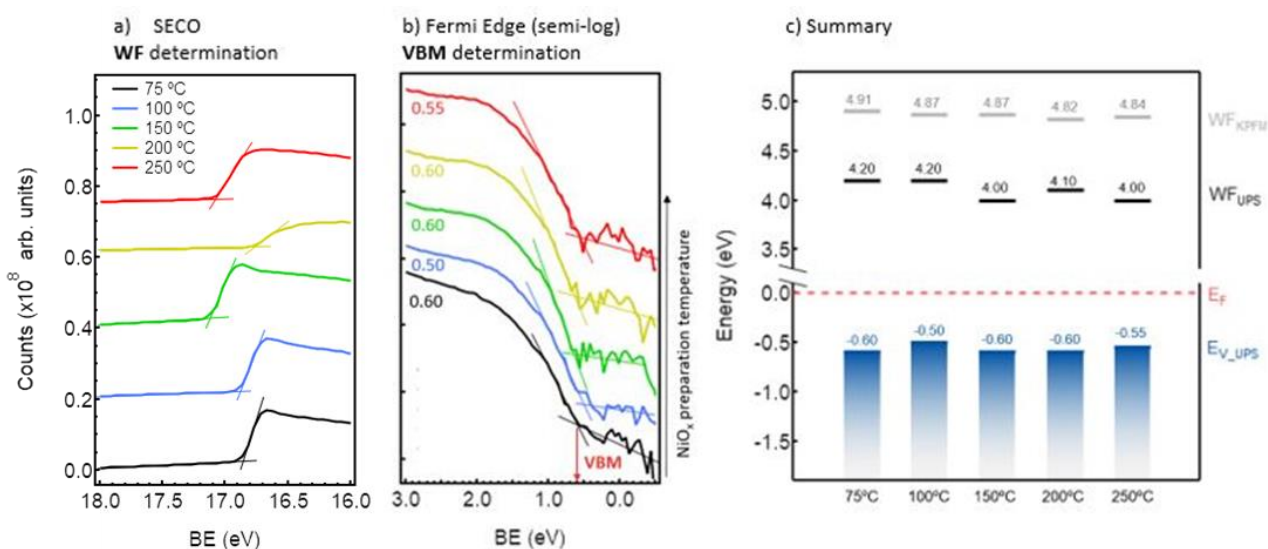


Figure 17 Work function (a) and VBM values (b) extracted from UPS spectra, by Fermi edge determination. (c) Summary of the work function and valence band maximum measurements by KPFM and UPS for all the samples. We can observe systematically higher WF measured by KPFM compared to this measured by UPS; both however shows similar trends.

The reason of systematically higher WF of NiO_x measured by KPFM compared to UPS could be explained by: i) different environment (UPS - UHV; KPFM - ambient air), which can cause more adsorption of chemical species originating from air during KPFM measurements, which will influence the measured WF; ii) different measurement principle. In KPFM, as described in 3.2.2.1, we measured surface potential difference (CPD) between the tip and the sample surface, from which

we could calculate sample work function. With the technique being an imaging approach, we obtained a CPD distribution map on a small area ($10 \times 10 \mu\text{m}^2$), which we then averaged given a reasonable uniformity. In UPS, on the other hand, we derived the WF from the zero kinetic energy of the photoelectrons that left the sample - the measured WF was thus the lowest energy that the electron needed to leave the sample, i.e. the secondary electron cutoff.

Table 2 Ni/C elemental ratio in ALD- NiO_x samples as a function of temperature deposition, from the Ni $2p_{3/2}$ and C 1s regions of the XPS spectra.

Deposition temperature	Ni/C ratio
75°C	0.89
100°C	0.86
150°C	0.55
200°C	0.88
250°C	0.78

Despite these differences in the absolute values, we observed the same trends and magnitude of change in the changes of the WF as a function of the NiO_x preparation temperature, thus, the discussion was valid for both techniques.

2) Effect of deposition temperature on the chemical composition

The same samples were analyzed by XPS, in order to evaluate the chemical composition of NiO_x subspecies at their surface. XPS signal from Ni 2p and O 1s regions are respectively shown in **Figure 18a** and **Figure 18b**. In order to access the chemical composition of our NiO_x samples, we proceeded in the decomposition of the Ni $2p_{3/2}$ spectra into its different NiO_xH_y sub-components. XPS signal in the Ni $2p_{3/2}$ region from pure samples of any NiO_xH_y phase typically resulted in shake-up structures^{90,92,107–110}. Based on theoretical calculations, Biesinger et al. proposed a method to ascribe the various features of this signal for most of these species⁹⁰. In general, a single sample of NiO_xH_y contains a combination of NiO, Ni(OH)_2 , NiOOH and metallic nickel phases, and the resulting shake-up structure could be thus difficult to interpret.

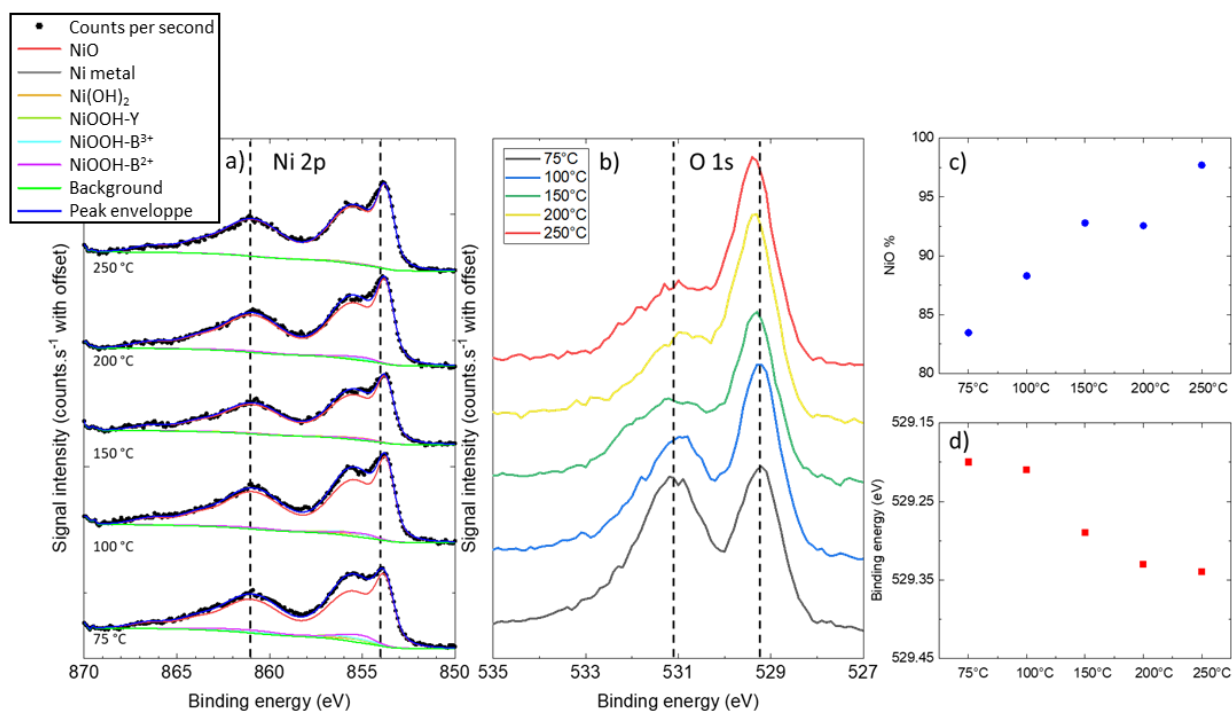


Figure 18 XPS spectra for (a) Ni 2p_{3/2} and (b) O 1s regions, (c) NiO %, as the proportion of stoichiometric NiO compared to other NiO_xH_y subspecies at the surface of the sample calculated from the Ni 2p_{3/2} region and (d) maximum O 1s binding energy shift for NiO_x samples prepared by ALD at different temperatures.

We based the present analysis from a detailed study from Biesinger et al., from which the Ni 2p_{3/2} signal from various NiO_xH_y subspecies was decomposed into their theoretical shake-up structure from a Gupta and Sen analysis^{111,112}. The results of this analysis has been adapted to the XPS apparatus that was used for the measurement, and Ni 2p_{3/2} signal was fitted using a Shirley background without offset. We decomposed the Ni 2p_{3/2} signal obtained from our samples based on the assumption that it would be a linear combination of individual signals from NiO, β- or α-Ni(OH)₂, β-NiOOH and γ-NiOOH and metallic nickel. This would imply that the shake-up and plasmon loss structures for each phase of our samples would be similar to that of a pure individual sample, which is not guaranteed. Indeed, inelastic interactions could occur between photoelectrons and other atoms or molecules in the structure of NiO_x¹¹³. These processes could have an influence over the XPS signal and were not taken into account here. Additionally, we observed a mismatch between the envelope arising from the fitted peaks and the Ni 2p_{3/2} signal from the XPS system. For these reasons, we assumed that we did not access the composition of our samples with a high degree of confidence and thus we refrain from commenting on the individual relative content in β-Ni(OH)₂, α-Ni(OH)₂, β-NiOOH and γ-NiOOH

phases which were detected at a low concentration. However, we considered the relative proportion of stoichiometric NiO compared to all NiO_xH_y subspecies (NiO %) as a more reliable information, due to the high proportion of NiO in the studied samples.

From this procedure, we derived that each sample is mainly constituted of stoichiometric NiO while other subspecies such as α -Ni(OH)₂, β -Ni(OH)₂, γ -NiOOH and β -NiOOH were present to a lesser extent. Metallic nickel signal was only detected in negligible amount ($\leq 0.05\%$). From **Figure 18c**, the NiO % increased with temperature from 84% at 75°C to 93% at 150°C. NiO % was then similar between the 150°C and 200°C prepared samples, and finally reached 98% for the 250°C prepared sample.

3) Interpretation of the O 1s region from the XPS spectrum

For all samples, the O 1s region comprised a high intensity section centred at binding energies (BE) between 529.2 and 529.5 eV, and another region at higher BE around 531.5 eV. We did not engage in the direct deconvolution of the O 1s signal into all its possible sub-components, due the challenges inherent to this task for NiO_x samples. We rather propose a qualitative assessment based on the relative peak area and position of these two different regions. In previous XPS studies of stoichiometric NiO, a high intensity peak at 529.2-529.3 eV has been related to O²⁻ species from the rocksalt structure of NiO^{90,107,114}. A peak related to oxygen atoms in γ -NiOOH has also been described at binding energy of 528.7 eV, and would be difficult to discriminate from NiO environment in our case¹⁰⁸.

The higher BE section of the O 1s region around 530 eV was likely to arise from several chemical environment, including α -Ni(OH)₂, β -Ni(OH)₂, γ -NiOOH, β -NiOOH and adsorbed contaminants species^{90,108-110}. Additionally, an additionnal feature at 531.1 eV was also detected for pure NiO samples in previous reports and has been the subject of various interpretations^{90,107}. In a study from Uhlenbrock et al., NiO single crystals were cleaved in vacuo and exposed to ion sputtering¹¹⁴. From XPS analysis of the Ni 2p region, the authors detected the formation of metallic Ni after the sputtering process, which was the only route for Ni²⁺ reduction in NiO. They attributed this change in composition to a loss of oxygen during the sputtering process. Regarding the O 1s region, only one peak at 529.2 eV was detected with a noticeable shift in binding energy and peak broadening after sputtering process. However, the appearance of such an additionnal feature at 531.2 eV was only detected after exposing the samples to the residual gas in the vacuum chamber for 24h, or after exposure to ambient air for 3 min. This feature was more pronounced for NiO samples exposed to

ambient air after ion sputtering. From these observations, we would conclude that the extra feature at 531.1 eV was not native to the environment of the pristine rocksalt NiO structure.

A shift in binding energy for the major O 1s peak was observed by Imran et al. after post-annealing of sol-gel prepared NiO_x layers on ITO⁹³. In their case, the BE of the major O 1s peak decreased to lower values as post-annealing temperature and NiO % concomitantly increased for their sample. For our samples, on the contrary we observed a shift to higher values with increase of temperature and NiO %. However, Imran et al. also observed a shift to lower BE in the entire Ni 2p region as temperature increased.

A shift in the O 1s region to higher binding energy could also be extracted from the results of Uhlenbrock et al., after perturbation of the pure NiO phase by ion sputtering or exposure to atmospheric conditions. However, in their case, due to the important chemical changes from sample to sample it was difficult to determine whether the shift observed for the O 1s region was concomitant to a shift of the whole Ni 2p region. In the situation described by Uhlenbrock et al., this BE shift might therefore be explained by the presence of defect states arising after metallic Ni formation. A decrease in WF means a shift in Fermi level (E_F) in the gap away from the VBM, and without modification of the VBM and CBM to a less p-type character of the NiO_x layer.

From these considerations, it remains ambiguous whether a shift in the O 1s region can be directly linked to the chemical composition of the NiO_x samples. A shift to higher BE could simply track a decrease in WF, and hence indicate a *de facto* de-doping of the NiO_x surface.

Regarding our samples, we observed a shift in binding energy for the major O 1s peak as the deposition temperature increased as reported in **Figure 18d**, which was however within the margin of error of the measurement. Peak position evolved from 529.2 ± 0.1 eV at 75 °C to 529.3 ± 0.1 eV at 250 °C, with an inflexion point at 529.3 ± 0.1 eV for the 150 °C sample.

We also noted that the relative intensity of the O 1s higher BE compared to the lower BE regions gradually decreased as the deposition temperature increases, particularly between the samples deposited at 75 °C and 200 °C. As stated before, the former was likely to include several contributions from a multitude of chemical environment. This trend was nonetheless in agreement with an increasing concentration of NiO % in samples annealed at higher temperatures as the concentration in α -Ni(OH)₂, β -Ni(OH)₂, γ -NiOOH and β -NiOOH gradually decreased.

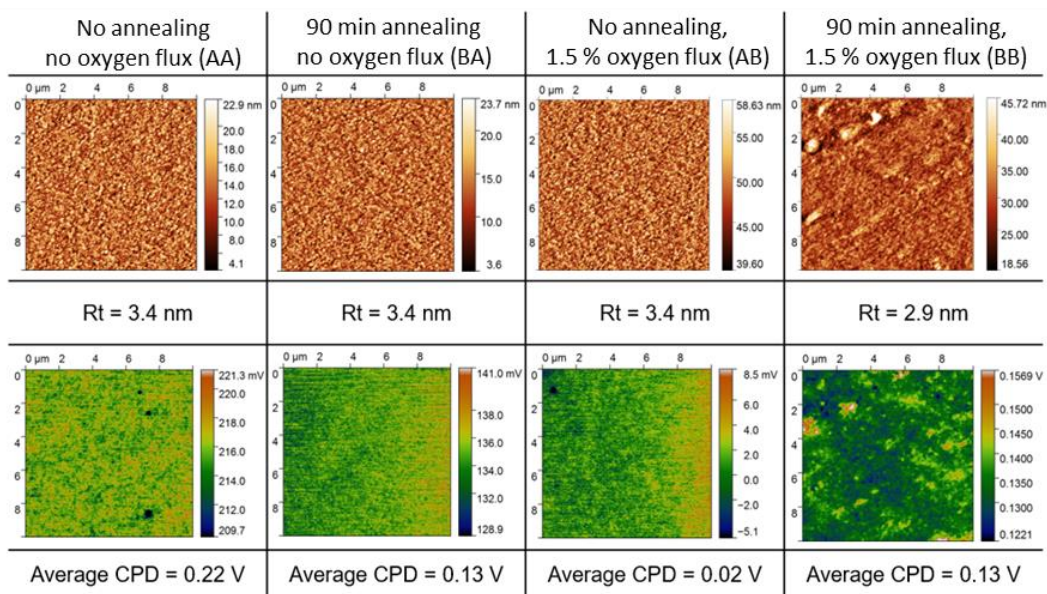
3.2.2.2. Chemical composition and electronic properties of NiO_x films prepared by plasma sputtering deposition

For a first series of samples prepared by sputtering at KIT, the influence of post-annealing treatment with and without oxygen flux over the physical and chemical properties NiO_x films were studied by KPFM, UPS and XPS analysis for 4 samples in total:

- No annealing, no oxygen flux (AA)
- 90 min annealing, no oxygen flux (BA)
- No annealing, 1.5 % oxygen partial pressure (AB)
- 90 min annealing, 1.5 % oxygen partial pressure (BB)

I) Effect of deposition temperature and oxygen partial pressure on the workfunction

Table 3 Results of KPFM measurements on sputtered-NiO_x samples prepared for different deposition temperature and oxygen flux conditions. For each sample, on the top line we can see AFM topography, in the middle RMS roughness (Rt), and on the bottom respective surface potential distribution (CPD values). Image size: 10 x 10 μm²



AFM and KPFM images acquired for sputter-deposited NiO_x samples prepared at different conditions are shown in **Table 3**. Similar root mean square roughness values between 2.9 nm and 3.4 nm were found for all the samples, although distinct features in the morphology were apparent for the BB sample, which translate into a more pronounced difference between maximum and minimum CPD values observed for this sample, with a distinguishable dispersion of results from KPFM imaging.

Average CPD values were measured between 0.02 V for the AB sample and 0.22 V for the AA sample. In between, CPD of 0.13 V was calculated for both BA and BB samples. These results suggest that without annealing, oxygen flux was the driving factor for a decrease in WF. On the other hand, annealing the sample led to a fix WF (4.81 eV) regardless of oxygen flux. At the same time, for the annealed samples oxygen flux had an impact over the morphology and distribution of CPD values across the sample.

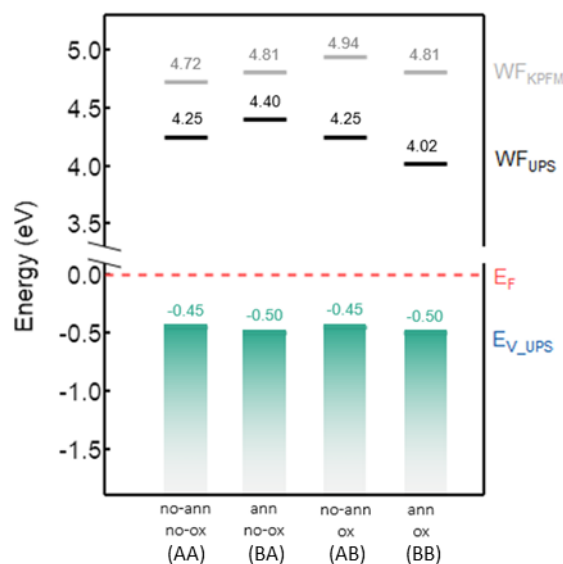


Figure 19 Summary of the work function and valence band maximum measurements by KPFM and UPS for sputtered-NiO_x samples prepared at KIT.

However, in contrast to our previous observations regarding ALD-NiO_x samples prepared by ZSW, a different pattern was observed from UPS data compared to KPFM data, for which a summary is shown on **Figure 19**. Indeed, the largest discrepancies in WF from this method was between 4.40 eV for BA and 4.02 eV for BB samples, that is between both annealed samples for which oxygen flux was suspected to not have an effect on the WF of 4.81 eV determined by KPFM measurements. On the other hand, from UPS data samples AA and AB submitted to oxygen flux had a similar WF of 4.25 eV regardless of annealing. However, similar trends were observed for both methods. Heating the sample under oxygen flux resulted in a decrease in WF from 4.25 eV for AB to 4.02 eV for BB samples, and in an increase in WF from 4.25 eV for AA to 4.40 for BA samples without oxygen flux. In general, differences in calculated WF can be observed after KPFM or UPS measurements as discussed in 3.2.2.1. In this case, the WF for samples AB and BB subjected to oxygen flux seemed especially shifted to higher values from KPFM to UPS (+0.71 eV) compared to the AA and BA samples (+0.47/0.41 eV). Absolute VBM position, on the other hand was comprised between -0.45

eV and -0.50 eV for all samples, which indicates that the Fermi level in the gap did not change and hence all sample surfaces exhibit the same doping level.

Table 4 Ni/C elemental ratio in sputtered-NiO_x samples from KIT as a function of temperature deposition, from the Ni 2p_{3/2} and C 1s regions of the XPS spectra.

Preparation conditions	Ni/C ratio
No annealing, no oxygen flux (AA)	1.84
01:30 h annealing, no oxygen flux (BA)	1.15
No annealing, 1.5 % oxygen partial pressure (AB)	2.51
01:30 h annealing, 1.5 % oxygen partial pressure (BB)	1.93

As mentioned earlier, WF measurements by KPFM can be also more sensitive to surface contamination than UPS. In **Table 4** we reported the Ni/C elemental ratio calculated for NiO_x samples prepared by KIT. From these results, we concluded that the higher Ni/C calculated for samples with oxygen flux (1.93 – 2.51 vs 1.15 – 1.84) are likely linked to the difference in WF calculated by KPFM and UPS. We noted however that differences in Ni/C did not exactly track the deviation in WF between KPFM and UPS measurements from sample to sample, which indicates a different nature of the surface contamination depending on the fabrication parameters.

Finally, as previously discussed, values calculated from KPFM were averages based on 10 x 10 μm² images while WF determined by UPS is derived from the secondary electron cutoff, i.e. the lowest energy for an electron to leave the sample averaged over an area of 500 x 500 μm². In the case of sample BB, the large difference observed between the KPFM and UPS measurements might be explained by the dispersion of values on the KPFM images shown in **Table 3** since the difference between maximum and minimum CPD was around 0.035 eV compared to values between 0.010 eV and 0.015 eV for the other samples.

Thus, variations in WF of the samples ultimately remain but measurements from UPS are likely more reliable due to the controlled environment during the measurements, which hence supports the hypothesis of a link between oxygen flux and an increase (for non-annealed samples) or decrease (for annealed samples) in WF.

2) Effect of deposition temperature and oxygen partial pressure on the chemical composition

Sputtered-NiO_x samples from KIT were also analyzed by XPS in order to evaluate the chemical composition of NiO_x subspecies at their surface. Signal for Ni 2p_{3/2} and O 1s regions are respectively shown in **Figure 20a** and **Figure 20b**. In order to access the chemical composition of our NiO_x

samples, we proceeded in the deconvolution of the Ni $2p_{3/2}$ spectra into its different NiO_xH_y sub-components following the method presented in 3.2.2.1.

From **Figure 20c**, NiO % was the highest with values $> 95\%$ for samples AA and BA prepared without oxygen flux, regardless of deposition temperature. For samples prepared with oxygen flux, NiO % was slightly lower between 90% and 95% for the AB sample and significantly diminished between 85% and 90% for the annealed BB sample.

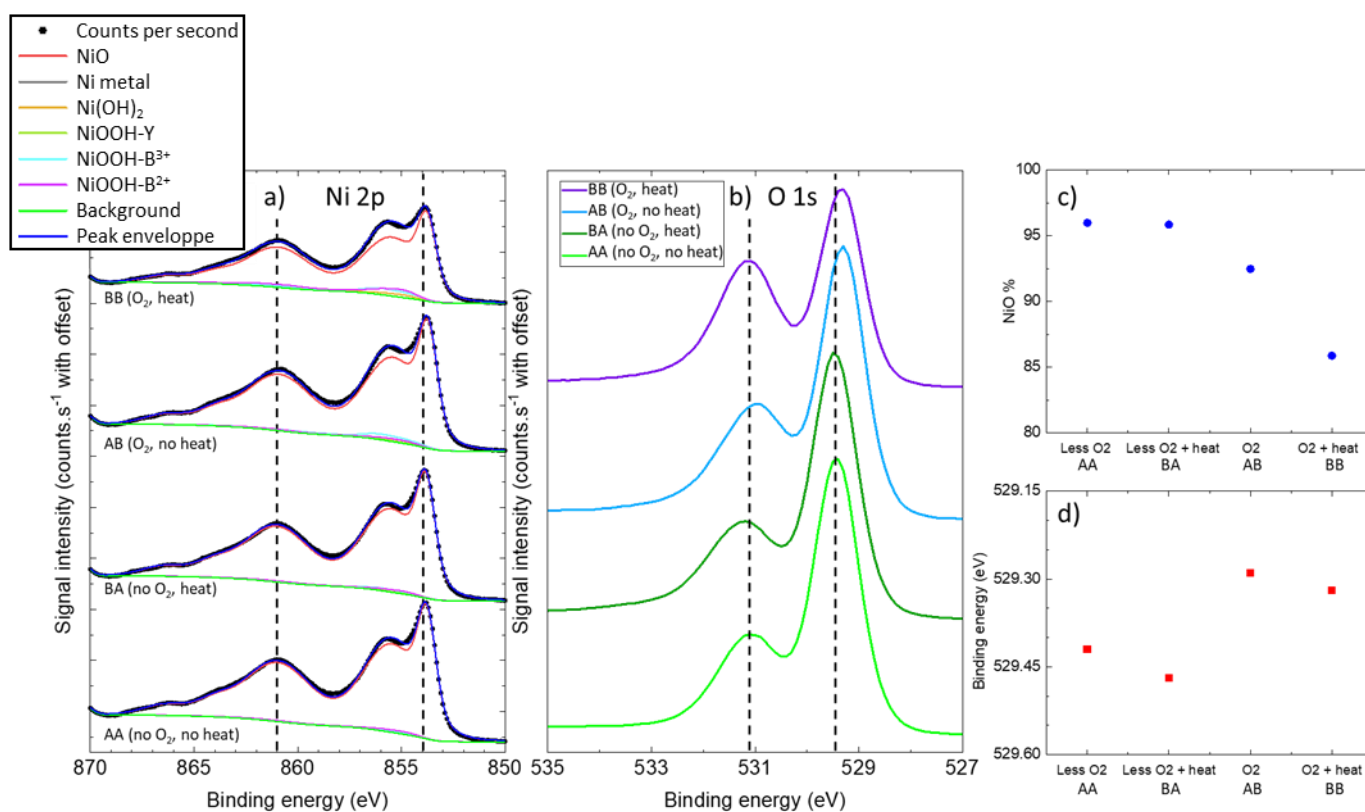


Figure 20 XPS spectra for (a) Ni $2p_{3/2}$ and (b) O $1s$ regions, (c) NiO%, as the proportion of stoichiometric NiO compared to other NiO_xH_y subspecies at the surface of the sample calculated from the Ni $2p_{3/2}$ region and (d) maximum O $1s$ binding energy shift for NiO_x samples prepared by sputtering at KIT.

The observed increase in concentration of α -Ni(OH)₂, β -Ni(OH)₂, γ -NiOOH and β -NiOOH species in the presence of oxygen flux is not surprising, with the further oxidation of Ni in stoichiometric NiO. In contrast to that NiO could not be oxidized by simply heating the sample without oxygen input, explaining why NiO % remained stable between the AA and BA samples. This result highlights the thermal stability of the material, without significant formation of Ni metal phase in the process. However, heating the samples under oxygen flux could indeed accelerate the oxidation process from stoichiometric NiO to other NiO_xH_y subspecies and thus result in a further decrease of NiO %. The

lower NiO % calculated for the BB sample might be also associated to spatially located phase transitions from the localized variations in CPD acquired by KPFM, from stoichiometric NiO to oxidized NiO_xH_y subspecies.

3) Interpretation of the O 1s region from the XPS spectrum

For all samples, the O 1s region comprised a high intensity section centred at binding energies (BE) between 529.2 and 529.5 eV, and another region at higher BE around 531.5 eV.

A shift in binding energy for the major O 1s peak from sample to sample is reported from **Figure 20d**. Position increased from 529.4 ± 0.1 eV for the AA sample to 529.5 ± 0.1 eV for the BA sample both prepared without oxygen flux. The BE was similar between the BA and AD samples prepared with oxygen flux, at 529.3 ± 0.1 eV for BA to 529.3 ± 0.1 eV. Overall, these shifts are within the margin of error of the measurement and hence we do not observe a significant effect on the Fermi level position in the gap that could be associated with a change of the doping concentration. Shift in peak position could again be associated to some extent with the evolution of WF, especially from the KPFM measurements. Indeed, WF from KPFM seemed to increase after oxygen flux and to decrease or slightly increase for the annealed samples.

It should be noted that in order to be interpreted correctly, the major O 1s peak should solely and entirely represent the contribution from O in the stoichiometric NiO crystal. However as mentioned before, the XPS spectra of NiO_x in the O 1s region is a mixture of several components. Contributions from these components are likely to overlap with pure NiO contribution, depending on their position and FWHM. As a result, the numerical value given for the major O 1s peak position should be interpreted with caution. Therefore, deviation in trends observed between the KPFM calculated WF and the position of the O 1s major peak from sample to sample might purely arise from the difficulty to assess the WF and the peak position with good accuracy. From previous discussions in 3.2.2.1, we therefore concluded that a shift to higher BE for the principal O 1s peak would translate well to an increase in E_F rather than a decrease in NiO %.

Again, the area of the higher BE section of the O 1s region increases as NiO % decreases, in accordance to an increase from α -Ni(OH)₂, β -Ni(OH)₂, γ -NiOOH and β -NiOOH contributions.

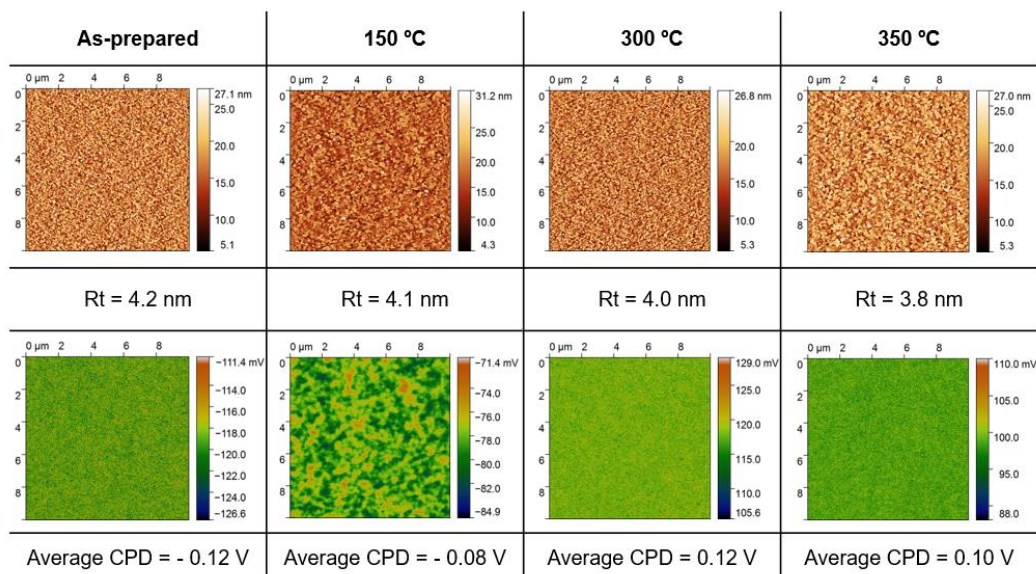
3.2.2.3. Chemical composition and electronic properties of NiO_x films prepared by plasma sputtering

For a second series of samples prepared by sputtering at IMEC, the influence of post-annealing temperature over the physical and chemical properties of NiO_x films were studied by KPFM, UPS and XPS analysis for 4 samples in total:

- As-prepared
- 150°C post-annealing for 30 min
- 300°C post-annealing for 30 min
- 350°C post-annealing for 30 min

I) Effect of post-annealing temperature on the workfunction

Table 5 Results of KPFM measurements on sputtered-NiO_x samples prepared for different post-annealing temperature. For each sample, on the top line we can see AFM topography, in the middle RMS roughness (Rt) of sample, and on the bottom respective surface potential distribution (CPD values). Image size: 10 x 10 μm²



AFM and KPFM images acquired for ALD NiO_x samples prepared at different temperatures are reported in **Table 5**. Similar root mean square roughness values between 3.8 nm and 4.2 nm were found for all the samples. Average CPD values were between -0.12 V for the as prepared sample and 0.12 V for the 300°C annealed sample were measured. In between, CPD were measured at -0.08 V for the 150°C annealed sample and 0.12 V for the 350°C annealed sample. Spatial unhomogeneities in CPD were particularly pronounced for the 150°C sample, with variations in values over

micrometric distances. In terms of WF, these results generally translated to a gradual decrease from 5.06 eV to 4.82 eV as annealing temperature increased to 300°C. A slightly higher, but close WF value of 4.84 eV was determined for the 350°C annealed sample.

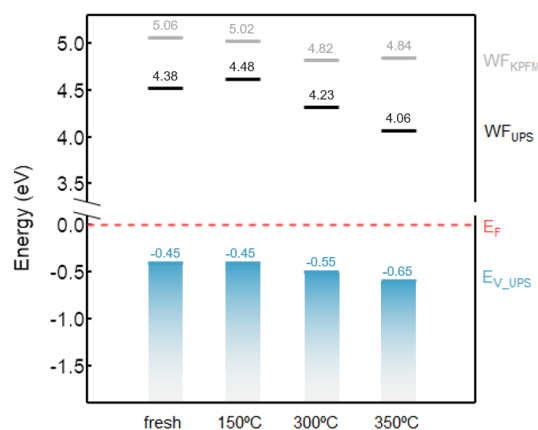


Figure 21 Summary of the work function and valence band maximum measurements by KPFM and UPS for sputtered-NiO_x samples prepared at IMEC.

This time again, similar trends were observed between KPFM and UPS data for which a summary is shown on **Figure 21**. Although we noticed an increase in WF between the as-prepared and 150°C annealed sample from 4.36 eV and 4.48 eV, and a decrease between the 300°C and 350°C annealed sample from 4.23 eV to 4.06 eV, the general tendency for these samples was a decrease in WF and therefore a shift of the E_F away from the valence band maximum for increasing annealing temperature. Values from UPS were slightly shifted to lower values compared to KPFM measurements, for the same reasons as given in 3.2.2.1. In particular, we reported on **Table 6** Ni/C elemental ratios between 1.28 to 2.36 for NiO_x samples prepared by IMEC. Differences from sample to sample might be linked to some extent to variations in WF values and trends from KPFM and UPS measurements. Absolute VBM position this time rather decreased from -0.45 eV for the as-prepared sample to -0.65 eV as annealing temperature was increased to 350°C, with an inflexion point at -0.55 eV at 300°C.

Table 6 Ni/C elemental ratio in sputtered-NiO_x samples from IMEC as a function of temperature deposition, from the Ni 2p_{3/2} and C 1s regions of the XPS spectra.

Preparation conditions	Ni/C ratio
As-prepared	1.28
150°C	1.33
300°C	2.36
350°C	1.55

In general, a more robust trend in decreasing WF as post-annealing temperature increased could be established as compared to the samples prepared by ZSW, with an additional concomitant decrease in absolute VBM position.

2) Effect of post-annealing temperature on the chemical composition

Sputtered-NiO_x samples from IMEC were also analyzed by XPS in order to evaluate the chemical composition of NiO_x subspecies at their surface. Signals for Ni 2p and O 1s regions were respectively shown in **Figure 22a** and **Figure 22b**. In order to access the chemical composition of our NiO_x samples, we proceeded in the deconvolution of the Ni 2p_{3/2} spectra into its different NiO_xH_y sub-components according to the method presented in 3.2.2.1.

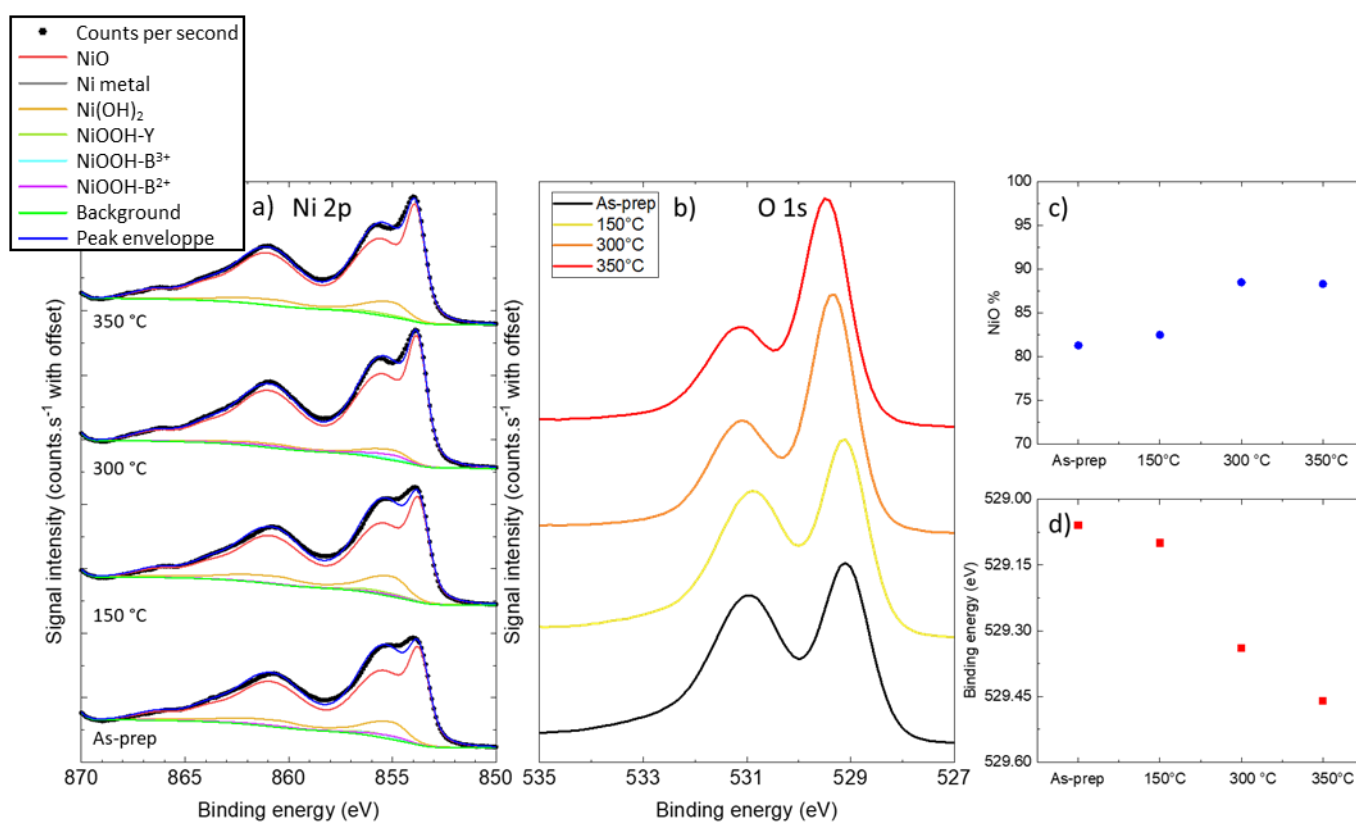


Figure 22 XPS spectra for (a) Ni 2p_{3/2} and (b) O 1s regions, (c) NiO%, as the proportion of stoichiometric NiO compared to other NiO_xH_y subspecies at the surface of the sample calculated from the Ni 2p_{3/2} region and (d) maximum O 1s binding energy shift for NiO_x samples prepared by sputtering for different post-annealing temperatures.

From **Figure 22c**, NiO % was the lowest between 80 % and 85 % for the as-prepared sample to almost 90 % for the 300°C and 350°C samples. NiO % for the 150°C annealed sample was slightly higher as compared to the as-prepared one, but not significantly.

We therefore observed a gradual increase in stoichiometric NiO concentration compared to the α -Ni(OH)₂, β -Ni(OH)₂, γ -NiOOH and β -NiOOH phases as post-deposition temperature increased. A slight increase in NiO % for the 150°C annealed sample, associated to un-homogeneities in CPD seen via the KPFM measurements could reflect an incomplete, localized phase transition from oxidized NiO_xH_y subspecies to stoichiometric NiO. The trend observed for post-annealed NiO_x samples prepared by sputtering was similar to that followed by ALD samples prepared at ZSW for different deposition temperatures, as discussed in 3.2.2.1. Lower absolute values of NiO % were nonetheless observed at high temperatures for the sputtered samples.

3) Interpretation of the O 1s region from the XPS spectrum

For all samples, the O 1s region comprised a high intensity section centred at binding energies (BE) between 529.0 and 529.5 eV, and another region at higher BE around 531.5 eV.

A shift in binding energy for the major O 1s peak from sample to sample is reported from **Figure 22d**. Position increased from 529.1 ± 0.1 eV for the as-prepared sample to 529.5 ± 0.1 eV for the 350°C annealed sample, with intermediate values of 529.1 ± 0.1 eV at 150°C and 529.3 ± 0.1 eV for the 300°C sample. This trend was in accordance with an increasing NiO % and a decreasing WF, supporting the hypothesis proposed in 3.2.2.1 that the binding energy of the NiO component in the O 1s region would track a decrease in WF.

Again, the relative area of the higher BE section of the O 1s region increased as NiO % decreased, in accordance to an increase from α -Ni(OH)₂, β -Ni(OH)₂, γ -NiOOH and β -NiOOH contributions.

In this subsection, we probed the chemical environment and electronic properties of the surface of NiO_x layers prepared by ALD and sputtering under different deposition and post-treatment conditions. We found that while similar VBM values were measured by UPS regardless of deposition temperature or oxygen flux in the case of the sputtered samples, post-annealing treatment on the other hand resulted in a decrease in absolute values for the sputtered samples from IMEC.

From both KPFM and UPS measurements, an increase in deposition or post-annealing temperature could be associated to a decrease in WF and thus an increase in E_F. This trend was particularly pronounced from post-annealed samples prepared by sputtering. It was however less robust for the series of ALD samples deposited at different temperatures, or for the sputtered samples prepared with

different oxygen partial pressure. We hypothesized that this increase in E_F , whether associated to a decrease in VBM or not, could translate to a less pronounced p-type character for the NiO_x layers. However, we did not possess information over the absolute CBM position for each sample which would be necessary to confirm or infirm this hypothesis.

In terms of composition, from XPS analysis increasing the deposition or post-annealing temperature almost systematically resulted in a higher percentage of stoichiometric NiO as compared to other NiO_xH_y species. Notably, this was not the case for sputtered NiO_x prepared under oxygen flux, for which annealing during deposition resulted in a decrease in NiO % concomitantly to a decrease in WF. For sputtered samples from IMEC, increasing the post-annealing temperature from 300°C to 350°C did not result in an increase in NiO % but did result in a decrease in WF and absolute VBM position. For each sample, we also followed the evolution in binding energy of the major O 1s peak. From various sets of samples, shifts in values were not significant and we concluded that it was more closely linked to the evolution of WF from sample to sample, than to an evolution in NiO %. A shift to higher BE was therefore likely to mirror a decrease in WF and therefore an increase in E_F .

Interestingly, a direct link between the evolutions in WF and NiO % could be found for the ZSW and IMEC samples, but not in the case of the KIT series. In other words, with our degree of analysis we could not exactly find a direct correspondence between the structural composition at the surface of NiO_x layers and the electronic properties at the surface of the films. This observation could mean that morphology, grain orientation or defect concentration might have an influence over the physical parameters of the NiO_x layers followed in this study, i.e. E_F and absolute VBM. To a certain degree, we nonetheless observe that an increase in NiO % was accompanied with a decrease in WF, along with a constant value or slight shift of the Fermi level towards the VBM.

To further extend the scope of our analysis, we tested to which extent these different properties affected the overall efficiency of perovskite solar cells. In the next subsection, we associated the chemical and physical properties of NiO_x layers to device performances based on PV parameters recorded for p-i-n devices based on ALD- NiO_x HTL prepared by ZSW at different temperature.

3.2.3. Applications of low-temperature ALD-NiO_x in perovskite solar cells^{iv}

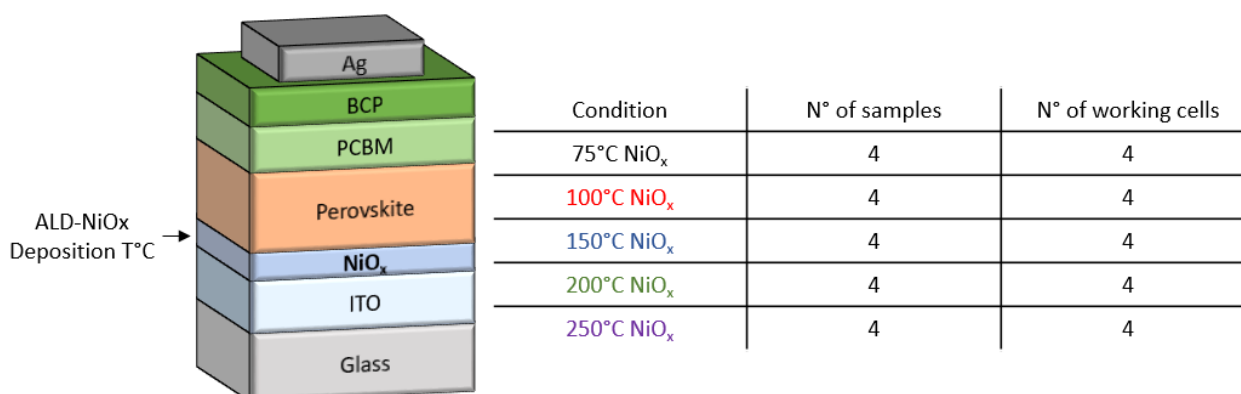


Figure 23 (left) Architecture of p-i-n perovskite solar cells prepared for J-V experiment using NiO_x as HTL. Layers were deposited at different temperature by ALD from Me-nickelocene precursor and O₂ plasma as oxidizer (right) Number of solar devices prepared and number of working solar cells (i.e. PCE>1%) per condition.

Figure 23 shows the architecture and conditions for solar cells fabricated from NiO_x samples prepared by ALD. PV parameters for these devices are presented in **Figure 24**. Deposition temperature seems to have a weak impact on device performances. Among devices fabricated using ALD NiO_x deposited at 75°C, one exhibited especially poor PV performances with a PCE < 4%. Similar values of V_{oc} between 925 and 1025 mV were measured for each device which indicates that ALD-NiO_x can play the role of an effective electron blocking layer even when processed at low temperature. Particularly close V_{oc} values from 990 mV to 1010 mV were recorded for samples prepared at 150°C and 200°C, except for an outlier value of 960 mV. Nonetheless, a trend of increasing average Fill factor from 66 % to 69 % and J_{sc} from 17.3 mA.cm⁻² to 18.6 mA.cm⁻² is observed with deposition temperature for samples deposited between 75°C and 200°C, For samples prepared at 250°C, a higher maximum V_{oc} of 1050 mV but lower J_{sc} and FF values are found compared to 200°C NiO_x samples.

While a clear trend of increasing efficiency is observed between 75°C and 200°C devices, overall these changes are subtle given the number of samples per condition and might not be significant enough to correlate electronic and chemical properties to PV parameters in solar cells. We can therefore conclude that these properties are not predominant on the performances of solar cells, at least for the range of values described in this study.

^{iv} Solar cells were fully prepared and measured at ZSW.

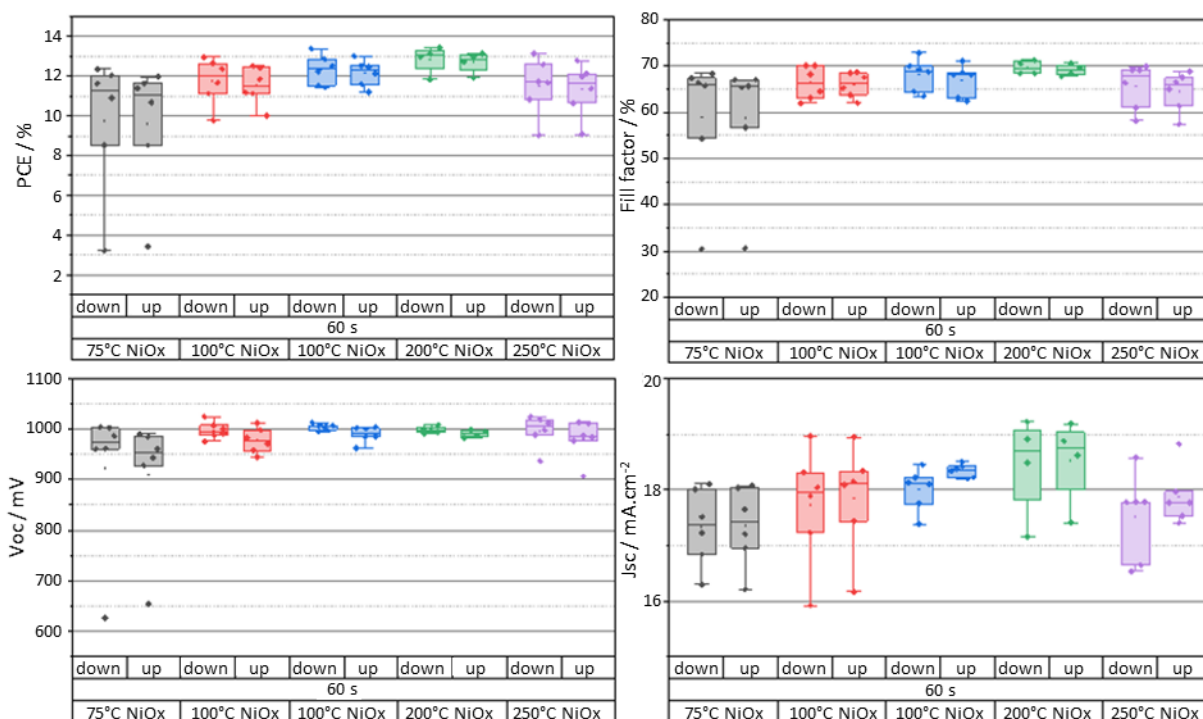


Figure 24 PV parameters measured for perovskite solar cells fabricated using ALD prepared NiO_x from Me-nickelocene precursor and O₂ plasma as oxidizer at different temperature as HTL. Solar cell stack was glass/ITO/NiO_x/perovskite/PCBM/BCP/Ag

The observed trend in efficiency is nonetheless correlated with an increasing amount of stoichiometric NiO obtained from XPS data. For a fixed CBM position, the effect of a subtle decrease in WF observed with KPFM, UPS and XPS for ALD-NiO_x could diminish the p-type of NiO_x and have the adverse effect to reduce the hole conductivity of the HTL. On the other hand, highest NiO % content and O 1s binding energy are found for 250°C prepared NiO_x. Devices prepared from this condition yielded highest V_{oc} values but lower PCE compared to 200°C NiO_x samples due to a loss in J_{sc} and FF . These results might not be statistically significant, but it is also possible that a too close-to-stoichiometry NiO_x sample would result in a lower conductivity, and thus lower FF and J_{sc} values.

Furthermore, detrimental catalytic activity from Ni³⁺ sites with organic A cation sites in the perovskite lattice have been reported to trigger degradation mechanisms in the perovskite layer that could hinder the performances of perovskite solar cells⁸⁷. These species can be found in NiO_x samples when the composition deviates from stoichiometry, notably when NiOOH sub-species are formed. Boyd et al. principally mentioned a loss of V_{oc} for devices when the surface Ni³⁺ sites concentration is high, which is in good agreement with our observation that deviation in composition from stoichiometric NiO composition could be detrimental to device performances. However, we show that deposition

temperature of ALD-NiO_x only marginally influences the PV performances of derived perovskite solar cells. Additionally, properties of the ITO substrates such as sheet resistance and transparency can be affected by deposition temperature and might explain to some extent the observed variations in FF and J_{sc} ¹¹⁵.

To conclude, characterization of solar cells prepared from ALD-NiO_x samples allowed us to study the correlation of the chemical properties discussed in 3.2.2 to PV parameters in PSCs. In particular, we found that work function measurements yielded close values despite different percentage of stoichiometric NiO in samples. Together, these observations could explain why slightly higher PCE values were observed for NiO_x samples prepared at higher temperature. However, our main conclusion is that the influence of deposition temperature over PV parameters in solar cells is only marginal, at least between 100°C and 250°C, and could be rather linked to a change in properties of the ITO substrate. This means that ALD is a suitable synthesis method of NiO_x for perovskite top cell deposition on top of a CI(G)S subcell. It should be noted that other authors, using a similar ALD process at 150°C, suggested that a post-treatment of NiO_x at 300°C in air would dramatically improve the performances of resulting PSCs^{40,42}.

In the next subsection, I specifically explore how the interface between NiO_x and perovskite can be tuned to gain information about the parameters that are crucial to reach high PV parameters in PSCs. I submitted NiO_x samples to different combinations of UV-Ozone treatment, 10 minutes post-annealing treatment at 250°C and FAI treatment. They were then analyzed by XPS to understand more deeply the influence of UV-Ozone treatment followed by 10 minutes post-annealing treatment at 250°C. Perovskite solar cells were then fabricated using these samples as HTL.

3.2.4. Enhancement of PV parameters of p-i-n perovskite solar cells by tuning the surface chemistry of NiO_x^y

In this subsection, I explore different post-treatments to tune the surface properties of NiO_x and gain insight into the key parameters that dictate the performance of resulting solar cells. By the time of this study, ALD-NiO_x was not yet readily available and I relied on NiO_x layers prepared by sol-gel process and combustion reaction. They were respectively annealed at 300°C for 1 hour and at 250°C for 45 minutes after spin coating. Detailed processes for the fabrication of these layers are available in Chapter 2.

^y XPS acquisition was realized by Muriel Bouttemy and Matthieu Frégnaux.

As mentioned in Chapter 2, low values of V_{oc} have been routinely reported for PSCs using NiO_x as HTL. It has been hypothesized that Ni^{3+} species at the surface of NiO_x layers would act as catalytic sites for the degradation of hybrid perovskite layers, by the deprotonation of organic cations $MA-H^+$ and $FA-H^+$ and the resulting formation of gaseous MA, FA and I_2 species⁸⁷. These reactions would also lead to the formation of a $PbI_{2-x}Br_x$ rich region at the NiO_x /perovskite interface which would in turn decrease the V_{oc} of devices by increasing recombination at the interface by acting as an energetic barrier.

UV-ozone treatment (UV- O_3) is a routinely used cleaning technique performed in ambient air for the study of semiconductors¹¹⁶. In the field of perovskite solar cells, the oxidative environment of UV- O_3 not only effectively degrades the carbon-based contaminants at the surface of a metal oxide sample, but also increases the wettability of metal oxides to some solvents by the formation of hydroxyl sites at their surface. This last feature can improve the coverage and homogeneity of subsequent deposited layers, limiting shunts pathways in complete devices. UV- O_3 treatment of the TiO_2 surface has been also reported to improve the performances of n-i-p perovskite solar cells¹¹⁷.

In the case of NiO_x layers, UV- O_3 has been reported to promote the formation of defects and/or oxy-hydroxide species with Ni atoms of equivalent or higher oxidation degrees such as $NiOOH$ ⁸⁷. For this reason, we can assume that UV- O_3 treatment on NiO_x layers before perovskite deposition would amplify the degradation process described earlier at their interface.

On the other hand, for several fabrication processes UV- O_3 could remove potential carbon contaminants from the NiO_x surface coming from either ALD precursor leftover or solvent residues in the case of sol-gel and combustion deposition. To test this hypothesis, I introduce a post-deposition treatment where NiO_x layers deposited on ITO are heated at 250°C for 10 minutes directly after 15 minutes UV-Ozone treatment to recover a surface with a high proportion of stoichiometric NiO from a rich oxy-hydroxyl surface. This combination of UV- O_3 and post-annealing treatments is denoted as $UVO_3 + A$ for the rest of the chapter. Indeed, NiO_x films visibly turn black after UV- O_3 treatment, suggesting the formation of $NiOOH$ species. After annealing the obtained samples at 250°C for 10 min, we observed that blacken films turned transparent again, indicating conversion back to stoichiometric NiO phase. It might be possible to increase the temperature and time of the post-treatment, but high temperatures might alter the electrical and optical properties of the underneath ITO layer.

From visual observations, NiO_x samples blacken after UV- O_3 and recover their former transparency after the short annealing step of $UVO_3 + A$. We hypothesize that the black color after UV- O_3 treatment

indicates the formation of NiOOH phases at the surface of the sample, while the aspect of the sample after UV-O₃ + A suggests that the films retrieved its former chemical composition after annealing.

3.2.4.1. Effect of UV-Ozone post-treatment on the surface chemistry of sol-gel NiO_x films

To test our first hypothesis, we use XPS analysis to evaluate the surface chemistry of samples prepared by sol-gel process before and after UV-O₃ treatment. Spectra for the Ni 2p and O 1s region are shown in **Figure 25**. On the Ni 2p_{3/2} region between 852 eV and 859 eV, we observe a relative increase in intensity for the secondary peak centered at 855.5 eV compared to the primary peak at 853.7 eV after UV-O₃, which would hint towards an increase in concentration of Ni(OH)₂ and NiOOH species compared to stoichiometric NiO. Using the fitting method introduced in part 3.2.2 for the Ni 2p_{3/2} region, we indeed find that the NiO % decreases from 85 % - 90 % to 75 % - 80 % while no presence of metallic Ni was detected in either sample.

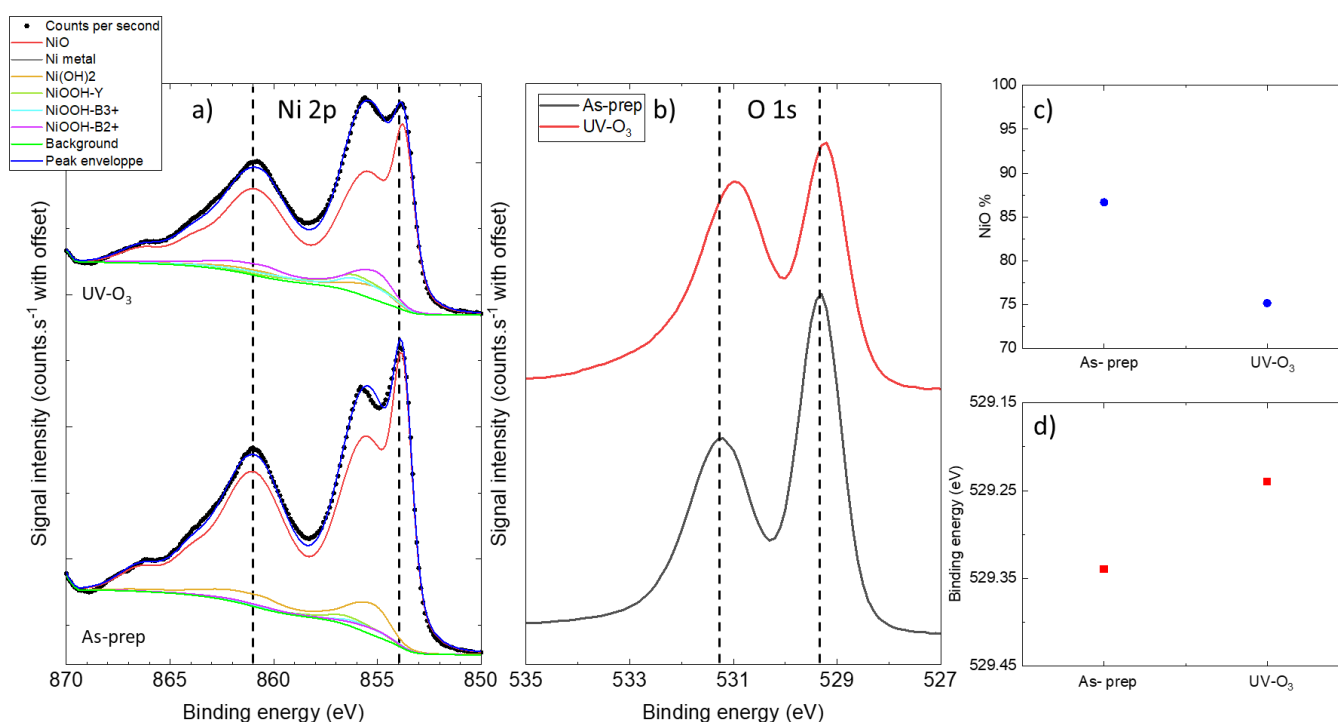


Figure 25 XPS spectra for (a) Ni 2p_{3/2} and (b) O 1s regions, (c) NiO %, as the proportion of stoichiometric NiO compared to other NiO_xH_y subspecies at the surface of the sample calculated from the Ni 2p_{3/2} region and (d) maximum O 1s binding energy shift for NiO_x samples prepared by sol-gel before and after UV-O₃ treatment.

We also measured a shift in BE for the major O 1s peak after UV-O₃ treatment, from 529.32 eV to 529.20 eV, which could indicate a lowering in WF induced by a change in surface chemistry. We then calculated the Ni/C elemental ratio by integrating the spectra in the Ni 2p_{3/2} and C 1s regions as

presented in **Table 7**. We found that Ni/C ratio decreased from 2.59 to 1.12 after UV-O₃ treatment. Indeed, even though UV-O₃ likely removed carbon contaminants from the surface of NiO_x it also functionalized its surface and renders it more reactive to the contaminants of various types naturally present in ambient air. In this particular case, UV-O₃ treatment was therefore not an effective method to reduce the amount of carbon species adsorbed at the surface of NiO_x.

Table 7 Ni/C elemental ratio measured by XPS based on the Ni 2P_{3/2} and C 1s regions for NiO_x samples prepared by **(a)** sol-gel process before and after UV-O₃ and **(b)** combustion process before and after UV-O₃ or UV-O₃ + A treatment.

a) NiO _x PDT (sol-gel)	Ni/C ratio	b) NiO _x PDT (combustion)	Ni/C ratio
As-prepared	2.59	As-prepared	0.92
UV-O ₃	1.12	UV-O ₃	1.51
		UV-O ₃ + A	1.44

We then tested our second hypothesis, that is the potential to restore a Ni²⁺ rich surface from UV-O₃ treated NiO_x samples by post-annealing at 250°C for 10 minutes. To this end, we synthesized samples by combustion process and evaluated their chemical composition by XPS analysis before and after UV-O₃, as well as after UV-O₃ + A treatment.

3.2.4.2. Effect of UV-Ozone post-treatment and surface recovery on the surface chemistry of combustion NiO_x films

Spectra corresponding to the Ni 2p and O 1s regions for combustion processed samples are shown in **Figure 26**. In this case, subtle decrease in NiO % was detected from 87% to 83% before and after UV-O₃ treatment. This change was less significant compared to the one observed for the sol-gel samples. NiO % was then similar between UV-O₃ and UV-O₃ + A conditions. This could be due to the fact that samples were not measured by XPS right after treatment, which means that the effect of the UV-O₃ treatment could have been lost and the so-modified surface could have partially reverted to its original chemistry.

On the other hand, Ni/C ratio increased from 0.9 to 1.5 either after UV-O₃ or UV-O₃ + A treatment. The initially low Ni/C ratio compared to sol-gel prepared samples suggests that the combustion process used for this experiment had a higher tendency to leave contaminants at the surface of NiO_x. For both series of samples, a similar ratio was calculated after UV-O₃ which tends to confirm the hypothesis that the quantitative effect of UV-O₃ surface cleaning depends on the type of process that is used to synthesize NiO_x. Interestingly, relative intensities of the different peaks from the C 1s region was different between the UV-O₃ and UV-O₃ + A samples, indicating that different species of contaminant species are adsorbed when the surface of UV-Ozone functionalized NiO_x is either left at room temperature or heated at 250°C. This observation was supported by the very similar peak position found for the major peak of the O 1s region for the three samples.

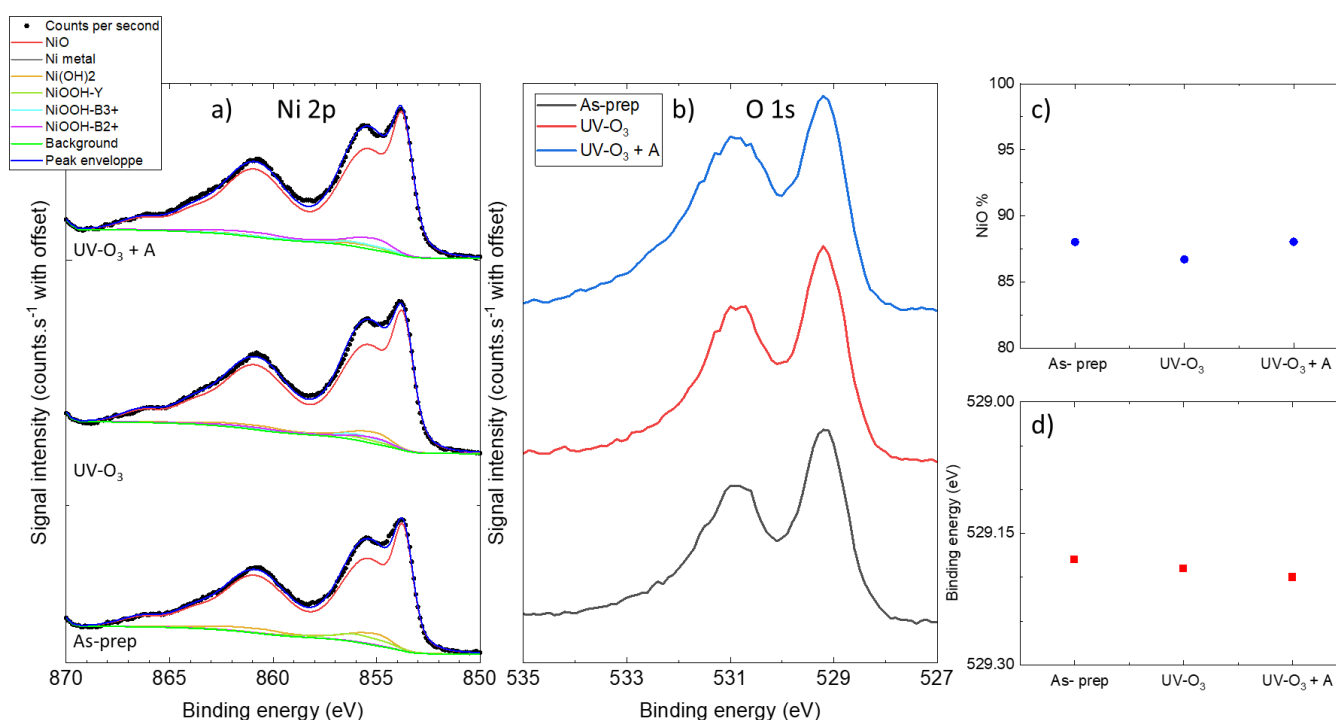


Figure 26 XPS spectra for (a) Ni 2p_{3/2} and (b) O 1s regions, (c) NiO %, as the proportion of stoichiometric NiO compared to other NiO_xH_y subspecies at the surface of the sample calculated from the Ni 2p_{3/2} region and (d) maximum O 1s binding energy shift for NiO_x samples prepared by sol-gel before and after UV-O₃ treatment or UV-O₃ + A treatment.

To conclude, we studied the change in surface chemistry and electronic properties of UV-O₃ treatment on sol-gel and combustion samples, which could be followed by a short annealing step in an attempt to recover the surface chemistry of the as-prepared sample. For the sol-gel samples, UV-O₃ was accompanied with a decrease in NiO %, concomitantly to a decrease in major O 1s peak binding energy. On the contrary, this change was not observed for the combustion sample, possibly due to the

fact that several days occurred between UV-O₃ treatment and XPS measurement. As a result, similar NiO % and major O 1s peak position were calculated for all samples prepared by combustion.

We nonetheless observed an evolution in Ni/C elemental ratio, which respectively increased and decreased after UV-O₃ treatment for respectively the sol-gel and the combustion samples. These results did not elucidate the cleaning role of UV-O₃, but we noted that this treatment could be beneficial for the wettability of subsequent layers on top of the HTL layer by the functionalization of Ni surface sites.

In order to relate these changes in surface chemistry to PV performances in PSCs, I prepared p-i-n devices based on NiO_x HTL after these different treatments. Additionally, we wanted to evaluate the effect of treating the surface of NiO_x with FAI before perovskite deposition as described by Boyd et al. to increase the performances of solar cells⁸⁷. Since the focus of our study was the influence of the surface chemistry of NiO_x, we needed to exclude the potential interference of a change in bulk NiO_x provoked by a 250°C annealing step for 10 min for the UV-O₃ + A treatment. We also wanted to exclude the effect of high temperature over the quality of the underneath ITO layer. To do so, we also introduced a new condition in which NiO_x films were annealed at the same program before UV-Ozone treatment (A + UV-O₃).

3.2.4.3. Surface-tuned NiO_x layers as HTL for perovskite solar cells: Effect of surface recovery after UV-Ozone and FAI quenching

As a first experiment, we deposited NiO_x layers by sol-gel process on ITO substrates and explored 4 types of treatments before perovskite deposition. 4 opaque solar cells were prepared per treatment based on a ITO/NiO_x/perovskite/PCBM/BCP/Ag architecture for a total of 16, as shown on **Figure 27**:

- UV-Ozone treatment for 15 min in air (UV-O₃)
- 250°C annealing for 10 min in air followed by UV-Ozone (A + UV-O₃)
- UV-Ozone treatment followed by 250°C annealing for 10 min in air (UV-O₃ + A)
- UV-O₃ + A treatment followed by the deposition of a 0.1 M FAI solution in DMF by spin-coating at 3000 rpm for 30 sec. Films were annealed at 100°C for 10 min after treatment (UV-O₃ + A + FAI wash)

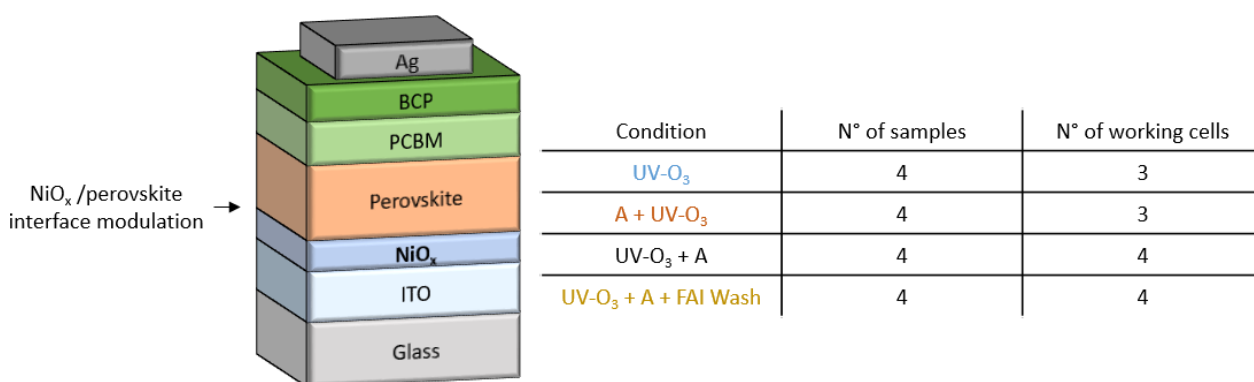


Figure 27 (*left*) Architecture of solar cells prepared for J-V experiment using different NiO_x post-deposition treatment (*right*) Number of solar devices prepared and number of working solar cells (i.e. PCE > 1%) per condition.

PV parameters recorded 3 and 14 days after fabrication are reported on **Figure 28** and **Figure 29**, respectively. After fabrication and between measurements, cells were stored in the dark in vacuum. Active area was defined prior to measurement by a 0.09 cm² square mask.

After 4 days, Similar J_{sc} values were recorded for all devices, although slightly higher values were obtained using UV-O₃ + A treated and UV-O₃ + A + FAI washed NiO_x. Lowest and highest V_{oc} values were respectively measured for the UV-O₃ and UV-O₃ + A + FAI wash condition. This result is consistent with the hypothesis that a Ni³⁺ rich surface would hinder the V_{oc} of p-i-n cells based on NiO_x, while a treatment with FAI before perovskite layer deposition would quench these sites and result in an increase of V_{oc} ⁸⁷. Using A + UV-O₃ and UV-O₃ + A + FAI washed NiO_x resulted in similar FF .

Overall, slightly superior PV parameters were found for A + UV-O₃ compared to UV-O₃ conditions, while V_{oc} was enhanced by UV-O₃ + A + FAI wash and FF by UV-O₃ + A treatment. The spread in performance parameters V_{oc} , FF and PCE was the largest for the UV-O₃ condition. The underlying message is that the short annealing “A” step on its own had little influence on PV parameters. On the other hand, consistently higher values of FF and PCE were obtained using UV-O₃ + A compared to A + UV-O₃ treatment. Differences in PV parameters using either condition can therefore be linked to a higher quality of interface between NiO_x and perovskite using UV-O₃ + A treated samples. Observed variations could be consistent with a restoration of a Ni²⁺ rich surface after a short annealing of UV-O₃ treated NiO_x samples, and thus an increase in PCE. However, this effect that we hypothesized earlier is not confirmed by XPS analysis. We also note that this increase in PCE is

essentially derived from higher FF values while V_{oc} values remain similar between A + UV-O₃ and UV-O₃ + A and only increased after UV-O₃ + A + FAI wash treatment.

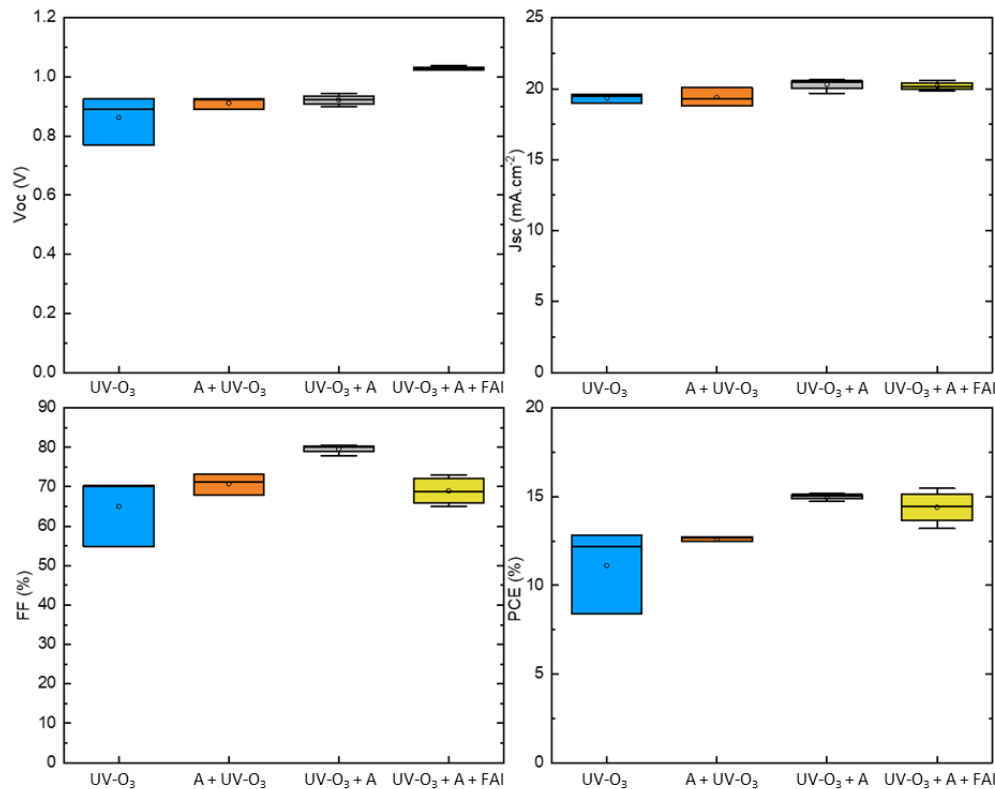


Figure 28 PV parameters recorded after 4 days after fabrication for perovskite champion cells using NiO_x after different post-deposition treatment as HTL.

I thus propose three explanations that are not mutually exclusive to account for this observation:

- 1) The hypothesized formation of a PbI_{1-x}Br_x phase at the NiO_x/perovskite interface would not only be detrimental to V_{oc} of devices, but would also decrease the FF and especially the series resistance of the cells.
- 2) A short annealing step at 250°C could be less effective than a FAI treatment to quench surface Ni³⁺ sites and obtain a Ni²⁺ rich NiO_x surface. This hypothesis would explain why we observe an increase in FF using UV-O₃ + A compared to A + UV-O₃ NiO_x, but not why we do not observe even an increase in V_{oc} ,
- 3) While the degradation mechanism described by Boyd et al. is indeed a cause of loss in performances in PSCs devices, the increase of V_{oc} observed after FAI treatment is only partially linked to a quenching of Ni³⁺ sites at the interface between NiO_x and perovskite. FAI excess would have a beneficial effect on V_{oc} through another mechanism.

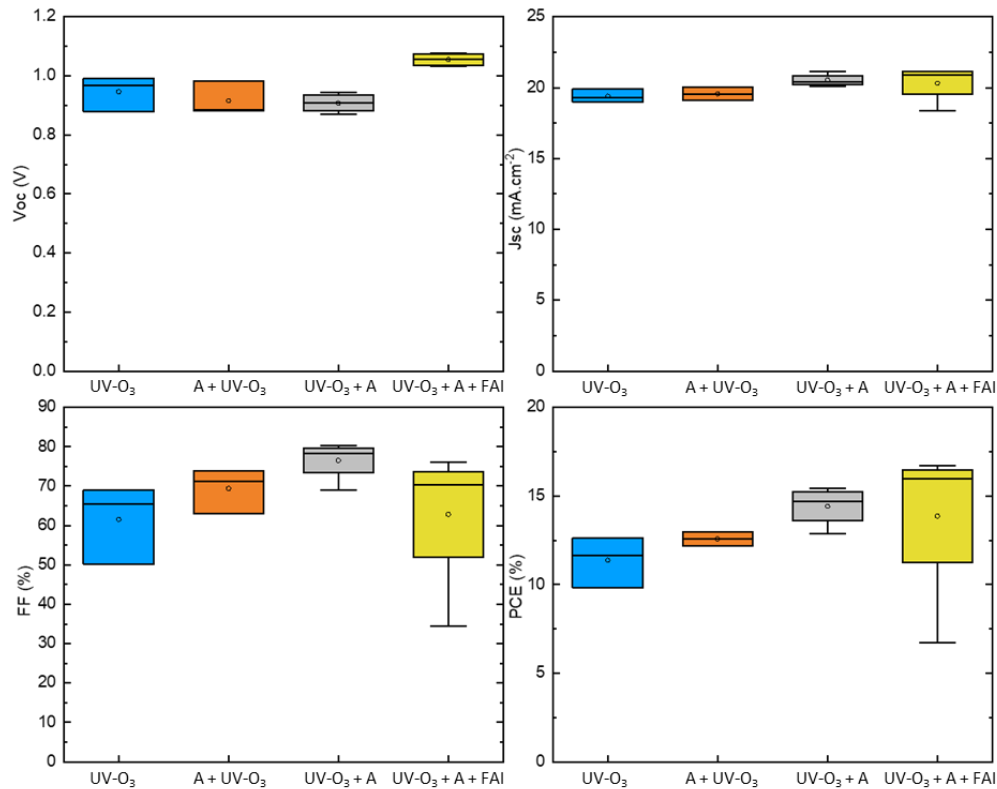


Figure 29 PV parameters recorded after 15 days after fabrication for perovskite champion cells using NiO_x after different post-deposition treatment as HTL.

Overall, higher average PCE values were reached for UV-O₃ + A samples, followed by UV-O₃ + A + FAI wash, A + UV-O₃ and UV-O₃ series. We also measured a higher PCE of 15.47% for the UV-O₃ + A + FAI wash champion cell compared to 15.18% for the UV-O₃ + A condition as shown in **Figure 30**. While statistical parameters have little significance over such a small number of samples, a better reproducibility was observed for the UV-O₃ + A condition, especially regarding *FF* distribution compared to other conditions while least consistent results were observed with devices using UV-O₃ treated NiO_x.

15 days after device fabrication, average *V*_{oc} values increased for most conditions while we observed a slight decrease for the UV-O₃ + A condition. On average, *J*_{sc} also increased for all devices. The average *FF* was also either stable or lower for UV-O₃, A + UV-O₃ and UV-O₃ + A series while it increased for nearly all devices using UV-O₃ + A + FAI washed NiO_x. 11 days aging between the measurements resulted in a decrease in average PCE for each NiO_x post-deposition treatment with the same trends in PCE observed 4 days after evaporation. Additionally, PCE of champion cells increased for all condition except UV-O₃. It went from 15.47% to 16.73% for UV-O₃ + A + FAI wash and from 15.18% to 15.46% for the UV-O₃ + A conditions.

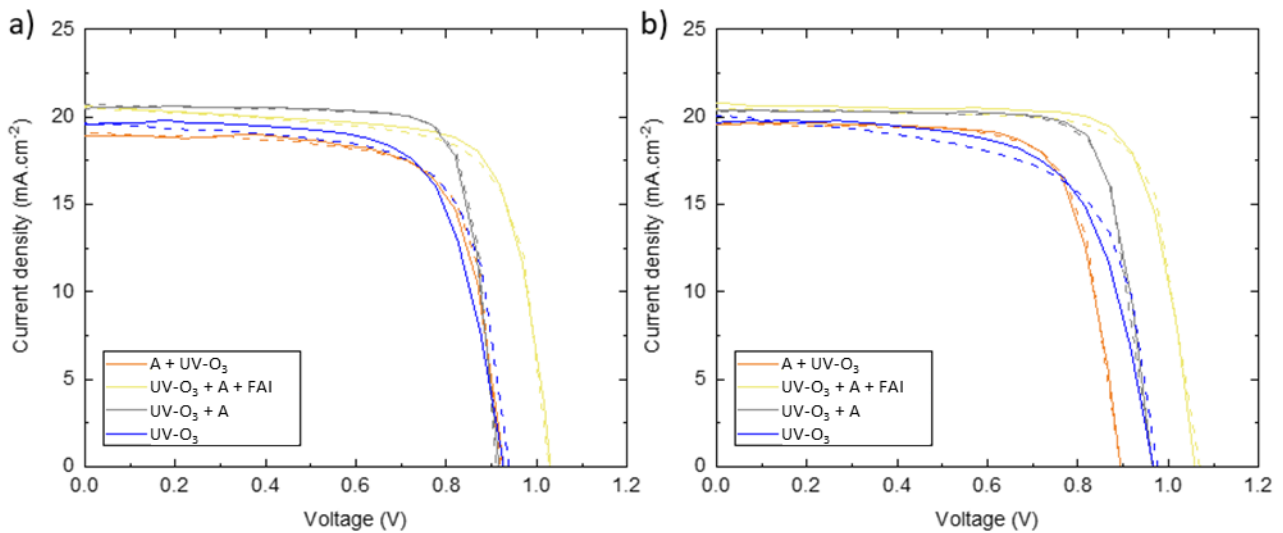


Figure 30 J-V curves recorded for perovskite champion cells using NiO_x after different post-deposition treatment as HTL (a) 4 and (b) 15 days after fabrication. Full and dashed lines respectively indicate forward and reverse current.

The increase in FF for devices using $\text{UV-O}_3 + \text{A} + \text{FAI}$ washed NiO_x might be explained by ion migration. Right after $\text{UV-O}_3 + \text{A} + \text{FAI}$ wash treatment, solid FAI visibly formed at the surface of NiO_x . After perovskite deposition, it is possible that FA^+ and halide species in excess would also remain in $\text{FAI}_{x-1}\text{Br}_x$ rich regions at the interface with NiO_x . This excess in FA^+ and halide ions could exist either in the form of defects or as secondary phases, acting as non-radiative carrier recombination sites which could have resulted in an apparent increase in series resistance during operation¹¹⁸. Additionally, accumulation of ions at the interface of a charge transport layer might have modified the charge transfer dynamics, which could potentially affect R_{sh} ¹¹⁹. On the other hand, lead halide perovskites have been described as self-healing materials prone to ion migration, and one could assume that over time FA^+ and halide ions would either diffuse in the bulk perovskite layer to form point defects, accumulate at interfaces or at grain boundaries or diffuse in other layers in the devices^{120,121}. This process would limit non-radiative recombination pathways and in turn decrease shunt resistance and increase FF in operation.

To conclude, highest FF values were reached with $\text{UV-O}_3 + \text{A}$ NiO_x while using $\text{UV-O}_3 + \text{A} + \text{FAI}$ washed samples resulted in highest V_{oc} . FF and PCE obtained with $\text{A} + \text{UV-O}_3$ condition were only slightly higher for $\text{A} + \text{UV-O}_3$ compared to UV , which would indicate that a short annealing step before UV-O_3 does not exert a strong influence on the PV performance. These results also confirm that FAI treatment on NiO_x is an effective way to improve V_{oc} in solar cells and hence their PCE.

From our results, UV-O₃ + A treatment is also a way to improve PCE of solar cells to a similar extent, by an improvement of *FF*.

To further increase the PCE of NiO_x-based perovskite solar cells, we explore a different method to quench the surface of NiO_x with FAI. Boyd et al. proposed that implementing directly excess cations in the perovskite composition would result in similar outcomes as pre-treating the NiO_x substrate with FAI in terms of PV performances⁸⁷. We thought that it was also a better way to control the amount of excess FAI species implemented in the system, as compared to pre-washing the substrate with a FAI solution.

3.2.4.4. Surface-tuned NiO_x layers as HTL for perovskite solar cells: Effect of surface recovery after UV-Ozone, FAI quenching and FAI excess

Our next study was based on NiO_x samples prepared by combustion process, for which high efficiency devices can be prepared with layers annealed at 250°C. Compared to the 300°C post-annealing step of the sol-gel process, we considered this temperature as more suited for ITO substrates. Preliminary in-house experiments resulted in comparable, if not higher PV performances for solar cells using UV-O₃ treated NiO_x layers prepared by combustion process compared to sol-gel. Here, in addition to the UV-O₃ + A + FAI wash condition we studied the effect of directly implementing excess FAI in the perovskite precursor solution.

Similarly to our previous experiment, we tested 4 types of treatments before perovskite deposition. The A + UV-O₃ condition was removed, as we did not expect more information from it. We kept the UV-O₃ and UV-O₃ + A conditions for reference. We added the FAI excess condition, for which the the NiO_x substrate was subjected to UV-O₃ + A treatment and the perovskite precursor solution contained 8 % of excess FAI. As indicated on **Figure 31**, 4 samples were prepared for each of the following series, for a total of 16 samples:

- UV-Ozone treatment for 15 min in air (UV-O₃).
- UV-Ozone treatment followed by 250°C annealing for 10 min in air (UV-O₃ + A).
- UV-O₃ + A treatment followed by the deposition of a 0.1 M FAI solution in DMF by spin-coating at 3000 rpm for 30 sec. Films were annealed at 100°C for 10 min after treatment (UV-O₃ + A + FAI wash).
- UV-O₃ + A treatment, and the perovskite precursor solution contained 8 % excess of FAI (FAI excess).

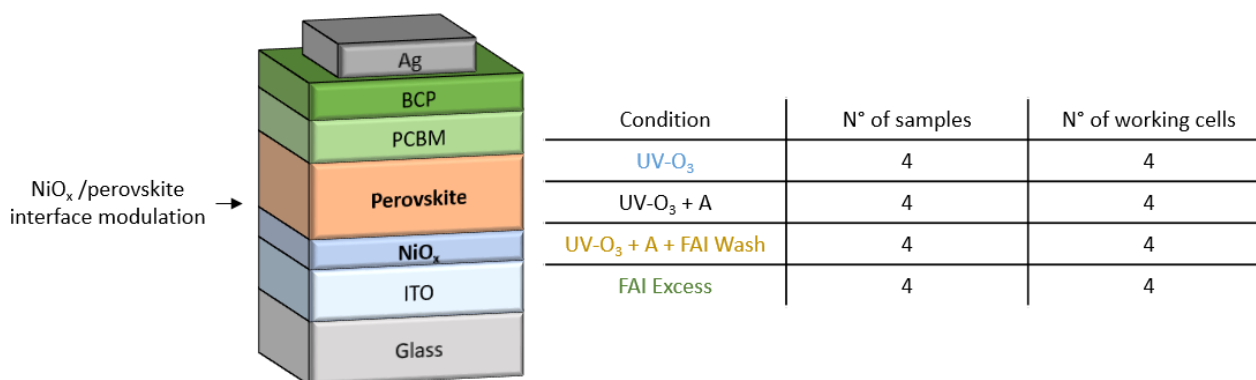


Figure 31 (left) Architecture of solar cells prepared for J-V experiment using different NiO_x post-deposition treatment and/or excess FAI in perovskite precursor solution (right) Number of solar devices prepared and number of working solar cells (i.e. PCE > 1%) per condition.

PV parameters were measured after 3 and 15 days, as reported on **Figure 32** and **Figure 34**, respectively. J-V curves for champion cells are shown on **Figure 33**. 3 days after fabrication, overall lower PV parameters for UV, UV-O₃ + A and UV-O₃ + A + FAI wash series were obtained compared to those obtained with sol-gel NiO_x in 3.2.4.3.

During p-i-n perovskite solar cell fabrication, we could observe variations in PV parameters from devices sharing an identical solar cell architecture, either from batch to batch or from sample to sample. In general, these differences could be attributed to many transient factors of the daily laboratory life, including variations in sample handling, composition of the glove-box atmosphere or potential aging of the perovskite precursor powder in the glove box.

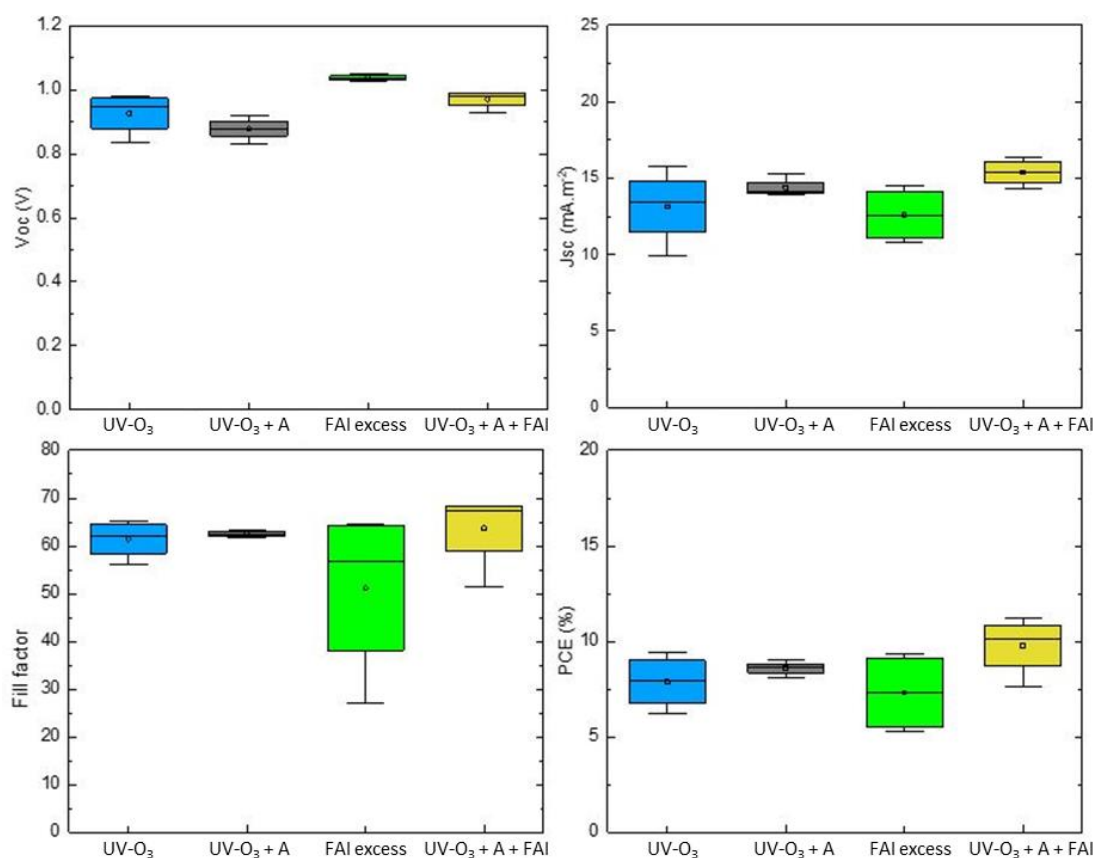


Figure 32 PV parameters recorded 3 days after fabrication for perovskite solar cells using NiO_x after different post-deposition treatment as HTL, or with FAI excess added directly in solution.

Regarding devices based on UV-O₃, UV-O₃ + A and UV-O₃ + A + FAI washed NiO_x, similar trends in J_{sc} , V_{oc} and FF were obtained compared to the ones observed with sol-gel samples. Lower V_{oc} are however reported with UV-O₃ + A samples. Highest PCE and V_{oc} were obtained with FAI excess NiO_x, indicating that this method is more robust than UV-O₃ + A + FAI wash to tune the surface of NiO_x. Interestingly, we do not consistently observe an increase in FF with UV-O₃ + A samples this time.

After 15 days, we observe an increase in average V_{oc} and J_{sc} without change in the trend observed earlier. FF decreased for all conditions except UV-O₃ + A + FAI wash, and less dispersed values are obtained with the UV-O₃ + A condition. On average, aging resulted in slightly lower average PCE values for UV-O₃ and FAI excess conditions, while it slightly increased for UV-O₃ + A and UV-O₃ + A + FAI wash.

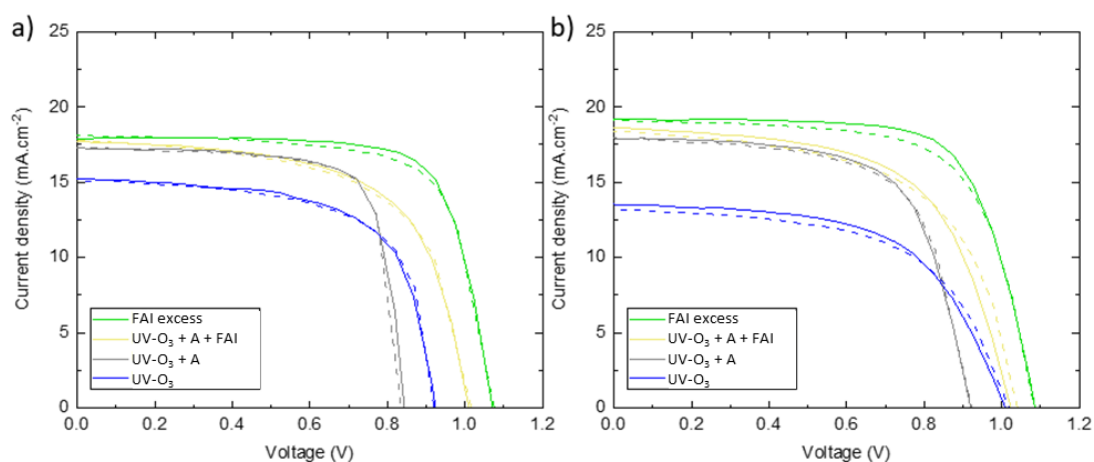


Figure 33 J-V curves recorded for perovskite champion cells using NiO_x after different post-deposition treatment as HTL, or with FAI excess directly added in solution (a) 3 and (b) 14 days after fabrication. Full and dashed lines respectively indicate forward and reverse.

In accordance with previous observations, V_{oc} obtained for UV- O_3 + A + FAI washed samples were higher compared to UV- O_3 + A condition. This time, slightly higher PCE values were also measured with the former devices. We measured higher V_{oc} , J_{sc} , FF and PCE with FAI excess condition compared to UV- O_3 + A + FAI wash. This difference could be due to a too high amount of FAI deposited using the pre-treatment method, or a too localized position of FA^+ and halides ions in excess at the interface with NiO_x . We however expect the FAI concentration in treatment solution or as excess in precursor solution to be determinant for the observed tendency between these two conditions. As such, these results show that both methods are an effective way to improve the performances of NiO_x based p-i-n solar cells.

To conclude, I assessed the change in surface chemistry of NiO_x layers after different post-treatments and measured their WF by UPS and KPFM. As a result, after UV- O_3 treatment I observed a shift in WF and the functionalization of the NiO_x surface by a decrease in relative NiO content and an increase in concentration for nonstoichiometric species such as NiOOH and $\text{N}(\text{OH})_2$. The resulting surface was thus likely more reactive, and from XPS analysis I observed a decrease in Ni/C elemental ratio after UV- O_3 treatment. Whether the original surface chemistry of NiO_x could be recovered after a 10 minutes annealing step at 250°C remains elusive, but the treatment had no influence over the surface Ni/C ratio.

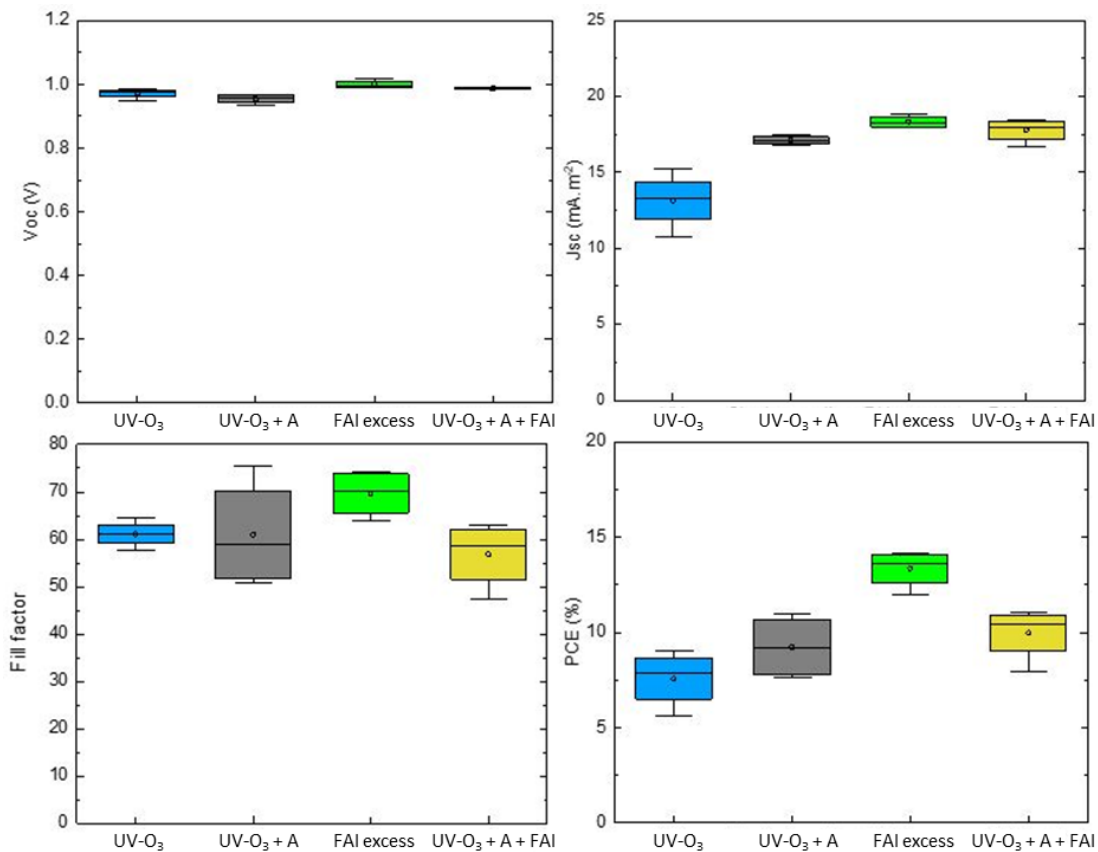


Figure 34 PV parameters recorded 14 days after fabrication for perovskite solar cells using NiO_x after different post-deposition treatment as HTL, or with FAI excess added directly in solution.

When such NiO_x samples were introduced as HTL in single junction p-i-n perovskite solar cells, I observed higher fill factor and PCE for the UV-O₃ + A samples compared to the UV-O₃ treated ones, which could be at the expense of a loss in V_{oc}. For UV-O₃ + A samples, introduction of FAI excess as a pre-treatment for perovskite deposition or directly in the perovskite solution both resulted in further improvement in PCE values mainly driven by an increase in V_{oc} compared to the other conditions. The mechanism behind this enhancement is thought to be the passivation of the Ni³⁺ states of the functionalized NiO_x surface. As shown by the low PV parameters obtained from UV-O₃ treated samples and the relatively higher performances of the UV-O₃ + A samples, the presence of these states at the NiO_x/perovskite interface seems to be detrimental to the overall functioning of the device regardless of the presence of carbon impurities. Indeed, we could show that improvement in PCE after UV-O₃ + A treatment was solely linked to a change in the surface chemistry of the samples. The general reason for lower performances using UV-O₃ treated samples could be often linked to a more pronounced mechanism of V_{oc} loss previously described by Boyd et al., although in the case of UV-O₃ + A samples we note that the gains in PCE are rather derived from an increase in FF. There might

be several reasons for that, including the possibility that increase in V_{oc} resulting in addition of FAI excess is also due to other factors.

After exploring the possibility to tune the surface of NiO_x to improve the performances of perovskite solar cells, in the next section I will focus on SAM based HTL and the possibility to combine them in a NiO_x /SAM HTL bilayer in single junction perovskite devices. Indeed, such an architecture could be beneficial by combining the benefits of a SAM/perovskite interface while improving the contact between the CI(G)S and perovskite subcell with NiO_x .

3.3. Self-assembled monolayer of small organic molecules as HTL in PSCs

In this section, I focus on the implementation of 2PACz and MeO-2PACz as SAM HTL for perovskite solar cells. High efficiency devices were reported in literature for these two small carbazole-based phosphonic acid terminated molecules⁴¹. I also aim to compare their performances in device compared to NiO_x layers deposited at temperature $<200^\circ\text{C}$ by ALD. I first prepare and measure single junction devices using either 2PACz, MeO-2PACz to assess their quality as HTL. Then, I compare the morphological and structural properties obtained from SEM imaging and XRD patterns of perovskite layers grown on either Glass/ITO/ NiO_x or glass/ITO/MeO-2PACz. In the final subsection, I explore the use of a bilayer HTL for single junction devices, and in particular assess the relevance of NiO_x post-treatment when a SAM HTL is deposited on top of it.

3.3.1. SAMs HTL in devices

As a first step, we want to estimate the effect of replacing NiO_x as HTL in perovskite solar cells standalone with either 2PACz or MeO-2PACz. Another control parameter, that we wanted to explore in this experimental series, was the PbI_2 precursor quality. We hence extended the sample matrix over two sets of samples with PbI_2 from two suppliers, Alfa Aesar and Sigma Aldrich. In both cases, the nominal purity of the PbI_2 was 99.999% and the products were exposed to the glove box atmosphere at the same time, one week before device fabrication.

We used the following device architecture: ITO/**SAM-HTL**/perovskite/PCBM/np-ZnO/Ag using double cation perovskite and corresponding cells were measured 7 days after fabrication. During preliminary experiments of perovskite solar cell fabrication using MeO-2PACz as HTL (not shown here), we noticed that PV performances would evolve in the course of minutes as devices were kept under illumination. This observation motivated us to first measure devices directly after light exposure from the IV setup, and a second time after light soaking for 3 minutes.

As summarized in **Figure 35**, 4 samples for each of the following series were prepared, for a total of 16 solar cells:

- MeO-2PACz as HTL using PbI₂ from Alfa Aesar (A-MeO)
- MeO-2PACz as HTL using PbI₂ from Sigma Aldrich (S-MeO)
- 2PACz as HTL using PbI₂ from Alfa Aesar (A-2PACz)
- 2PACz as HTL using PbI₂ from Sigma Aldrich (S-2PACz)

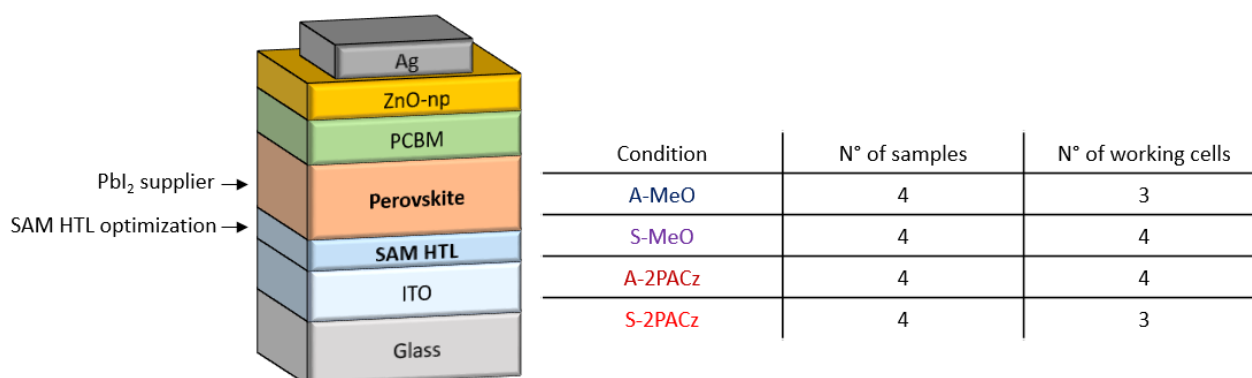


Figure 35 (*left*) Architecture of solar cells prepared for J-V experiment using different types of SAM molecules as HTL and different PbI₂ supplier for perovskite precursor solution (*right*) Number of solar devices prepared and number of working solar cells (i.e. PCE > 1%) per condition.

After device preparation, I witnessed several occurrences of a combination of very low V_{oc} and FF values obtained from certain devices during IV measurements. As a result, PCE values below 1% were obtained, and PV parameters for these devices are not reported here.

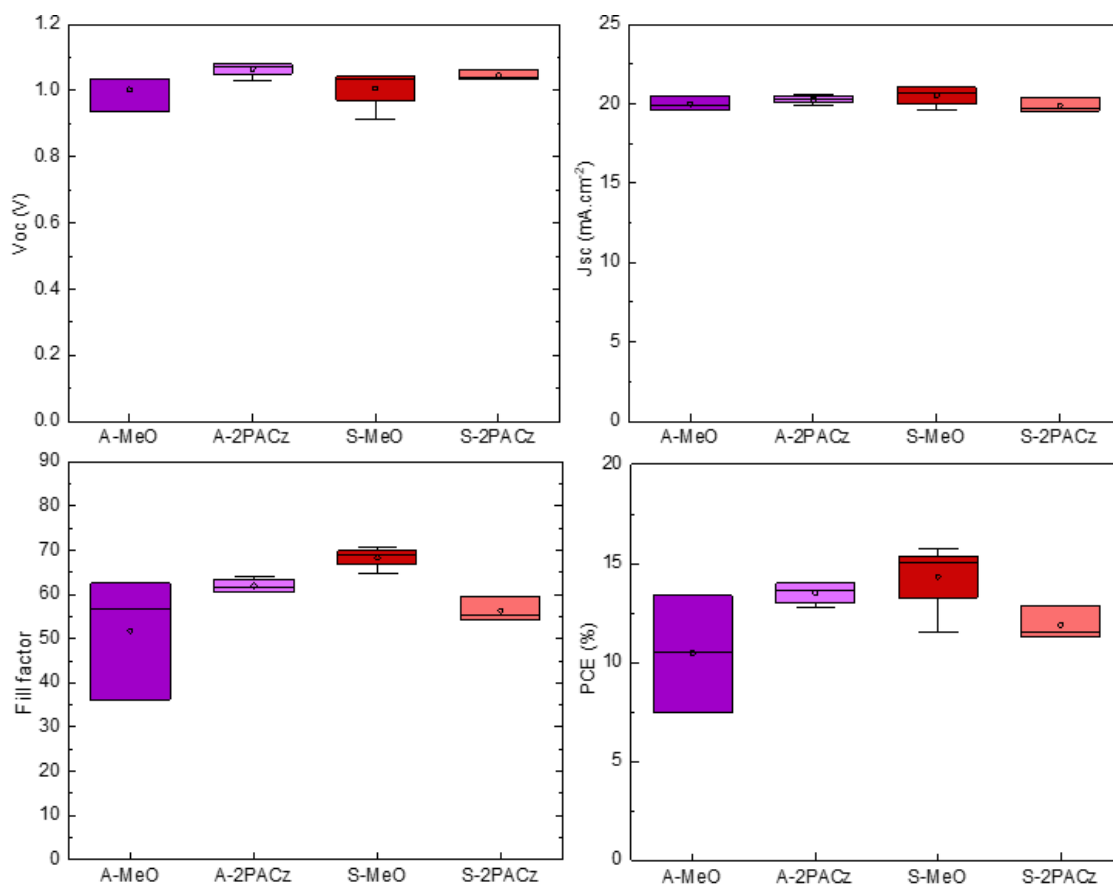


Figure 36 PV parameters recorded before light soaking for perovskite solar cells using 2PACz or MeO-2PACz as HTL and PbI₂ from different suppliers.

PV parameters for perovskite solar cells are reported in **Figure 36** and **Figure 37**, respectively before and after 3 min light soaking. On average, higher and more reproducible V_{oc} were reported for 2PACz based solar cells before light soaking compared to MeO-2PACz based solar cells. Nonetheless, J-V curves shown for champion cells of each condition. **Figure 38** shows that a more stable current response is obtained after light soaking. The J_{sc} was in the same range of values for all conditions. We measured a reproducible FF for every condition, expect for an outlier value for A-MeO.

Eventually, trends in the final PCE remained ambiguous. Highest PCE were measured for the S-MeO sample, either before or after light soaking. It is unclear whether or not the HTL or PbI₂ supplier had an impact on solar cell efficiencies. Since J_{sc} was similar for all cells and slightly higher V_{oc} values with lesser spread were measured for 2PACz based devices, the most pronounced discrepancies in the measured PCE values arose from broadly distributed FF values.

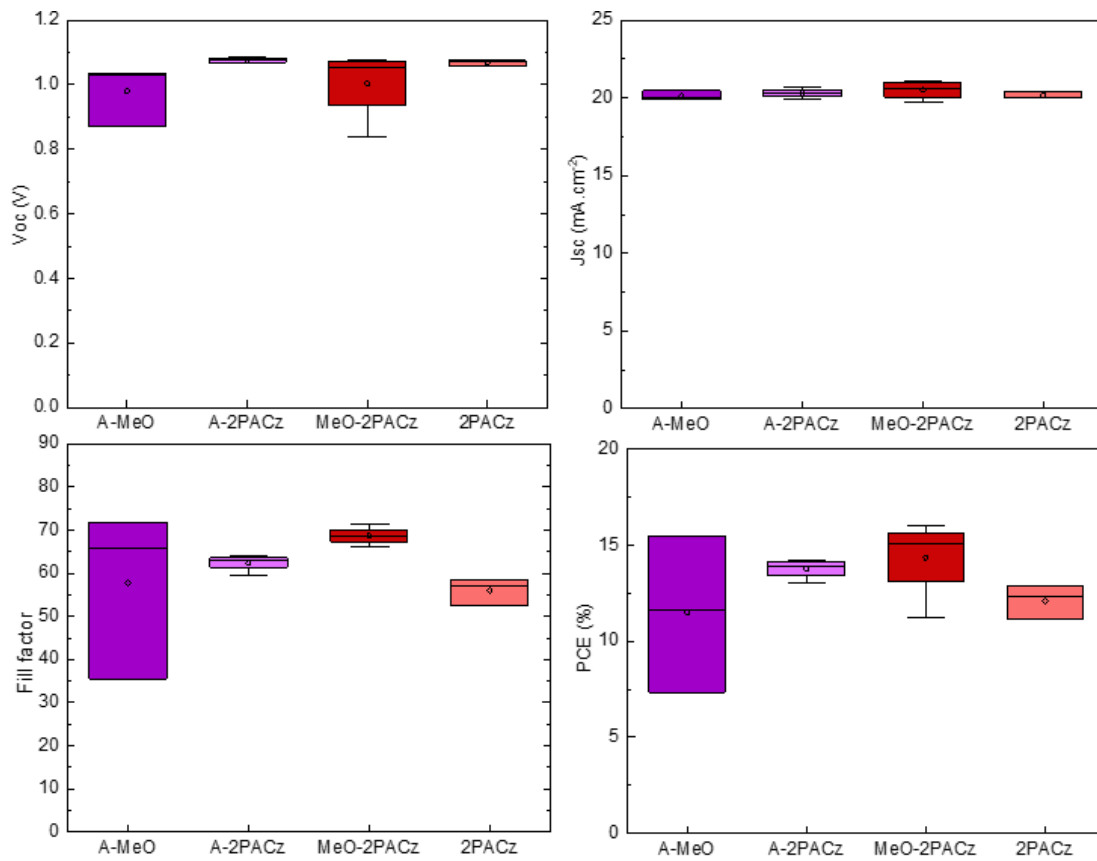


Figure 37 PV parameters recorded after light soaking for perovskite solar cells using 2PACz or MeO-2PACz as HTL and PbI₂ from different suppliers.

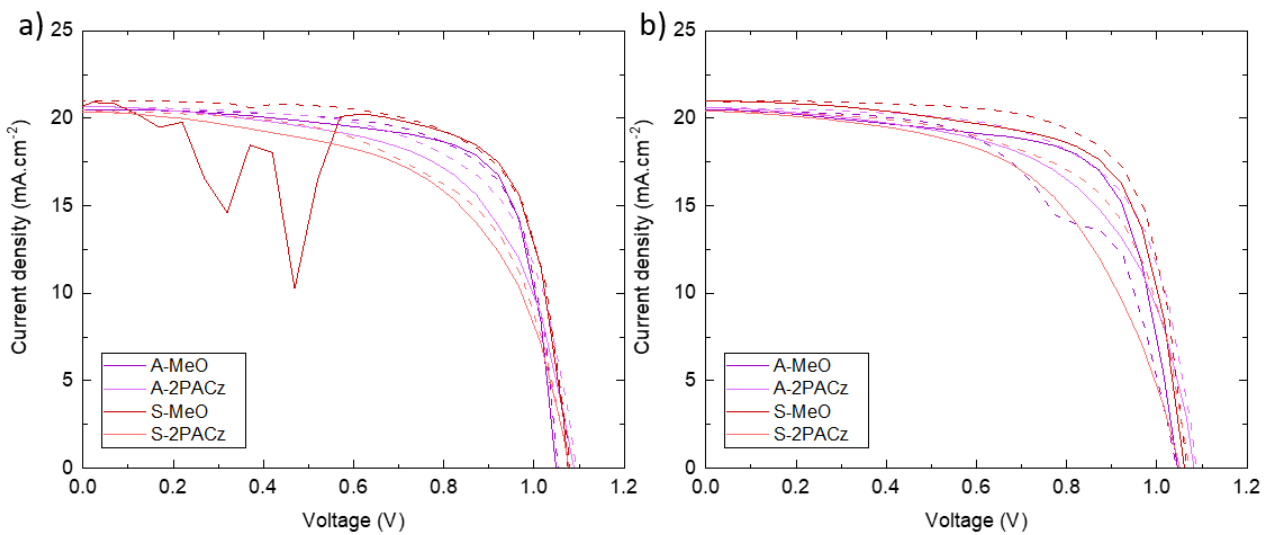


Figure 38 J-V curves recorded for perovskite champion cells using 2PACz or MeO-2PACz as HTL and PbI₂ from different suppliers (a) before and (b) after 5 minutes light soaking. Full and dashed lines respectively indicate forward and reverse current.

As a conclusion, we were able to show that steady PCE can be reached using either MeO-2PACz or 2PACz as a HTL for perovskite solar cells. So far we could not discern any statistically significant difference in PCE between MeO-2PACz and 2PACz. At a first glance, we obtained higher V_{oc} values with 2PACz while using MeO-2PACz resulted in higher FF values. Additionally, we did not observe sensible differences in IV measurements before and after light soaking. Based on these experimental data, using 2PACz as HTL bears the potential for more reproducible values for devices, especially regarding V_{oc} and FF. This aspect would be beneficial to optimize other parameters for the final solar cell development steps.

Overall, PV parameters measured for 2PACz and MeO-2PACz based solar cells were in the range of the highest efficiencies reached using the surface-treated NiO_x from section 3.2.4, i.e. UV- O_3 + A and UV- O_3 + A + FAI wash conditions, even though a different ETL was used for this experiment. The two approaches hence remain competitive and merit further exploration.

During subsequent attempts at fabricating solar cells based on 2PACz we observed a bad coverage of the layer on either ITO or NiO_x and hence poor device performance. While the problem remained, I constrained myself to the use of MeO-2PACz for the next experimental series, for which the focus was on optimization of other parts of the device stack.

In the next subsection, I explore the morphological and structural properties of perovskite layers grown on NiO_x and MeO-2PACz by SEM imaging and XRD to understand how it grows on different substrates.

3.3.2. Morphological and structural properties of MHP layers deposited on NiO_x or 2PACz

We conducted a morphology study of triple cation perovskite films grown on either UV- O_3 treated NiO_x and MeO-2PACz by recording surface SEM images and XRD patterns. In both cases surface SEM images show a pinhole-free, conformably deposited perovskite layer as shown in **Figure 39**. From six average grain size measurements based on two SEM images per type of HTL, I calculated slightly higher values of 179 ± 9 nm for NiO_x compared to 168 ± 16 nm for MeO-2PACz. The difference in values was within their margin of errors. The standard deviation values given here strictly represent a difference from average to average, and contains no information about the actual distribution in grain size, which we do not have. In conclusion, from our observations growing perovskite on either NiO_x or MeO-2PACz has little influence over the morphology of the resulting film.

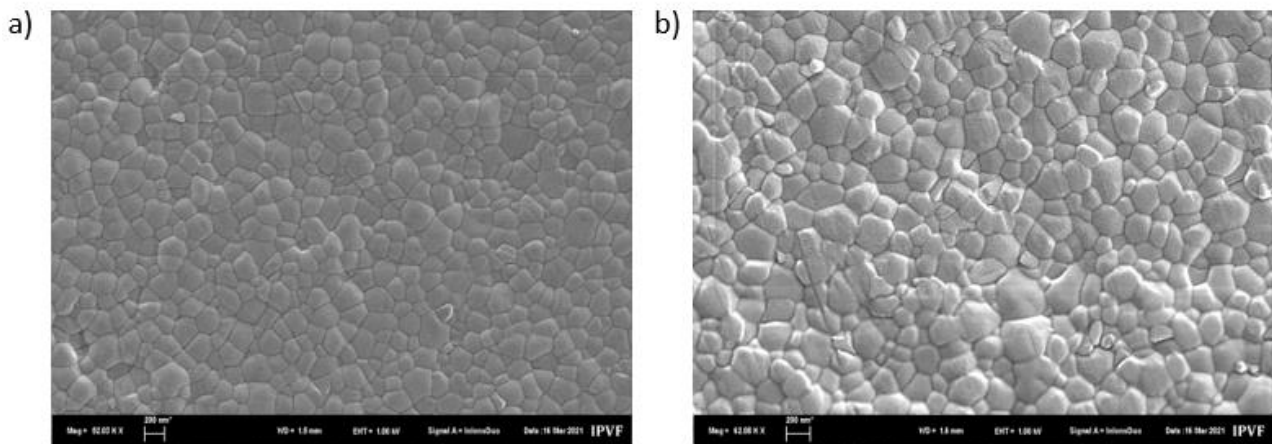


Figure 39 SEM images recorded for triple cation perovskite layers deposited on top of (a) 2PACz or (b) UV-O₃ treated NiO_x. The magnification of the image was not identical for both images:

(a) - 52.03 K X (b) - 62.08 K X.

We also recorded XRD patterns for perovskite grown on both substrates which are shown in **Figure 40**. Two samples were employed per substrate to verify reproducibility of the results. The (110) peak of PbI₂ at $2\theta = 12.6^\circ$ could be detected for some films, but was mostly within the background noise level which indicated almost complete conversion of the precursors to perovskite phase^{122,123}. Signal from the thin NiO_x layer was indiscernible from the ITO substrate signal. Regarding the black phase perovskite contributions, we note that a particular orientation seems to be favored when perovskite films are grown on top of MeO-2PACz compared to NiO_x with higher intensity values for the (001) peak situated at $2\theta = 14.1^\circ$.

To verify this observation, I first evaluated the full width half-maximum (FWHM) of the (001) peaks for films deposited on both HTL, which was consistently lower for films grown on MeO-2PACz with values of 0.125 and 0.130 compared to 0.150 and 0.149 for films grown on NiO_x. As a comparison, the FWHM calculated for the (111) orientation was similar for both substrates. It was of 0.160 and 0.170 for NiO_x, and 0.160 for both perovskite films grown on MeO-2PACz.

We then calculated the relative area of the (001) contribution compared to that of other principal peak orientations for the black perovskite phase: (011), (111), and (012). We find values of 39% and 50% using MeO-2PACz coated ITO as substrate compared to 30% and 32% for NiO_x. Similarly, by calculating the relative areas corresponding to the (002) orientation compared to that of these orientations we found values of 38% and 52% for perovskite layers grown on MeO-2PACz compared to 32% and 37% for films grown on NiO_x. Together, these results indicate that using MeO-2PACz as substrate results in a preferred orientation of the perovskite film grown along the (001) direction.

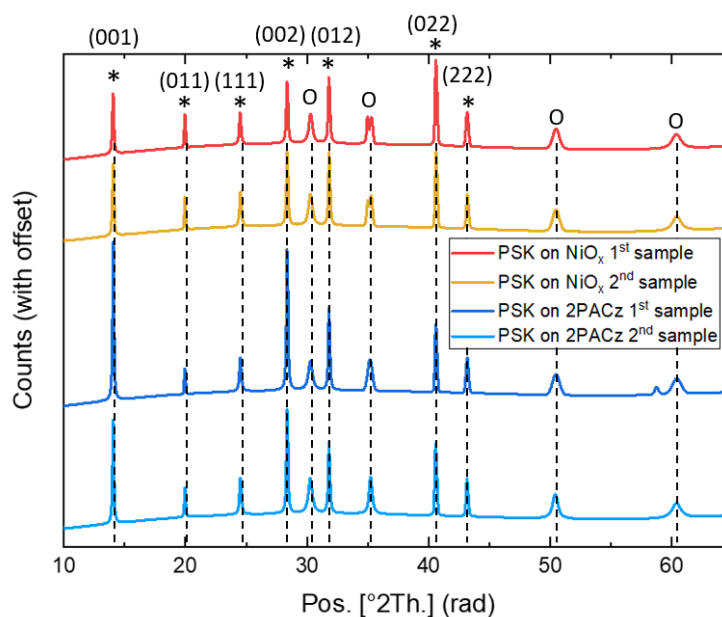


Figure 40 XRD diffractograms for triple cation perovskite layers deposited over NiO_x (red, yellow) or MeO-2PACz (blue) HTL. Two identical samples were synthesized and characterized per condition for experimental repeatability.

*: Contribution from perovskite black phase; O: Contribution from ITO substrate.
Crystalline orientations are annotated for the perovskite black phase.

Crystal anisotropy of the perovskite layer can have an influence over its optoelectronic properties. For MAPI films, the (001) orientation in particular has been linked to improved optoelectronic performance and charge transfer properties¹²⁴. Therefore, and despite the differences in composition between MAPI and our triple cation perovskite, higher PV parameters observed using MeO-2PACz as HTL compared to NiO_x could be partly due to a different orientation of the perovskite crystal on top of either HTL.

To conclude, despite similar morphology of perovskite films grown on top of either MeO-2PACz or NiO_x, the (001) orientation was favored when depositing on top of carbazole-based organic molecules. This observation could denote a contribution to the improvement in PV parameters obtained for devices using these HTLs compared to those using NiO_x.

Even though, another important aspect of two terminal tandem solar cells resides in the design of the tunnel recombination junction. In our target architecture for perovskite/CI(G)S tandem cells, a p-type oxide such as NiO_x may still be relevant at the interface between the CI(G)S top oxide layer and a carbazole based HTM such as 2PACz or MeO-2PACz.

3.4. Interim summary

In the first part of this chapter, we studied different low-temperature routes for HTL deposition in p-i-n perovskite solar cells. We first evaluated the electron blocking properties of NiO_x layers prepared at 100 °C and 160 °C by ALD, to determine an optimal thickness layer between 10 nm and 15 nm depending on the deposition temperature. Thus, for semi-transparent solar cell development in Chapter 4, ALD-NiO_x layers employed for devices were prepared at 160°C for a thickness of 15 nm.

The second part was dedicated to the study of the surface chemical and electronic properties of films prepared by ALD at ZSW and sputtering by IMEC and KIT by the means of XPS, UPS and KPFM, in order to determine the influence of respectively deposition temperature, post-annealing temperature and combined influence of annealing temperature and oxygen flux on these properties. While the physical properties of the deposited layers could not be directly associated with a change in surface chemistry, we could identify a trend of increasing WF as concentration in stoichiometric NiO increased. Nonetheless, overall only slight variations in WF and VBM were observed despite significant modification in stoichiometric NiO concentration. Solar cells were completed at ZSW using ALD-NiO_x layers prepared for different deposition temperature, to determine how these properties would affect the PV performances of devices. Again, a subtle yet consistent trend of higher PCE values was observed with increasing concentration in stoichiometric NiO.

We then explored the possibility to tune the surface chemistry of NiO_x layers prepared by sol-gel and combustion process by combinations of UVO₃, short post-annealing treatments. While it was difficult to relate the effects of these treatments with clear modifications in surface composition from XPS analysis, devices prepared using UVO₃ treated films resulted in poor PV performances while a short annealing step after UVO₃ resulted in higher *FF* and PCE. Highest PCE were reached by the passivation of the NiO_x/perovskite interface using an excess of FAI cations, either by treating NiO_x samples before perovskite deposition or by implementing an excess amount directly in the perovskite solution. Solar cells prepared from these samples stood out by particularly high values in *V_{oc}*, for maximum PCE values > 16 %.

Finally, we evaluated the PV performances of devices using small-molecules 2PACz and MeO-2PACz as HTL, and similar PV parameters were obtained using either material. Maximum PCE > 16 % were obtained. Morphological and structural properties of perovskite layers deposited on either NiO_x or MeO-2PACz were then studied by SEM and XRD. Similar grain sizes between 160 nm and 180 nm were measured using either HTL, but we determined a higher prevalence in (001) orientation for the perovskite layer deposited on top of MeO-2PACz. In literature, this orientation has been linked

Prospective

to better optoelectronic properties of the perovskite layer, at least for MAPI compositions. We thus conclude that in complete devices, a MeO-2PACz/perovskite interface would be preferable to a NiO_x/perovskite interface. However, the presence on an underneath NiO_x layer may or may not remain beneficial in the case of tandem cells, for proper TRJ design or coverage of an electron blocking layer on top of the back electrode.

Chapter 4

Semi-transparent perovskite solar cell for monolithic tandem integration

Summary: In this chapter, we focused on adapting a fabrication process for p-i-n perovskite opaque solar cells to a semi-transparent design, where the window layer is sputtered on top of the perovskite ETL. After unsuccessful preliminary trials relying on a fully organic ETL bilayer, we opted for using a hybrid bilayer composed of PCBM and metal oxide nanoparticles of ZnO or AZO on top to protect the device from harsh sputtering process. In further phases of development, we compared the PV performances of semi-transparent solar cells using PCBM/np-ZnO or C₆₀/ALD-SnO₂ as ETL and AZO or ITO as front TCO layer.

Contents

4.1. Introduction	95
4.1.1. Bathocuproine (BCP).....	95
4.1.2. ZnO.....	96
4.1.3. SnO ₂	96
4.2. Development of a metal oxide based ETL for semi-transparent p-i-n PSCs	97
4.2.1. ETL adaptation to plasma sputtering condition	97
4.2.1. J-V characterization of opaque PSCs using and organic or hybrid bilayer as ETL.....	98
4.2.1.2. J-V characterization of opaque PSCs using PCBM/np-ZnO or PCBM/np-AZO as ETL	102
4.2.1.3. Morphology of the PCBM/np-metal oxide bilayer prepared by spin-coating	107
4.2.1.4. J-V characterization of semi-transparent PSCs using AZO or ITO as front TCO.....	109
4.3. Optimization of ETL and TCO for semi-transparent PSCs	112
4.4. Interim summary	

4.1. Introduction

In this chapter, I focused on the development of a p-i-n semi-transparent perovskite solar cell with the aim to integrate it in monolithic tandem devices. In the final phase of development, we aimed to deposit a high transparency TCO layer as the top electrode of our monolithic solar cell as a way to find a compromise between i) the light transmittance of the top layers to maximize the absorption in both absorber layers and ii) the lateral conductivity to decrease the series resistance of the tandem cell. Indeed, at equivalent thickness transparent conductive oxides present a lower lateral conductivity compared to their opaque metallic counterparts such as Cu, Ag and Au. Increasing the thickness of the layer would result in lower series resistance for the device, at the expense of diminishing the transmittance of the layer in accordance with the Beer-Lambert law. Resorting to extrinsic or intrinsic doping could also increase the conductivity of a metal oxide layer, but depending on the mechanism behind increased conductivity (increase in carrier concentration or mobility) could modify the optical properties of the layer¹²⁵.

However, TCOs are usually deposited by a plasma sputtering process that can degrade the top layers of the perovskite devices, especially for those based on organic materials. In our case, the direct sputtering of a TCO layer on top of a PCBM/BCP ETL for perovskite solar cells resulted in non-functional solar cells or very low device efficiencies.

In the following, I first introduce the different candidates at the ETL side of the perovskite solar cell architecture to form a structure that would withstand the harsh conditions of plasma sputtering. Then, I briefly review our first attempts at designing these structures using an ETL based on PCBM/BCP. I continue by studying the effect of implementing either np-ZnO or np-AZO layers for this purpose on the performances of solar cells. Finally, we optimized our architecture by comparing the PV parameters and EQE spectra for different combinations of ETL and TCO candidates, that is employing respectively PCBM/np-ZnO or C6/SnO₂ and AZO or ITO.

4.1.1. Bathocuproine (BCP)

Figure 41 shows the Lewis structure of bathocuproine. BCP constitutes a large bandgap organic layer. Ideally, it should act as a potential barrier blocking both holes and electrons. However, implementation of BCP in p-i-n devices on top of a fullerene ETL has the effect of improving their J_{sc} , V_{oc} and FF . It has been proposed that rather than constituting a layer on its own that would block carriers, BCP would penetrate the PCBM layer to increase electron mobility as well as passivate MA cations at the perovskite interface¹²⁶.

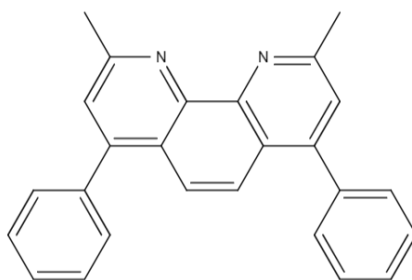


Figure 41 Lewis structure for Bathocuproine

4.1.2. ZnO

Implementing a direct perovskite/ZnO interface in a device would result in a poor thermal stability and induce degradation of the perovskite layer by the formation of PbI_2 ¹²⁷. Nonetheless, performances and stability can be improved by the implementation of an organic interlayer between ZnO and perovskite and PCE > 18 % have been reached by this method¹²⁸. Fullerene based molecules can fulfill the same role, although with so far lower reported PCE values¹²⁷. In p-i-n semi-transparent devices, It has also been demonstrated that ZnO nanoparticles could protect the organic layers underneath during the sputtering process and provide a beneficial band alignment with an AZO window layer¹²⁹.

In this work, we used commercial solutions of ZnO and AZO nanoparticles in IPA.

4.1.3. SnO₂

Due to its wide bandgap, optical transmittance, good carrier mobility and favorable conduction band alignment with the most relevant lead halide perovskites such as MAPbI_3 or the double cation mixed halide composition used in this work, SnO_2 is a good candidate for ETL¹³⁰. Likewise to commonly used TiO_2 , it can act both as an ETL and as a compact hole blocking layer, while exhibiting higher chemical stability and introducing the possibility of low-temperature deposition routes¹³¹. In p-i-n configuration, it can be deposited by ALD to form a bilayer ETLs with an organic fullerene material which can passivate defects at the perovskite surface^{127,132}. In semi-transparent devices, the fullerene layer would protect the perovskite layer from oxidizing agents during ALD, and SnO_2 would act as a protective buffer layer during TCO sputtering deposition.

4.2. Development of a metal oxide based ETL for semi-transparent p-i-n PSCs

4.2.1. ETL adaptation to plasma sputtering condition^{vi}

During preliminary attempts to develop a p-i-n solar cell architecture that could adopt plasma sputtering for TCO deposition, we restricted ourselves to tune the deposition parameters of the ETL and TCO layers on the basis of our in-house device architecture including a PCBM/BCP bilayer as ETL. Principally, we tuned the spin coating speed during PCBM and/or BCP deposition to increase the thickness of the layers. We then either sputtered ITO or IZO on top using a soft process for TCO deposition, and completed the cell by Ag evaporation. After J-V measurements, solar cells prepared by this method exhibited very low V_{oc} , Fill factor and PCE values which indicated shunt pathways, probably coming from either a damaged ETL or absorber layer from the sputtering process. Devices prepared using IZO as TCO, in particular, resulted systematically in dysfunctional solar cells (PCE < 1%).

In general, another factor that affected p-i-n solar cell development was a low reproducibility of solar cell measurements from batch to batch, and even in most cases from sample to sample. Several potential causes could be identified, such as incomplete coverage of layers during solar cell fabrication (pinholes) that would result in shunt pathways or issues related to the perovskite/PCBM interface. Coverage of the HTL and perovskite layers deposited by spin coating could be enhanced by tuning the spinning speed or pre-washing the substrate with a solvent to increase its wettability. Interfacial engineering was also explored by tuning the amount of PbI_2 excess in the perovskite precursor solution, or by the introduction of different organic molecules candidates between the perovskite and the PCBM layers to passivate this interface. Those were generally dissolved in IPA at concentration of 1 mg/mL and deposited by spin coating before PCBM deposition. Either way, these attempts to enhance the reproducibility of our experiments did not succeed in a way that would allow us to significantly optimize devices during p-i-n solar cell development. Indeed, dispersion of results within samples prepared for a single condition resulted in the impossibility to compare in a relevant way series of samples between each other, and the quasi systematic occurrence of non-functioning devices within a series significantly impaired the statistical relevance of these attempts. Nonetheless, in some occasions this problem of reproducibility could be overcome, such as for the series of samples presented in **Chapter 3**. The reasons for these succinct changes in pattern were not fully resolved, and to our knowledge not linked to a particular solar cell architecture or sample handling.

^{vi} TCO sputtering was realized by Cecilia Tel.

In a second phase of development, and despite the difficulties encountered, the adoption of ZnO or AZO nanoparticles as an element of ETL allowed us to manufacture functional semi-transparent p-i-n solar cells. Obviously, a metal oxide layer exhibited a better robustness towards plasma sputtering than its organic counterpart. In a first attempt to include zinc oxide as part of our solar cell architecture, we compared the PV parameters of opaque solar cells prepared using either PCBM/BCP, ZnO nanoparticles, PCBM/np-ZnO or PCBM/np-AZO as ETL. Problems in reproducibility for this first experiment led us to focus on the comparison between opaque solar cells using either PCBM/np-ZnO and PCBM/np-AZO as ETL. Finally, we prepared semi-transparent cells on the basis of a metal oxide layer as part of our ETL.

4.2.1.1. J-V characterization of opaque PSCs using an organic or hybrid bilayer as ETL^{vii}

Herein we draw the conclusion over a preliminary experiment to compare the PV parameters of solar cells prepared using metal oxide and organic based ETLs. The objective of this experiment is first to determine if we can obtain reasonable performances for opaque cells implementing ZnO or AZO in their architecture, as compared to solar cells using PCBM/BCP as their ETL. To this goal, and as shown on **Figure 42**, 4 samples of each of the following conditions were prepared for a total of 16 samples:

- PCBM/BCP as ETL
- Bare np-ZnO as ETL
- PCBM/np-ZnO as ETL
- PCBM/np-AZO as ETL

The solar stack consists of a ITO/MeO-2PACz/perovskite/ETL/Ag architecture, as we did not implement the NiO_x/MeO-2PACz bilayer HTL at the time of the experiment. Commercially available solutions of the metal oxides were deposited twice by spin coating for each device, to ensure an adequate coverage of the layer. The deposition process was detailed in **2.1.2**. All cells prepared using PCBM/np-AZO as ETL operated properly, while half of the cells using PCBM/BCP and np-ZnO and three cells using PCBM/np-ZnO did not exhibit any PV functionality.

^{vii} Solar cells were prepared and measured by Nitin Malik.

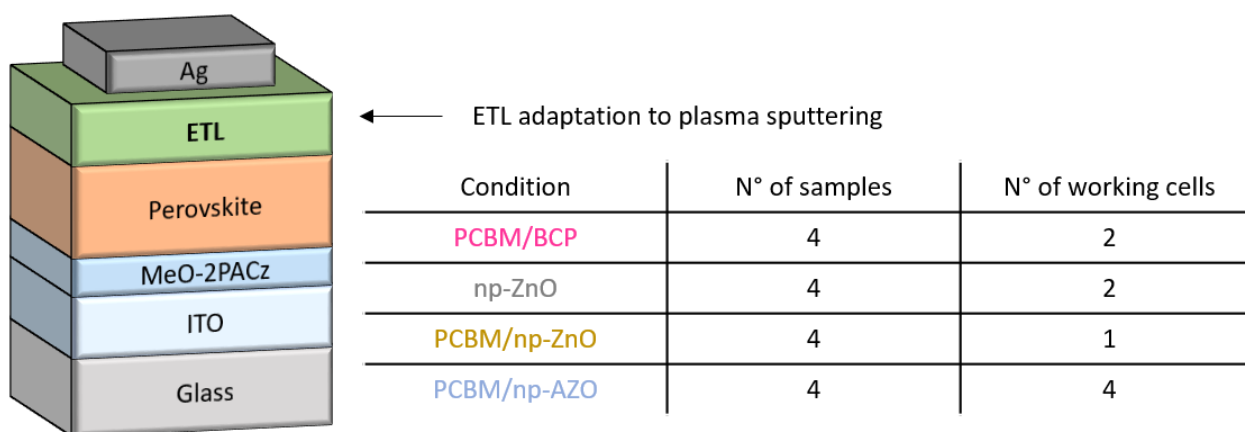


Figure 42 (*left*) Architecture of opaque solar cells prepared for J-V experiment using different types of ETL (*right*) Number of solar devices prepared and number of working solar cells (i.e. $PCE > 1\%$) per condition.

Figure 43 shows the PV parameters recorded for all solar cells that operated properly. PCE of 8.5 % and 13.5 % were obtained for the standard PCBM/BCP based devices, while substituting BCP for np-AZO resulted in a range of values between 11.7 % and 16.3 %. On average, 11.0 % and 14.3 % PCE were obtained for the PCBM/BCP and PCBM/np-AZO conditions, respectively. These results show that np-AZO could effectively replace BCP as a buffer layer between PCBM and the Ag electrode, without any loss in performances. Curiously, a PCE of 14.4 % was reached for the only working device using PCBM/np-ZnO as ETL. This result was similar to the average over the PCBM/np-AZO serie, in contrast to the small number of working devices which suggested an intrinsic problem related to the architecture. Lower PCE values of 3.4 % and 4.6 % were obtained using np-ZnO, illustrating the inherent problem related to the perovskite/ZnO interface and the relevance to retain a PCBM interlayer in the architecture¹²⁷. Taking a closer look at the other PV parameters, more reproducible V_{oc} values between 1.042 V and 1.064 V were measured with PCBM/np-AZO compared to 0.917 V and 1.037 V for the two PCBM/BCP devices, despite the higher number of working solar cells using PCBM/np-AZO. V_{oc} reached 1.025 V for the only functional PCBM/np-ZnO device. Replacing BCP by either ZnO or AZO therefore resulted in a systematic increase in PCE for the working devices, although we refrain from drawing a definitive conclusion at this point based on such a low number of reference devices.

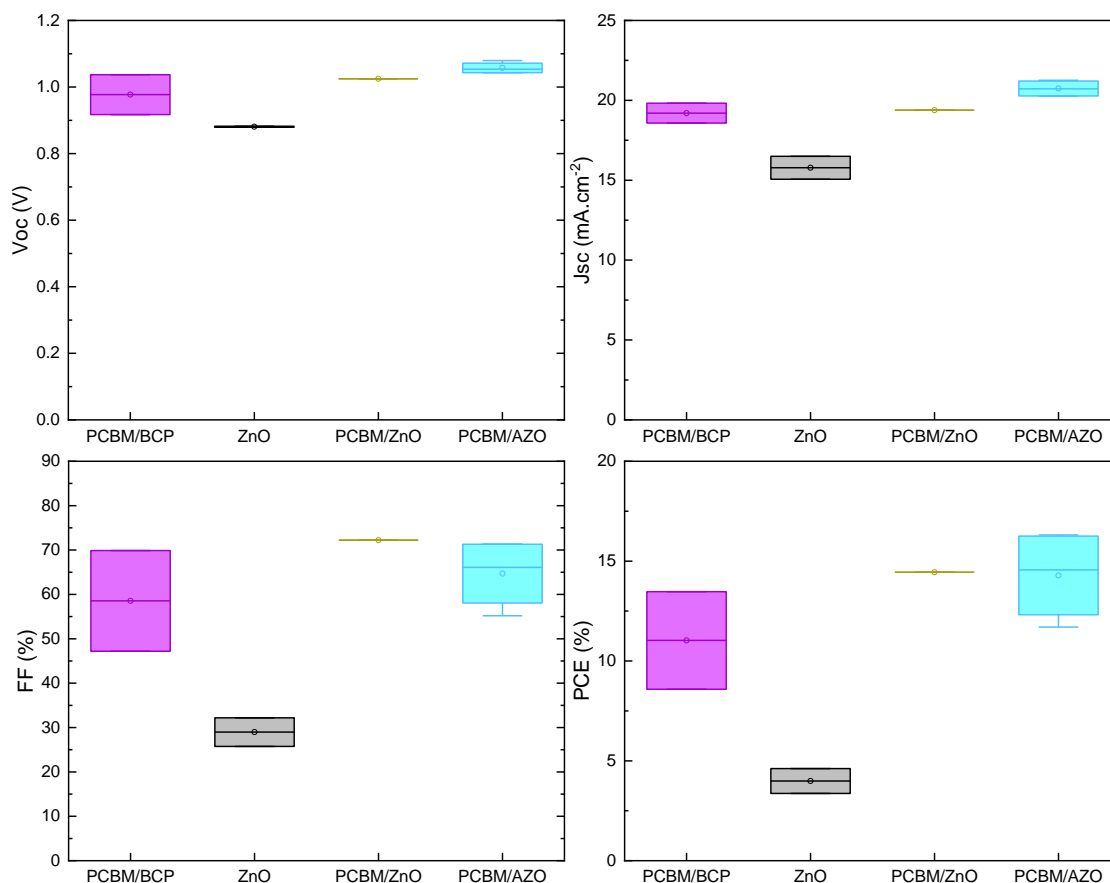


Figure 43 PV parameters recorded for opaque perovskite solar cells using either PCBM/BCP, np-ZnO, PCBM/np-ZnO or PCBM/np-AZO as ETL.

Higher J_{sc} were also reached with PCBM/np-AZO compared to PCBM/BCP, with values ranging between 20.27 mA.cm⁻² and 21.16 mA.cm⁻² for the former and between 18.58 mA.cm⁻² and 19.83 mA.cm⁻² for the latter.

FF was on average higher for the devices using PCBM/np-AZO compared to devices using PCBM/BCP with values of respectively 64.7 % and 58.5 %, and individual values were less dispersed between 55.2 % and 71.4 % for the former and 47.2 % and 69.9 % for the latter.

For these two last parameters, the single PCBM/np-ZnO cell exhibited slightly lower J_{sc} of 19.39 mA.cm⁻² and slightly higher FF of 72.2 % compared to the PCBM/np-AZO cells. These similarities suggest that either metal oxide layer could equally replace BCP in opaque devices with a slight increase in PV performances.

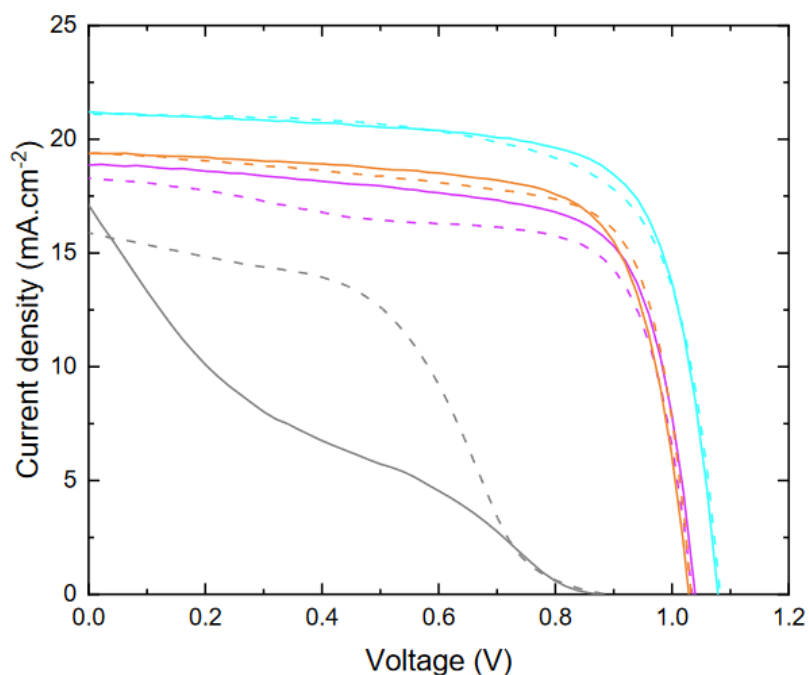


Figure 44 J-V curves recorded for perovskite champion cells using PCBM/BCP, np-ZnO, PCBM/np-ZnO and PCBM/np-AZO as ETL. Full and dashed lines respectively indicate forward and reverse current.

In all cases, lowest parameters were obtained using bare np-ZnO as ETL. For the two working devices we determine a V_{oc} of 0.882 V and 0.879 V as well as a J_{sc} of 15.06 mA.cm⁻² and 16.50 mA.cm⁻², respectively. FF were between 25.8 % and 32.2 %.

To conclude, we showed that either np-AZO or np-ZnO could effectively replace the BCP buffer layer on top of PCBM before Ag evaporation without loss in performances. In fact, for all PV parameters higher average values were reached by using np-AZO as a buffer layer instead of BCP. Individual values were systematically higher in the case of V_{oc} and J_{sc} . Those results should however be interpreted with caution, as only two cells were working using the reference PCBM/BCP ETL.

At this stage of the study, it was still unclear whether the number of working solar cells was linked to the choice in ETL or not. PV parameters similar to that of devices from the PCBM/np-AZO series were reached for the single PCBM/np-ZnO device. However, an improper coverage of the metal oxide buffer layer could be sufficient to introduce shunts or lead to device failure. It would be also plausible for this coverage to depend upon the nature of the deposited nanoparticle layer. Then, the number of working devices could be linked to the architecture, and using np-ZnO instead of np-AZO would result in a higher probability of fatal shunts in devices. On the other hand, if we observe from future experiments that the number of nonfunctional devices is on average similar using either PCBM/np-ZnO or PCBM/AZO as ETL, then we must conclude that for the particular experiment

described in this section, the difference in the number of working cells between series had a different cause. In this case, the difference in working cells between the PCBM/BCP and the PCBM/np-AZO might also be explained by this other cause, instead of a difference in choice in ETL.

Especially low PV parameters were obtained by simply depositing np-ZnO on top of the perovskite layer. This method was therefore not further explored during the rest of the study.

From this batch, similar performances were obtained from functional devices using either PCBM/np-ZnO or PCBM/np-AZO as ETL. In a further phase of development, we wanted to discriminate these two candidates by criteria of average PV parameters and shelf-life stability over a wider number of solar cells.

4.2.1.2. J-V characterization of opaque PSCs using PCBM/np-ZnO or PCBM/np-AZO as ETL

We further optimized our architecture by the J-V characterization of a wider number of solar cells prepared using either PCBM/np-ZnO or PCBM/np-AZO as ETL. As a second parameter, we wanted to evaluate if it was necessary to deposit the metal oxide solution by spin coating once or twice on top of PCBM for adequate coverage.

In the course of several weeks, we prepared three rows of 16 cells, each including 4 samples of the following conditions:

- PCBM/np-AZO (1 spin) as ETL (AZO 1)
- PCBM/np-AZO (2 spin) as ETL (AZO 2)
- PCBM/np-ZnO (1 spin) as ETL (ZnO 1)
- PCBM/np-ZnO (2 spin) as ETL (ZnO 2)

12 samples of each condition were prepared in total as shown in **Figure 45**, although roughly two third of the completed solar cells resulted in PCE values > 1 %.

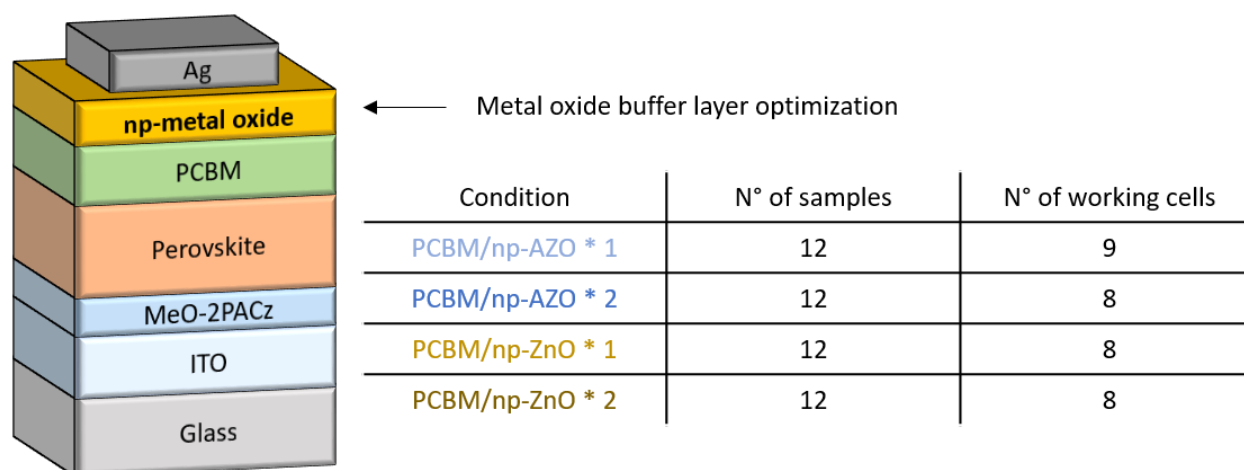


Figure 45 (*left*) Architecture of opaque solar cells prepared for J-V experiment using different types of ETL layers (*right*) Number of solar devices prepared and number of working solar cells (i.e. PCE > 1%) per condition.

PV parameters for functional solar cells recorded after 3 days are presented on **Figure 46**. Average V_{oc} of 1.02 V was calculated for both AZO 1 and AZO 2 samples, which was higher to the values of 0.97 V and 0.98 V found for respectively ZnO 1 and ZnO 2. These values were accompanied with standard deviations of 0.01 V and 0.04 V for AZO 1 and AZO 2 and 0.12 V and 0.09 V for ZnO 1 and ZnO 2.

J_{sc} was also slightly higher on average was also higher for AZO based solar cells, with average values of $18.95 \pm 1.59 \text{ mA.cm}^{-2}$ and $20.29 \pm 0.57 \text{ mA.cm}^{-2}$ for AZO 1 and AZO 2 samples compared to $19.28 \pm 0.78 \text{ mA.cm}^{-2}$ and $19.16 \pm 1.25 \text{ mA.cm}^{-2}$ for ZnO 1 and ZnO 2. Each average value was however within the range of error from each other.

In terms of FF, average values were however significantly higher for ZnO based samples with values of $69.11 \pm 6.47 \%$ for ZnO 1 and 68.86 ± 5.51 for ZnO 2 samples as compared to $55.79 \pm 6.19 \%$ for AZO 1 and $60.36 \pm 7.41 \%$.

As a result, higher PCE were obtained from ZnO samples compared to AZO. $13.43 \pm 1.87 \%$ and $13.02 \pm 2.32 \%$ were calculated for ZnO 1 and ZnO 2, as well as $12.20 \pm 2.34 \%$ and $12.61 \pm 1.96 \%$ for AZO 1 and AZO 2 series. As it was noted for J_{sc} , these values were within the range of error of each other and therefore not considered as significant. However, the fact that it was strictly higher for two different series of samples over two others renders this tendency more robust.

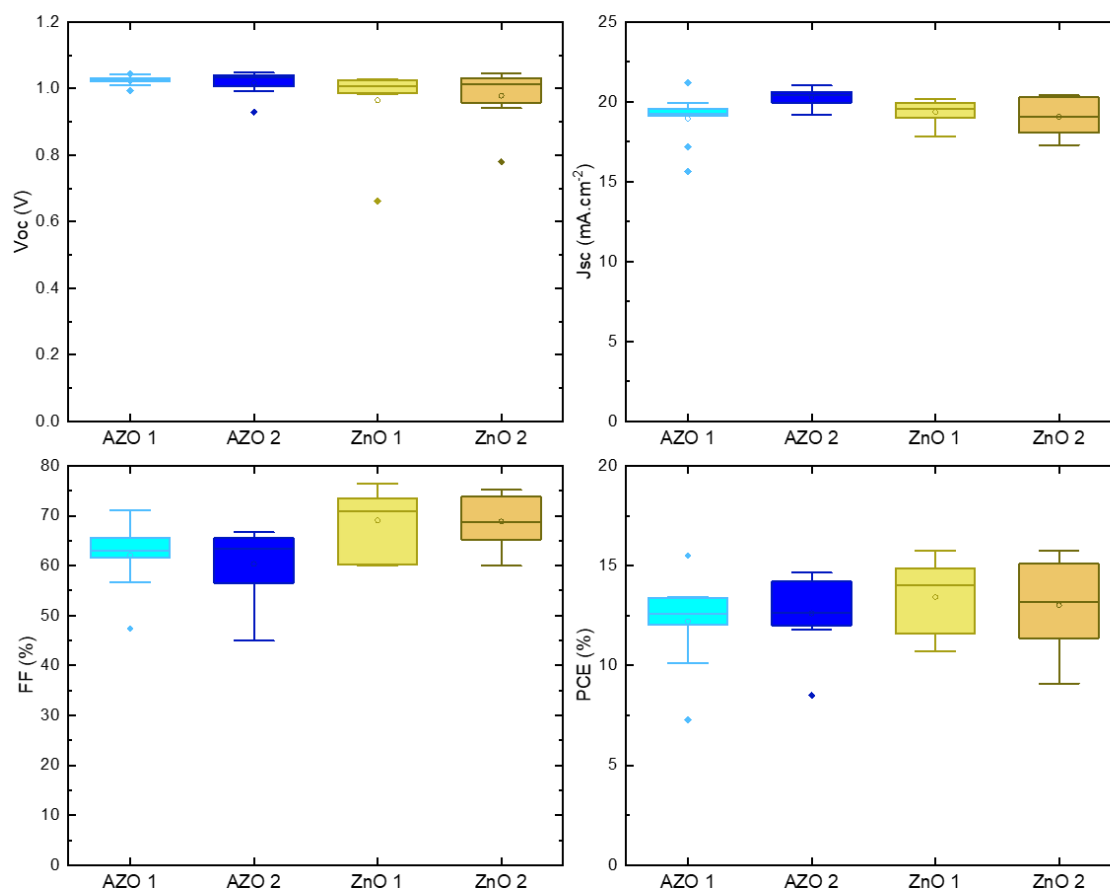


Figure 46 PV parameters recorded 3 days after fabrication for opaque perovskite solar cells using either PCBM/np-ZnO or PBM/np-AZO as ETL. Metal oxide layer was spin coated either one time (AZO 1, ZnO 1) or two times (AZO 2, ZnO 2) on top of the PCBM layer.

Figure 47 shows the evolution of the PV parameters for these solar cells 7 days after fabrication. Fewer devices were functional after storage in vacuum:

- 9 for AZO 1 (-0)
- 7 for AZO 2 (-1)
- 6 for ZnO 1 (- 2)
- 7 for ZnO 2 (- 1)

V_{oc} stayed similar for AZO samples, with an average of 1.01 ± 0.06 V for AZO 1 and 1.02 ± 0.02 V for AZO 2 samples. It however increased in the case of ZnO samples, for average values of 1.03 ± 0.03 V and 1.02 ± 0.05 V.

J_{sc} also increased or stayed similar for ZnO samples while it decreased for AZO. As a result, higher average values of $19.07 \pm 1.48 \text{ mA.cm}^{-2}$ and $20.07 \pm 0.82 \text{ mA.cm}^{-2}$ were found for ZnO 1 and ZnO 2 compared to $17.84 \pm 2.02 \text{ mA.cm}^{-2}$ and $18.17 \pm$ for AZO 1 and AZO 2. This difference in J_{sc} might have solely reflected the supposedly higher conductivity of AZO compared to ZnO.

FF decreased for all series of samples, to $58.29 \pm 12.96 \%$ and $64.69 \pm 8.94 \%$ for ZnO 1 and ZnO 2 compared to $55.79 \pm 6.19 \%$ and $53.50 \pm 6.82 \%$ for AZO 1 and AZO 2.

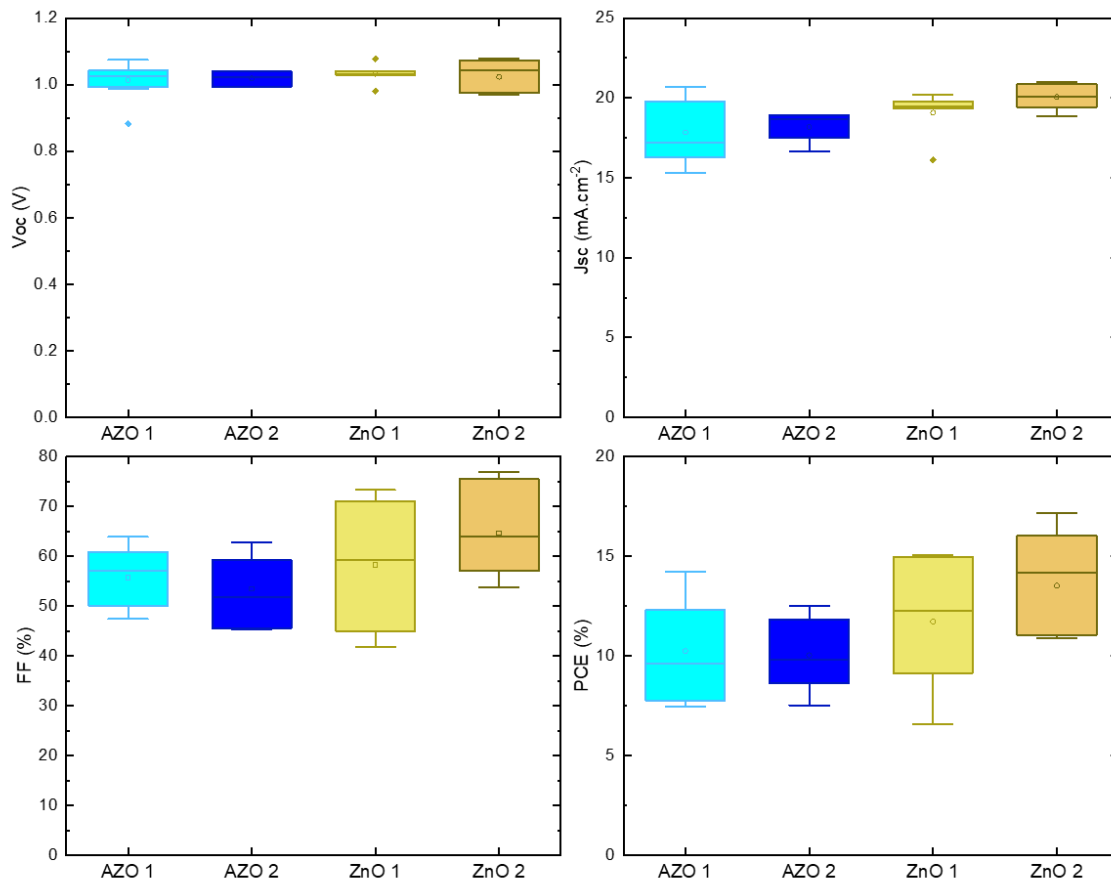


Figure 47 PV parameters recorded 7 days after fabrication for opaque perovskite solar cells using either PCBM/np-AZO or PBM/np-ZnO as ETL. Metal oxide layer was spin coated either one time (AZO 1, ZnO 1) or two times (AZO 2, ZnO 2) on top of the PCBM layer.

As a result, compared to the PV parameters measured after 3 days PCE was on average lower for the ZnO 1 samples at $11.73 \pm 3.33 \%$, stable for the ZnO 2 series at $13.53 \pm 2.56 \%$ and lower for both AZO 1 and AZO 2 series with values of $10.25 \pm 2.55 \%$ and $10.03 \pm 1.76 \%$. It should be noted that only the AZO 1 series of samples kept the same number of functional devices both 3 days and 7

days after fabrication. As a result, for fair comparison between series of samples we should either include the PV parameters from non-working devices in the calculus of the average parameters or exclude the 2 worst performing devices from the AZO 1 series, and single worst performing device from ZnO 2 and AZO 2 series.

Finally, the J-V curve for champion cells from each series is presented on **Figure 48**. We could distinguish clearly the increase in V_{oc} and J_{sc} for the ZnO 2 champion cell after storage, and these parameters decreased in the case of the AZO 2 champion cell under the same conditions. Additionally, we noticed a steeper slope in J_{sc} for the high current regime of the J-V curve for AZO based devices, which indicated a lower shunt resistance for these devices. Thus, we could rationalize the lower FF values obtained in general with these series as a consequence of the formation of shunt recombination pathways in the devices.

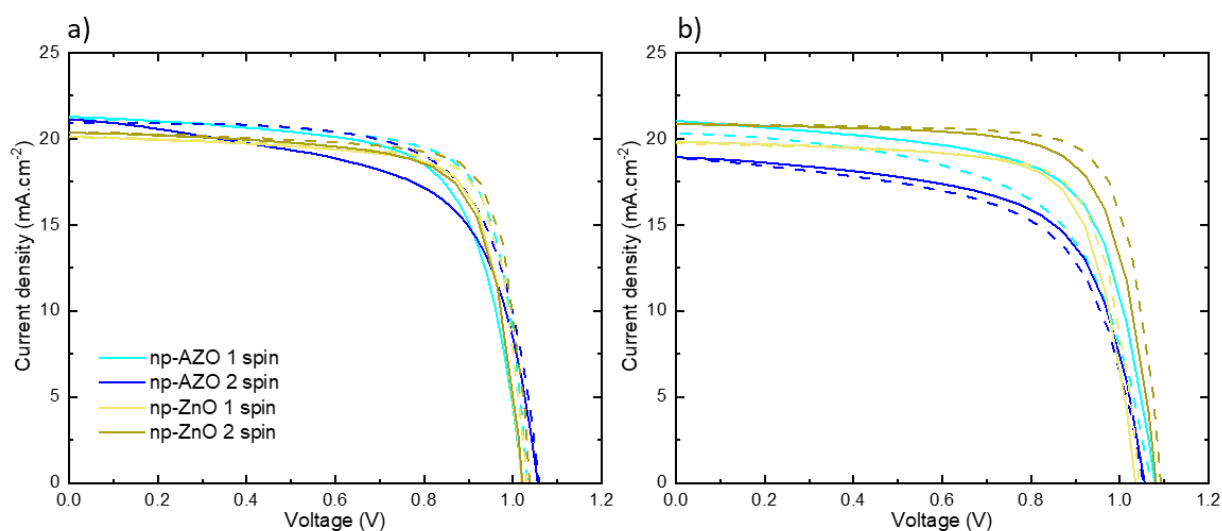


Figure 48 J-V curves recorded for perovskite champion cells using PCBM/np-AZO or PCBM/np-ZnO as ETL, **(a)** 3 days and **(b)** 7 days after fabrication. Full and dashed lines respectively indicate forward and reverse current. Metal oxide layer was spin coated either one time or two times on top of the PCBM layer.

Contrarily to ZnO, it would be possible that AZO did not act as an effective hole blocking layer that could prevent recombination between holes and electrons from the perovskite layer in the top electrode region. Indeed, for both ZnO and AZO it would be reasonable to consider the PCBM/np-Metal Oxide region as two intricated layers rather than a classical bilayer arrangement with a well-defined interface and spatial delimitation between the start and the end of each one. In this case, it would be possible for the np-AZO or np-ZnO to act as a continuous bridge between perovskite and the silver top electrode in some sections of the bilayer. Contrarily to ZnO, AZO is a degenerate n-

type film¹²⁵. For devices using the latter, it would be possible for electrons and holes from the perovskite layer to be collected in the anode region for direct recombination, decreasing the shunt resistance and thus the fill factor of the device. We also noticed a lower stability for these devices as compared to the ones prepared using ZnO as metal oxide buffer layer.

To conclude, we compared the performances of ZnO and AZO as a buffer layer between the PCBM ETL and the Ag electrode in the p-i-n configuration. Satisfactory PV parameters were obtained in general as compared to previous fabrication of p-i-n devices in this work with PCBM and BCP. After 3 days, ZnO-based devices presented higher efficiency as compared to the AZO cells, mainly due to a significantly increased FF and at the expense of a lower V_{oc} and J_{sc} . After 7 days, the gap widened between efficiency of ZnO-based devices and cells using AZO. It occurred from an increase in J_{sc} and V_{oc} now equivalent to that of AZO devices, while FF decreased for all devices.

We could therefore conclude that ZnO devices presented a better stability when stored in vacuum. Spinning the metal oxide twice on top of PCBM might have also improved the stability of devices in the case of ZnO. However, it had little to no effect on performances after 3 days regardless of the type of metal oxide used.

4.2.1.3. Morphology of the PCBM/np-metal oxide bilayer prepared by spin-coating^{viii}

Here we took a closer look at the morphology of the PCBM/np-Metal oxide ETL bilayer on top of perovskite, which could explain the difference in performance and stability between solar cells using np-ZnO and np-AZO as buffer layer between PCBM and the top electrode layer.

Figure 49 presents the surface SEM images for perovskite p-i-n solar cells using either PCBM/np-AZO or PCBM/np-ZnO. In both cases the nanoparticles layer fully covered the surface of the device. At this magnification, it seemed that the layer was mostly composed of particles of nanometer to tens of nanometer size, although in the case of AZO we distinguished elements measuring 100 nm to 200 nm.

^{viii} Samples were prepared by Nitin Malik. SEM images were acquired by Alexandre Blaizot.

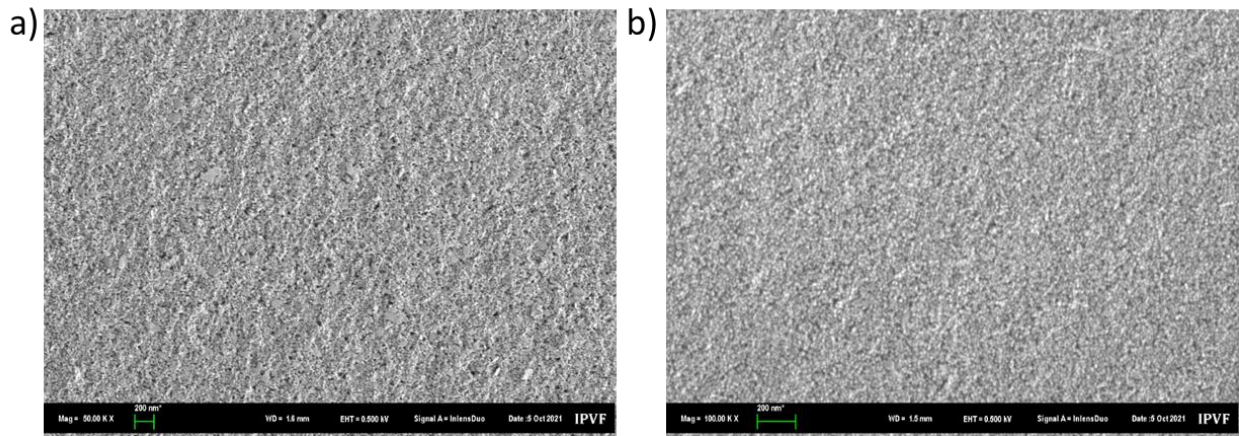


Figure 49 Surface SEM images of perovskite p-i-n solar cells using MeO-2PACz as HTL **(a)** a PCBM/AZO bilayer as ETL and **(b)** a PCBM/ZnO bilayer as ETL. Np-Metal oxide layers were deposited twice by spin coating on top of PCBM.

Figure 50 shows the cross-section SEM images for perovskite solar cells of similar architectures, with the addition of that of a perovskite cell using NiO_x as HTL and PCBM/BCP as ETL bilayer. For the latter, a smooth 50 nm – 80 nm thick layer covered the perovskite surface corresponding to PCBM and BCP. It was difficult to spatially discriminate between the two layers. Similarly, for AZO and ZnO using devices the thickness of the ETL bilayer was respectively between 100 nm and 150 nm and between 70 nm to 90 nm. Instead of a smooth bilayer from organic compounds, for these two samples the PCBM/np-Metal oxide bilayer formed a continuum up to the interface of the perovskite. As a consequence, we assumed that regions of direct contact existed between the nano-particles and the perovskite layer.

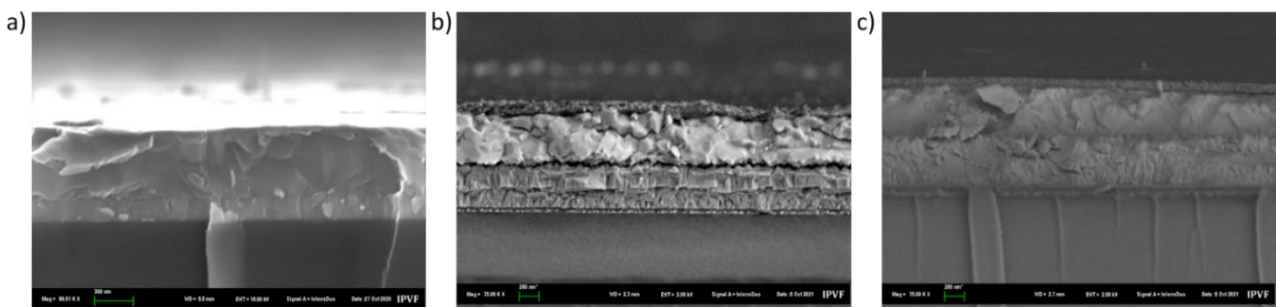


Figure 50 Cross-section SEM image for a p-i-n perovskite solar cell prepared using **(a)** NiO_x as ETL and a PCBM/BCP bilayer as ETL or **(b)** MeO-2PACz anchored to ITO as HTL and a PCBM/np-AZO bilayer as ETL or **(c)** MeO-2PACz anchored to ITO as HTL and a PCBM/np-ZnO bilayer as ETL. Np-Metal oxide layers were deposited twice by spin coating on top of PCBM.

From this analysis, we first conclude that the np-AZO metal oxide layer could contain particles of larger size between 100 nm and 200 nm, in addition to the nanometer - tens of nanometers size particles that composed both np-Metal oxides. Their presence might be due to nanoparticle agglomeration, and they might have been formed in the commercial solution before deposition. Their size is comparable to the thickness of the ETL bilayer, so they might alone serve as bridge for minority carrier recombination even though we didn't observe this kind of arrangement from cross-section images. Regardless, from cross-section SEM images a clear difference in morphology between PCBM/BCP and PCBM/np-Metal oxide was observed. In the latter, no sign of smooth layer was found and the entire layer seemed composed of nanometer – tens of nanometer thick particles. As a result, it is probable that both layers were intricated on top of perovskite, and for AZO based devices this could facilitate bridging and non-radiative recombination at the AZO/Ag interface or within the bilayer itself.

For the future, we therefore decided to use np-ZnO as the buffer layer between PCBM and the silver evaporated or sputtered metal oxide transparent electrode. Additionally, for the sake of simplicity in the future we will restrain ourselves to spinning the metal oxide solution only once on top of PCBM. In the next part of this chapter, we applied these guidelines to fabricate our first semi-transparent perovskite solar cells.

4.2.1.4. J-V characterization of semi-transparent PSCs using AZO or ITO as front TCO^{ix}

In this part, we present the fabrication of our first p-i-n semi-transparent solar cell using PCBM/np-ZnO as ETL and sputtered AZO as front TCO of the device. A C-shape silver mask was evaporated on top of AZO to decrease the series resistance during operation, as depicted on **Figure 51**. The final architecture was Glass/ITO/NiO_x/MeO-2PACz/Perovskite/PCBM/np-ZnO/AZO/Ag. Additionally, a metal mask was used to delimitate an active area of 0.16 cm² during J-V measurements, for both front and rear illumination. The mask was coated with tape to avoid electrical contact with the perovskite top electrode during J-V characterization under front illumination.

^{ix} AZO sputtering deposition was realized by Amelle Rebai

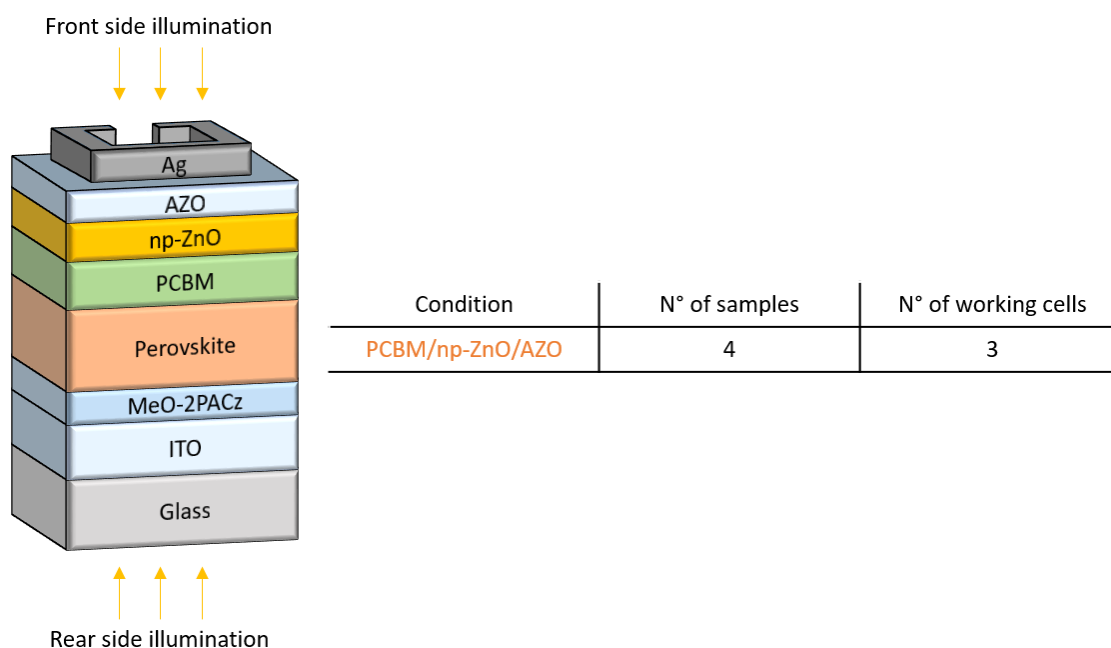


Figure 51 (*left*) Architecture of semi-transparent solar cells prepared for J-V experiment using PCBM/np-ZnO as ETL and sputtered AZO as front TCO (*right*) Number of solar devices prepared and number of working solar cells (i.e. PCE > 1%) per condition.

PV parameters recorded for both front and rear illumination are reported on **Figure 52**. Similar and reproducible V_{oc} values of 1.04 ± 0.01 V and 1.03 ± 0.01 V were measured for both rear and front illumination. As expected, average J_{sc} of 13.62 ± 0.14 mA.cm⁻² was much lower in front illumination compares to 19.35 ± 2.5 mA.cm⁻² in rear illumination. Values were more dispersed for the latter.

Average FF was nonetheless higher in front illumination, at 62.15 ± 3.07 % compared to 57.46 ± 3.62 % in rear illumination. J-V curves for the champion cell illuminated from both rear and front side are plotted in **Figure 53**. After inspection, differences in FF between front and rear illumination principally arose from a difference in R_{sh} , which was in average higher in front illumination. Again, dispersion of FF values was higher in rear illumination.

These parameters resulted in higher average PCE of 11.81 ± 1.73 % in rear illumination compared to 8.89 ± 0.34 % in front illumination.

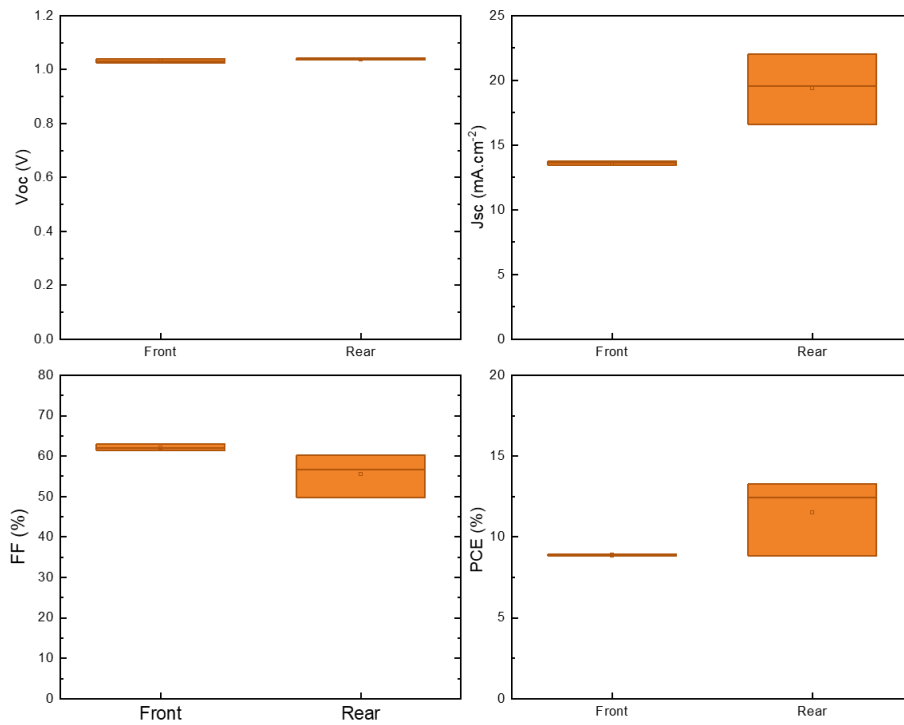


Figure 52 Average PV parameters recorded 7 days after fabrication for semi-transparent perovskite solar cells using PBM/np-ZnO as ETL and sputtered AZO as front TCO. Parameters were extracted for J-V curves under both front and rear illumination.

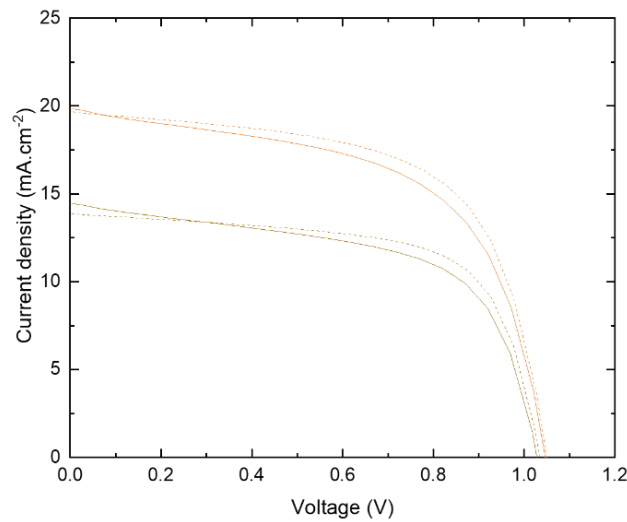


Figure 53 J-V curves recorded under front (brown) and rear (orange) illumination, for perovskite champion cells using PCBM/np-AZO as ETL and sputtered AZO as front TCO. Full and dashed lines respectively indicate forward and reverse current.

To conclude, we successfully prepared semi-transparent perovskite solar cells in p-i-n configuration using PCBM/np-ZnO as ETL bilayer. Compared to previous series of device fabrication, PV performances were comparable under rear illumination. However, significantly lower J_{sc} and thus PCE values were obtained under front illumination, probably due to parasitic absorption. By optimizing the optical parameters of the ETL bilayer and front TCO layer, we may diminish the gap between J_{sc} under rear and front illumination which would be ultimately beneficial in 2T configuration.

In the following study, we optimized our semi-transparent p-i-n architecture by comparing PV performances of complete solar cells using the different ETL and TCO candidates introduced in section 4.2.

4.3. Optimization of ETL and TCO for semi-transparent PSCs^x

In this section, I develop on the J-V and EQE characterization of semi-transparent perovskite solar cells integrating different ETL or TCO candidates in their architecture. Cells were illuminated under both rear and front illumination. Preliminary tests of ALD-SnO₂ deposition on top of PCBM resulted in particularly low V_{oc} and FF values in opaque solar cells, yielding PCE values < 1%. This combination of ETL was therefore not included in this study. We rather prepared devices with PCBM/ZnO-*np* or C₆₀/ALD-SnO₂ as ETL, and we extended sample matrix over the use of either AZO and ITO as TCO. As shown on **Figure 54**, 16 samples were prepared in total, that is 4 of each of the following conditions:

- PCBM/*np*-ZnO as ETL and sputtered AZO as TCO (PCBM – AZO)
- C₆₀/ALD-SnO₂ as ETL and sputtered AZO as TCO (C₆₀ – AZO)
- PCBM/*np*-ZnO as ETL and sputtered ITO as TCO (PCBM – ITO)
- C₆₀/ALD-SnO₂ as ETL and sputtered ITO as TCO (C₆₀ – ITO)

^x ALD NiO_x and SnO₂ layers were deposited by Damien Coutancier. C₆₀ layers were deposited by Van-Son Nguyen. AZO and ITO sputtering deposition was realized by Valérie Daniau. Other than that, solar cells were prepared by Marion Provost.

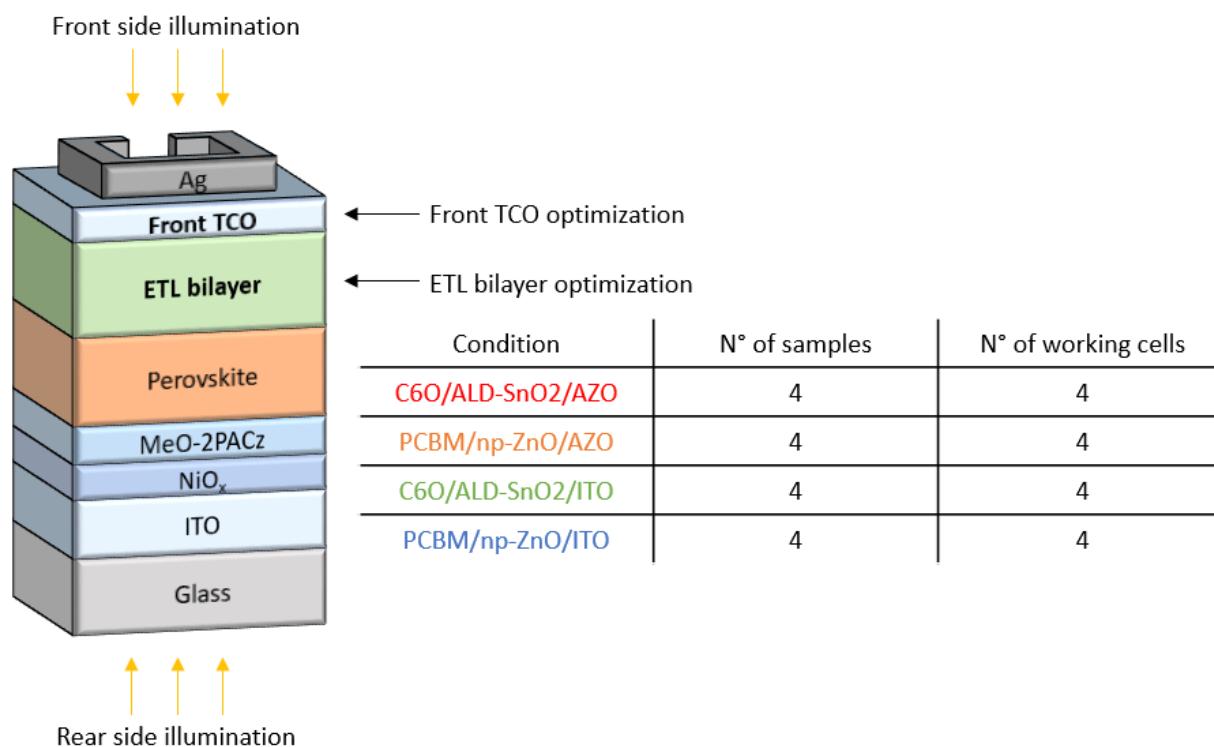


Figure 54 (*left*) Architecture of semi-transparent solar cells prepared for J-V experiment using different types of ETL and TCO layers (*right*) Number of solar devices prepared and number of working solar cells (i.e. PCE > 1%) per condition.

We fabricated solar cells based on the following architecture: ITO/NiO_x/MeO-2PACz/perovskite/ETL/TCO/Ag. Silver was evaporated on top of the sputtered TCO using a C-shape mask pattern to optimize the lateral conductivity of the device. Additionally, a metal mask was used to delimitate an active area of 0.16 cm² during J-V measurements, for both front and rear illumination. The mask was coated with tape to avoid electrical contact with the perovskite top electrode during J-V characterization under front illumination. EQE spectra were also recorded for all cells under both rear and front illumination, in order to derive more accurate values of J_{sc} and evaluate the influence of the optical characteristics of the ETL/TCO combination on the conversion efficiency over the range of absorption of the perovskite layer.

PV parameters for these devices under rear illumination are presented on **Figure 55**. V_{oc} and FF values were directly derived from J-V measurements, whereas presented J_{sc} values were gathered from integration of the EQE spectra for each sample. As a result, PCE values recorded on **Figure 55** were also corrected with J_{sc} calculated from EQE. Measurements of solar cells under rear illumination do not take into account the optical parameters of front TCO and ETL, and therefore are a good basis to compare their performances purely at the electronic level.

Prospective

Average V_{oc} recorded were similar and reproducible for PCBM – ITO, C₆₀ – ITO and C₆₀ – AZO conditions with respective values of 1056 ± 17 mV, 1060 ± 6 mV and 1064 ± 7 mV. Values were lower and more dispersed with an average at 994 ± 63 mV for the PCBM – AZO condition.

Average corrected J_{sc} values were very similar for C₆₀ – ITO (19.14 ± 0.15 mA.cm⁻²) and C₆₀ – AZO (19.12 ± 0.07 mA.cm⁻²) conditions. Slightly more dispersed and lower values were calculated for PCBM – AZO condition (18.78 ± 0.34 mA.cm⁻²), while a clearly lower average of 16.53 ± 0.21 mA.cm⁻² was reached for the PCBM – ITO condition. Realistically, lower J_{sc} values for the PCBM-ITO condition compared to PCBM - AZO would be related to the ZnO/ITO interface.

Fill factor values were also similar between C₆₀ based solar cells, although more dispersed values were obtained using ITO compared to AZO with average values of respectively 67.65 ± 2.71 % and 68.49 ± 0.57 %. Average values were lower with a larger margin of error for PCBM based solar cells, at 62.96 ± 4.30 % using ITO as front TCO and 53.14 ± 11.19 % using AZO. Maximum FF values were nonetheless similar between PCBM – AZO and PCBM – ITO conditions.

As a result, on average corrected PCE of 13.94 ± 0.12 % and 13.72 ± 0.52 % were reached for respectively C₆₀ – AZO and C₆₀ – ITO cells. Lower values were reached for PCBM cells, with averages of 11.05 ± 0.76 % for ITO as TCO and 10.06 ± 2.43 % using AZO.

A recurring feature of these measurements was the limited reproducibility of the PCBM – AZO condition. This could be either intrinsic to the architecture, or due to randomness. Within this series, it was possible to reach either V_{oc} , J_{sc} and FF values similar to that of C₆₀ based solar cells, but the three at the same time were never obtained from an individual solar cell. Other than that, similar V_{oc} were found for all conditions. J_{sc} was also similar, except for the PCBM - ITO condition, and FF was slightly higher for cells using C₆₀/SnO₂ compared to the one using PCBM/np-ZnO as ETL. From these results, we conclude that the C₆₀/SnO₂ ETL systematically resulted in better performances compared to PCBM/np-ZnO, regardless of the TCO layer.

PV parameters were also recorded under front illumination, as presented on **Figure 56**. As in the case of rear illumination, J_{sc} and PCE values were corrected from EQE measurements. This mode of operation is a more realistic approach of the perovskite subcell performances in tandem configuration by taking into account the optical parameters of the ETL and TCO layers.

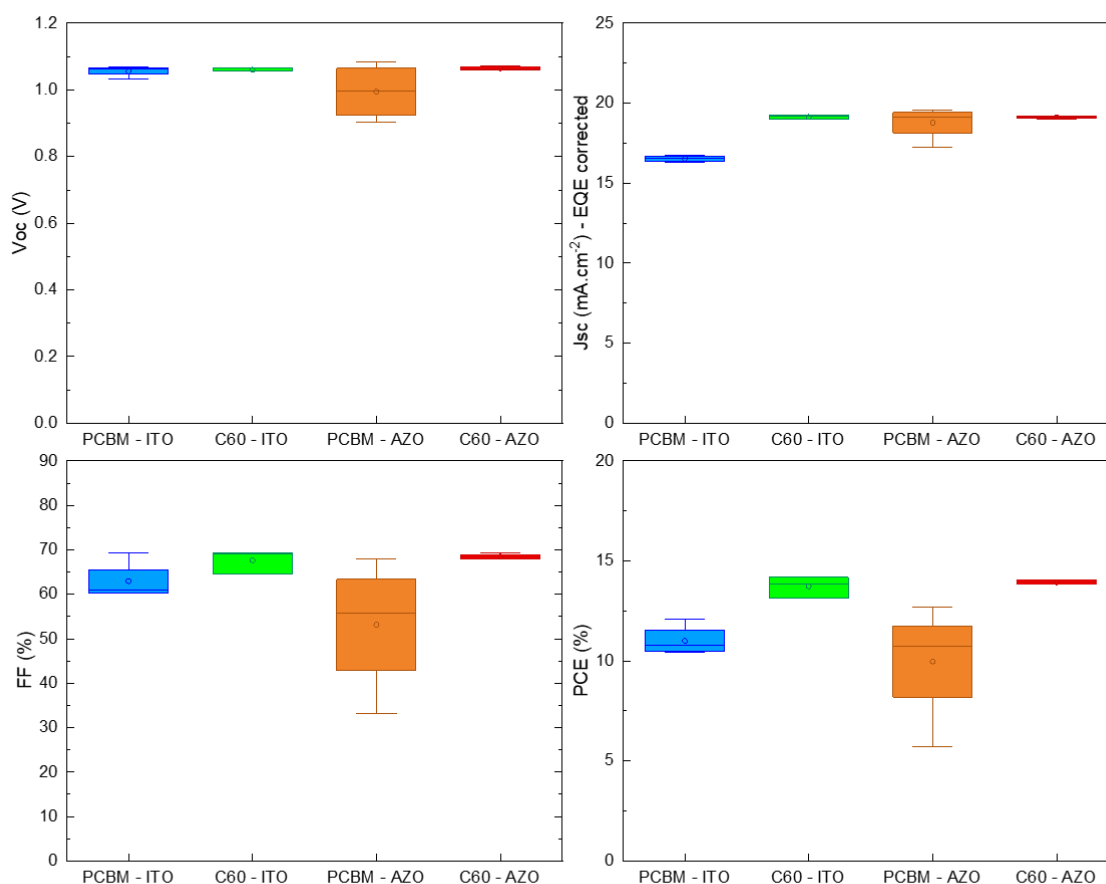


Figure 55 PV parameters recorded under rear illumination for semi-transparent perovskite solar cells using either PCBM/np-ZnO or C₆₀/ALD-SnO₂ as ETL and either ITO or AZO as front TCO.

J_{sc} values were corrected by EQE, and PCE values were modified accordingly.

Recorded V_{oc} were similar compared to rear illumination, with similar average values of 1051 ± 16 mV, 1035 ± 2 mV and 1033 ± 10 mV for respectively PCBM – ITO, C₆₀ – ITO and C₆₀ – AZO. Values were again lower and more dispersed for PCBM - AZO condition with an average at 989 ± 56 mV.

As expected, average corrected J_{sc} values were lower under front compared to rear illumination for all conditions. They were the highest for cells using C₆₀/SnO₂ as ETL, although this time higher using ITO with an average at 17.96 ± 0.17 mA.cm⁻² using ITO compared to 17.27 ± 0.06 mA.cm⁻² using AZO. Lower average J_{sc} was found for PCBM - AZO (16.78 ± 0.19 mA.cm⁻²), and it was the lowest with PCBM – ITO (15.82 ± 0.33 mA.cm⁻²). Despite high reproducibility for the C₆₀/SnO₂ cells, J_{sc} values were lower using AZO compared to ITO. Additionally, average J_{sc} value for the C₆₀ – AZO

condition was no longer within the margin of error of the average for the PCBM – AZO cells. Thus, we could hypothesize that the PCBM/np-ZnO ETL bilayer also presented lower optical transmittance as compared to the C₆₀/SnO₂ bilayer within the range of operation of the perovskite absorber layer. J_{sc} for the PCBM – ITO condition remained the lowest, probably in link with the np-ZnO/ITO electrical interface.

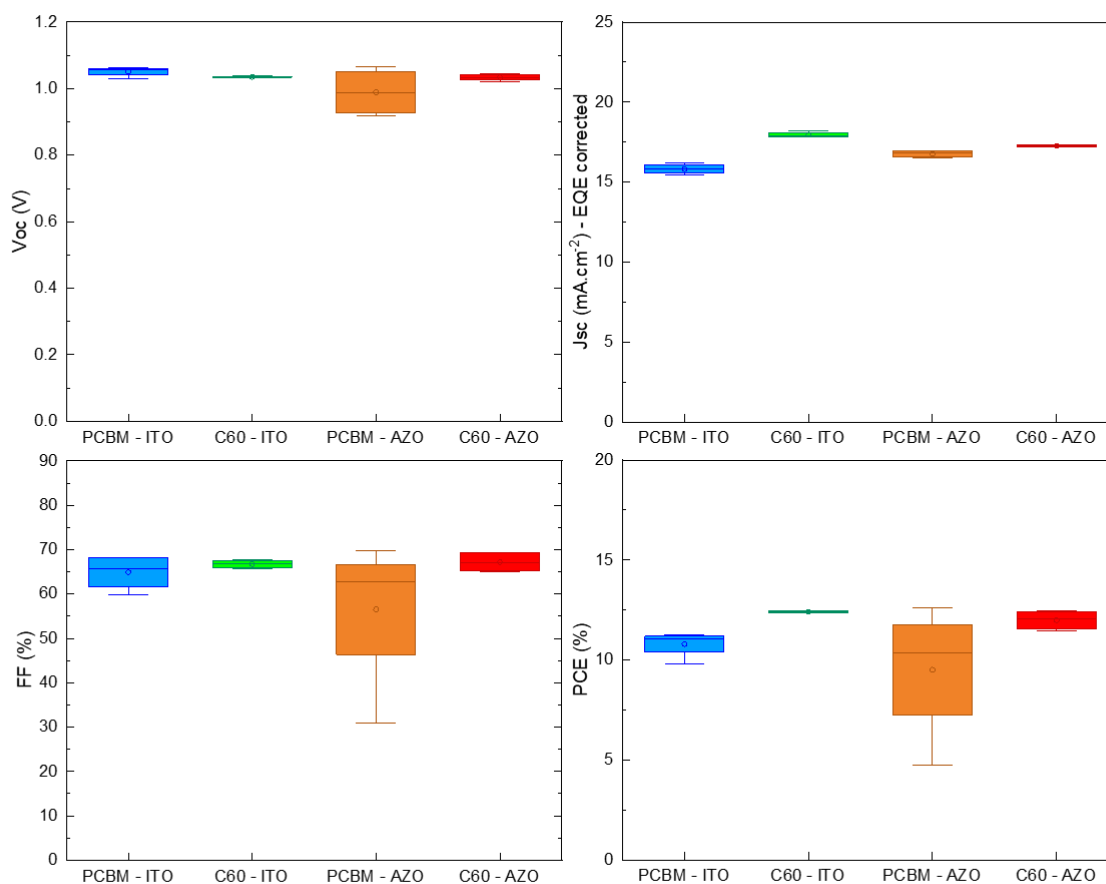


Figure 56 PV parameters recorded under front illumination for semi-transparent perovskite solar cells using either PCBM/np-ZnO or C₆₀/ALD-SnO₂ as ETL and either ITO or AZO as front TCO.

J_{sc} values were recorded by EQE, and PCE values were corrected accordingly.

Compared to rear illumination, similar average FF values but with a higher dispersion were obtained for C₆₀ based devices with averages at 67.18 ± 2.37 % using AZO as TCO and 66.75 ± 0.93 % using ITO. Values were close as compared to rear illumination for the PCBM - AZO condition with an average at 64.91 ± 4.00 %, and this time were the lowest for PCBM – AZO at 56.53 ± 15.19 % with a very high dispersion of values. The fact that similar FF were obtained for both illumination modes suggest that none of the interface was saturated by charge carriers under illumination. Otherwise, we would have expected an increase in R_s and thus a decrease in FF .

As a result, average PCE value was the highest for the C_{60} – ITO condition ($12.41 \pm 0.05 \%$), followed by C_{60} – AZO ($11.99 \pm 0.52 \%$), PCBM – ITO ($10.81 \pm 0.65 \%$) and PCBM – AZO ($9.47 \pm 2.74 \%$).

Figure 57 shows the J-V curve for champion cells, and EQE spectra for all cells under rear and front illumination. Strikingly, under rear illumination the J_{sc} of the champion cell for the PCBM – ITO condition from the J-V curve was significantly lower than that for the other conditions. For this condition only, in rear illumination J_{sc} calculated from EQE spectra was higher to that of the J_{sc} calculated from J-V measurement. Hysteresis was also high, with a lowering of the FF in reverse scan. Other than that, V_{oc} and J_{sc} values were similar for all conditions. Nonetheless, hysteresis for the PCBM – AZO condition was more pronounced than that of either champion cell using C_{60}/SnO_2 , which also resulted in lower FF in reverse scan compared to forward scan.

The lower J_{sc} for PCBM – ITO cells was further corroborated by EQE measurements under rear illumination from **Figure 57b**. In general, differences in EQE observed in this configuration would essentially arise from electronic considerations, as glass, ITO, NiO_x , MeO-2PACz and perovskite layers were identical for all cells. It might be however possible for photons passing through the perovskite layer to be preferentially reflected back to the absorber layer depending on the ETL and TCO layers. External quantum efficiency spectra were also almost identical for solar cells from C_{60} – ITO, C_{60} – AZO and PCBM – AZO cells. One cell from the PCBM – AZO condition however displayed a lower EQE across the whole spectrum. On the other hand, EQE for all cells from the PCBM – ITO condition were systematically $< 80 \%$ for any wavelength, and especially low compared to other conditions between the 300 nm and 550 nm range. This result would suggest that high energy photo-excited electrons would undergo a physical process that would limit the performances of the overall cell.

Finally, in the 760 nm – 800 nm region we observe a higher EQE from all cells using PCBM/np-ZnO compared to those using C_{60}/SnO_2 . This last result might be linked to the high reflectance of np-ZnO compared to SnO_2 in this range of wavelength, for which absorption from the perovskite layer would be limited. Practically, in 2T configuration this range of wavelength would be disputed between the perovskite top cell and the CI(G)S bottom cell. EQE from the perovskite semi-transparent solar cell in this region might therefore not be decisive for our analysis.

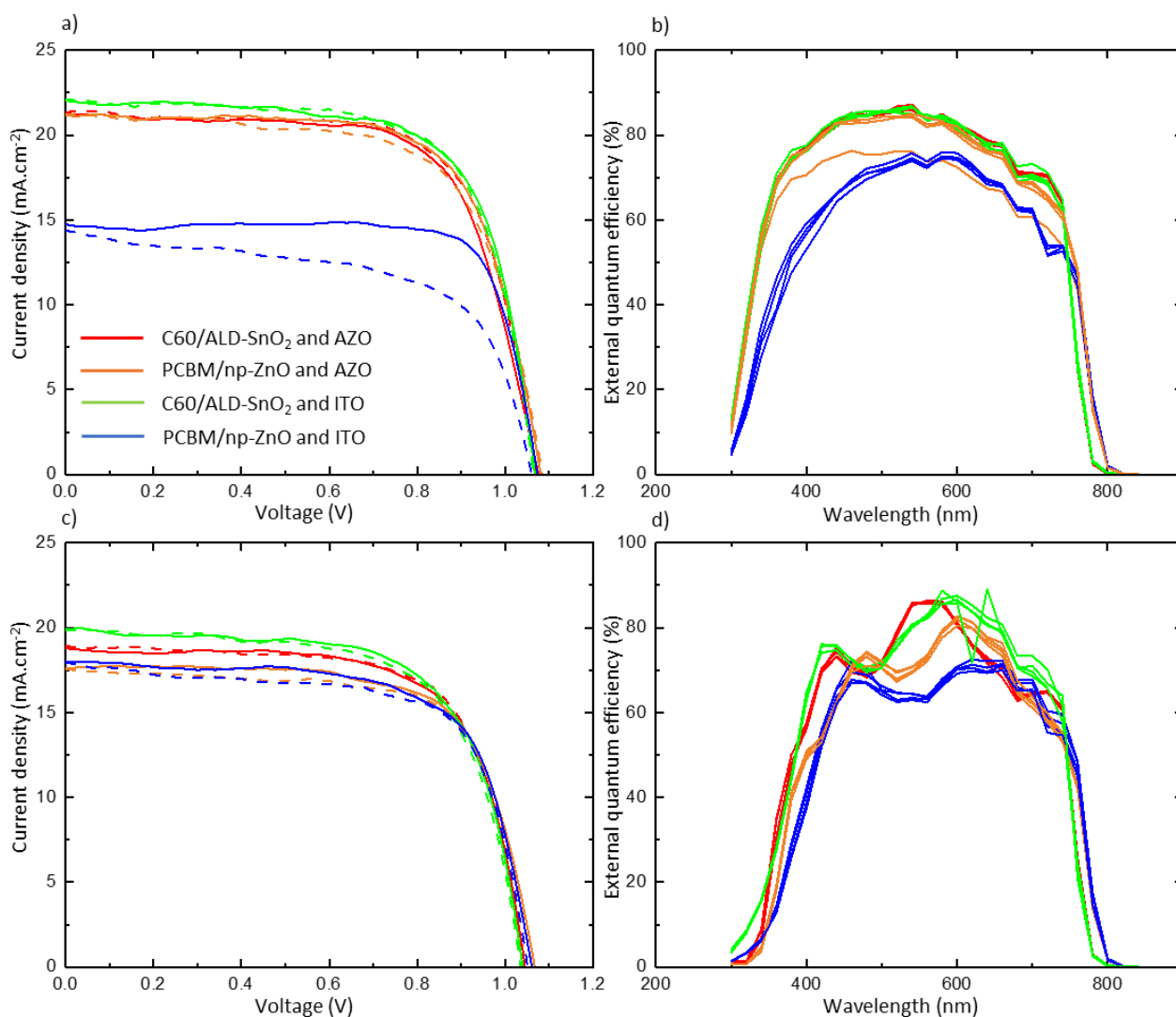


Figure 57 J-V curves for champion cells under (a) rear and (c) front illumination and EQE spectra under (b) rear and (d) front illumination for semi-transparent perovskite solar cells using either C_{60}/BCP or $PCBM/np-ZnO$ as ETL, and either ITO or AZO as front TCO.

Under front illumination, from **Figure 57c** relative J_{sc} for the champion cells from each condition started to reflect the trend in average J_{sc} observed earlier. It was the highest for $C_{60} - ITO$, followed by $C_{60} - AZO$, $PCBM - AZO$ and then $PCBM - ITO$. Other parameters were similar, except for a slightly higher V_{oc} obtained with $PCBM - ITO$ and $PCBM - AZO$ conditions as compared to $C_{60} - ITO$ and $C_{60} - AZO$. Interestingly, hysteresis for the $PCBM - ITO$ condition was much less pronounced than in rear illumination and was almost similar to that of $PCBM - AZO$. Champion cells from both C_{60}/SnO_2 conditions presented almost no hysteresis.

Prospective

From EQE spectra under front illumination shown on **Figure 57d**, EQE signal for the C_{60} – ITO, C_{60} – AZO and PCBM – AZO were now clearly different from each other with the introduction of relative optical considerations. Integration over the 300 nm – 800 nm range yielded highest EQE signal from solar cells of C_{60} – ITO condition, although superior values were measured in the 500 nm – 570 nm region for cells from the C_{60} – AZO condition. Particularly, EQE was higher for the C_{60} – ITO condition in the 570 nm – 760 nm range.

EQE values recorded for the PCBM – AZO conditions were overall lower and seemingly red-shifted compared to the C_{60} – AZO conditions. An apparent “shift” in values might have appeared due to a difference in interference fringes between sputtered AZO layer on top of either np-ZnO or SnO₂. Finally, lowest EQE values were recorded for the PCBM – ITO conditions.

On average, under front illumination solar cells from PCBM – ITO, C_{60} – ITO, C_{60} – AZO and PCBM – AZO retained respectively 96 %, 94 %, 90 % and 89 % of J_{sc} compared to rear illumination. Higher results obtained from the ITO based solar cells showed that this TCO had a higher transmittance over the region exploited by the perovskite absorber layer.

In this subsection, I evaluated the PV performances of PCBM/ZnO-np and C_{60} /ALD-SnO₂ in complete solar cells using either AZO or ITO as top TCO layer. As a result, I observe that higher average PV parameters are obtained by using C_{60} /ALD-SnO₂, along with a lower standard deviation in values both in rear and front illumination. Evaluation of AZO or ITO as front TCO layer on the other hand depended on the configuration. In rear illumination, I recorded similar PV performances with C_{60} /SnO₂ using either AZO or ITO. However, in front illumination slightly higher J_{sc} and PCE values were obtained with ITO over AZO. This was mostly due to a higher transparency of ITO over the 300 nm – 800 nm range compared to AZO layer, as suggested by EQE measurements. Using PCBM/np-ZnO as ETL bilayer and sputtered AZO as front TCO could result in PV parameters in rear illumination, although with less reproducibility. Performances were however limited under front illumination compared to the C_{60} /SnO₂ based solar cells, due to a better transmittance of the former ETL bilayer in the range of wavelength exploited by the perovskite absorber layer. Finally, depositing ITO on top of PCBM/np-ZnO bilayer resulted in systematically lower performances, probably due to interface phenomena between np-ZnO and sputtered ITO.

In this chapter, I evaluated different ETL and TCO candidates to develop a semi-transparent solar cell that would be suited for two-terminal tandem application with CI(G)S. Most importantly, I first developed an ETL bilayer that would withstand the plasma sputtering step for TCO deposition. It was then possible to optimize this ETL further and evaluate different candidates as TCO layer. In the end,

it appeared that a $C_{60}/\text{ALD-SnO}_2$ ETL combined with ITO as a TCO layer was the most suited for tandem application among the retained candidates.

Developing a low temperature NiO_x layer and a semi-transparent architecture were crucial steps for monolithic integration of perovskite top cell in tandem device with CI(G)S. However, surface roughness of CI(G)S could remain an issue for conformal, homogeneous deposition of layers of the top cell. In the next chapter, we aimed to develop a process to chemically etch the surface of CI(G)S and smoothen its surface.

4.4. Interim summary

In this chapter, we describe our process development to manufacture semi-transparent perovskite solar cells through the introduction of a metal oxide ETL layer. In the first part of this chapter, we briefly described our first attempts at realizing semi-transparent perovskite solar cells based on an organic ETL bilayer. Due to the harsh sputtering process for TCO deposition, very low PCE values were obtained regardless of spin-coating conditions and therefore layer thickness of PCBM and BCP.

Then, we substituted BCP in our architecture for either ZnO or AZO as nanoparticles as buffer layer on top of PCBM. Equivalent if not higher PV parameters were measured in both case as compared to PCBM. In further optimization steps, we determined that np-ZnO presented a better shelf-life stability compared to np-AZO and finally, it was possible to manufacture semi-transparent solar cells based on a PCBM/np-ZnO ETL bilayer and a sputtered AZO window layer. This architecture demonstrated PV parameters comparable to that of opaque devices using the same ETL.

In our last step of development, we compared the PV parameters in front and rear operation for semi-transparent devices using either a PCBM/np-ZnO or a C_{60}/SnO_2 ETL bilayer and either ITO or AZO as a front TCO layer. We observed particularly low J_{sc} from J-V and EQE measurements for devices using both PCBM/np-ZnO and ITO, probably due to an issue in the electrical contact between np-ZnO and ITO. Best PV parameters in both front and rear illumination were reached using C_{60}/SnO_2 and ITO, probably due an improved electrical contact and a higher transmittance.

Chapter 5

CI(G)S morphological adaptation to monolithic integration

Summary: *In this chapter, we study the impact of a smoothed CI(G)S absorber surface on the solar cell performance. This modification is operated by a bromine wet etching process employed on Glass/Mo/CI(G)S samples before the finalization of the solar cell as defined in previous chapters 1 and 2. We employ a protocol that has already been studied for CIGS absorber layers but which had to be optimized for CIS layers, the samples of this study containing only Ga at the rear side. The main objective was to smoothen the surface with a minimal decrease in thickness for the CI(G)S layer. First, we evaluated the effect of changing the treatment time and spinning parameters over the morphology of CI(G)S layers. At 40 rpm, it was possible to consistently reduce the RMS roughness of CI(G)S < 30 nm, for reasonable treatment duration between 2 min and 6 min, as compared to highly accelerated dissolution process at 80 rpm. Additionally, we studied the effects of the treatment over the surface chemistry of our samples, qualitatively and quantitatively. As established for CIGS layers, Br-etching results in the formation of a superficial Se⁰ layer, which could be almost completely remove by KCN treatment. Finally, we prepared solar cells based on as-prepared and etched absorber layers. Similar performances were obtained with both CI(G)S samples, although a lower J_{sc} was observed for the etched sample. These results were encouraging; however they should be repeated to clearly evaluate the impact of Br-etching over performances of solar cells.*

Contents

5.1. Introduction	123
5.2. Proof of concept: Planarization of co-evaporated CI(G)S samples	123
5.2.1. Influence of velocity and treatment time parameters of a Br-etching wet process over the thickness and roughness of CI(G)S layers.....	124
5.2.1.1. Co-evaporated CI(G)S morphology after Br-etching (80 rpm)	124
5.2.1.2. Co-evaporated CI(G)S morphology after Br-etching (40 rpm & 30 rpm)	128
5.2.2. Reliability and homogeneity	130
5.2.2.1. Reliability of the Br-etching process (40 rpm)	131
5.2.2.2. Reproducibility of the Br-etching process (30 rpm, 4 min)	133
5.2.2.3. Thickness homogeneity of co-evaporated CI(G)S layers prior to Br-etching	135
5.2.2.4. Thickness homogeneity of co-evaporated CI(G)S layers after Br-etching.....	137
5.2.3. Influence of Br-etching and KCN treatment over the surface chemistry of CI(G)S	140
5.2.3.1. Qualitative assesment over the surface chemistry of CI(G)S by XPS analysis	140
5.2.3.2. Evolution Na and Cd content at the CI(G)S surface after Br-etching and KCN treatment .	143
5.2.3.3. Elemental composition of CI(G)S absorber layers by GD-OES.....	144

Prospective

5.2.3.4. Elemental composition of Cl(G)S absorber layers by XPS analysis..... 146

5.2.4. J-V and EQE characterization of devices based on as-prepared and smoothed Cl(G)S 147

5.3. Interim summary

5.1. Introduction

CI(G)S absorber layers can exhibit a high surface roughness. This property can help improve light absorption and thus J_{sc} of complete devices through light scattering. However, this surface roughness is transmitted to the top layers of the cell and can also result in non-conformal and in-homogeneities in thickness during subsequent layer deposition, especially for tandem application. In the case of perovskite/CI(G)S two-terminal tandem, a thin HTL layer usually has to be deposited on top of the top TCO layer of the CI(G)S subcell. When NiO_x or small molecules are considered as HTL, ALD or dip coating processes can help circumventing this problem. However, highest performances in perovskite single junction devices using low temperature NiO_x deposition have been reported in literature for nanoparticle synthesis. Deposition of NiO_x nanoparticles is usually processed by spin or slot die coating, for which surface roughness of the substrate is an important parameter.

In this chapter, I focus on the development of a wet chemical process to minimize the surface roughness of CI(G)S as described in 2.1.7. In short, a superficial sacrificial part of the CI(G)S layer is dissolved by bromine etching under agitation. This process yields a thinner CI(G)S layer with a smoothed surface, and results in a change of the surface chemistry that can be corrected by a conventional KCN treatment before the buffer layer deposition to adjust the band alignment at this absorber/buffer interface. To account for the material loss in our process, slightly thicker than usual CI(G)S layers were deposited by co-evaporation or sequential method. In the first part, a setup to chemically smoothen CI(G)S samples of size up to $2*2\text{ cm}^2$ is adapted, based on previous publications on the smoothing of regular bandgap CIGS. Then, the surface chemistry of etched samples and the J-V performances of completed solar cells based on etched absorber layers are studied. All samples employed for these studies were provided by TNO, Netherlands through a PERCISTAND collaboration.

5.2. Optimization of the planarization procedure of co-evaporated CI(G)S samples

In this section, a setup to minimize the surface roughness of CI(G)S samples based on a $1*1\text{ cm}^2$ scale wet chemical process is described to show that a RMS roughness $< 30\text{ nm}$ for $1*1\text{ cm}^2$ samples can be reached starting from a 60 nm roughness. This setup is described more in details in Chapter 2. First, the impact of rotation speed and treatment time on the morphological properties of CI(G)S is studied. Both parameters are optimized to minimize the final roughness of CI(G)S along with the amount of sacrificial material that is removed in the process. Then, the reliability and homogeneity of our process is assessed by AFM, SEM and ICP-OES measurements. The final subsection describes how the surface chemistry of the samples is modified by the treatment and how it is completely

restored by KCN treatment. Finally, completed solar cells based on smoothed and as-prepared CI(G)S samples were completed after KCN treatment to see how the treatment would affect their PV parameters.

5.2.1. Influence of velocity and treatment time parameters of a Br-etching wet process over the thickness and roughness of CI(G)S layers

We adapted the previous work on chemical etching of CIGS layers by Bouttemy et al. on our CI(G)S samples. Using the best conditions for CIGS etching (Br_2 and HBr concentrations of 0.02 mol.L^{-1} and 0.2 mol.L^{-1} , respectively), we investigated the effect of rotation speed and etching duration over the thickness and roughness of the final layer. The principal objective of this study is to develop a reproducible procedure to reduce the R_t value of CI(G)S absorber layers $< 30 \text{ nm}$ by minimizing the loss in layer thickness. Reaching even lower R_t values could be beneficial for wet process deposition and thus monolithic tandem application. All CI(G)S samples employed during this study were deposited by co-evaporation. Planarization experiments, ICP-OES and XPS analyses were conducted at ILV.

5.2.1.1. CI(G)S morphology after Br-etching (80 rpm)

In order to optimize our process on low band gap CI(G)S samples, we aimed i) to find a relationship between etching time and CI(G)S dissolution rate and ii) to reach an acceptable compromise between the final thickness and roughness parameters of the smoothed CI(G)S layer. To do so, we first conducted etching experiments on $1 \times 1 \text{ cm}^2$ CI(G)S samples by employing the setup described in 2.1.7.1. They were obtained by cutting a parent sample consisting of a 2800 nm thick co-evaporated CI(G)S layer deposited on a Mo layer on glass. The samples were fixed upside-down to a rotating electrode spinning at 80 rpm and directly dipped in the solution.

Table 8 Final thickness, dissolution rate and Root mean square (RMS) roughness for CI(G)S absorber layers chemically etched at 80 rpm between 30 sec and 10 min .

80 rpm	Etching time (min)	Average Thickness (nm)	Dissolution rate (nm/min)	R_t $50 \times 50 \mu\text{m}$ AFM (nm)	R_t $10 \times 10 \mu\text{m}$ AFM (nm)
$1 \times 1 \text{ cm}^2$	Initial	2800	-	57.0	52.4
	00:30	2441 ± 49	718	44.3	41.1
	01:00	2249 ± 25	551	65.3	33.3
	02:00	1718 ± 68	541	15.5	16.2
	10:00	686 ± 46	211	20.4	19.4
	20:00	Complete dissolution	280	29.0	26.0

Prospective

We first conducted a series of experiments for several samples etched during periods ranging from 30 sec to 20 min to entirely dissolve the CI(G)S layer. **Table 8** summarizes the values of root mean square roughness (Rt) and thickness of absorber layers measured before and after smoothing, as well as the dissolution rates of the etching process calculated from each time parameter. Rt values and thickness were calculated from AFM and cross-section SEM measurements, respectively. AFM images were recorded for areas of 50*50 μm and 10*10 μm for each sample. In general, Rt values were higher for higher area images and for simplicity we retained only the highest Rt value obtained for each sample. Images of 5*5 μm^2 area were recorded to evaluate the microscopic surface morphology of CI(G)S. Dissolution rates were calculated in nm of thickness removed from the CI(G)S layer, and directly derived from the difference between the thickness of a reference CI(G)S sample and that of an etched absorber layer from cross-section SEM measurements.

From an initial value of 57.0 nm, Rt decreased to 44.3 nm after 30 sec etching and 16.2 nm after 2 minutes. Complete dissolution of the CI(G)S layer was observed after 20 min, leaving the exposed Mo layer. A sacrificial layer of nearly 1 μm was dissolved to reach Rt < 30 nm, for a remaining thickness around 1720 nm. After 10 minutes of etching, Rt of the absorber layer did not decrease, despite the dissolution of a nearly 2 μm thick sacrificial layer. The remaining thickness for the absorber layer was thus around 680 nm. These results suggest a threshold value of Rt for our etching process, In addition, in contrast to the significant decrease in Rt after 2 min and 10 min, Rt values of 44 nm and 65 nm were calculated for samples etched for 30 sec and 1 min, respectively. These values were similar or higher to the initial roughness of 59 nm for the reference sample. These observations have to be correlated with morphological studies of present CI(G)S layers which will be presented later.

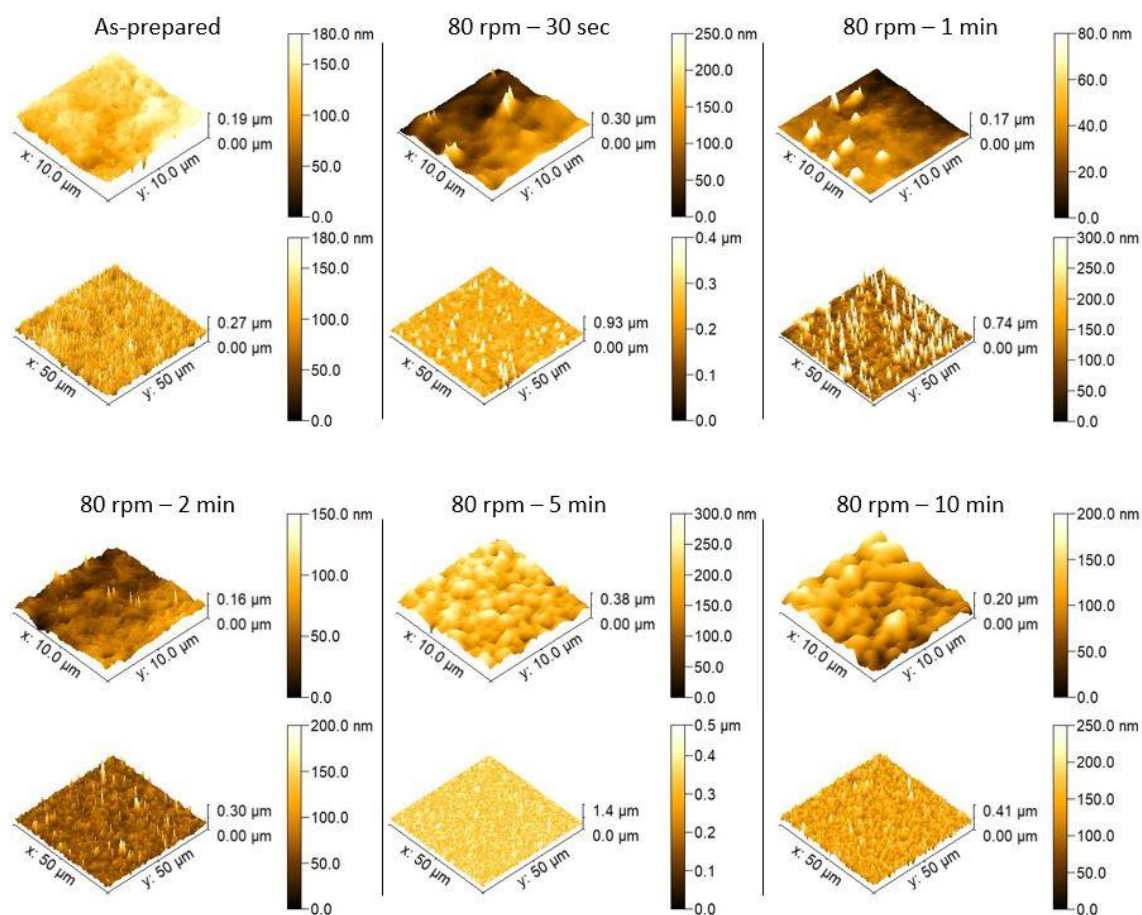


Figure 58 $10 \times 10 \mu\text{m}^2$ and $50 \times 50 \mu\text{m}^2$ AFM images acquired for $1 \times 1 \text{ cm}^2$ CI(G)S samples etched at 80 rpm for 30 sec, 1 min, 2 min, 5 min and 10 min compared to an as-prepared reference. Peak to valley distance is indicated by vertical arrows.

Figure 58 show the $10 \times 10 \mu\text{m}^2$ and $50 \times 50 \mu\text{m}^2$ AFM images acquired to calculate the R_t values for the samples presented in **Table 8**. Peak to valley distance is also indicated for each sample. Based on the $50 \times 50 \mu\text{m}^2$ images, peak to valley distance increased from $0.27 \mu\text{m}$ before etching to values between $0.30 \mu\text{m}$ and $1.4 \mu\text{m}$ afterwards, without evident link between the intensity of the value and etching duration. Indeed, from the aspect of the images we clearly distinguished the formation of pillar structures at the surface of etched CI(G)S samples which was unusual and inherent to the present metallurgy of bare surfaces presenting some surstructures as well as some defaults of density. The number of pillar structures was noticeably high for etching time between 30 sec and 1 min 30 sec etching. It seemed less intense for longer durations but surfaces kept non uniform aspects. It should be noted that the presence of the pillars probably induced errors in AFM measurements, and exceptionally low values of valley depth were recorded from the tip after crossing a pillar. Thus, difference in peak to valley distances from sample to sample should be interpreted with caution.

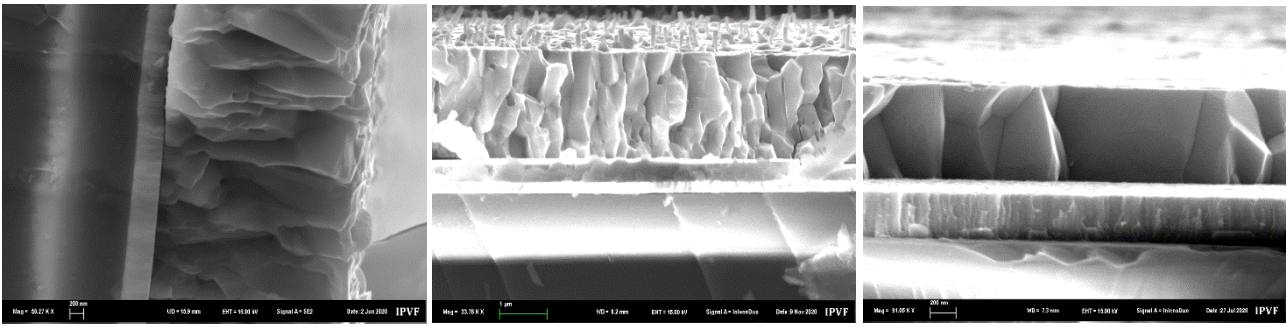


Figure 59 Cross-section SEM images acquired for (left) as-prepared, (middle) 1 min etched and (right) 10 min etched CI(G)S absorber layers.

Figure 59 shows cross-section SEM images acquired for as-prepared, 1 min etched and 10 min etched CI(G)S samples. These images showed the appearance of a columnar pattern at the surface of the sample after 1 min etching, and its disappearance for the sample etched for 10 min resulting in a planar surface. A pillar height of up to 530 nm was calculated from the cross section image corresponding to the 1 min etched sample, somewhat in agreement with the peak to valley distance of 740 nm calculated from AFM. This surprising evolution of the surface morphology is in line with previous observations and confirm a specific behaviour of the samples studied here. A planar, mirror-like surface is nonetheless obtained after 10 min etching.

In general, a high dispersion of values was observed for CI(G)S thickness and thus dissolution rate. Values calculated after 80 rpm etching were measured over a range between 220 nm/min and 730 nm/min, although values between 541 and 551 nm/min were consistently obtained for samples etched for 1 min and 2 min. But a precise measurement of the thickness on SEM cross-section is rather difficult as it requires a perfect orientation perpendicularly to the surface.

This first procedure nonetheless permitted to reach R_t values < 20 nm, which is within the goal of < 30 nm that was defined at the beginning of the study. But this result was accompanied with an important decrease in absorber material, for a final thickness around 1720 nm after 2 min etching. For solar cell application however, and particularly using low band gap CI(G)S, the final thickness of the absorber layer should ideally stay above 2000 nm for decent optical absorption and to avoid back contact carrier recombination at the Mo interface. But here, lowering the duration of the process to limit the loss in material might result in a columnar morphology at the surface, as previously observed for samples etched between 30 sec and 2 min.

We therefore decided to explore a procedure at lower spinning rate which will lead to lower dissolution kinetics and possibly a better smoothing result with lower CIS removal. In addition, we decided to pursue the study on CI(G)S samples elaborated according to the optimized procedure of

TNO leading to a 2100 nm thickness, procedure which is better controlled than the previous employed to reach higher thicknesses at 2800 nm. This leads to better quality absorber layers but emphasizes the need to find a dissolution process minimizing the CI(G)S layers thinning for a targeted < 30 nm Rt.

5.2.1.2. CI(G)S morphology after Br-etching (40 rpm & 30 rpm)

A similar study was conducted at 40 and 30 rpm, but on conventional absorber layers of 2100 nm. **Table 9** presents the final thickness and dissolution rates for samples etched between 30 sec and 4 min. Measured Rt values and thicknesses were evaluated by AFM and cross-section SEM, respectively. To decrease the time of acquisition, areas of 10*10 μm^2 and 5*5 μm^2 were defined for AFM imaging instead of 50*50 μm^2 and 10*10 μm^2 .

Table 9 Final thickness, dissolution rate and Rt for CI(G)S absorber layers chemically etched at 40 rpm and 30 rpm for durations between 30 sec and 4 min. *: Rt value obtained from a 50*50 μm^2 AFM image.

	Etching time (min)	Average Thickness (nm)	Dissolution rate (nm/min)	Rt 10*10 μm AFM (nm)	Rt 5*5 μm AFM (nm)
40 rpm 1*1 cm ²	Initial	2085 \pm 132	-	50.8*	46.9
	00:30	1987 \pm 47	197	27.5	31.6
	01:00	2013 \pm 38	72	35.5	33.3
	01:30	1897 \pm 58	188	25.2	20.4
	02:00	1867 \pm 29	218	19.2	20.0
30 rpm	04:00	1816 \pm 17	67	20.8	10.7

Samples etched for 1 min 30 sec and 2 min consistently exhibited Rt values < 30 nm. Starting from an initial Rt of 51 nm, it was possible to make it as low as 26.3 nm after only 2 min smoothing for a final thickness around 1970 nm.

From the dissolution rates calculated by cross-section SEM imaging we observe that a Rt value < 30 nm for CI(G)S absorber layers can be reached at an etching speed of 40 rpm or 30 rpm with a lesser loss in absorber material compared to 80 rpm. An etching duration between 1 min 30 and 2 min at 40 rpm yielded a Rt < 30 nm with a loss in material estimated between 100 nm and 300 nm, which is reasonable. At 30 rpm, even for longer etching time such as 4 min, Rt values < 30 nm for CI(G)S absorber layers were reached with a limited amount of dissolved material. These specific parameters will be more detailed in 5.2.2.2.

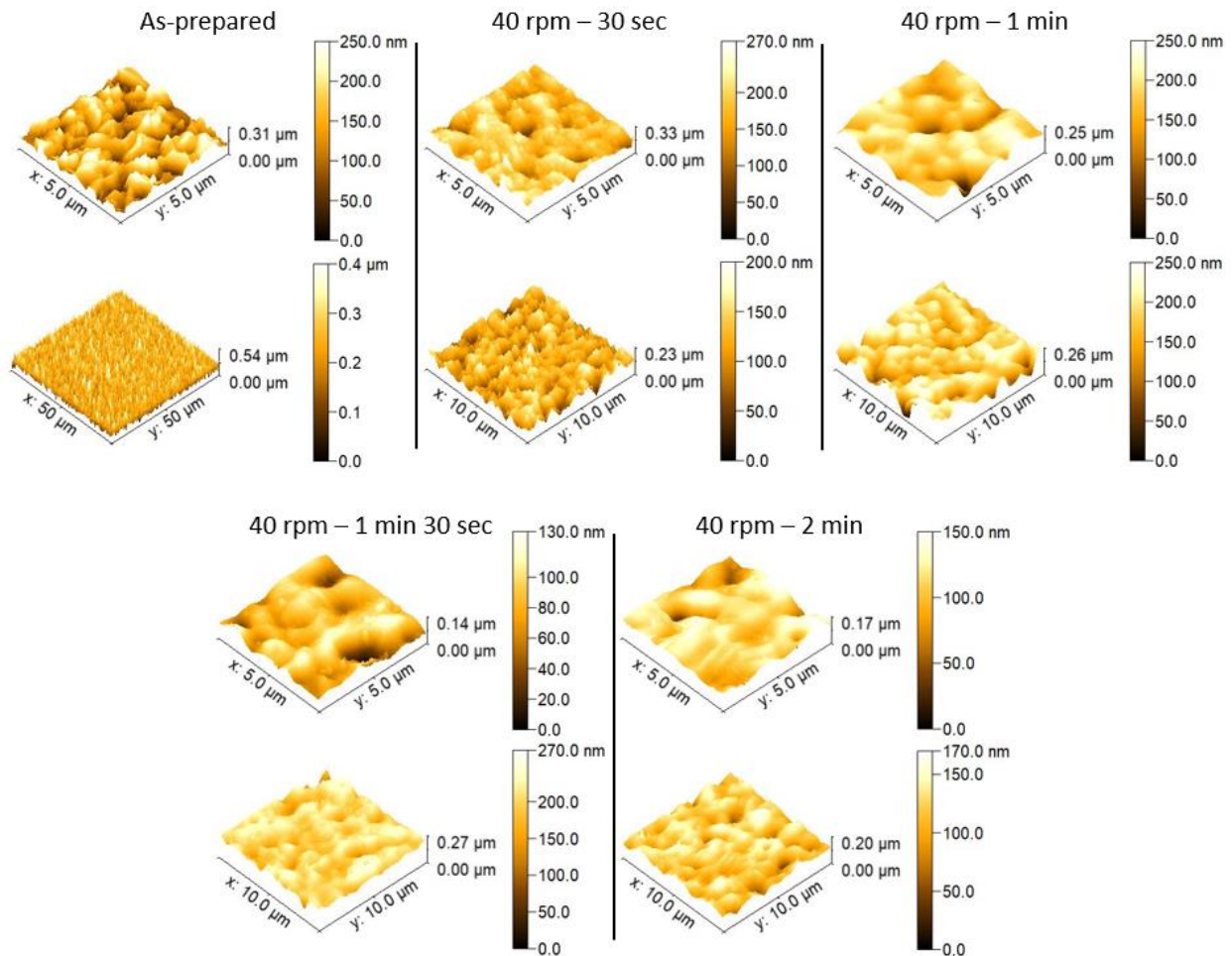


Figure 60 5*5 μm^2 and 10*10 μm^2 AFM images acquired for 1*1 cm^2 CI(G)S samples etched at 40 rpm for 30 sec, 1 min, 1 min 30 sec and 2 min and compared to an as-prepared reference (5*5 μm^2 and 50*50 μm^2 images). Peak to valley distance is indicated by vertical arrows.

Figure 60 shows the AFM Images acquired for samples etched at 40 rpm presented in **Table 9**. In contrast to samples etched at 80 rpm, and to some extent in manual stirring mode, we did not observe a columnar pattern at the surface of the samples. Instead, lowered peak to valley distances between 0.17 μm and 0.27 μm were measured after etching compared to 0.54 μm for the as-prepared sample. These values were nonetheless calculated from AFM images of different areas. This supports the previous assessment about a less controlled metallurgy when forcing the CI(G)S growth from 2100 to 2800 nm. Anyway, decreasing the rotation speed facilitates manipulations and a 2 min etching seems appropriated to respect the requirement for solar cell fabrication : 1900 nm absorber thickness and $R_t < 30$ nm.

The roughly equivalent thicknesses measured by SEM for all the samples may be attributed to the estimative values that can be obtained. Measurements of the thickness by cross-section SEM were

acquired at one spot of the sample at a time, resulting in an additional source of error for the calculation of dissolution rate.

These observations led us to infer the dissolution rate of our process using a more reliable method, ICP-OES. By this method, we aim to remove the uncertainties linked to SEM imaging. We believed that ICP-OES was a more reliable method to assess the relative dissolution rates between samples on the basis of a well-defined physical quantity. Indeed, ICP-OES provided a direct access to the concentrations of dissolved elemental species in the etching solution. Concentrations obtained in $\mu\text{g.L}^{-1}$ from this method were less subjected to experimental errors and did not rely on a reference sample. Normalizing this value to the area of an etched sample resulted in a dissolution rate in $\mu\text{g.L}^{-1}.\text{m}^{-2}$, representing an average value over its whole surface. Dissolution rates obtained by ICP were proportional to a quantity in nm/min, however the conversion would require to know the density of the CI(G)S absorber layer.

In the next section, I aim to evaluate the reliability of our process by ICP-OES and to assess its homogeneity by acquiring cross-section SEM images at different positions before and after etching. Planarization experiments were conducted at 40 rpm and 30 rpm.

5.2.2. Reliability and homogeneity^{xi}

From the results presented in **5.2.1**, we showed that our setup developed for Br wet etching could be an effective way to minimize the thickness of a CI(G)S layer at the expense of a moderate loss in absorber material. However, we noticed discrepancies in dissolution rate calculated from SEM imaging from sample to sample and wanted to determine the reliability of our process using a more robust protocol.

Additionally, these experiments were conducted on $1*1\text{ cm}^2$ samples which were not suited for solar cell application. We therefore conducted subsequent experiments for a larger sample size that would be still adapted to our setup. We determined that a sample size of $2*2\text{ cm}^2$ would be suited for this task, that we introduce for smoothing experiments conducted at 40 rpm. Spatial homogeneity of the process over the thickness of the absorber layer should also be inspected as the amount of etched material could be different at the edge and the center of the sample due to the hydrodynamic properties induced by our setup.

^{xi} ICP-OES measurements and determination of normalized concentration were realized by Solène Béchu. SEM and AFM images were recorded by Alexandre Blaizot.

In the following section, we thus want to determine the reliability and homogeneity of our process for 1*1 cm² and 2*2 cm² samples.

5.2.2.1. Reliability of the Br-etching process (40 rpm)

To assess the reliability of our process, we first aimed to compare the discrepancies of the dissolution rates obtained from SEM images and ICP-OES. ICP-OES dosages were conducted for HBr:Br₂:H₂O solutions after etching 2*2 cm² CI(G)S samples at 40 rpm for 2 min, 4 min and 6 min. It allowed to measure the concentrations of the elements Cu, In, Ga, Se and Na dissolved after smoothing. The concentrations were measured in $\mu\text{g.L}^{-1}$ and were then normalized to the surface of the etched samples in $\mu\text{g.L}^{-1}.\text{m}^{-2}$, as shown on **Figure 61**.

For these elements, we observed an almost ideal linear relationship between normalized concentration in Br solution and etching duration. A simple linear regression resulted in R-Squared systematically > 0.99 . Intercept to zero (min) were also calculated between $-12 \mu\text{g.L}^{-1}.\text{m}^{-2}$ and $67 \mu\text{g.L}^{-1}.\text{m}^{-2}$, as compared to normalized concentrations values in the order of thousands of $\mu\text{g.L}^{-1}.\text{m}^{-2}$. This linear time dependency of the amount of dissolved elements had also been reported for the same etching process on CIGS, and our results confirmed the reproducibility of this method over CI(G)S.¹³³

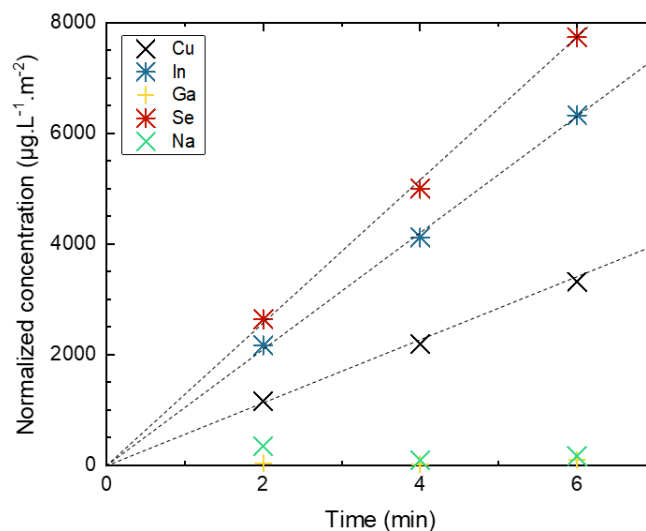


Figure 61 ICP dosage for Cu, In, Ga, Se and Na from Br solutions after etching of CI(G)S absorber layers at 40 rpm for 2 min, 4 min and 6 min. Values in μg were normalized with volume of solution and sample area. Hypothetical linear concentration relationship between Cu, In and Se concentration as a function of etching time were represented by dashed lines.

On the other hand, we did not observe linear relationships between normalized concentrations in Ga and Na and etching durations. The initial concentrations for these elements were initially very low in the low band gap CI(G)S absorber layer, and might have varied from sample to sample. The Ga

grading in CI(G)S also implied that we did not expect a linear time dependency of its concentration in etching solution. One should note also that a perfect procedure would need to mask the borders where dissolution is accelerated and the glass, source of Na.

Table 10 Final thickness, dissolution rate and Rt values for CI(G)S absorber layers chemically etched at 40 rpm for durations between 2 min and 6 min. ²: Rt value obtained from a 50*50 μm² AFM image.

40 rpm	Etching time (min)	Average Thickness (nm)	Dissolution rate (nm/min)	Rt 30*30 μm AFM (nm)	Rt 5*5 μm AFM (nm)
2*2 cm ²	Initial	2085 ± 132	-	50.8 ²	46.9
	02:00	1970 ± 31	58	26.6	27.2
	04:00	1809 ± 45	69	23.0	18.0
	06:00	1469 ± 60	103	14.3	10.7

These results were in contrast to the dissolution rates measured by cross-section SEM shown in **Table 10**, for a set of 2*2 CI(G)S cm² samples etched under the same conditions. Rather consistent dissolution rates of 58 nm/min and 69 nm/min were calculated for 2 min and 4 min etching time, while an especially high value of 103 nm/min was found for the sample etched for 6 min. Rt value of 23 nm was calculated from AFM image of the sample etched for 2 min. A thickness of 1809 nm was reached after further extending the dissolution time to 4 min, while not resulting in significantly lower Rt values. 15 nm were reached after a 6 min duration at the for a final absorber layer thickness of 1469 nm.

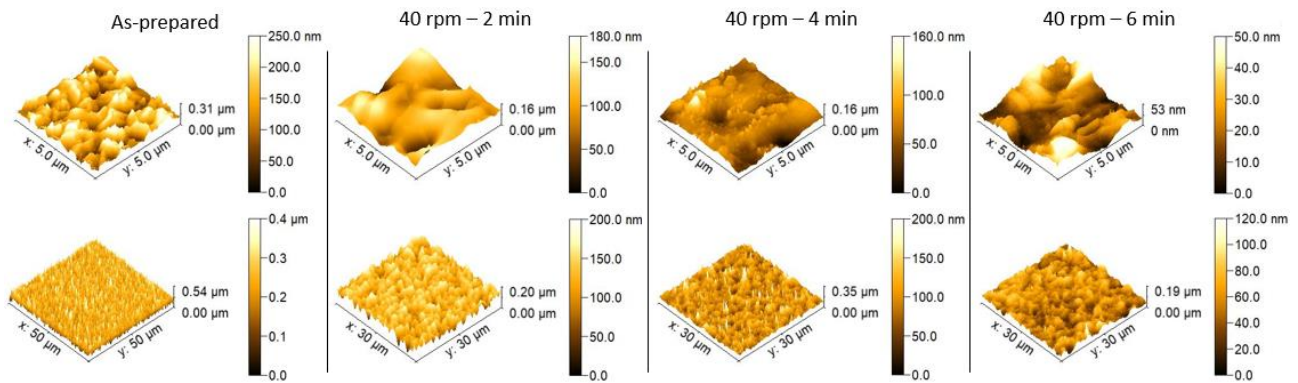


Figure 62 5*5 μm² and 30*30 μm² AFM images acquired for 2*2 cm² CI(G)S samples etched at 40 rpm for 2 min, 4 min and 6 min and compared to an as-prepared reference (5*5 μm² and 50*50 μm² images). Peak to valley distance is indicated by vertical arrows.

Therefore, we showed that the average dissolution rate over the surface of a sample was consistent for a given rotation speed. Deviations observed by SEM rather reflected the difficulty to access the

average thickness of a sample using this method, or inhomogeneities in the thickness of the parent sample or during etching process.

5.2.2.2. Reproducibility of the Br-etching process (30 rpm, 4 min)

To further minimize the amount of etched CI(G)S necessary to reach a R_t value < 30 nm, we investigated the possibility to decrease the etching speed of the process to 30 rpm. For simplicity, these experiments were conducted on 1×1 cm² samples. Additionally, we wanted to further assess the general reproducibility of our process, that was already well established in section 5.2.2.1.

Table 11 Final thickness, dissolution rate and R_t values for three CI(G)S absorber layers chemically etched at 30 rpm for 4 min. *: R_t value obtained from a 50×50 μm^2 AFM image.

30 rpm	Etching time (min)	Average Thickness (nm)	Dissolution rate (nm/min)	R_t 30×30 μm AFM (nm)	R_t 5×5 μm AFM (nm)
1*1 cm ²	Initial	2085 ± 132	-	50.8*	46.9
Sample 1	04:00	1725 ± 43	90	18.4	15.5
Sample 2	04:00	1816 ± 17	67	20.8	10.7
Sample 3	04:00	1768 ± 55	79	17.0	10.6

Table 11 presents the average thickness, dissolution rates and R_t values obtained from SEM and AFM imaging for three samples etched at 30 rpm for 4 min. Similarly to previous observations for experiments conducted at 40 rpm, all three etched samples exhibited consistent R_t values. They were systematically below or close to 20 nm, showing the robustness of our setup at low spinning speed.

Discrepancies in dissolution rates were also observed, in accordance to previous observations. For two samples, a consistent rate between 90 nm/min and 79 nm/min was calculated whereas it was 67 nm/min for the third one. These three values were surprisingly superior to those obtained after 40 rpm etching for 2 min and 6 min etching, and reflected the difference in initial and final morphology for the three samples. An absorber layer thickness between 1709 nm and 1725 nm was reached for the first two samples while it was around 1816 nm for the third one.

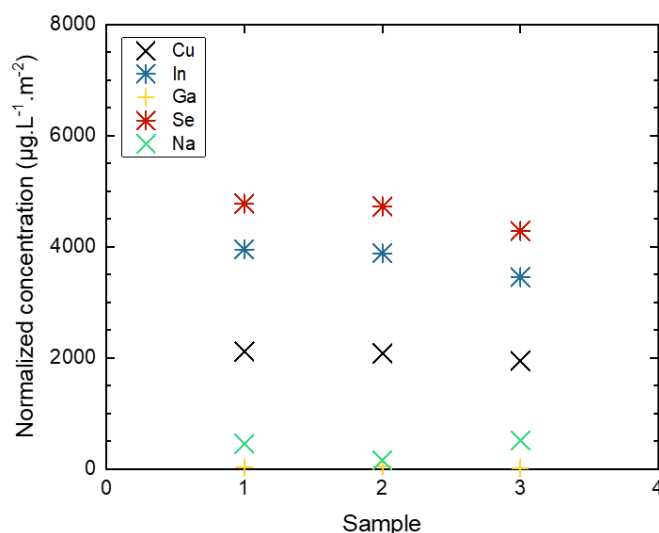


Figure 63 ICP dosage for Cu, In, Ga, Se and Na from three Br solutions used to etch CI(G)S absorber layers at 30 rpm for 4 min. Values in μg were normalized with volume of solution and sample area to yield values in $\mu\text{g.L}^{-1}.\text{m}^{-2}$.

ICP-OES dosage was conducted to assess the reproducibility of the dissolution rate with a more reliable method. Normalized concentration values in Cu, In, Ga, Se and Na are reported in **Figure 63** for the HBr:Br₂:H₂O solutions that served to etch the three samples a 30 rpm for 4 min. Average concentrations for major elements in CI(G)S were respectively $2046 \pm 87 \mu\text{g.L}^{-1}.\text{m}^{-2}$ for Cu, $3763 \pm 272 \mu\text{g.L}^{-1}.\text{m}^{-2}$ for In and $4594 \pm 271 \mu\text{g.L}^{-1}.\text{m}^{-2}$ for Se for all three samples, resulting in standard deviation systematically lower than 8% for these elements. This deviation is significant, and might be linked to the experimental errors during the etching process. Nonetheless, the average value for etching rate from cross-section SEM images was calculated at $84 \pm 15 \text{ nm/min}$, which corresponded to a standard deviation $> 17\%$ of the average value.

Concentrations were much lower for Na and Ga, with higher relative standard deviations. Average values of respectively $189 \pm 50 \mu\text{g.L}^{-1}.\text{m}^{-2}$ and $13 \pm 39 \mu\text{g.L}^{-1}.\text{m}^{-2}$ were calculated. The argument developed in 5.2.2.1 would also be valid to explain discrepancies from sample to sample.

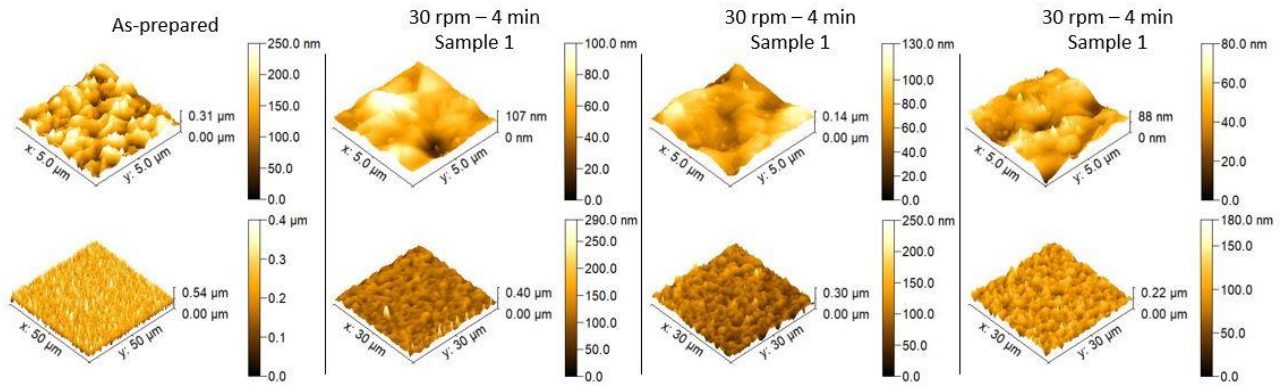


Figure 64 $5 \times 5 \mu\text{m}^2$ and $30 \times 30 \mu\text{m}^2$ AFM images acquired for three $2 \times 2 \text{ cm}^2$ CI(G)S samples etched at 30 rpm for 4 min and one as-prepared reference sample ($5 \times 5 \mu\text{m}^2$ and $50 \times 50 \mu\text{m}^2$ images). Peak to valley distance is indicated by vertical arrows.

Overall, these results indicated that reproducible values could be obtained both in terms of roughness of the etched layer and of dissolution rate of the process. Additionally, lowering the rotation speed from 80 rpm to 40 rpm and 30 rpm allowed to increase the etching time to reach a certain Rt value, leading to a better robustness of our protocol regarding difference in handling from sample to sample. Concomitantly, the amount of etched material to reach Rt value $< 30 \text{ nm}$ seemingly decreased after lowering the rotation speed, especially for the series of experiments at 40 rpm.

In the next part, we evaluate the spatial homogeneity of our etching process over CI(G)S samples of $2 \times 2 \text{ cm}^2$ area that would be suited for solar cell fabrication. To do so, we first study the morphology of the as-prepared parent sample.

5.2.2.3. Thickness homogeneity of co-evaporated CI(G)S layers prior to Br-etching

We first assessed the spatial homogeneity of CI(G)S samples prepared by co-evaporation prior to Br wet etching. To do so, the thickness of the CI(G)S and Mo layers across two CI(G)S samples of co-evaporated variety grown on top of a Mo layer by cross-section SEM imaging was measured. Briefly, two parent $5 \times 5 \text{ cm}^2$ samples were cut in two rectangular $2.5 \times 5 \text{ cm}^2$ half-samples as depicted on **Figure 65**. For each parent sample, cross-section SEM images for a single $2.5 \times 5 \text{ cm}^2$ half-sample were recorded to assess the thickness homogeneity across the CI(G)S and Molybdenum layers. In total, 7 images were acquired across each half-sample A and B at different locations.

Thickness values measured from these images are reported on **Figure 66**. Mo layers from both samples presented a similar and homogenous morphology, with a thickness of respectively $471 \pm 27 \text{ nm}$ and $450 \pm 62 \text{ nm}$ for samples A and B. For sample B, we nonetheless measured lower values at left- and right-position 3 of respectively 413 nm and 335 nm which may indicate edge effect during

deposition. This feature was not observed for sample A, with values of 480 nm and 475 recorded for respectively left- and right-positions 3 which were above the average value of 471 nm.

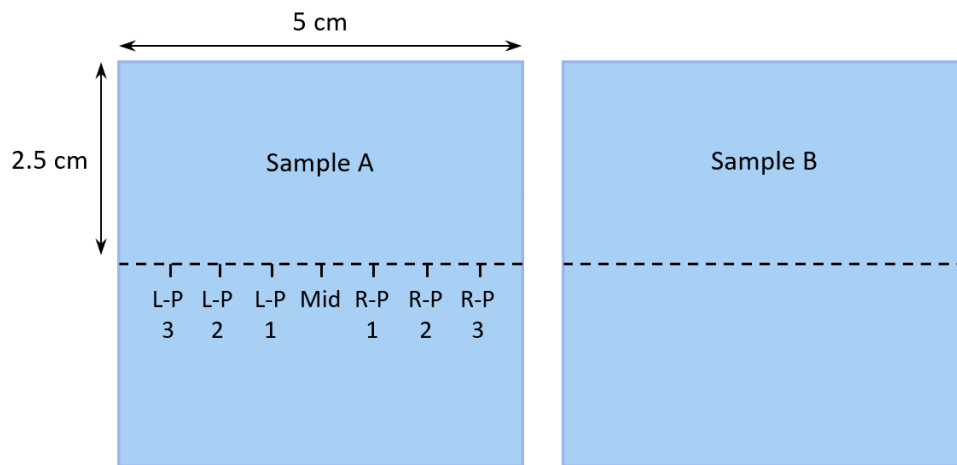


Figure 65 Schematic of 2 CI(G)S parent samples of 5*5 cm² area cut in two half-samples A and B of 2.5*5 cm² area. Cutting lines are indicated by dotted lines. L-P: Left-position. R-P: Right-position. Mid: Middle

Regarding the CI(G)S layer, I measured average values of 1884 ± 317 nm for sample A and 1843 ± 168 nm for sample B. Large discrepancies of thickness values were observed for sample A, whereas the standard deviation was less than 10% of the average value for sample B. Nonetheless, outlier values for sample A were measured from images at the edge of the samples at left- and right-position 3. In particular, not considering the outlier value of 1221 nm from left-position 3 would yield an average value of 1994 with a deviation of ± 134 nm, which would correspond to a standard deviation values <10% of the average value. This deviation could explain to some extent the lack of consistency observed between values of dissolution rates calculated from SEM measurements.

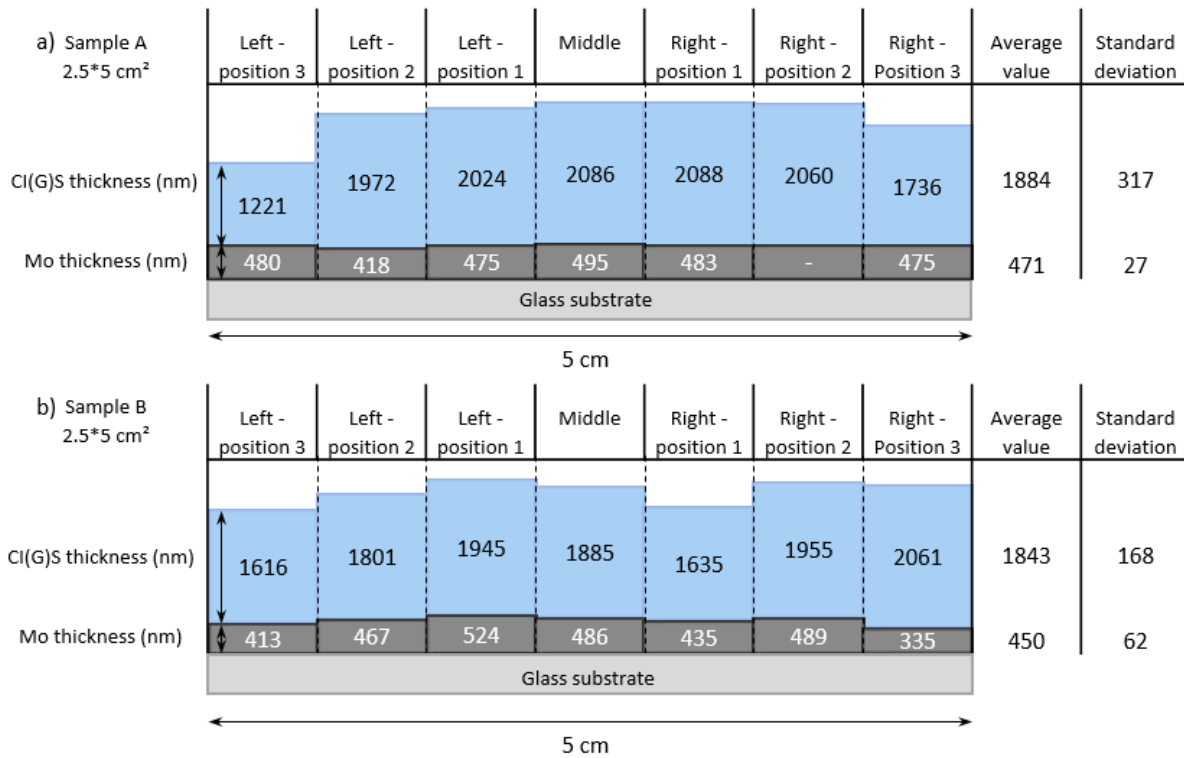


Figure 66 Thickness of CI(G)S and Mo layers across two CI(G)S samples grown by co-evaporation on top on a Mo layer, prior to Br wet etching. Two samples, (a) A and (b) B, were measured for reproducibility. Thickness values were measured from cross-section SEM images taken at 7 positions for two 2.5*5 cm² half-samples. These half-samples were obtained from two distinct 5*5 cm² parent samples cut in half.

Samples of area up to 2*2 cm² could be chemically smoothed using the small-scale setup. The initial discrepancy in thickness observed for 5*5 cm² samples served as a basis to assess the spatial homogeneity of our process for smaller samples of this size.

5.2.2.4. Thickness homogeneity of co-evaporated CI(G)S layers after Br-etching

A similar method as that developed in section 5.2.2.2 was employed to assess the spatial homogeneity of the thickness of CI(G)S after etching. Parent 2*2cm² samples were submitted to Br etching for 1 min and 2 in, respectively. They were then cut in half after etching into half-samples C and D, of rectangular dimensions 1*2 cm² as shown in **Figure 67**. Then, cross-section SEM images were acquired at 3 different positions for each half sample, from which I measured the thickness of the CI(G)S absorber layers.

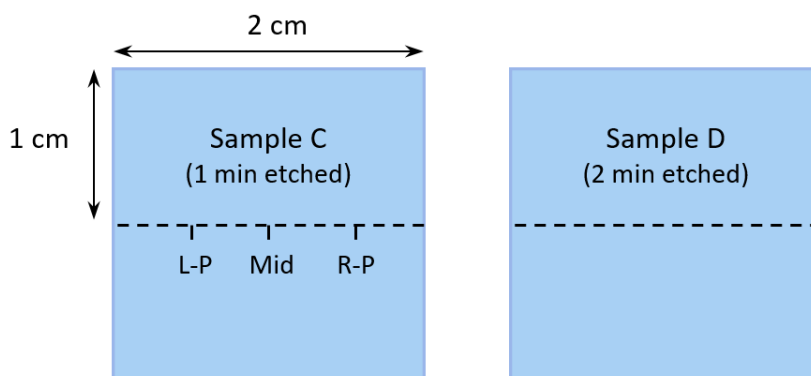


Figure 67 Schematic of 2 CI(G)S parent samples of 2*2 cm² area cut in two half-samples C and D of 1*2 cm² area. Etching parameters were 40 rpm for 1 min and 2 min, respectively. Cutting lines are indicated by dotted lines. L-P: Left-position. R-P: Right-position. Mid: Middle

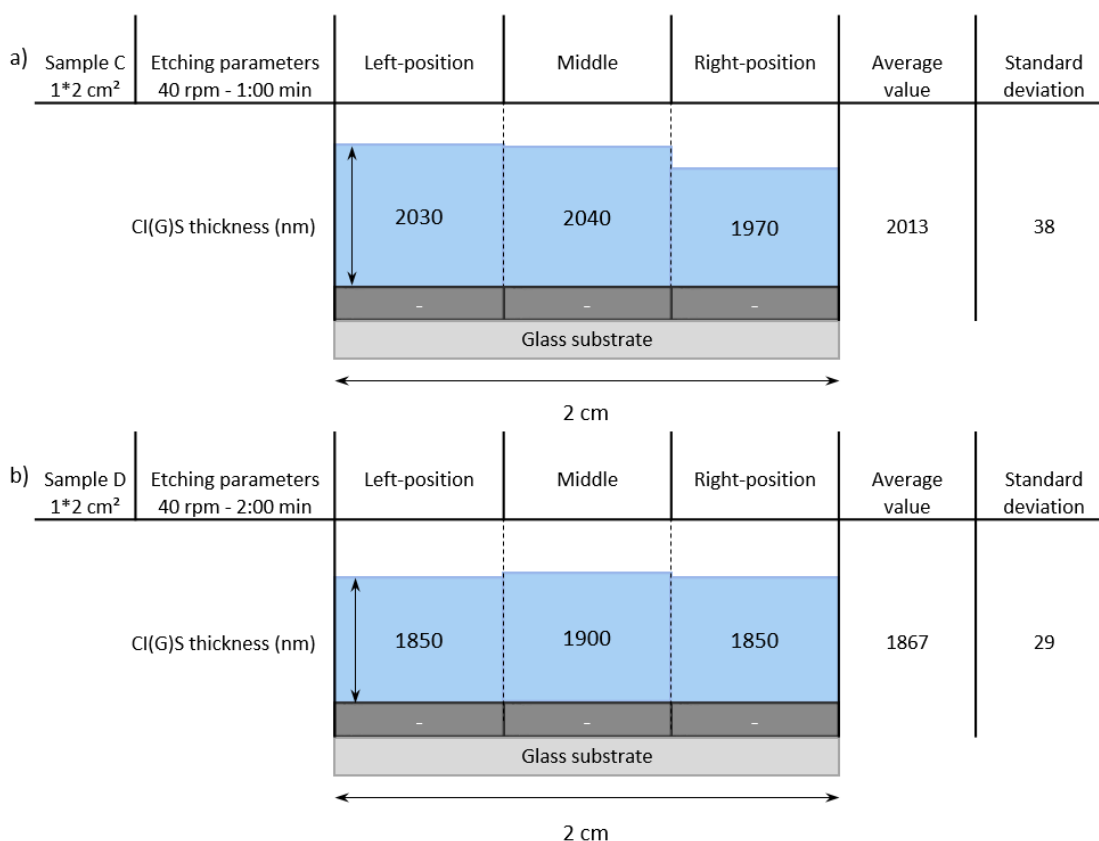


Figure 68 Thickness of CI(G)S and Mo layers across two CI(G)S samples grown by co-evaporation on top on a Mo layer, after (a) 1 min and (b) 2 min of Br etching at 40 rpm. Thickness values were measured from cross-section SEM images taken at 3 positions for two 1*2 cm² half-samples. These half-samples were obtained from two distinct 2*2 cm² parent samples cut in half.

Average thickness values of 2013 ± 38 nm and 1867 ± 29 nm for CI(G)S absorber layers are reported on **Figure 68** after respectively 1 min and 2 min Br etching at 40 rpm. These values corresponded to standard deviations values $< 2\%$ that of their respective average, indicated inferior discrepancies in values compared to that of $5*5\text{cm}^2$ samples measured in section 5.2.2.2. The datasets considered were nonetheless of different sizes. Moreover, the distance between two successive SEM image acquisitions was slightly different for A & B samples on one side and C & D samples on the other side. For the $2.5*5\text{ cm}^2$ as-prepared half-samples, this gap was approximately 0.625 cm and it was closer to 0.5 cm for the $1*2\text{ cm}^2$ etched half-samples.

Despite the difference in spacing between two consecutive SEM images, we can consider dataset of similar size by considering average and standard deviation values extracted for each combination of 3 spatially successive measurements for samples A & B. These values are reported on **Table 12**.

For datasets of similar size to that of sample C & D, average values between 1739 nm and 2078 nm with standard deviation values between 16 nm and 449 nm were obtained for sample A. They were calculated between 1787 nm and 1884 nm with standard deviation values between 72 nm and 222 nm for sample B. The average ratio between standard deviation and their average values for samples A and B was between 8% and 9% for both samples A and B, superior to the values calculated for samples C and D.

Table 12 Average values for CI(G)S absorber layer thickness for sample A and B, calculated from thickness measurements for 5 series of 3 consecutives SEM images for each sample.

a) Sample A $2.5*5\text{cm}^2$	Average Thickness (nm)	b) Sample B $2.5*5\text{cm}^2$	Average Thickness (nm)
<i>L-P 3 to L-P 1</i>	1739 ± 449	<i>L-P 3 to L-P 1</i>	1787 ± 165
<i>L-P 2 to Mid</i>	2027 ± 57	<i>L-P 2 to Mid</i>	1877 ± 72
<i>L-P 1 to R-P 1</i>	2066 ± 36	<i>L-P 1 to R-P 1</i>	1822 ± 164
<i>Mid to R-P 2</i>	2078 ± 16	<i>Mid to R-P 2</i>	1825 ± 168
<i>R-P 1 to R-P 3</i>	1961 ± 196	<i>R-P 1 to R-P 3</i>	1884 ± 222

To conclude, from cross-section SEM measurements acquired at different position we found a similar thickness homogeneity across cutting lines between as-prepared and etched CI(G)S samples. Due to the low number of acquired SEM images, for the etched CI(G)S samples these results could be rather interpreted as a good correspondence between the thickness at the edge and at the center of the sample. Discrepancies in thickness values across the cutting line were similar between the 1 min etched and the 2 min etched half-samples, indicating that the homogeneity of the layer did not vary as a function of etching time. However, we note that these results were derived from cross-section SEM measurements using a protocol for which we demonstrated certain limits in 5.2.2.1 and 5.2.2.2.

In this subsection, the reliability and homogeneity of our small scale planarization setup was evaluated. ICP-OES measurements after etching samples at 40 rpm for 2, 4 and 6 min show a linear concentration of dissolved metals upon treatment time, while repeating three times a 30 rpm etching for 4 min yielding similar concentrations. The standard deviation of thickness along a lateral cut of a CI(G)S sample was similar before and after etching. These results show that our process has a reasonable reliability and yields homogeneously etched surfaces.

5.2.3. Influence of Br-etching and KCN treatment over the surface chemistry of CI(G)S^{xii}

As mentioned in earlier reports, the surface chemistry of planarized CI(G)S is left modified after Br-etching and has to be restored before integration of the layer into full cells⁵⁵. We explored the role of KCN treatment to recover a pristine CI(G)S chemistry from a Br-etched surface, on the basis of XPS analysis and as described in other protocols^{55,133}. Additionally, we wanted to evaluate the effect of Br-etching on the concentration of other components present at the surface of as-prepared CI(G)S, such as alkali elements who play a role in CI(G)S solar cells performances and Cd leftover species from the removal of the protective layer described in 2.1.9. Moreover, we assessed the surface chemistry of Br-etching at the center and at the edge of the sample as an additional mean to assess the homogeneity of our process.

5.2.3.1. Qualitative assessment over the surface chemistry of CI(G)S by XPS analysis

Here, we take a closer look at the surface chemical properties of CI(G)S samples after each step of this process.

The surface of the following samples was probed by XPS:

- As-prepared CI(G)S layers
- CI(G)S after Br-etching (4 min, 40 rpm)
- CI(G)S after Br-etching (4 min, 40 rpm) followed by KCN treatment (5min)

Corresponding spectra are shown on **Figure 69** for the Cu 3p, Cu 2p_{3/2}, Se 3d and In 4d regions. Information about the chemical state of Cu could be gathered from the Cu 3p region between 70 eV and 81 eV and the Cu 2p_{3/2} region between 929 eV and 935 eV. In both cases, only one chemical state was identified for each CI(G)S sample. For the pristine sample, Cu 2p_{3/2} peak position was

^{xii} XPS data acquisition was realized by Muriel Bouttemy and Matthieu Frégnaux. Peak fitting of the XPS spectra was realized in collaboration with Muriel Bouttemy and Solène Béchu. KCN treatment was carried out by Solène Béchu.

detected at 932.5 ± 0.1 eV, while the Cu $3p_{3/2}$ and Cu $3p_{1/2}$ peaks were respectively positioned at 74.8 ± 0.1 eV and 77.3 ± 0.1 eV. Those were in agreement with a chemical environment corresponding to that of Cu in CI(G)S. Cu $2p_{3/2}$ peak position was then 932.2 ± 0.1 eV after Br-etching, and 932.2 ± 0.1 eV after KCN treatment. Likewise, peak positions of the Cu $3p_{3/2}$ and $1/2$ environment were respectively at 74.6 ± 0.1 eV and 77.1 ± 0.1 eV for the Br-etched sample, and at 74.8 ± 0.1 eV and 77.1 ± 0.1 eV after KCN treatment. These similarities indicated that the chemical state of Cu was likely not altered either by Br-etch or KCN treatment. For the CI(G)S sample after Br-etch, an additional feature between 67.5 ± 0.1 eV and 70 ± 0.1 eV could be attributed to Br 3d orbital contribution, indicating trace amounts of this element. It was not detected from the as-prepared sample and disappeared after KCN treatment.

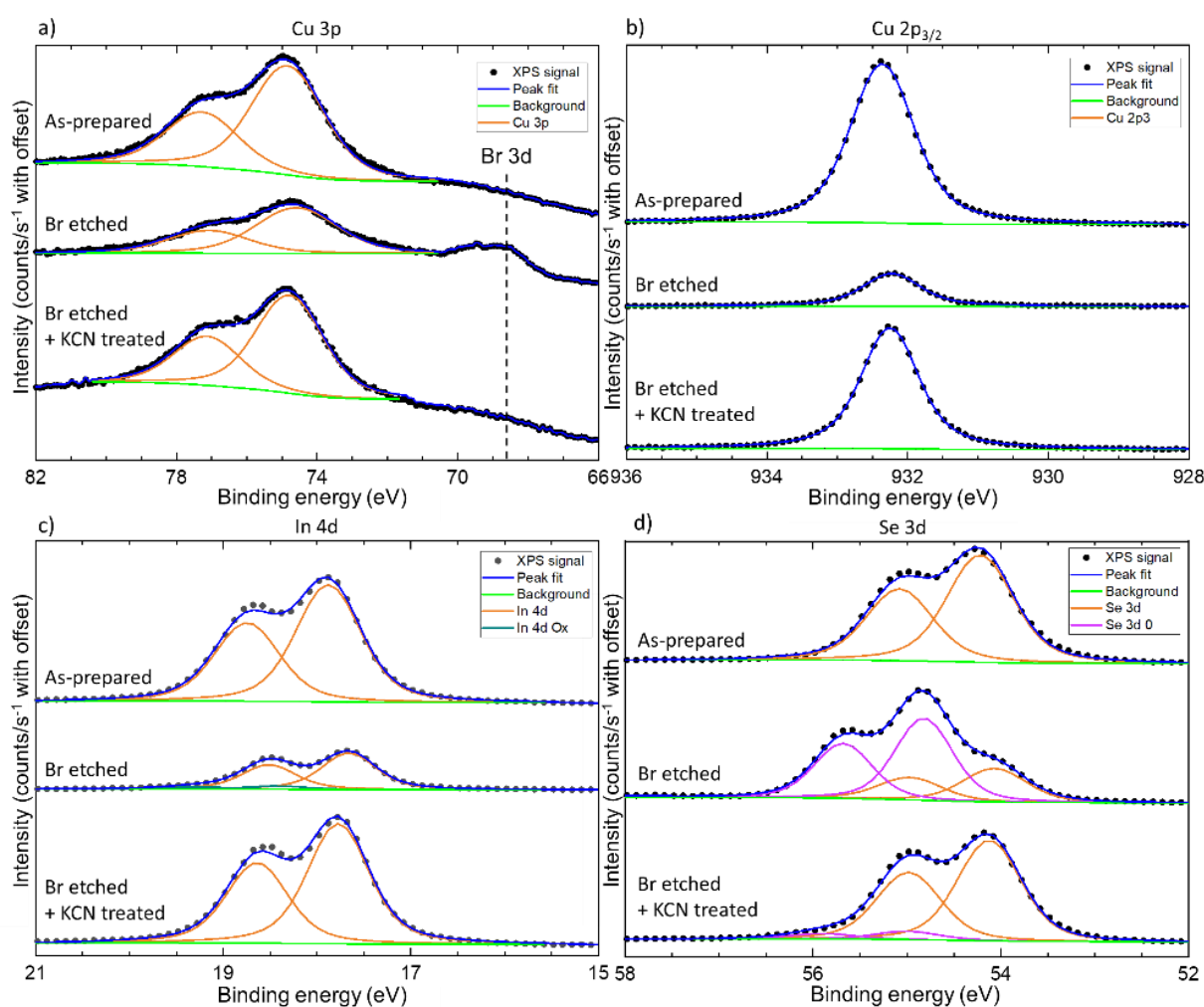


Figure 69 Superimposed XPS spectra for CI(G)S samples recorded in the (a) Cu 3p, (b) Cu $2p_{3/2}$, (c) In 4d and (d) Se 3d regions. For each graph, from top to bottom: As-prepared CI(G)S sample, CI(G)S sample after Br-etch (4 min, 40 rpm), and CI(G)S samples after Br-etch (4 min, 40 rpm) and KCN treatment.

Regarding the Se 3d region, the surface chemistry of CI(G)S was modified after etching. For the as-prepared samples, we identified one Se contribution from CI(G)S environment with Se 3d_{5/2} and 3d_{3/2} contributions at respectively 54.2 ± 0.1 eV and 55.1 ± 0.1 eV. This chemical state was also identified in Br-etched and KCN treated samples, with Se 3d_{5/2} contributions at 54.1 ± 0.1 eV and 54.1 ± 0.1 eV. However, a supplementary chemical state of selenium attributed to elemental Se⁰ was identified for these samples. It was characterized by a Se 3d_{5/2} component positioned respectively at 54.84 ± 0.1 eV and 54.98 ± 0.1 eV for the Br-etched and KCN treated samples. Elemental selenium was the most represented Se environment for the Br-etched sample, while its contribution was only residual after KCN treatment.

The formation of a characteristic Se⁰ superficial layer was indeed consistently reported after KBr:Br₂ and HBr:Br₂ etching. Elemental selenium has been considered as a corrosion intermediate in the etching process, and its subsequent oxidation in dissolved ions as a rate-limiting step of the overall mechanism. As a result, evolution of the Se chemistry state in the etching process has been hypothesized as a key element in the reduction of mean roughness of the absorber layer discussed in **5.2.1**.^{54,55} Our results obtained on CI(G)S show that bromine in aqueous environment is an efficient oxidizing agent for CI(G)S etching process, as already demonstrated for CIGS⁵⁵.

We also identified XPS features indicative of In-O bonding after bromide etching. In 4d signal from CI(G)S environment was identified with a 4d_{5/2} component at 17.9 ± 0.1 eV and a 4d_{3/2} component at 18.8 ± 0.1 eV for pristine CIGS. This contribution was also identified in the Br-etched and KCN treated samples, with In 4d_{5/2} components at 17.7 ± 0.1 eV and 17.7 ± 0.1 eV. After etching, an additional yet subtle 4d component was detected at 18.5 ± 0.1 eV and 19.3 ± 0.1 eV for 4d_{5/2} and 4d_{3/2} orbitals, respectively. It could be associated to the presence of indium oxide, whose formation was also reported after KBr:Br₂ and HBr:BR₂ etching and completely disappeared after KCN treatment^{54,55,134,135}. Here, this oxidation is most probably due to air exposition between sample preparation and subsequent introduction as no specific care was taken for the transfer of the sample from the solution to the XPS spectrometer^{135,136}.

In any case, elemental selenium was only marginally detected by XPS after KCN treatment, showing that the superficial Se⁰ layer could be mostly removed after KCN treatment as established by previous works.^{54,55,133,135} Likewise, presence of indium oxide was not detected for the KCN treated sample, indicating that pristine chemical environment could be restored by this method.

In this subsection, the effect of bromide treatment on the surface chemistry of CI(G)S was studied by XPS. Our conclusions are similar to those presented in 2011 by Bouttemy et al. regarding the

evolution of the surface chemistry of CIGS^{55,56}. Namely, Se^0 is present at the CI(G)S surface after Br-etching, but both Se^0 and native oxides are efficiently removed with KCN leaving an adapted surface for the subsequent buffer layer deposition. In the next sections we provided a quantitative look on the species presently identified by XPS.

5.2.3.2. Evolution of Na and Cd content at the surface after Br-etching and KCN treatment

Here we focus on the presence of other elements at the surface of CI(G)S samples before and after Br-etching, i.e. Cd and Na. CI(G)S samples delivered by TNO were capped with a CdS layer to protect them during shipment, which was subsequently removed by HCl treatment as presented in 2.1.9. However, traces of this element were susceptible to remain after acidic treatment. Additionally, alkali elements are an important factor in CI(G)S solar cell performances.^{134,137} For CI(G)S samples deposited on soda-lime glass substrates, Na migrates from the glass substrate to the surface of the sample, and it has been demonstrated that KCN treatment and even immersion of CI(G)S in water would provoke alkali leaching from the surface.^{134,136} XPS analysis permitted to verify that Cd was completely removed from the surface of CI(G)S after planarization, and to study quantitatively the presence of Na before and after Br-etching. Small Na contents were measured at the surface, although no Na was expected after Br etching, which could be explained by the fact that the oxidation of CI(G)S should be accompanied by a concomitant Na migration toward the surface, as previously reported for CIGS¹³⁴.

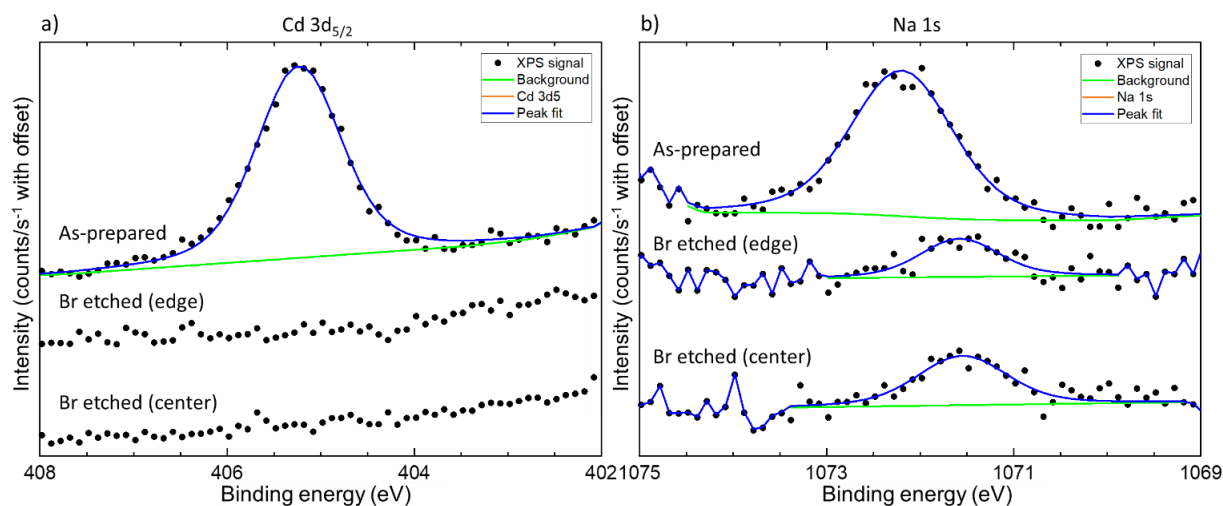


Figure 70 Superimposed XPS spectra for CI(G)S samples recorded in the (a) Cd $3d_{5/2}$ and (b) Na 1s regions. For each graph, from top to bottom: As-prepared CI(G)S sample, edge, and center of a CI(G)S sample after Br-etching (10 min, 80 rpm)

Figure 70 shows the XPS spectra of the Cd 3d_{5/2} region between 402 eV and 408 eV and the Na 1s region between 1069 eV and 1075 eV, for an as-prepared sample and a sample etched for 10 min at 80 rpm. Two spots were investigated by XPS, one at the edge and one at the center of the sample. For the as-prepared sample, a Cd 3d_{5/2} component was identified at 405.2 ± 0.1 eV. This feature confirms that HCl treatment was not entirely effective at removing the CdS protective layer over the surface of CI(G)S. However, it completely disappeared from the surface of treated CI(G)S from both the edge and the center spot XPS spectra. Regarding Na, a single peak could be fitted centered at 1072.2 ± 0.1 eV for the as-prepared sample. The element was still detected after etching, although at a lower intensity with Na 1s components at 1071.6 ± 0.1 eV for both spots.

To conclude, we demonstrated that HCl treatment was not entirely effective at removing the CdS capping layer from the surface of delivered CI(G)S samples. However, no trace of Cd remained after Br-etch treatment. Our analysis also confirmed that alkali leaching occurred during Br-etching and subsequent H₂O rinsing, with a decrease in intensity of the peak corresponding to the Na 1s orbital. The Na presence is most probably inherent to the exposition of the surface to air after the planarization step, as already observed for CIGS. The concentration in Na is susceptible to further decrease after KCN treatment. In general, a change in surface Na concentration would induce consequences in the short term over PV parameters of fabricated solar cells but would be restored over time by migration from the glass substrate.

From XPS analysis, we obtained a qualitative picture over the evolution of the surface chemistry of CI(G)S samples through Br-etching and KCN treatment. In the next sections, we focus on the elemental profile of the as-prepared CI(G)S layer by GD-OES and the evolution through the etching process of the composition at the surface by XPS.

5.2.3.3. Elemental composition of CI(G)S absorber layers by GD-OES

Figure 71 shows the elemental depth profile of an as-prepared co-evaporated CI(G)S sample. Due to the nature of the process and the morphology of the starting material, measurements across the first 100 nanometers of material were not reliable and are thus not taken into account here. Otherwise, atomic percentages in Se, In and Cu were rather constant across the samples at roughly 50 %, 28 % and 20 % respectively. In and Se concentration decrease near the Mo interface, concomitantly with an increase in Ga atomic concentration to 12 %. Ga concentration remained < 1 % within the first 500 nanometers of the material, then increased to 5 % at 1300 nm depth and to 10 % at 1730 nm. Ga concentration never exceeded 14 %, at any CI(G)S depth.

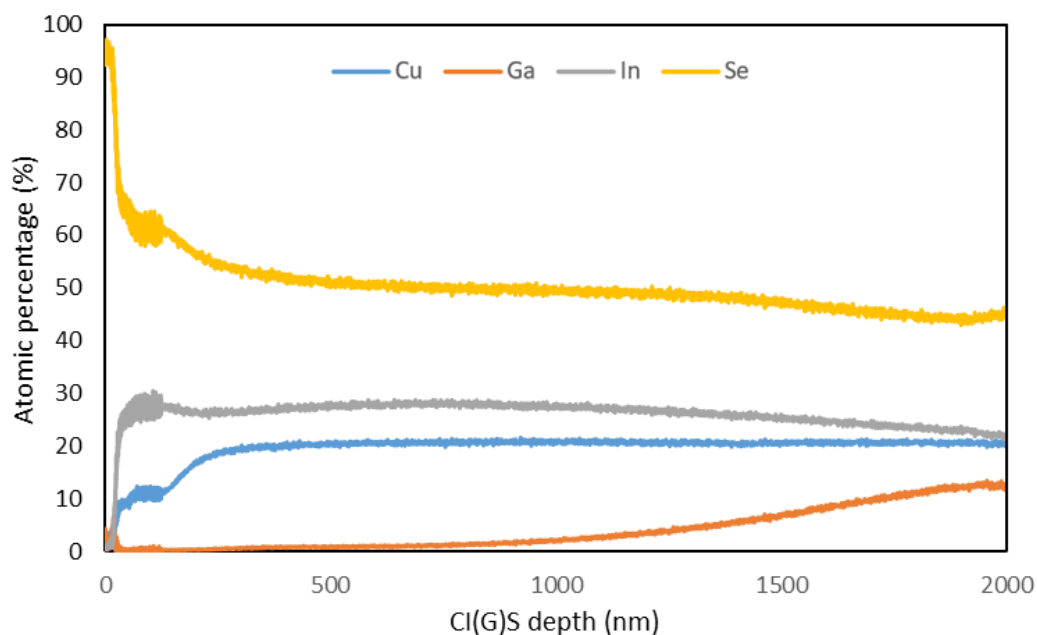


Figure 71 Elemental profile of as-prepared CI(G)S layers prepared by co-evaporation established using GD-OES. CI(G)S depth was measured by cross-section SEM and elemental profiles were calibrated from XRF measurements.

Table 13 shows the bulk atomic percentage of the main constituents of the co-evaporated CI(G)S sample. 36 measurements were recorded across the sample, and lateral homogeneity was found satisfactory with a standard deviation in atomic percentage systematically $< 1\%$ of the average value. The Se, In and Cu overall concentrations roughly corresponds to the one discussed earlier, and Ga overall concentration was measured at $1.13 \pm 0.04\%$ for a GGI ratio of 0.04.

Table 13 Average atomic percentage and standard deviation for the main elements of an as-prepared CI(G)S sample prepared y co-evaporation from XRF measurements at 36 different positions.

Element	Cu	In	Se	Ga
Avg At %	20.47	27.61	50.79	1.13
Std deviation	0.13	0.25	0.24	0.04

Overall, these results indicate a low Ga content with a single concentration grading along the depth of the CI(G)S sample, with a concentration from $< 1\%$ at the front of the sample to 14% at the Mo back contact. Therefore, it might be difficult to detect Ga from both as-prepared and etched samples with surface sensitive techniques such as XPS, as Ga concentration might be within the detection limit for depths up to hundreds of nanometers.

5.2.3.4. Elemental composition of CI(G)S absorber layers by XPS analysis

The elemental composition at the surface was also studied for an as-prepared sample, after etching, and for an etched sample treated by KCN as represented in **Table 14**. The composition of the Br-etched sample was probed at two spots, one at the center and one at the edge of the sample. Concomitantly with the formation of a Se^0 layer at the surface of the samples, atomic percentage of Se increased from 51.7 % to 53.8 % (center) and 62.6 % (edge) after etching, and is accompanied with a decrease in atomic percentages of Cu and In. Percentage in Se was the lowest at 47.8 % for the KCN treated sample, which presented similar Cu and In percentage as compared to the as-prepared sample. Likewise, the atomic percentage of oxygen evolved from 5.6 % to 12.8 % (center) and 16.0 % (edge) after etching, which to some extent might be linked to superficial oxidation of the surface exposed to air after sample extraction of the etching solution, rinsing and drying.

We could also detect Ga after etching. A concentration of approximately 1 % of Ga was revealed after etching, for a final GGI ratio at the surface between 0.05 and 0.1. The CGI ratio also increased, from 1.25 to 1.48 (center) and 2.17 (edge). We didn't detect Ga after Br-etching and KCN treatment, probably due to its low concentration as discussed in 5.2.3.3.

Table 14 Elemental composition of CI(G)S samples before and after Br-etching.

Atomic %	Cu	In	Se	Ga	Na	O	Cd
Reference photopeak	Cu 3p	In 4d	Se 3d	Ga 3d	Na 1s	O 1s	Cd 3d _{5/2}
As-prepared	22.6	18.0	51.7	-	0.9	5.6	1.2
Br-etched (edge)	13.3	6.8	62.6	1.0	0.3	16.0	-
Br-etched (center)	19.3	12.6	53.9	1.3	0.2	12.8	-
Br-etch + KCN	19.9	19.0	47.8	-	0.0	9.5	-

Overall, after etching changes in the CI(G)S stoichiometry at the center of the sample were minor, except for the appearance of buried Ga atoms revealed by the etching process. However, Se is more represented at the edge, and it might be explained by a larger Se^0 superficial layer since no KCN treatment was realized on the studied samples. During spinning, diffusion driven mechanism of ion transfer should indeed favor faster reaction rates at the edge than at the center of the sample, and might have resulted in a thicker Se^0 layer in this region.

After KCN, concentrations in Cu, In, Se and O evolve to reach values close to that of the as-prepared samples. However, Na is still detected to some extent after Br-etching, but is completely removed from the surface after KCN treatment.

5.2.4. J-V and EQE characterization of devices based on as-prepared and smoothed CI(G)S^{xiii}

We now evaluate the PV parameters of complete solar cells based on as-prepared and smoothed CI(G)S absorber layers. As discussed in the previous section, KCN treatment could be used to restore the chemical properties of smoothed CI(G)S absorber layers before integration into solar cells. However, both Br-etching and KCN treatment induce alkali leaching, which temporarily alter the surface chemistry of CI(G)S. Therefore, to quickly evaluate the effect of wet etching on the PV parameters of solar cells and rule out the effect of alkali leaching, KCN treatment was systematically applied on both as-prepared and smoothed CI(G)S absorber layers before solar cell fabrication for the samples studied in this section.

For proof of concept of our treatment on CI(G)S, one solar cell was first completed based on each absorber layer, that is as-prepared and smoothed types.

To compare the PV performances of solar cells before and after wet chemical etching, I first considered two CI(G)S samples of co-evaporation variety and 2*2 cm² area. One complete CI(G)S cell was prepared from a smoothed absorber, after 4 min and 40 rpm bromide etching. Another was prepared based on an as-prepared absorber layer from the same batch for reference. KCN treatment, as well as buffer and window layer deposition were conducted simultaneously for both samples, although using different solutions. The following architecture was completed: Glass/Mo/CI(G)S/Zn(O,S)/ZnMgO/AZO, as described on **Figure 72**.

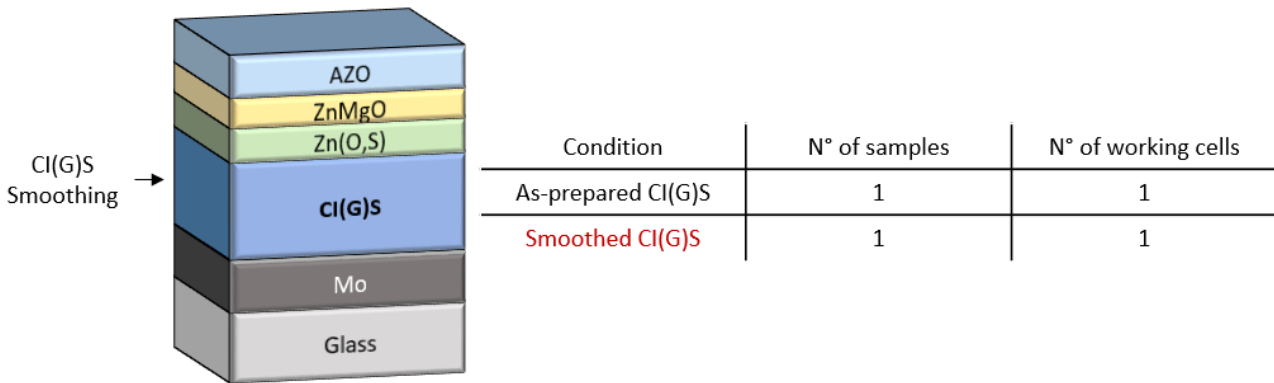


Figure 72 (left) Architecture of solar cells prepared for J-V experiment using either as-prepared or smoothed CI(G)S (right) Number of solar devices prepared and number of working solar cells (i.e. PCE > 1%) per condition.

^{xiii} KC treatment, Zn(O,S) deposition by CBD and ZnMgO/AZO deposition by sputtering were realized by Amelle Rebai.

J-V curves for 0.09 cm² active area solar cells completed out of these samples is shown on **Figure 73**. PV parameters were measured for both cells by 4 probes IV measurements to dampen the effect of the lateral conductivity of the electrodes on fill factor, as this parameter will not affect the efficiency of a 2T tandem solar cell. From **Figure 73b**, Similar V_{oc} of respectively 497 mV and 492 mV were measured before and after smoothing. FF values of respectively 67 % and 69 % were also obtained for both samples. Higher J_{sc} value of 34.2 mA.cm⁻² was nonetheless reported for the solar cell based on as-prepared CI(G)S, against 32.7 mA.cm⁻² for the solar cell completed from a smoothed absorber layer. As a result, corresponding PCE were respectively 11.41 % and 11.01 %.

To investigate more in details this difference in J_{sc} , EQE spectra were measured for both cells. As seen in **Figure 73a**, a slight increase in the EQE was visible in the 400 nm and 600 nm regions of the spectra for the smoothed absorber compared to the as-prepared. These gains, however, were overcompensated by greater losses between 450 and 600 nm and between 750 and 1000 nm. These regions could correspond to the interference fringes of the various zinc oxide based layers on top of CI(G)S, and less intense EQE could be linked to an increase in reflectance due to the mirror-like surface of CI(G)S. Less absorption and conversion was also observed for wavelength > 1100 nm for the smoothed sample.

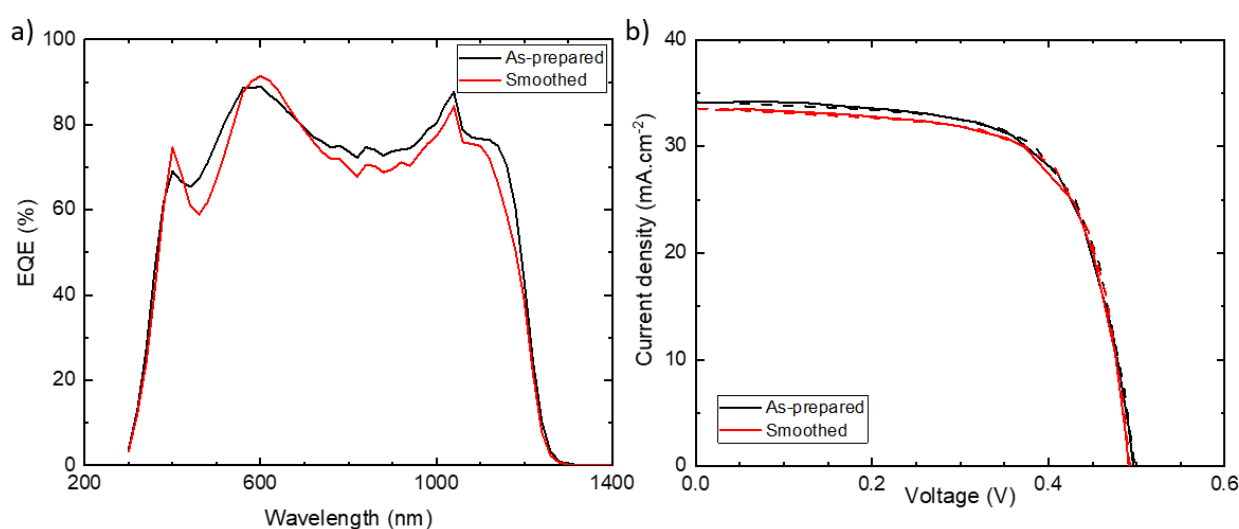


Figure 73 (a) EQE signal and **(b)** J-V curve for CI(G)S solar cells based on as-prepared (black) and smoothed (red) CI(G)S absorbers layers. J-V curve was recorded using a 4 probes setup. Forward and reverse current on J-V curve are depicted in full and dotted lines, respectively.

A less intense EQE spectra in the high band-edge region of the CI(G)S absorption spectrum could be related to a lower thickness of the absorber layer, and carrier generation closer to the Mo/CI(G)S

interface which could be a source of shunt recombination pathways in CI(G)S cells. For both samples, a shoulder in EQE spectra was observed around 1050 nm which is probably a measurement artefact.

These results indicated that KCN was indeed an effective treatment to restore the CI(G)S surface after planarization for solar cell application. Very similar PV parameters were obtained using a smoothed and an as-prepared absorber, with a decrease in J_{sc} for the device based on a smoothed absorber layer. However, our EQE analysis indicated that losses in J_{sc} were partly due to a decrease in carrier generation from low frequency photons, which would play a determinant role for current matching in a 2T tandem. These losses in the high range of wavelength might be partly prevented by using thicker CI(G)S absorber layers as starting material for planarization experiments.

In this subsection, I compared the PV parameters and EQE spectra of solar cells completed from as-prepared and etched CI(G)S layers. These results suggest that similar PV parameters can be obtained out of planarized and as-prepared samples. However, this observation was not systematic and I noted that it was necessary to use different KCN and buffer layer solutions for etched and non-etched samples. Moreover, the J_{sc} of solar cell prepared out of smoothed absorber layers is generally lower as shown by EQE measurements due to a slightly lower thickness and different light scattering dynamics.

These results showed the capability of our process to effectively reduce the surface roughness of CI(G)S absorber layers, with negligible loss in thickness and the possibility to restore the surface chemistry and prepare solar cells of equivalent performances compared to as-prepared absorbers. These results were however based on one solar cell per condition and thus lacked statistical significance. Additionally, the etching setup relying on a rotating sample in solution, which would not be suited for large scale substrates for hydrodynamic reasons. In terms of weight, larger substrates would be also too heavy to be fixed upside down to a rotating electrode. Those observations led us to design a new setup adapted to larger samples, up to 5*5 cm² which presented good preliminary results in terms of homogeneity of the thinning and smoothing (**Figure 74**). The protocol is still under optimization.

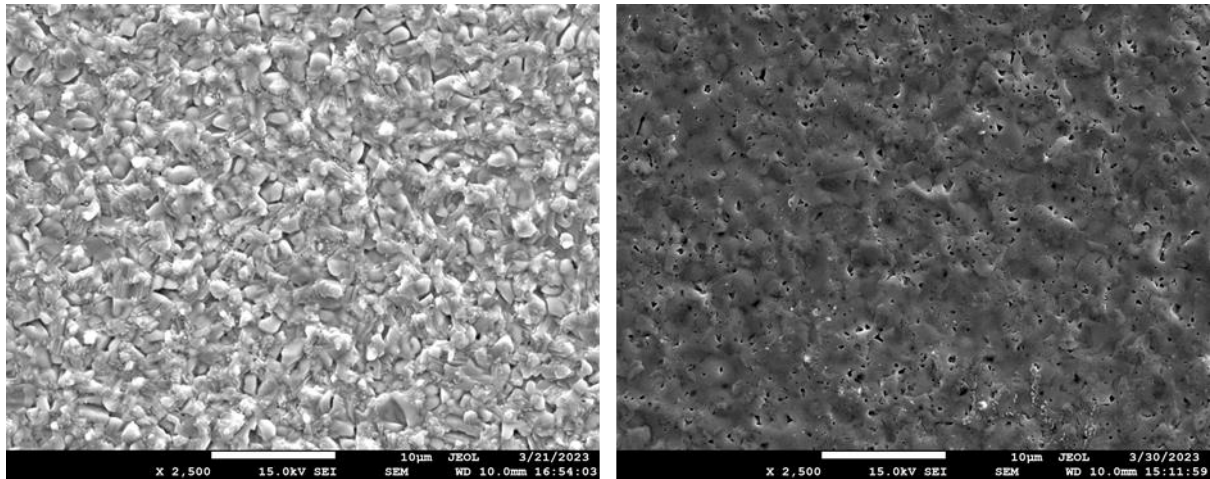


Figure 74 Surface SEM images of a 3.25*3.25 cm² sequential CI(G)S sample before (left) and after (right) etching using a setup adapted for sample sizes in the order of 5*5 cm².

5.3. Interim summary

In this chapter, we describe a wet Br-etching procedure to decrease the roughness of CI(G)S absorber layers and facilitate the process of a perovskite topcell in tandem architecture. This process was essentially based on a method already described for CIGS, and adapted to low bandgap absorber layers. In the first part, we focus of the optimization of the process duration and spinning speed on samples of area inferior or equal to 2*2 cm², in order to minimize the final roughness and the thickness of the sacrificial CI(G)S layer. As a result, determined that etching the sample for 2 min at 40 rpm constituted a good trade-off between both parameters, as its led to RMS roughness values < 20 nm with for a loss of 400 nm.

Then, we verified the thickness homogeneity of as-prepared and smoothed samples, with similar values measured across either 2*2 cm² sample and a good homogeneity of the parent 5*5 cm² CI(G)S sample. We also demonstrated the reproducibility of our protocol by analysing the composition of our etching solutions after smoothing with ICP-OES. Indeed, a strong linear correlation between concentrations in Cu, In and Se and treatment time at 40 rpm was observed, and these concentrations were rather similar for three samples treated for 4 min at 30 rpm

We therefore studied the effect of the Br-etch treatment, either followed by KCN treatment or not over the surface chemistry of CI(G)S. It was heavily altered by the formation of a superficial Se⁰ layer on top of the layer, oxidation of indium species, and partial leaching of Na. The original chemistry of Se and In was mostly restored after KCN treatment, but concentration in Na was still lower to that of the pristine layer. Moreover, concentrations in Cu, In stayed rather similar between the pristine and

Br-treated samples, while Se concentration slightly increased and Ga started to appear as a constituent of the surface.

Finally, we prepared solar cells based on as-prepared and smoothed absorber layers, both after KCN treatment. For one device of each condition, similar PV parameters were observed except for J_{sc} which was slightly higher for the as-prepared sample, leading to a slight increase in PCE. Indeed, a mirror-like surface is obtained after planarization which is less efficient than rough CI(G)S at trapping reflected photons back in the layer. This difference likely led to a decrease in intensity in region of the EQE distinctive of interference fringes for zinc oxide based layers, such as ZnMgO and AZO layers employed for the devices. Overall, we demonstrated that the etching process designed for CIGS could readily be adapted to low bandgap CI(G)S. However, J-V measurements should be repeated on a bigger set of samples to further confirm that V_{oc} and FF are not affected by the treatment.

Conclusion and Suggestions

This doctoral thesis aimed to study and overcome different challenges linked to the monolithic integration of perovskite/CI(G)S tandem solar cells. They are principally linked to the necessary adaptation of the topcell fabrication processes on top of the CI(G)S substrates, i.e. the need for low-temperature deposition methods and for conformal deposition on top of a rough surface. An alternative to conformal deposition would be to diminish the roughness of the CI(G)S substrate by etching in acidic media. Additionally, the semi-transparent perovskite topcell should be designed in p-i-n configuration for proper polarization of the device. Here we proposed to explore low-temperature routes for conformable deposition of the HTL, the development of a protective layer for sputtering processes in semi-transparent perovskite solar cells as well as the bromide etching of CI(G)S absorber layers to reduce their thickness and facilitate the deposition of the topcell layers.

Low temperature HTL development

We first described a protocol inspired from previous publications to evaluate the electron blocking properties of NiO_x layers prepared by ALD, and reviewed the different difficulties in interpreting the result from our cyclic voltammetry setup. We nonetheless demonstrated a conformal coverage of the NiO_x layer on top of ITO, and determined that a thickness of 10 nm for the 100 °C prepared samples and of 15 nm for those prepared at 160 °C would be optimal for solar cell fabrication as a trade-off between electron blocking layer properties and resistivity along the axis perpendicular to the substrate.

Then, we studied the chemical and electronic properties of different NiO_x samples prepared by ALD and sputtering provided by our partners ZSW, KIT and IMEC. Those studies mainly aimed to relate temperature deposition and post-annealing temperature to physical properties and chemical composition of the layers. For sputtering deposited samples prepared by KIT, the effects of the oxygen flux over these properties during deposition were also studied. To some extent, we could link the evolution of the O 1s principal peak position toward higher energy to a decrease in WF from sample to sample, and possibly to an increase in the percentage of stoichiometric NiO in their relative composition. For perovskite solar cells prepared from ALD-NiO_x layers provided by ZSW, we could associate this increase in percentage of stoichiometric NiO to higher PCE values. However, while the observed tendencies were rather consistent from sample to sample their magnitude was subtle for most series of samples. We nonetheless hypothesized that the effect was more pronounced after post-annealing treatment than by varying deposition temperature.

By employing XPS analysis, we also studied the effects of UV-O₃ treatment followed by a short annealing step on NiO_x layers prepared by sol-gel and combustion processes. We could link UV-O₃ treatment to a decrease in the relative proportion of stoichiometric NiO in the sample, but results were more ambiguous when studying the effect of the subsequent annealing step. Nonetheless, complete devices fabricated from this last UV-O₃ + A condition exhibited significantly higher PCE values on average compared to those prepared from UV-O₃ treated samples, mainly due to an increase in *FF*. We hypothesized that the short annealing step resulted in a higher proportion of Ni²⁺ states at the surface of the NiO_x layers compared to the UV-O₃ treated samples, and that the trends in PCE were in accordance to the observations of Boyd et al. although for different reasons⁸⁷. Treating UV-O₃ + A samples with FAI to further increase the Ni²⁺ sites concentration yielded the highest efficiencies in devices, but rather due to an increase in *V*_{oc} while *FF* values were lowered compared to the simple UV-O₃ + A condition, which was more in line with their observations.

Finally, we studied the substitution of the NiO_x HTL by a self-assembly of small molecules composed of either 2PACz or MeO-2PACz. Fabricated devices yielded comparable PCE compared to that obtained from FAI treated NiO_x layers, and only subtle differences in PV parameters were observed from either organic HTL. We then characterized perovskite samples deposited on either NiO_x or MeO-2PACz by XRD, and concluded that deposition on the SAM HTL resulted in a preferred orientation in the (001) axis. In other studies, this crystalline orientation was linked to better optoelectronic properties for MAPI layers, hence in future steps of development we integrated MeO-2PACz either as an interfacial layer between perovskite and NiO_x or as an HTL of its own.

Semi-transparent perovskite solar cells for monolithic integration

Our first attempts at adapting the p-i-n opaque perovskite cell design to a semi-transparent architecture by using an ETL bilayer of organic compounds (PCBM and BCP) resulted in suboptimal PV performances, due to the harsh sputtering process employed for TCO deposition. We then implemented nanoparticles composed of either ZnO or AZO on top of the PCBM layer as a substitute to BCP, which resulted in equivalent if not higher PCE values in opaque devices. Further optimization steps led to the exclusive use of a PCBM/np-ZnO ETL bilayer over PCBM/np-AZO for the fabrication of devices, due to faster degradation of PV performances observed after storing the samples in vacuum.

We then fabricated semi-transparent devices based on the PCBM/np-ZnO ETL and a sputtered AZO window layer, which yielded reasonable performances under rear illumination. However, significant losses in *J*_{sc} were observed under front illumination, certainly for optical reasons.

Therefore, we characterized by J-V measurements and EQE solar cells prepared using either PCBM/ η p-ZnO or C₆₀/ALD-SnO₂ as ETL and either ITO or AZO as conductive window layer. Under both front and rear illumination, best PV performances were obtained with the combination of C₆₀/SnO₂ with ITO. From EQE spectra, it was noted that this configuration led to higher conversion of photons over portions of the solar spectrum, resulting in higher J_{sc} values. This result was likely mainly driven by a higher transmittance from combining C₆₀/SnO₂ and ITO.

CI(G)S morphological adaptation for monolithic integration

Here we proposed to adapt a well-established protocol for CIGS Br-etching to low bandgap Ci(G)S layers. First, we optimized the rotation speed and the duration parameters, and a trade-off between RMS roughness reduction to < 20 nm and lower amounts of dissolved material of 600 nm are retained after etching the films at 40 rpm for 2 min. Etched films visually presented a flat, mirror-like surface. Moreover, based on the morphology of the parent 5*5 cm² sample, we established that our process did not induce variation in homogeneity between samples. We also demonstrated the high accuracy of the process, with etching solution concentrations in Cu, In and Se proportional to the dipping time at 40 rpm.

We then analysed the qualitative and quantitative compositions of pristine, Br-etched and Br-etched then KCN treated samples by XPS measurements. These measurements revealed the formation of a Se⁰ elemental layer on top of CI(G)S after etching and oxidation of In species, in accordance to previous reports. Additionally, KCN treatment was efficient at treating Se⁰ phases to recover a pristine-like surface composed of mainly Se from the CI(G)S crystal. Na leaching was observed after either treatment, which is a reversible process due to migration of the element from the glass substrate to the surface of CI(G)S. Ga concentration at the surface was also higher after Br-etching from nearly zero to a few percent, as expected from single-graded CI(G)S layers.

Finally, devices were prepared out of pristine and planarized CI(G)S absorber layers. J-V measurements were carried out on one device of each condition, hence lacking statistical significance. Nonetheless, similar PV parameters were observed except for a slightly higher J_{sc} value for the as-prepared sample, leading to a slight increase in PCE. Indeed, the mirror-like surface obtained after planarization would be less efficient at trapping reflected photons back in the layer than rough CI(G)S. Likely, this difference led to a decrease in intensity in regions of the EQE spectra that could correspond to interference fringes for zinc oxide based layers, such as the ZnMgO and AZO layers employed for the devices. These results showed, at least, that it was possible to reach comparable PV performances from pristine and smoothed absorber layers.

Prospective

A setup for Br-etching on larger size substrates has been used at ILV to smoothen CI(G)S samples prepared by sequential deposition^{xiv}. Despite promising results^{xv}, solar cells prepared from such samples did not work and we still plan to use this setup on co-evaporated CIGS samples to prepare single junction and tandem solar cells.

Based on the development of Chapter 3 and 4, monolithic tandem solar cells prototypes were prepared based on a full-house IPVF process^{xvi}.

For the first prototype, the subcell consisted in a co-evaporated CIGS absorber layer deposited on Mo, followed by Zn(O,S) buffer layer deposition then ZnMgO and AZO sputtering. The HTL of the double cation perovskite layer consisted in a bilayer of ALD-NiO_x and an organic MeO-2PACz layer. The 1*2.5cm² substrate was divided in 8 cells, with the following PV parameters for the champion cells: $V_{oc} = 1.31$ V, $J_{sc} = 8.60$ mA.cm⁻², $FF = 21.1$ % and $PCE = 2.40$ %.

Regarding the second prototype, the subcell consisted in a co-evaporated low bandgap CI(G)S absorber layer deposited on Mo, followed by Zn(O,S) buffer layer deposition then ZnMgO and AZO sputtering. The HTL of the double cation perovskite layer consisted in a single MeO-2PACz layer. The 2.5*2.5cm² substrate was divided in 6 cells, with the following PV parameters for the champion cells: $V_{oc} = 1.09$ V, $J_{sc} = 14.12$ mA.cm⁻², $FF = 50.14$ % and $PCE = 7.75$ %.

Both perovskite topcells were completed by deposition of a PCBM/np-ZnO ETL bilayer and sputtered AZO as a window layer.

As further steps of development, we propose to implement the different low temperature HTL materials discussed in Chapter 3 to fully completed two terminal perovskite/CI(G)S tandem devices. Indeed, it is still unclear whether a single NiO_x layer, a SAM monolayer or a combination of the two as a bilayer would be the optimal choice of HTL in single junction or two-terminal tandems.

Furthermore, we showed that the CI(G)S planarization process discussed in Chapter 5 had subtle yet detrimental effects in PV parameters of complete CI(G)S solar cells. Further studies need to be conducted to determine the implication of this treatment on monolithic tandem devices. The roughness of as-prepared co-evaporated CI(G)S layers prepared for this study might be already sufficiently low for conformal deposition of perovskite top cell layers, however the smoothing

^{xiv} Large-scale setup for planarization and smoothing experiments on sequential CI(G)S samples have been realized by Muriel Bouttemy and Arnaud Etcheberry.

^{xv} AFM images were acquired by José Alvarez at GEEPS.

^{xvi} CI(G)S and CIGS subcells were manufactured by Amelle Rebai and Jackson Lontchi, as well as AZO sputtering deposition for the perovskite topcell window layer.

Prospective

process could be relevant for sequential CI(G)S layers which usually exhibit higher mean roughness values. Preliminary results using a setup adapted to 5*5 cm² samples suggest that it could be difficult to obtain a morphology suited for solar cell fabrication after smoothing CI(G)S layers prepared by sequential deposition.

References

- (1) Solar PV. <https://www.iea.org/reports/solar-pv> (accessed 2023-05-31).
- (2) Documenting a Decade of Cost Declines for PV Systems. NREL. <https://www.nrel.gov/news/program/2021/documenting-a-decade-of-cost-declines-for-pv-systems.html> (accessed 2023-05-31).
- (3) Lin, Q.; Huang, H.; Jing, Y.; Fu, H.; Chang, P.; Li, D.; Yao, Y.; Fan, Z. Flexible Photovoltaic Technologies. *J. Mater. Chem. C* **2014**, *2* (7), 1233. <https://doi.org/10.1039/c3tc32197e>.
- (4) Kim, S.; Quy, H. V.; Bark, C. W. Photovoltaic Technologies for Flexible Solar Cells: Beyond Silicon. *Mater. Today Energy* **2021**, *19*, 100583. <https://doi.org/10.1016/j.mtener.2020.100583>.
- (5) Ruiz-Preciado, M. A.; Gota, F.; Fassel, P.; Hossain, I. M.; Singh, R.; Laufer, F.; Schackmar, F.; Feeney, T.; Farag, A.; Allegro, I.; Hu, H.; Gharibzadeh, S.; Nejang, B. A.; Gevaerts, V. S.; Simor, M.; Bolt, P. J.; Paetzold, U. W. Monolithic Two-Terminal Perovskite/CIS Tandem Solar Cells with Efficiency Approaching 25%. *ACS Energy Lett.* **2022**, 2273–2281. <https://doi.org/10.1021/acseenergylett.2c00707>.
- (6) Wurfel, U.; Cuevas, A.; Wurfel, P. Charge Carrier Separation in Solar Cells. *IEEE J. Photovolt.* **2015**, *5* (1), 461–469. <https://doi.org/10.1109/JPHOTOV.2014.2363550>.
- (7) Lipovšek, B.; Smole, F.; Topič, M.; Humar, I.; Sinigoj, A. R. Driving Forces and Charge-Carrier Separation in p-n Junction Solar Cells. *AIP Adv.* **2019**, *9* (5), 055026. <https://doi.org/10.1063/1.5092948>.
- (8) Basic Characteristics and Characterization of Solar Cells. In *Materials Concepts for Solar Cells; WORLD SCIENTIFIC (EUROPE)*, 2018; pp 3–43. https://doi.org/10.1142/9781786344496_0001.
- (9) Shockley, W.; Queisser, H. J. Detailed Balance Limit of Efficiency of P-n Junction Solar Cells. **11**.
- (10) Rühle, S. Tabulated Values of the Shockley–Queisser Limit for Single Junction Solar Cells. *Sol. Energy* **2016**, *130*, 139–147. <https://doi.org/10.1016/j.solener.2016.02.015>.
- (11) Best Research-Cell Efficiency Chart, 2023. <https://www.nrel.gov/pv/cell-efficiency.html>.
- (12) Vos, A. D. Detailed Balance Limit of the Efficiency of Tandem Solar Cells. *J. Phys. Appl. Phys.* **1980**, *13* (5), 839–846. <https://doi.org/10.1088/0022-3727/13/5/018>.
- (13) Bremner, S. P.; Levy, M. Y.; Honsberg, C. B. Analysis of Tandem Solar Cell Efficiencies under AM1.5G Spectrum Using a Rapid Flux Calculation Method. *Prog. Photovolt. Res. Appl.* **2008**, *16* (3), 225–233. <https://doi.org/10.1002/pip.799>.
- (14) De Bastiani, M.; Subbiah, A. S.; Aydin, E.; Isikgor, F. H.; Allen, T. G.; De Wolf, S. Recombination Junctions for Efficient Monolithic Perovskite-Based Tandem Solar Cells: Physical Principles, Properties, Processing and Prospects. *Mater. Horiz.* **2020**, *7* (11), 2791–2809. <https://doi.org/10.1039/D0MH00990C>.
- (15) Würfel, P.; Würfel, U. *Physics of Solar Cells: From Basic Principles to Advanced Concepts*, 3rd edition.; Wiley-VCH Verlag GmbH & Co. KGaA: Weinheim, 2016.
- (16) Hahn, H.; Frank, G.; Klingler, W.; Meyer, A.-D.; Störger, G. Untersuchungen über ternäre Chalkogenide. V. über einige ternäre Chalkogenide mit Chalkopyritstruktur. *Z. Für Anorg. Allg. Chem.* **1953**, *271* (3–4), 153–170. <https://doi.org/10.1002/zaac.19532710307>.
- (17) <https://www.nrel.gov/pv/cell-efficiency.html> (Accessed on 9 June 2022).
- (18) Uhl, A. R.; Rajagopal, A.; Clark, J. A.; Murray, A.; Feurer, T.; Buecheler, S.; Jen, A. K. -Y.; Hillhouse, H. W. Solution-Processed Low-Bandgap CuIn(S,Se)₂ Absorbers for High-Efficiency Single-Junction and Monolithic Chalcopyrite-Perovskite Tandem Solar Cells. *Adv. Energy Mater.* **2018**, *8* (27), 1801254. <https://doi.org/10.1002/aenm.201801254>.
- (19) Uhl, A. R.; Yang, Z.; Jen, A. K.-Y.; Hillhouse, H. W. Solution-Processed Chalcopyrite-Perovskite Tandem Solar Cells in Bandgap-Matched Two- and Four-Terminal Architectures. *J. Mater. Chem. A* **2017**, *5* (7), 3214–3220. <https://doi.org/10.1039/C7TA00562H>.
- (20) Feurer, T.; Carron, R.; Torres Sevilla, G.; Fu, F.; Pisoni, S.; Romanyuk, Y. E.; Buecheler, S.; Tiwari, A. N. Efficiency Improvement of Near-Stoichiometric CuInSe₂ Solar Cells for

- Application in Tandem Devices. *Adv. Energy Mater.* **2019**, *9* (35), 1901428. <https://doi.org/10.1002/aenm.201901428>.
- (21) Feurer, T.; Fu, F.; Weiss, T. P.; Avancini, E.; Löckinger, J.; Buecheler, S.; Tiwari, A. N. RbF Post Deposition Treatment for Narrow Bandgap Cu(In,Ga)Se₂ Solar Cells. *Thin Solid Films* **2019**, *670*, 34–40. <https://doi.org/10.1016/j.tsf.2018.12.003>.
- (22) Rendement Record de 21,4% Pour Les Cellules Solaires Flexibles. www.empa.ch/web/s604/cigs-efficiency-record-2021 (accessed 2023-05-15).
- (23) Klinkert, T.; Jubault, M.; Donsanti, F.; Lincot, D.; Guillemoles, J.-F. Differential In-Depth Characterization of Co-Evaporated Cu(In,Ga)Se₂ Thin Films for Solar Cell Applications. *Thin Solid Films* **2014**, *558*, 47–53. <https://doi.org/10.1016/j.tsf.2014.02.071>.
- (24) Lv, X.; Zheng, Z.; Zhao, M.; Wang, H.; Zhuang, D. Investigation on Preparation and Performance of High Ga CIGS Absorbers and Their Solar Cells. *Materials* **2023**, *16* (7), 2806. <https://doi.org/10.3390/ma16072806>.
- (25) Ramanujam, J.; Singh, U. P. Copper Indium Gallium Selenide Based Solar Cells – a Review. *Energy Environ. Sci.* **2017**, *10* (6), 1306–1319. <https://doi.org/10.1039/C7EE00826K>.
- (26) Parisi, A.; Pernice, R.; Rocca, V.; Curcio, L.; Stivala, S.; Cino, A. C.; Cipriani, G.; Di Dio, V.; Ricco Galluzzo, G.; Miceli, R.; Busacca, A. C. Graded Carrier Concentration Absorber Profile for High Efficiency CIGS Solar Cells. *Int. J. Photoenergy* **2015**, *2015*, 1–9. <https://doi.org/10.1155/2015/410549>.
- (27) Zhang, S. B.; Wei, S.-H.; Zunger, A.; Katayama-Yoshida, H. Defect Physics of the CuInSe₂ Chalcopyrite Semiconductor.
- (28) Sun, Y.; Lin, S.; Li, W.; Cheng, S.; Zhang, Y.; Liu, Y.; Liu, W. Review on Alkali Element Doping in Cu(In,Ga)Se₂ Thin Films and Solar Cells. *Engineering* **2017**, *3* (4), 452–459. <https://doi.org/10.1016/J.ENG.2017.04.020>.
- (29) Ong, K. H.; Agileswari, R.; Maniscalco, B.; Arnou, P.; Kumar, C. C.; Bowers, J. W.; Marsadek, M. B. Review on Substrate and Molybdenum Back Contact in CIGS Thin Film Solar Cell. *Int. J. Photoenergy* **2018**, *2018*, 1–14. <https://doi.org/10.1155/2018/9106269>.
- (30) Zhao, W.; Yao, Z.; Guo, R.; Yu, F.; Wu, G.; Liu, S. F. Low-Temperature-Processed CdS as the Electron Selective Layer in an Organometal Halide Perovskite Photovoltaic Device. *Part. Part. Syst. Charact.* **2018**, *35* (8), 1800137. <https://doi.org/10.1002/ppsc.201800137>.
- (31) Gour, K. S.; Parmar, R.; Kumar, R.; Singh, V. N. Cd-Free Zn(O,S) as Alternative Buffer Layer for Chalcogenide and Kesterite Based Thin Films Solar Cells: A Review. *J. Nanosci. Nanotechnol.* **2020**, *20* (6), 3622–3635. <https://doi.org/10.1166/jnn.2020.17537>.
- (32) Zhang, G.; Monllor-Satoca, D.; Choi, W. Band Energy Levels and Compositions of CdS-Based Solid Solution and Their Relation with Photocatalytic Activities. *Catal. Sci. Technol.* **2013**, *3* (7), 1790. <https://doi.org/10.1039/c3cy00066d>.
- (33) Scheer, R.; Messmann-Vera, L.; Klenk, R.; Schock, H.-W. On the Role of Non-Doped ZnO in CIGSe Solar Cells: Non-Doped ZnO in CIGSe Solar Cells. *Prog. Photovolt. Res. Appl.* **2012**, *20* (6), 619–624. <https://doi.org/10.1002/pip.1185>.
- (34) Kojima, A.; Teshima, K.; Shirai, Y.; Miyasaka, T. Organometal Halide Perovskites as Visible-Light Sensitizers for Photovoltaic Cells. *J. Am. Chem. Soc.* **2009**, *131* (17), 6050–6051. <https://doi.org/10.1021/ja809598r>.
- (35) Masi, S.; Gualdrón-Reyes, A. F.; Mora-Seró, I. Stabilization of Black Perovskite Phase in FAPbI₃ and CsPbI₃. *ACS Energy Lett.* **2020**, *5* (6), 1974–1985. <https://doi.org/10.1021/acsenerylett.0c00801>.
- (36) Braunger, S.; Mundt, L. E.; Wolff, C. M.; Mews, M.; Rehmann, C.; Jošt, M.; Tejada, A.; Eisenhauer, D.; Becker, C.; Guerra, J. A.; Unger, E.; Korte, L.; Neher, D.; Schubert, M. C.; Rech, B.; Albrecht, S. Cs_xFA_{1-x}Pb(I_{1-y}Br_y)₃ Perovskite Compositions: The Appearance of Wrinkled Morphology and Its Impact on Solar Cell Performance. *J. Phys. Chem. C* **2018**, *122* (30), 17123–17135. <https://doi.org/10.1021/acs.jpcc.8b06459>.
- (37) Zhang, M.; Yun, J. S.; Ma, Q.; Zheng, J.; Lau, C. F. J.; Deng, X.; Kim, J.; Kim, D.; Seidel, J.; Green, M. A.; Huang, S.; Ho-Baillie, A. W. Y. High-Efficiency Rubidium-Incorporated

- Perovskite Solar Cells by Gas Quenching. *ACS Energy Lett.* **2017**, *2* (2), 438–444. <https://doi.org/10.1021/acsenergylett.6b00697>.
- (38) Boyd, C. C.; Cheacharoen, R.; Leijtens, T.; McGehee, M. D. Understanding Degradation Mechanisms and Improving Stability of Perovskite Photovoltaics. *Chem. Rev.* **2019**, *119* (5), 3418–3451. <https://doi.org/10.1021/acs.chemrev.8b00336>.
- (39) Leung, T. L.; Ahmad, I.; Syed, A. A.; Ng, A. M. C.; Popović, J.; Djurišić, A. B. Stability of 2D and Quasi-2D Perovskite Materials and Devices. *Commun. Mater.* **2022**, *3* (1), 63. <https://doi.org/10.1038/s43246-022-00285-9>.
- (40) Jošt, M.; Bertram, T.; Koushik, D.; Marquez, J. A.; Verheijen, M. A.; Heinemann, M. D.; Köhnen, E.; Al-Ashouri, A.; Braunger, S.; Lang, F.; Rech, B.; Unold, T.; Creatore, M.; Lauermann, I.; Kaufmann, C. A.; Schlattmann, R.; Albrecht, S. 21.6%-Efficient Monolithic Perovskite/Cu(In,Ga)Se₂ Tandem Solar Cells with Thin Conformal Hole Transport Layers for Integration on Rough Bottom Cell Surfaces. *ACS Energy Lett.* **2019**, *4* (2), 583–590. <https://doi.org/10.1021/acsenergylett.9b00135>.
- (41) Al-Ashouri, A.; Magomedov, A.; Roß, M.; Jošt, M.; Talaikis, M.; Chistiakova, G.; Bertram, T.; Márquez, J. A.; Köhnen, E.; Kasparavičius, E.; Levenco, S.; Gil-Escrig, L.; Hages, C. J.; Schlattmann, R.; Rech, B.; Malinauskas, T.; Unold, T.; Kaufmann, C. A.; Korte, L.; Niaura, G.; Getautis, V.; Albrecht, S. Conformal Monolayer Contacts with Lossless Interfaces for Perovskite Single Junction and Monolithic Tandem Solar Cells. *Energy Environ. Sci.* **2019**, *12* (11), 3356–3369. <https://doi.org/10.1039/C9EE02268F>.
- (42) Koushik, D.; Jošt, M.; Dučinskas, A.; Burgess, C.; Zardetto, V.; Weijtens, C.; Verheijen, M. A.; Kessels, W. M. M.; Albrecht, S.; Creatore, M. Plasma-Assisted Atomic Layer Deposition of Nickel Oxide as Hole Transport Layer for Hybrid Perovskite Solar Cells. *J. Mater. Chem. C* **2019**, *7* (40), 12532–12543. <https://doi.org/10.1039/C9TC04282B>.
- (43) George, S. M. Atomic Layer Deposition: An Overview. *Chem. Rev.* **2010**, *110* (1), 111–131. <https://doi.org/10.1021/cr900056b>.
- (44) Zardetto, V.; Williams, B. L.; Perrotta, A.; Di Giacomo, F.; Verheijen, M. A.; Andriessen, R.; Kessels, W. M. M.; Creatore, M. Atomic Layer Deposition for Perovskite Solar Cells: Research Status, Opportunities and Challenges. *Sustain. Energy Fuels* **2017**, *1* (1), 30–55. <https://doi.org/10.1039/C6SE00076B>.
- (45) Ghosh, S.; Mishra, S.; Singh, T. Antisolvents in Perovskite Solar Cells: Importance, Issues, and Alternatives. *Adv. Mater. Interfaces* **2020**, *7* (18), 2000950. <https://doi.org/10.1002/admi.202000950>.
- (46) Jackson, P.; Hariskos, D.; Wuerz, R.; Kiowski, O.; Bauer, A.; Friedlmeier, T. M.; Powalla, M. Properties of Cu(In,Ga)Se₂ Solar Cells with New Record Efficiencies up to 21.7%: Properties of Cu(In,Ga)Se₂ Solar Cells with New Record Efficiencies up to 21.7%. *Phys. Status Solidi RRL - Rapid Res. Lett.* **2015**, *9* (1), 28–31. <https://doi.org/10.1002/pssr.201409520>.
- (47) Jackson, P.; Wuerz, R.; Hariskos, D.; Lotter, E.; Witte, W.; Powalla, M. Effects of Heavy Alkali Elements in Cu(In,Ga)Se₂ Solar Cells with Efficiencies up to 22.6%. *Phys. Status Solidi RRL - Rapid Res. Lett.* **2016**, *10* (8), 583–586. <https://doi.org/10.1002/pssr.201600199>.
- (48) Schöldström, J. *Thermal Radiation from Co-Evaporated Cu(In, Ga)Se₂ End Point Detection and Process Control*; Acta Universitatis Upsaliensis: Uppsala, 2012.
- (49) Klinkert, T.; Hildebrandt, T.; Jubault, M.; Donsanti, F.; Guillemoles, J.-F.; Naghavi, N. Adaptation of the Surface-near Ga Content in Co-Evaporated Cu(In,Ga)Se₂ for CdS versus Zn(S,O)-Based Buffer Layers. *Thin Solid Films* **2015**, *582*, 295–299. <https://doi.org/10.1016/j.tsf.2014.09.074>.
- (50) Dong, C.; Hu, D.; Ben Tayeb, K.; Simon, P.; Addad, A.; Trentesaux, M.; De Souza, D. O.; Chernyak, S.; Peron, D. V.; Rebai, A.; Guillemoles, J.-F.; Wallart, X.; Grandidier, B.; Khodakov, A. Y.; Naghavi, N.; Ordonsky, V. V. Photocatalytic Partial Oxidation of Methane to Carbon Monoxide and Hydrogen over CIGS Solar Cell. *Appl. Catal. B Environ.* **2023**, *325*, 122340. <https://doi.org/10.1016/j.apcatb.2022.122340>.
- (51) Park, S.-U.; Sharma, R.; Ashok, K.; Kang, S.; Sim, J.-K.; Lee, C.-R. A Study on Composition, Structure and Optical Properties of Copper-Poor CIGS Thin Film Deposited by Sequential

- Sputtering of CuGa/In and In/(CuGa+In) Precursors. *J. Cryst. Growth* **2012**, *359*, 1–10. <https://doi.org/10.1016/j.jcrysgro.2012.08.013>.
- (52) Guire, M. R. D.; Bauermann, L. P.; Parikh, H.; Bill, J. Chemical Bath Deposition. In *Chemical Solution Deposition of Functional Oxide Thin Films*; Schneller, T., Waser, R., Kosec, M., Payne, D., Eds.; Springer Vienna: Vienna, 2013; pp 319–339. https://doi.org/10.1007/978-3-211-99311-8_14.
- (53) Depla, D.; Mahieu, S.; Greene, J. E. Sputter Deposition Processes. In *Handbook of Deposition Technologies for Films and Coatings*; Elsevier, 2010; pp 253–296. <https://doi.org/10.1016/B978-0-8155-2031-3.00005-3>.
- (54) Canava, B.; Guillemoles, J. F.; Vigneron, J.; Lincot, D.; Etcheberry, A. Chemical Elaboration of Well Defined Cu(In,Ga)Se₂ Surfaces after Aqueous Oxidation Etching. *J. Phys. Chem. Solids* **2003**, *64* (9–10), 1791–1796. [https://doi.org/10.1016/S0022-3697\(03\)00201-4](https://doi.org/10.1016/S0022-3697(03)00201-4).
- (55) Bouttemy, M.; Tran-Van, P.; Gerard, I.; Hildebrandt, T.; Causier, A.; Pelouard, J. L.; Dagher, G.; Jehl, Z.; Naghavi, N.; Voorwinden, G.; Dimmler, B.; Powalla, M.; Guillemoles, J. F.; Lincot, D.; Etcheberry, A. Thinning of CIGS Solar Cells: Part I: Chemical Processing in Acidic Bromine Solutions. *Thin Solid Films* **2011**, *519* (21), 7207–7211. <https://doi.org/10.1016/j.tsf.2010.12.219>.
- (56) Jehl, Z.; Erfurth, F.; Naghavi, N.; Lombez, L.; Gerard, I.; Bouttemy, M.; Tran-Van, P.; Etcheberry, A.; Voorwinden, G.; Dimmler, B.; Wischmann, W.; Powalla, M.; Guillemoles, J. F.; Lincot, D. Thinning of CIGS Solar Cells: Part II: Cell Characterizations. *Thin Solid Films* **2011**, *519* (21), 7212–7215. <https://doi.org/10.1016/j.tsf.2010.12.224>.
- (57) Ermrich, M.; Opper, D. *XRD for the Analyst: Getting Acquainted with the Principles*, 2nd revised edition.; PANalytical: Almelo, 2013.
- (58) Jalili, N.; Laxminarayana, K. A Review of Atomic Force Microscopy Imaging Systems: Application to Molecular Metrology and Biological Sciences. *Mechatronics* **2004**, *14* (8), 907–945. <https://doi.org/10.1016/j.mechatronics.2004.04.005>.
- (59) Melitz, W.; Shen, J.; Kummel, A. C.; Lee, S. Kelvin Probe Force Microscopy and Its Application. *Surf. Sci. Rep.* **2011**, *66* (1), 1–27. <https://doi.org/10.1016/j.surfrep.2010.10.001>.
- (60) Akhtar, K.; Khan, S. A.; Khan, S. B.; Asiri, A. M. Scanning Electron Microscopy: Principle and Applications in Nanomaterials Characterization. In *Handbook of Materials Characterization*; Sharma, S. K., Ed.; Springer International Publishing: Cham, 2018; pp 113–145. https://doi.org/10.1007/978-3-319-92955-2_4.
- (61) Béchu, S.; Ralairisoa, M.; Etcheberry, A.; Schulz, P. Photoemission Spectroscopy Characterization of Halide Perovskites. *Adv. Energy Mater.* **2020**, *10* (26), 1904007. <https://doi.org/10.1002/aenm.201904007>.
- (62) Stevie, F. A.; Donley, C. L. Introduction to X-Ray Photoelectron Spectroscopy. *J. Vac. Sci. Technol. A* **2020**, *38* (6), 063204. <https://doi.org/10.1116/6.0000412>.
- (63) Doh, W. H.; Papaefthimiou, V.; Zafeiratos, S. Applications of Synchrotron-Based X-Ray Photoelectron Spectroscopy in the Characterization of Nanomaterials. In *Surface Science Tools for Nanomaterials Characterization*; Kumar, C. S. S. R., Ed.; Springer Berlin Heidelberg: Berlin, Heidelberg, 2015; pp 317–366. https://doi.org/10.1007/978-3-662-44551-8_9.
- (64) Hoye, R. L. Z.; Schulz, P.; Schelhas, L. T.; Holder, A. M.; Stone, K. H.; Perkins, J. D.; Vigil-Fowler, D.; Siol, S.; Scanlon, D. O.; Zakutayev, A.; Walsh, A.; Smith, I. C.; Melot, B. C.; Kurchin, R. C.; Wang, Y.; Shi, J.; Marques, F. C.; Berry, J. J.; Tumas, W.; Lany, S.; Stevanović, V.; Toney, M. F.; Buonassisi, T. Perovskite-Inspired Photovoltaic Materials: Toward Best Practices in Materials Characterization and Calculations. *Chem. Mater.* **2017**, *29* (5), 1964–1988. <https://doi.org/10.1021/acs.chemmater.6b03852>.
- (65) Makonnen, Y.; Beauchemin, D. The Inductively Coupled Plasma as a Source for Optical Emission Spectrometry and Mass Spectrometry. In *Sample Introduction Systems in ICPMS and ICPOES*; Elsevier, 2020; pp 1–55. <https://doi.org/10.1016/B978-0-444-59482-2.00001-4>.
- (66) Olesik, J. W. ICP-OES. In *Encyclopedia of Materials Characterization*; Elsevier, 1992; pp 633–644. <https://doi.org/10.1016/B978-0-08-052360-6.50059-X>.

- (67) Zheng, D.; Volovitch, P.; Pauporté, T. What Can Glow Discharge Optical Emission Spectroscopy (GD-OES) Technique Tell Us about Perovskite Solar Cells? *Small Methods* **2022**, *6* (11), 2200633. <https://doi.org/10.1002/smt.202200633>.
- (68) Kodalle, T.; Greiner, D.; Brackmann, V.; Priezel, K.; Scheu, A.; Bertram, T.; Reyes-Figueroa, P.; Unold, T.; Abou-Ras, D.; Schlattmann, R.; Kaufmann, C. A.; Hoffmann, V. Glow Discharge Optical Emission Spectrometry for Quantitative Depth Profiling of CIGS Thin-Films. *J. Anal. At. Spectrom.* **2019**, *34* (6), 1233–1241. <https://doi.org/10.1039/C9JA00075E>.
- (69) Aidene, S.; Khaydukova, M.; Pashkova, G.; Chubarov, V.; Savinov, S.; Semenov, V.; Kirsanov, D.; Panchuk, V. Does Chemometrics Work for Matrix Effects Correction in X-Ray Fluorescence Analysis? *Spectrochim. Acta Part B At. Spectrosc.* **2021**, *185*, 106310. <https://doi.org/10.1016/j.sab.2021.106310>.
- (70) Elgrishi, N.; Rountree, K. J.; McCarthy, B. D.; Rountree, E. S.; Eisenhart, T. T.; Dempsey, J. L. A Practical Beginner's Guide to Cyclic Voltammetry. *J. Chem. Educ.* **2018**, *95* (2), 197–206. <https://doi.org/10.1021/acs.jchemed.7b00361>.
- (71) Di Girolamo, D.; Di Giacomo, F.; Matteocci, F.; Marrani, A. G.; Dini, D.; Abate, A. Progress, Highlights and Perspectives on NiO in Perovskite Photovoltaics. *Chem. Sci.* **2020**, *11* (30), 7746–7759. <https://doi.org/10.1039/D0SC02859B>.
- (72) Sajid, S.; Elseman, A. M.; Huang, H.; Ji, J.; Dou, S.; Jiang, H.; Liu, X.; Wei, D.; Cui, P.; Li, M. Breakthroughs in NiOx-HTMs towards Stable, Low-Cost and Efficient Perovskite Solar Cells. *Nano Energy* **2018**, *51*, 408–424. <https://doi.org/10.1016/j.nanoen.2018.06.082>.
- (73) Moumen, A.; Kumarage, G. C. W.; Comini, E. P-Type Metal Oxide Semiconductor Thin Films: Synthesis and Chemical Sensor Applications. *Sensors* **2022**, *22* (4), 1359. <https://doi.org/10.3390/s22041359>.
- (74) Liu, A.; Liu, G.; Zhu, H.; Song, H.; Shin, B.; Fortunato, E.; Martins, R.; Shan, F. Water-Induced Scandium Oxide Dielectric for Low-Operating Voltage n- and p-Type Metal-Oxide Thin-Film Transistors. *Adv. Funct. Mater.* **2015**, *25* (46), 7180–7188. <https://doi.org/10.1002/adfm.201502612>.
- (75) Ru, P.; Bi, E.; Zhang, Y.; Wang, Y.; Kong, W.; Sha, Y.; Tang, W.; Zhang, P.; Wu, Y.; Chen, W.; Yang, X.; Chen, H.; Han, L. High Electron Affinity Enables Fast Hole Extraction for Efficient Flexible Inverted Perovskite Solar Cells. *Adv. Energy Mater.* **2020**, *10* (12), 1903487. <https://doi.org/10.1002/aenm.201903487>.
- (76) Chen, W.; Wu, Y.; Fan, J.; Djurišić, A. B.; Liu, F.; Tam, H. W.; Ng, A.; Surya, C.; Chan, W. K.; Wang, D.; He, Z.-B. Understanding the Doping Effect on NiO: Toward High-Performance Inverted Perovskite Solar Cells. *Adv. Energy Mater.* **2018**, *8* (19), 1703519. <https://doi.org/10.1002/aenm.201703519>.
- (77) Chen, W.; Wu, Y.; Yue, Y.; Liu, J.; Zhang, W.; Yang, X.; Chen, H.; Bi, E.; Ashraful, I.; Grätzel, M.; Han, L. Efficient and Stable Large-Area Perovskite Solar Cells with Inorganic Charge Extraction Layers. *Science* **2015**, *350* (6263), 944–948. <https://doi.org/10.1126/science.aad1015>.
- (78) Hufnagel, A. G.; Henß, A.-K.; Hoffmann, R.; Zeman, O. E. O.; Häringer, S.; Fattakhova-Rohlfing, D.; Bein, T. Electron-Blocking and Oxygen Evolution Catalyst Layers by Plasma-Enhanced Atomic Layer Deposition of Nickel Oxide. *Adv. Mater. Interfaces* **2018**, *5* (16), 1701531. <https://doi.org/10.1002/admi.201701531>.
- (79) Nie, W.; Tsai, H.; Blancon, J.; Liu, F.; Stoumpos, C. C.; Traore, B.; Kepenekian, M.; Durand, O.; Katan, C.; Tretiak, S.; Crochet, J.; Ajayan, P. M.; Kanatzidis, Mercouri G.; Even, J.; Mohite, A. D. Critical Role of Interface and Crystallinity on the Performance and Photostability of Perovskite Solar Cell on Nickel Oxide. *Adv. Mater.* **2018**, *30* (5), 1703879. <https://doi.org/10.1002/adma.201703879>.
- (80) Kaneko, R.; Chowdhury, T. H.; Wu, G.; Kayesh, Md. E.; Kazaoui, S.; Sugawa, K.; Lee, J.-J.; Noda, T.; Islam, A.; Otsuki, J. Cobalt-Doped Nickel Oxide Nanoparticles as Efficient Hole Transport Materials for Low-Temperature Processed Perovskite Solar Cells. *Sol. Energy* **2019**, *181*, 243–250. <https://doi.org/10.1016/j.solener.2019.01.097>.

- (81) Lee, J. H.; Noh, Y. W.; Jin, I. S.; Park, S. H.; Jung, J. W. A Solution-Processed Cobalt-Doped Nickel Oxide for High Efficiency Inverted Type Perovskite Solar Cells. *J. Power Sources* **2019**, *412*, 425–432. <https://doi.org/10.1016/j.jpowsour.2018.11.081>.
- (82) Liu, A.; Zhu, H.; Guo, Z.; Meng, Y.; Liu, G.; Fortunato, E.; Martins, R.; Shan, F. Solution Combustion Synthesis: Low-Temperature Processing for p-Type Cu:NiO Thin Films for Transparent Electronics. *Adv. Mater.* **2017**, *29* (34), 1701599. <https://doi.org/10.1002/adma.201701599>.
- (83) Bashir, A.; Lew, J. H.; Shukla, S.; Gupta, D.; Baikie, T.; Chakraborty, S.; Patidar, R.; Bruno, A.; Mhaisalkar, S.; Akhter, Z. Cu-Doped Nickel Oxide Interface Layer with Nanoscale Thickness for Efficient and Highly Stable Printable Carbon-Based Perovskite Solar Cell. *Sol. Energy* **2019**, *182*, 225–236. <https://doi.org/10.1016/j.solener.2019.02.056>.
- (84) Teo, S.; Guo, Z.; Xu, Z.; Zhang, C.; Kamata, Y.; Hayase, S.; Ma, T. The Role of Lanthanum in a Nickel Oxide-Based Inverted Perovskite Solar Cell for Efficiency and Stability Improvement. *ChemSusChem* **2019**, *12* (2), 518–526. <https://doi.org/10.1002/cssc.201802231>.
- (85) Chen, X.; Xu, L.; Chen, C.; Wu, Y.; Bi, W.; Song, Z.; Zhuang, X.; Yang, S.; Zhu, S.; Song, H. Rare Earth Ions Doped NiO Hole Transport Layer for Efficient and Stable Inverted Perovskite Solar Cells. *J. Power Sources* **2019**, *444*, 227267. <https://doi.org/10.1016/j.jpowsour.2019.227267>.
- (86) Xia, X.; Jiang, Y.; Wan, Q.; Wang, X.; Wang, L.; Li, F. Lithium and Silver Co-Doped Nickel Oxide Hole-Transporting Layer Boosting the Efficiency and Stability of Inverted Planar Perovskite Solar Cells. *ACS Appl. Mater. Interfaces* **2018**, *10* (51), 44501–44510. <https://doi.org/10.1021/acsami.8b16649>.
- (87) Boyd, C. C.; Shallcross, R. C.; Moot, T.; Kerner, R.; Bertoluzzi, L.; Onno, A.; Kavadiya, S.; Chosy, C.; Wolf, E. J.; Werner, J.; Raiford, J. A.; de Paula, C.; Palmstrom, A. F.; Yu, Z. J.; Berry, J. J.; Bent, S. F.; Holman, Z. C.; Luther, J. M.; Ratcliff, E. L.; Armstrong, N. R.; McGehee, M. D. Overcoming Redox Reactions at Perovskite-Nickel Oxide Interfaces to Boost Voltages in Perovskite Solar Cells. *Joule* **2020**, *4* (8), 1759–1775. <https://doi.org/10.1016/j.joule.2020.06.004>.
- (88) Kumar, A.; Islam, R.; Pramanik, D.; Saraswat, K. On the Limit of Defect Doping in Transition Metal Oxides. *J. Vac. Sci. Technol. A* **2019**, *37* (2), 021505. <https://doi.org/10.1116/1.5055563>.
- (89) Traore, B.; Pedesseau, L.; Blancon, J.-C.; Tretiak, S.; Mohite, A. D.; Even, J.; Katan, C.; Kepenekian, M. Importance of Vacancies and Doping in the Hole-Transporting Nickel Oxide Interface with Halide Perovskites. *ACS Appl. Mater. Interfaces* **2020**, *12* (5), 6633–6640. <https://doi.org/10.1021/acsami.9b19457>.
- (90) Biesinger, M. C.; Payne, B. P.; Lau, L. W. M.; Gerson, A.; Smart, R. St. C. X-Ray Photoelectron Spectroscopic Chemical State Quantification of Mixed Nickel Metal, Oxide and Hydroxide Systems. *Surf. Interface Anal.* **2009**, *41* (4), 324–332. <https://doi.org/10.1002/sia.3026>.
- (91) Tkalych, A. J.; Yu, K.; Carter, E. A. Structural and Electronic Features of β -Ni(OH)₂ and β -NiOOH from First Principles. *J. Phys. Chem. C* **2015**, *119* (43), 24315–24322. <https://doi.org/10.1021/acs.jpcc.5b08481>.
- (92) Grosvenor, A. P.; Biesinger, M. C.; Smart, R. St. C.; McIntyre, N. S. New Interpretations of XPS Spectra of Nickel Metal and Oxides. *Surf. Sci.* **2006**, *600* (9), 1771–1779. <https://doi.org/10.1016/j.susc.2006.01.041>.
- (93) Imran, M.; Coskun, H.; Khan, N. A.; Ouyang, J. Role of Annealing Temperature of Nickel Oxide (NiOx) as Hole Transport Layer in Work Function Alignment with Perovskite. *Appl. Phys. A* **2021**, *127* (2), 117. <https://doi.org/10.1007/s00339-021-04283-5>.
- (94) Wang, A.; Cao, Z.; Wang, J.; Wang, S.; Li, C.; Li, N.; Xie, L.; Xiang, Y.; Li, T.; Niu, X.; Ding, L.; Hao, F. Vacancy Defect Modulation in Hot-Casted NiO Film for Efficient Inverted Planar Perovskite Solar Cells. *J. Energy Chem.* **2020**, *48*, 426–434. <https://doi.org/10.1016/j.jechem.2020.02.034>.
- (95) You, J.; Meng, L.; Song, T.-B.; Guo, T.-F.; Yang, Y. (Michael); Chang, W.-H.; Hong, Z.; Chen, H.; Zhou, H.; Chen, Q.; Liu, Y.; De Marco, N.; Yang, Y. Improved Air Stability of

- Perovskite Solar Cells via Solution-Processed Metal Oxide Transport Layers. *Nat. Nanotechnol.* **2016**, *11* (1), 75–81. <https://doi.org/10.1038/nnano.2015.230>.
- (96) Ratcliff, E. L.; Meyer, J.; Steirer, K. X.; Garcia, A.; Berry, J. J.; Ginley, D. S.; Olson, D. C.; Kahn, A.; Armstrong, N. R. Evidence for Near-Surface NiOOH Species in Solution-Processed NiO_x Selective Interlayer Materials: Impact on Energetics and the Performance of Polymer Bulk Heterojunction Photovoltaics. *Chem. Mater.* **2011**, *23* (22), 4988–5000. <https://doi.org/10.1021/cm202296p>.
- (97) Cremers, V.; Puurunen, R. L.; Dendooven, J. Conformality in Atomic Layer Deposition: Current Status Overview of Analysis and Modelling. *Appl. Phys. Rev.* **2019**, *6* (2), 021302. <https://doi.org/10.1063/1.5060967>.
- (98) Xie, L.-Y.; Xiao, D.-Q.; Pei, J.-X.; Huo, J.; Wu, X.; Liu, W.-J.; Ding, S.-J. Growth, Physical and Electrical Characterization of Nickel Oxide Thin Films Prepared by Plasma-Enhanced Atomic Layer Deposition Using Nickelocene and Oxygen Precursors. *Mater. Res. Express* **2020**, *7* (4), 046401. <https://doi.org/10.1088/2053-1591/ab82c9>.
- (99) Han, Q.; Hsieh, Y.-T.; Meng, L.; Wu, J.-L.; Sun, P.; Yao, E.-P.; Chang, S.-Y.; Bae, S.-H.; Kato, T.; Bermudez, V.; Yang, Y. High-Performance Perovskite/Cu(In,Ga)Se₂ Monolithic Tandem Solar Cells. *Science* **2018**, *361* (6405), 904–908. <https://doi.org/10.1126/science.aat5055>.
- (100) Magomedov, A.; Al-Ashouri, A.; Kasparavičius, E.; Strazdaite, S.; Niaura, G.; Jošt, M.; Malinauskas, T.; Albrecht, S.; Getautis, V. Self-Assembled Hole Transporting Monolayer for Highly Efficient Perovskite Solar Cells. *Adv. Energy Mater.* **2018**, *8* (32), 1801892. <https://doi.org/10.1002/aenm.201801892>.
- (101) Phung, N.; Verheijen, M.; Todinova, A.; Datta, K.; Verhage, M.; Al-Ashouri, A.; Köbler, H.; Li, X.; Abate, A.; Albrecht, S.; Creatore, M. Enhanced Self-Assembled Monolayer Surface Coverage by ALD NiO in p-i-n Perovskite Solar Cells. *ACS Appl. Mater. Interfaces* **2022**, *14* (1), 2166–2176. <https://doi.org/10.1021/acsami.1c15860>.
- (102) *Handbook of Electrochemistry*, 1st ed.; Zoski, C. G., Ed.; Elsevier: Amsterdam; Boston, 2007.
- (103) Pavlishchuk, V. V.; Addison, A. W. Conversion Constants for Redox Potentials Measured versus Different Reference Electrodes in Acetonitrile Solutions at 25°C. *Inorganica Chim. Acta* **2000**, *298* (1), 97–102. [https://doi.org/10.1016/S0020-1693\(99\)00407-7](https://doi.org/10.1016/S0020-1693(99)00407-7).
- (104) Chan, X.-H.; Robert Jennings, J.; Anower Hossain, Md.; Koh Zhen Yu, K.; Wang, Q. Characteristics of P-NiO Thin Films Prepared by Spray Pyrolysis and Their Application in CdS-Sensitized Photocathodes. *J. Electrochem. Soc.* **2011**, *158* (7), H733. <https://doi.org/10.1149/1.3590742>.
- (105) Cook, S. K.; Horrocks, B. R. Heterogeneous Electron-Transfer Rates for the Reduction of Viologen Derivatives at Platinum and Bismuth Electrodes in Acetonitrile. *ChemElectroChem* **2017**, *4* (2), 320–331. <https://doi.org/10.1002/celec.201600536>.
- (106) Barth, C.; Foster, A. S.; Henry, C. R.; Shluger, A. L. Recent Trends in Surface Characterization and Chemistry with High-Resolution Scanning Force Methods. *Adv. Mater.* **2011**, *23* (4), 477–501. <https://doi.org/10.1002/adma.201002270>.
- (107) Mansour, A. N. Characterization of NiO by XPS. *Surf. Sci. Spectra* **1994**, *3* (3), 231–238. <https://doi.org/10.1116/1.1247751>.
- (108) Mansour, A. N.; Melendres, C. A. Characterization of Electrochemically Prepared γ -NiOOH by XPS. *Surf. Sci. Spectra* **1994**, *3* (3), 271–278. <https://doi.org/10.1116/1.1247756>.
- (109) Mansour, A. N. Characterization of β -Ni(OH)₂ by XPS. *Surf. Sci. Spectra* **1994**, *3* (3), 239–246. <https://doi.org/10.1116/1.1247752>.
- (110) Mansour, A. N.; Melendres, C. A. Characterization of α -Ni(OH)₂ by XPS. *Surf. Sci. Spectra* **1994**, *3* (3), 255–262. <https://doi.org/10.1116/1.1247754>.
- (111) Gupta, R. P.; Sen, S. K. Calculation of Multiplet Structure of Core p-Vacancy Levels. *Phys. Rev. B* **1974**, *10* (1), 71–77. <https://doi.org/10.1103/PhysRevB.10.71>.
- (112) Gupta, R. P.; Sen, S. K. Calculation of Multiplet Structure of Core p-Vacancy Levels. II. *Phys. Rev. B* **1975**, *12* (1), 15–19. <https://doi.org/10.1103/PhysRevB.12.15>.

- (113) Major, G. H.; Fairley, N.; Sherwood, P. M. A.; Linford, M. R.; Terry, J.; Fernandez, V.; Artyushkova, K. Practical Guide for Curve Fitting in X-Ray Photoelectron Spectroscopy. *J. Vac. Sci. Technol. A* **2020**, *38* (6), 061203. <https://doi.org/10.1116/6.0000377>.
- (114) Uhlenbrock, S.; Scharfschwerdt, C.; Illing, G.; Freund, H.-J. The Influence of Defects on the Ni 2p and O 1s XPS of NiO.
- (115) Wu, W.-F.; Chiou, B.-S. Effect of Annealing on Electrical and Optical Properties of RF Magnetron Sputtered Indium Tin Oxide Films. *Appl. Surf. Sci.* **1993**, *68* (4), 497–504. [https://doi.org/10.1016/0169-4332\(93\)90233-2](https://doi.org/10.1016/0169-4332(93)90233-2).
- (116) Pu, H.; Dai, H.; Zhang, T.; Dong, K.; Wang, Y.; Deng, Y. Metal Nanoparticles with Clean Surface: The Importance and Progress. *Curr. Opin. Electrochem.* **2022**, *32*, 100927. <https://doi.org/10.1016/j.coelec.2021.100927>.
- (117) Wang, Z.; Fang, J.; Mi, Y.; Zhu, X.; Ren, H.; Liu, X.; Yan, Y. Enhanced Performance of Perovskite Solar Cells by Ultraviolet-Ozone Treatment of Mesoporous TiO₂. *Appl. Surf. Sci.* **2018**, *436*, 596–602. <https://doi.org/10.1016/j.apsusc.2017.12.085>.
- (118) Almora, O.; Zhao, Y.; Du, X.; Heumueller, T.; Matt, G. J.; Garcia-Belmonte, G.; Brabec, C. J. Light Intensity Modulated Impedance Spectroscopy (LIMIS) in All-Solid-State Solar Cells at Open-Circuit. *Nano Energy* **2020**, *75*, 104982. <https://doi.org/10.1016/j.nanoen.2020.104982>.
- (119) Lopez-Varo, P.; Jiménez-Tejada, J. A.; García-Rosell, M.; Ravishankar, S.; Garcia-Belmonte, G.; Bisquert, J.; Almora, O. Device Physics of Hybrid Perovskite Solar Cells: Theory and Experiment. *Adv. Energy Mater.* **2018**, *8* (14), 1702772. <https://doi.org/10.1002/aenm.201702772>.
- (120) Rakita, Y.; Lubomirsky, I.; Cahen, D. When Defects Become ‘Dynamic’: Halide Perovskites: A New Window on Materials? *Mater. Horiz.* **2019**, *6* (7), 1297–1305. <https://doi.org/10.1039/C9MH00606K>.
- (121) Yuan, Y.; Huang, J. Ion Migration in Organometal Trihalide Perovskite and Its Impact on Photovoltaic Efficiency and Stability. *Acc. Chem. Res.* **2016**, *49* (2), 286–293. <https://doi.org/10.1021/acs.accounts.5b00420>.
- (122) Moghadamzadeh, S.; Hossain, I. M.; Duong, T.; Gharibzadeh, S.; Abzieher, T.; Pham, H.; Hu, H.; Fassel, P.; Lemmer, U.; Nejad, B. A.; Paetzold, U. W. Triple-Cation Low-Bandgap Perovskite Thin-Films for High-Efficiency Four-Terminal All-Perovskite Tandem Solar Cells. *J. Mater. Chem. A* **2020**, *8* (46), 24608–24619. <https://doi.org/10.1039/D0TA07005J>.
- (123) Saliba, M.; Matsui, T.; Seo, J.-Y.; Domanski, K.; Correa-Baena, J.-P.; Nazeeruddin, M. K.; Zakeeruddin, S. M.; Tress, W.; Abate, A.; Hagfeldt, A.; Grätzel, M. Cesium-Containing Triple Cation Perovskite Solar Cells: Improved Stability, Reproducibility and High Efficiency. *Energy Environ. Sci.* **2016**, *9* (6), 1989–1997. <https://doi.org/10.1039/C5EE03874J>.
- (124) Li, B.; Shen, T.; Yun, S. Recent Progress of Crystal Orientation Engineering in Halide Perovskite Photovoltaics. *Mater. Horiz.* **2023**, *10* (1), 13–40. <https://doi.org/10.1039/D2MH00980C>.
- (125) Abdolazadeh Ziabari, A.; Rozati, S. M. Carrier Transport and Bandgap Shift in N-Type Degenerate ZnO Thin Films: The Effect of Band Edge Nonparabolicity. *Phys. B Condens. Matter* **2012**, *407* (23), 4512–4517. <https://doi.org/10.1016/j.physb.2012.08.024>.
- (126) Chiang, S.-E.; Chandel, A.; Thakur, D.; Chen, Y.-T.; Lin, P.-C.; Wu, J.-R.; Cai, K.-B.; Kassou, S.; Yeh, J.-M.; Yuan, C.-T.; Shen, J.-L.; Chang, S. H. On the Role of Solution-Processed Bathocuproine in High-Efficiency Inverted Perovskite Solar Cells. *Sol. Energy* **2021**, *218*, 142–149. <https://doi.org/10.1016/j.solener.2021.02.047>.
- (127) Schulz, P.; Cahen, D.; Kahn, A. Halide Perovskites: Is It All about the Interfaces? *Chem. Rev.* **2019**, *119* (5), 3349–3417. <https://doi.org/10.1021/acs.chemrev.8b00558>.
- (128) Azmi, R.; Hadmojo, W. T.; Sinaga, S.; Lee, C.-L.; Yoon, S. C.; Jung, I. H.; Jang, S.-Y. High-Efficiency Low-Temperature ZnO Based Perovskite Solar Cells Based on Highly Polar, Nonwetting Self-Assembled Molecular Layers. *Adv. Energy Mater.* **2018**, *8* (5), 1701683. <https://doi.org/10.1002/aenm.201701683>.

- (129) Fu, F.; Feurer, T.; Weiss, T. P.; Pisoni, S.; Avancini, E.; Andres, C.; Buecheler, S.; Tiwari, A. N. High-Efficiency Inverted Semi-Transparent Planar Perovskite Solar Cells in Substrate Configuration. *Nat. Energy* **2017**, *2* (1), 16190. <https://doi.org/10.1038/nenergy.2016.190>.
- (130) Correa Baena, J. P.; Steier, L.; Tress, W.; Saliba, M.; Neutzner, S.; Matsui, T.; Giordano, F.; Jacobsson, T. J.; Srimath Kandada, A. R.; Zakeeruddin, S. M.; Petrozza, A.; Abate, A.; Nazeeruddin, M. K.; Grätzel, M.; Hagfeldt, A. Highly Efficient Planar Perovskite Solar Cells through Band Alignment Engineering. *Energy Environ. Sci.* **2015**, *8* (10), 2928–2934. <https://doi.org/10.1039/C5EE02608C>.
- (131) Xiong, L.; Guo, Y.; Wen, J.; Liu, H.; Yang, G.; Qin, P.; Fang, G. Review on the Application of SnO₂ in Perovskite Solar Cells. *Adv. Funct. Mater.* **2018**, *28* (35), 1802757. <https://doi.org/10.1002/adfm.201802757>.
- (132) Jiang, Q.; Zhang, X.; You, J. SnO₂: A Wonderful Electron Transport Layer for Perovskite Solar Cells. *Small* **2018**, *14* (31), 1801154. <https://doi.org/10.1002/smll.201801154>.
- (133) Béchu, S.; Loubat, A.; Bouttemy, M.; Vigneron, J.; Gentner, J.-L.; Etcheberry, A. A Challenge for X-Ray Photoelectron Spectroscopy Characterization of Cu(In,Ga)Se₂ Absorbers: The Accurate Quantification of Ga/(Ga + In) Ratio. *Thin Solid Films* **2019**, *669*, 425–429. <https://doi.org/10.1016/j.tsf.2018.11.029>.
- (134) Loubat, A.; Béchu, S.; Bouttemy, M.; Vigneron, J.; Lincot, D.; Guillemoles, J.-F.; Etcheberry, A. Cu Depletion on Cu(In,Ga)Se₂ Surfaces Investigated by Chemical Engineering: An x-Ray Photoelectron Spectroscopy Approach. *J. Vac. Sci. Technol. A* **2019**, *37* (4), 041201. <https://doi.org/10.1116/1.5097353>.
- (135) Béchu, S.; Bouttemy, M.; Guillemoles, J.-F.; Etcheberry, A. The Influence of Relative Humidity upon Cu(In,Ga)Se₂ Thin-Film Surface Chemistry: An X-Ray Photoelectron Spectroscopy Study. *Appl. Surf. Sci.* **2022**, *576*, 151898. <https://doi.org/10.1016/j.apsusc.2021.151898>.
- (136) Béchu, S.; Bouttemy, M.; Vigneron, J.; Lincot, D.; Guillemoles, J.; Etcheberry, A. Evolution of Cu(In,Ga)Se₂ Surfaces under Water Immersion Monitored by X-ray Photoelectron Spectroscopy. *Surf. Interface Anal.* **2020**, *52* (12), 975–979. <https://doi.org/10.1002/sia.6896>.
- (137) Loubat, A.; Eypert, C.; Mollica, F.; Bouttemy, M.; Naghavi, N.; Lincot, D.; Etcheberry, A. Optical Properties of Ultrathin CIGS Films Studied by Spectroscopic Ellipsometry Assisted by Chemical Engineering. *Appl. Surf. Sci.* **2017**, *421*, 643–650. <https://doi.org/10.1016/j.apsusc.2016.10.037>.

Annexe

Chapter 3

Table S.1 Peak parameters for XPS fitting in the Ni 2p_{3/2} region

Peak position (eV)	Peak 1	Peak 2	Peak 3	Peak 4	Peak 5	Peak 6	Peak 7
NiO (A)	853.7 ± 0.2	A + 1.7	A + 7.2	A + 10.3	A + 12.8	-	-
Ni ⁰ (B)	852.6 ± 0.2	B + 3.7	B + 6.1	-	-	-	-
α-Ni(OH) ₂ (C)	855.9 ± 0.2	C + 0.8	C + 2.8	C + 5.6	C + 6.6	C + 11.6	-
γ-NiOOH (D)	854.4 ± 0.2	D + 0.7	D + 1.06	D + 1.84	D + 2.17	D + 3.37	D + 8.75
β-NiOOH (3+) (E)	854.6 ± 0.2	E + 0.7	E + 1.06	E + 1.84	E + 2.17	E + 5.37	E + 8.75
β-NiOOH (2+) (F)	854.9 ± 0.2	F + 0.8	F + 2.8	F + 5.6	F + 6.6	F + 11.6	-

Area constraint	Peak 1	Peak 2	Peak 3	Peak 4	Peak 5	Peak 6	Peak 7
NiO (A)	A	A*3.09	A*2.38	A*0.25	A*.027	-	-
Ni ⁰ (B)	B	B*0.08	B*0.015	-	-	-	-
α-Ni(OH) ₂ (C)	C	C*6.12	C*0.41	C*0.19	C*5.30	C*0.50	-
γ-NiOOH (D)	D	D*0.90	D*0.70	D*1.50	D*0.63	D*1.69	D*0.83
β-NiOOH (3+) (E)	E	E*0.90	E*0.70	E*1.50	E*0.63	E*1.70	E*0.83
β-NiOOH (2+) (F)	F	F*6.04	F*0.40	F*0.20	F*5.24	F*0.48	-

FWHM (eV)	Peak 1	Peak 2	Peak 3	Peak 4	Peak 5	Peak 6	Peak 7
NiO	1.05 ± 0.05	3.25 ± 0.05	3.75 ± 0.05	2.05 ± 0.05	2.45 ± 0.05	-	-
Ni ⁰	0.95 ± 0.15	2.40 ± 0.2	1.45 ± 0.15	-	-	-	-
α-Ni(OH) ₂	1.15 ± 0.05	2.25 ± 0.05	1.55 ± 0.05	1.05 ± 0.05	4.65 ± 0.05	3.05 ± 0.05	-
γ-NiOOH	1.45 ± 0.05	1.55 ± 0.05	1.45 ± 0.05	1.45 ± 0.05	1.95 ± 0.05	4.05 ± 0.05	4.45 ± 0.05
β-NiOOH (3+)	1.45 ± 0.05	1.55 ± 0.05	1.45 ± 0.05	1.45 ± 0.05	1.975 ± 0.025	4.05 ± 0.05	4.45 ± 0.05
β-NiOOH (2+)	1.15 ± 0.05	2.25 ± 0.05	1.65 ± 0.05	1.1 ± 0.05	4.65 ± 0.05	3.15 ± 0.05	-

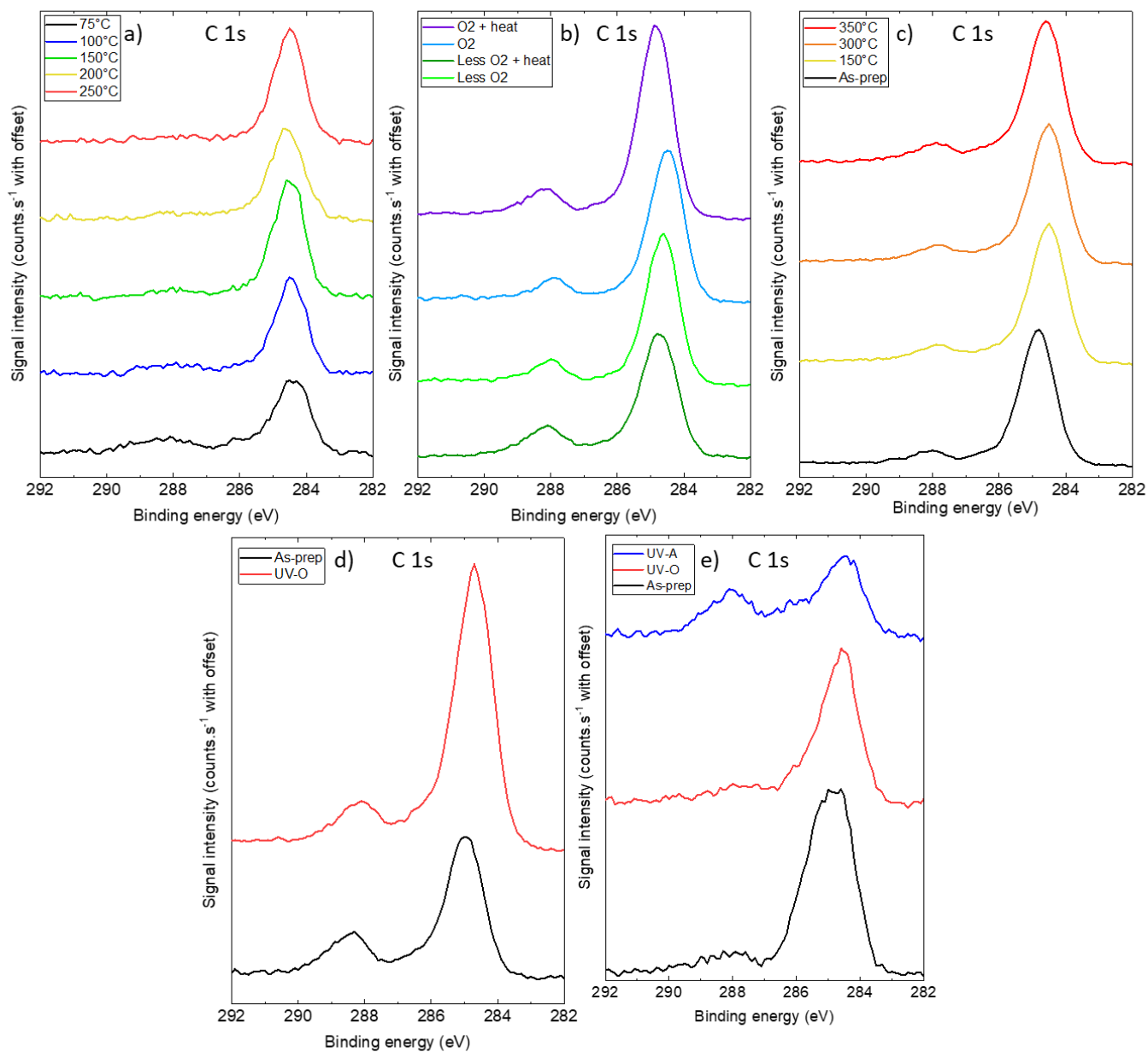


Figure S.1 XPS spectra in the C 1s region for (a) ALD-NiO_x samples from ZSW, (b) sputtered NiO_x samples from KIT, (c) sputtered NiO_x samples from IMEC, (d) sol-gel NiO_x samples and (e) NiO_x samples prepared by combustion process.

Résumé en Français

Au chapitre 3, nous avons étudié différentes méthodes de dépôt basse température pour la fabrication d'HTL pour cellules solaires en pérovskite de type p-i-n. Par voltammétrie cyclique nous avons d'abord évalué les propriétés de blocage des électrons de couches de NiO_x préparées à 100 °C et 160 °C par ALD, afin de déterminer une épaisseur optimale entre 10 nm et 15 nm en fonction de la température de dépôt. Ainsi, pour le développement de cellules solaires semi-transparentes au chapitre 4, les couches de NiO_x préparées par ALD utilisées pour les dispositifs ont été préparées à 160 °C avec une épaisseur de 15 nm.

Une deuxième partie était consacrée à l'étude des propriétés chimiques et électroniques de surface des films préparés par ALD au ZSW et par pulvérisation par IMEC et KIT au moyen d'analyses XPS, UPS et KPFM, afin de déterminer l'influence de la température de dépôt, de la température de recuit et de l'influence combinée de la température de recuit et du flux d'oxygène sur ces propriétés. Bien que les propriétés physiques des couches déposées n'aient pas pu être clairement associées à des modifications de la chimie en surface, nous avons pu identifier une tendance à une augmentation du travail de sortie (WF) avec l'augmentation de la concentration en NiO stœchiométrique. Néanmoins, seules de légères variations de la WF et de la VBM ont été observées malgré une modification significative de la concentration en NiO stœchiométrique. Les résultats étaient néanmoins plus prononcés dans le cas d'un recuit en atmosphère ambiante que pour des températures de dépôt sous vide.

Des cellules solaires ont été complétées au ZSW à partir de couches de NiO_x préparées à par ALD différentes températures de dépôt, afin de déterminer comment ce paramètre affecterait les performances des dispositifs photovoltaïques. Encore une fois, une tendance subtile mais cohérente a été observée avec des valeurs de PCE plus élevées à mesure que la concentration en NiO stœchiométrique augmentait.

Nous avons ensuite exploré la possibilité de modifier la chimie de surface des couches de NiO_x préparées par procédés sol-gel et par combustion en combinant des traitements UV-O₃ et des recuits courts à 250 °C. Bien qu'il ait été difficile de relier les effets de ces traitements à des modifications claires de la chimie de surface via analyse XPS, les dispositifs préparés à l'aide de films traités à l'UV-O₃ ont donné de moins performances photovoltaïques, tandis qu'une étape de recuit court après l'UV-O₃ a conduit à une augmentation du *FF* et du PCE. Les meilleurs PCE ont été obtenus par passivation de l'interface NiO_x/pérovskite en utilisant un excès de cations FAI, soit en traitant les échantillons de NiO_x avant le dépôt de la pérovskite, soit en ajoutant directement une quantité de FAI en excès dans la solution de précurseurs pérovskite. Les cellules solaires préparées à partir de ces échantillons se

sont distinguées par des valeurs particulièrement élevées de V_{oc} , pour des valeurs de PCE maximales supérieures à 16 %.

Enfin, nous avons évalué les performances photovoltaïques des cellules solaires perovskite utilisant les molécules 2PACz et MeO-2PACz comme couches de transport de trous et des paramètres PV similaires ont été obtenus avec les deux matériaux. Des PCE maximales supérieures à 16 % ont également été obtenues. Les propriétés morphologiques et structurales des couches de pérovskite déposées sur des couches NiO_x ou MeO-2PACz ont ensuite été étudiées par SEM et XRD. Des tailles de grains similaires entre 160 nm et 180 nm ont été mesurées avec les deux HTL, mais nous avons observé une prévalence plus élevée de l'orientation (001) pour la couche de pérovskite déposée sur du MeO-2PACz. Dans la littérature, cette orientation a été liée à de meilleures propriétés optoélectroniques de la couche de pérovskite, du moins pour les compositions de type MAPI. Nous concluons donc qu'établir une interface MeO-2PACz/pérovskite dans l'architecture p-i-n serait préférable à une interface NiO_x /pérovskite pour maximiser les performances. Cependant, la présence d'une couche de NiO_x pourrait toujours être bénéfique dans le cas de cellules tandem, pour la conception d'une jonction tunnel appropriée ou pour compléter la couverture d'une couche de blocage d'électrons.

Au chapitre 4, nous avons décrit le développement d'un processus de fabrication de cellules solaires en pérovskite semi-transparente grâce à l'introduction d'une couche ETL d'oxyde métallique. Dans la première partie de ce chapitre, nous avons brièvement décrit nos premières tentatives de réalisation de cellules solaires en pérovskite semi-transparente basées sur une double couche ETL organique. En raison du processus de pulvérisation de TCO qui endommageait les couches de PCBM et de BCP, des valeurs de PCE très faibles ont été obtenues quelles que soient les conditions de dépôt par tournette et donc l'épaisseur des couches. Ensuite, nous avons étudié la substitution de la couche de BCP dans notre architecture par une couche ZnO ou AZO sous forme de nanoparticules en tant que couche tampon par-dessus la couche de PCBM. Des paramètres PV équivalents, voire supérieurs, ont été mesurés dans les deux cas par rapport à la combinaison PCBM/BCP.

Par des étapes d'optimisation ultérieures, nous avons déterminé que le np-ZnO présentait une meilleure stabilité dans le temps par rapport au np-AZO et il a finalement été possible de fabriquer des cellules solaires semi-transparentes basées sur une double couche PCBM/np-ZnO ETL et une couche de fenêtre d'AZO pulvérisée. Cette architecture a montré des paramètres PV comparables à ceux des dispositifs opaques utilisant la même ETL.

Une dernière étape de développement nous a permis d'évaluer les paramètres PV en éclairage avant et arrière pour les cellules solaires semi-transparentes utilisant soit une double couche PCBM/np-ZnO, soit une double couche C_{60}/SnO_2 en tant qu'ETL, et ITO ou AZO en tant que couche fenêtre

avant. Nous avons observé des valeurs de J_{sc} particulièrement faibles à partir des mesures J-V et EQE pour les dispositifs utilisant à la fois PCBM/np-ZnO et ITO, probablement en raison d'un problème de contact électrique entre le ZnO et l'ITO. Les meilleurs paramètres PV en éclairage avant et arrière ont été obtenus en utilisant C_{60}/SnO_2 et ITO, probablement en raison d'un meilleur contact électrique et d'une plus grande transmittance des matériaux.

Au chapitre 5, nous avons décrit une procédure d'arasage par une solution HBr:Br₂:H₂O pour réduire la rugosité des couches absorbantes CI(G)S et faciliter la déposition des couche de la cellule pérovskite dans une architecture tandem. Ce procédé était basé sur une méthode essentiellement déjà décrite pour le CIGS et adaptée aux couches absorbantes à bande interdite basse. Dans la première partie, nous nous sommes concentrés sur l'optimisation de la durée du processus et de la vitesse de rotation sur des échantillons d'une superficie inférieure ou égale à 2*2 cm², afin de minimiser la rugosité finale et l'épaisseur de la couche CI(G)S sacrifiée. Nous avons ainsi déterminé que l'arasage de l'échantillon pendant 2 minutes à 40 tours par minute constituait un bon compromis entre ces deux paramètres, conduisant à des valeurs de rugosité RMS inférieures à 20 nm avec une perte de couche de 400 nm.

Ensuite, nous avons vérifié l'homogénéité d'épaisseur des échantillons préparés et lissés, avec des valeurs similaires mesurées sur des échantillons de 2*2 cm² et une bonne homogénéité de l'échantillon parent CI(G)S de 5*5 cm². Nous avons également démontré la reproductibilité de notre protocole en analysant la composition de nos solutions au brome après lissage avec ICP-OES. En effet, une forte corrélation linéaire entre les concentrations en cuivre, indium In et sélénium Se dans la solution abrasive et le temps de traitement à 40 tours par minute a été observée, et les concentrations étaient également plutôt similaires dans le cas de trois échantillons traités pendant 4 minutes à 30 tours par minute.

Nous avons donc étudié l'effet du traitement au brome, suivi ou non d'un traitement au KCN, sur la chimie de surface du CI(G)S. Après planarisation au brome, celle-ci est fortement altérée par la formation d'une couche superficielle de Se⁰, une relative oxydation de l'indium et la lixiviation partielle de Na. La chimie d'origine des éléments Se et In était en grande partie restaurée après le traitement au KCN, mais la concentration en Na était toujours inférieure à celle de la couche initiale. De plus, les concentrations en Cu et In sont restées plutôt similaires entre les échantillons non traités et ceux traités au brome, tandis que la concentration en Se a légèrement augmenté et que le gallium a commencé à émerger en tant que constituant de la surface.

Enfin, nous avons préparé des cellules solaires à partir de couches CI(G)S avec ou sans abrasae au brome, toutes deux traitées au KCN. Avec un dispositif de chaque condition, des paramètres PV similaires ont été observés, à l'exception du J_{sc} , légèrement plus élevé pour l'échantillon non planarisé,

ce qui a entraîné une légère augmentation du PCE. En effet, une surface semblable à un miroir est obtenue après le lissage, qui est moins efficace que le CI(G)S rugueux pour piéger les photons réfléchis dans la couche. Cette différence a probablement entraîné une diminution de l'intensité dans la région de l'EQE caractéristique des franges d'interférence pour les couches à base d'oxyde de zinc, telles que les couches de ZnMgO et d'AZO utilisées pour les dispositifs.

Dans l'ensemble, nous avons démontré que le processus d'arasage conçu pour le CIGS pouvait facilement être adapté au CI(G)S à faible bande interdite. Cependant, des mesures J-V devraient être répétées sur un plus grand nombre d'échantillons pour confirmer davantage que V_{oc} et FF ne sont pas affectés par le traitement.

Un dispositif d'arasage brome pour des couches plus large a été établi à l'ILV, avec des premiers résultats prometteurs sur des couches CI(G)S préparées par dépôt séquentiels. Néanmoins, les cellules réalisées à partir de échantillons ne fonctionnaient pas, et nous avons pour plan d'effectuer l'abrasage à plus grande échelle et la fabrication de cellules à partir de couches CIGS préparées par co-évaporation.

Sur la base du développement des chapitres 3 et 4, des prototypes de cellules solaires tandem monolithiques ont été réalisées à l'IPVF.

Pour le premier prototype, la sous-cellule était constituée d'une couche d'absorbeur CIGS déposée par co-évaporation sur une couche Mo, suivie du dépôt par CBD d'une couche tampon Zn(O,S), puis de la pulvérisation de couches ZnMgO et d'AZO. La double couche HTL de la pérovskite était composée d'une couche NiO_x déposée par ALD et d'une couche de MeO-2PACz. Le substrat de 1*2,5 cm² était divisé en 8 cellules, avec les paramètres PV suivants pour les cellules championnes : $V_{oc} = 1,31$ V, $J_{sc} = 8,60$ mA.cm⁻², FF = 21,1 % et PCE = 2,40 %.

En ce qui concerne le deuxième prototype, la sous-cellule était constituée d'une couche d'absorbeur CI(G)S à bande interdite basse déposée par co-évaporation sur du Mo, suivie du dépôt d'une couche tampon Zn(O,S), puis de la pulvérisation de ZnMgO et d'AZO. MeO-2PACz a été utilisée comme seule couche HTL de la cellule supérieure pérovskite. Le substrat de 2,5*2,5 cm² était divisé en 6 cellules, avec les paramètres PV suivants pour la cellule championne : $V_{oc} = 1,09$ V, $J_{sc} = 14,12$ mA.cm⁻², FF = 50,14 % et PCE = 7,75 %.

Les deux sous-cellules pérovskites avaient été complétées par le dépôt d'une double couche ETL PCBM/np-ZnO et d'une couche fenêtre AZO synthétisée par pulvérisation.

Titre : Intégration et optimisation de cellules solaires tandem monolithique pérovskite/CI(G)S.

Mots clés : Photovoltaïque, Cellule solaire, pérovskites hybrides halogénées, CIGS, CIS, CI(G)S, Cellule solaire tandem, deux terminaux, Planarisation, Oxyde de nickel

Résumé : Pour plusieurs applications industrielles, il existe un intérêt pour les cellules solaires légères et flexibles. Les technologies à films minces sont déjà utilisées à cette effet, mais pourraient être combinées dans une architecture tandem afin d'améliorer les performances de ces dispositifs.

Dans cette étude, nous examinons la possibilité de combiner des couches d'absorbeur CIGS et pérovskite dans une configuration tandem monolithique, afin d'exploiter la possibilité pour les deux matériaux de régler leur bande interdite en modifiant leur composition chimique. La technologie CIGS a été développée pour des applications photovoltaïque dans les années 1970, et est encore utilisée aujourd'hui dans des dispositifs flexibles.

D'autre part, les cellules solaires à base de pérovskite halogénée existent seulement depuis la dernière décennie, mais offrent déjà la promesse de panneaux solaires flexibles à faible coût et à haut rendement, malgré des inquiétudes concernant leur stabilité environnementale à long terme.

Les principaux défis liés à l'intégration monolithique des dispositifs pérovskite/CIGS ont été établis dans la littérature et abordés par différentes approches. Principalement, les couches de la sous-cellule pérovskite doivent être déposées à basse température pour éviter la dégradation de la sous-cellule CIGS, dont la rugosité de surface élevée peut entraver le dépôt conforme desdites couches.

La première partie de cette thèse est consacrée à l'étude de procédés à basse température dans la réalisation de couches HTL afin d'obtenir des cellules solaires à haut rendement à base de pérovskite. Nous commençons par étudier les propriétés de blocage d'électrons de couches de NiO_x déposées par ALD, ainsi que la chimie de surface et les propriétés électroniques de films NiO_x pour différentes températures de dépôt, de recuit, et différents traitements. Nous évaluons ensuite comment ces modifications affectent les performances photovoltaïques des dispositifs.

Au cours du deuxième chapitre, nous décrivons l'adaptation d'une architecture de cellule solaire p-i-n opaque à une configuration semi-transparente, nécessaire pour les applications en tandem. Nous considérons donc l'intégration de différents oxydes à cette architecture pour la rendre plus résiliente à des dépôts par pulvérisation.

Enfin, nous étudions la planarisation par voie chimique des couches d'absorbeur CI(G)S à partir d'un protocole bien établi pour les échantillons de CIGS. Après avoir optimisé le processus d'abrasage au bromure et traité l'échantillon pour obtenir la morphologie et chimie de surface souhaitées du CI(G)S, nous évaluons l'impact du traitement complet sur les performances des cellules solaires.

Title: Integration and optimization of perovskite/CI(G)S monolithic tandem solar cells.

Keywords: Photovoltaics, Perovskite solar cell, CIGS, CIS, CI(G)S, Tandem solar cell, Two-terminal, Planarization, Nickel oxide

Abstract: For several industrial applications, there is an interest for lightweight, flexible solar cells. Thin film technologies are already employed for this purpose, but could be combined in tandem architecture to further improve the performances of such devices. Here we study the possibility to combine CIGS and perovskite absorber layers in a monolithic tandem design, in order to exploit the possibility for both materials to change their bandgap by modifying their chemical composition.

CIGS is a photovoltaic technology developed in the 1970s decade that is still employed to this day for flexible applications. On the other hand, lead halide perovskite solar cells exist since only since the last decade but already hold the promise of low-cost, high efficiency flexible solar panels, despite concerns regarding their long-term environmental stability.

The main challenges concerning monolithic integration of perovskite/CIGS devices have been established in literature, and tackled by various approaches. Mainly, the layers of the perovskite top cell should be deposited at low-temperatures to avoid the degradation of the CIGS bottom cell, whose high surface roughness can hinder the conformal deposition of said layers.

The first part of this thesis is dedicated to the study of low-temperature route HTL for high efficiency perovskite solar cells. We start by investigating the electron blocking properties of ALD NiO_x layers films, as well as the surface chemistry and electronic properties of NiO_x films for different deposition temperature, post-annealing temperatures and surface modification protocols. We then study the effect of these treatments on complete solar cells. During the second chapter, we describe the adaptation of a p-i-n opaque solar cell architecture to a semi-transparent configuration, necessary for tandem applications. We therefore consider several metal oxide options to integrate in the solar cell architecture to make it more resilient towards harsh sputtering processes.

Finally, we studied the possibility to minimize the roughness of CI(G)S absorber layers from a wet process protocol well-established for CIGS samples. After optimizing the Br-etching process and treating the sample to yield the desired CI(G)S morphology and surface chemistry, we evaluate the impact of the whole treatment over the performances of complete solar cells.

